



UNIVERSITÉ DE LA ROCHELLE

Ecole Doctorale Euclide

UMR 7266 LIENSs - Littoral Environnement et Sociétés

PhD Thesis

by

BRIEUC RIOU

Presented on

08/11/2019

for the grade of:

Docteur de l'Université de La Rochelle

Shallow marine sediment record of tsunamis: analysis of the sediment-fill of the bays of Tutuila (American Samoa) and backwash deposits of the 2009 South Pacific Tsunami

Jury:

Xavier Bertin	Chargé de recherche, LIENSs	President
Eric Chaumillon	Professeur, Université de La Rochelle	Supervisor
Jean-Luc Schneider	Professeur, Université de Bordeaux	Supervisor
Raphaël Paris	Chargé de recherche, LMV	Rapporteur
Laurent Dezileau	Professeur, Université de Caen	Rapporteur
Pedro Costa	Lecturer, University of Coimbra	Examiner
Max Engel	Research assistant, University of Cologne	Examiner



UNIVERSITÉ DE LA ROCHELLE

Ecole Doctorale Euclide

UMR 7266 LIENSs - Littoral Environnement et Sociétés

PhD Thesis

by

BRIEUC RIOU

Presented on

08/11/2019

for the grade of:

Docteur de l'Université de La Rochelle

Shallow marine sediment record of tsunamis: analysis of the sediment-fill of the bays of Tutuila (American Samoa) and backwash deposits of the 2009 South Pacific Tsunami

Jury:

Xavier Bertin	Chargé de recherche, LIENSs	President
Eric Chaumillon	Professeur, Université de La Rochelle	Supervisor
Jean-Luc Schneider	Professeur, Université de Bordeaux	Supervisor
Raphaël Paris	Chargé de recherche, LMV	Rapporteur
Laurent Dezileau	Professeur, Université de Caen	Rapporteur
Pedro Costa	Lecturer, University of Coimbra	Examiner
Max Engel	Research assistant, University of Cologne	Examiner

A Mamie

A Pappy

Acknowledgments

That's it! The time has come to open a new chapter as an adult once and for all. With these lines, I leave behind me 8 long years of studies that I will never forget. Those years were full of passionate learning, never-ending nights getting ready for tests, but most of all of amazing encounters and so many wonderful people. Since I was a little kid, I have always been mesmerized by the mysteries of rocks, and this passion led me all the way to where I am now, about to become a "Doctor of rocks".

First of all, I would like to thank warmly the members of my jury for accepting to review this work I have spent the last three years of my life on. Thank you Raphaël Paris and Laurent Dezileau for the time you are about to spend reading this memoir in the slightest details. Thank you Pedro Costa and Max Engel for taking part in the examination of my work. I have no doubt on the fact that this defense will lead to fruitful discussions with such experts on the matter.

Then, my thoughts naturally go to my two supervisors, Jean-Luc and Eric, who placed all their trust in me after just a few chats and have helped me as much as they could throughout these three years. Thank you Jean-Luc for welcoming me in the EPOC Lab in Bordeaux as soon as I arrived. You were the first person I dealt with when arriving in Bordeaux and you managed to get me comfortable straight away with your joyful mood and your passion for sedimentology. Despite your personal obligations and your overbooked schedule, you allowed me to keep my autonomy and independence and answered present whenever I asked for help. I admire your cultural and scientific knowledge and I am forever grateful for sharing part of it with me. Thank you Eric for keeping an eye on me all the way from the start, and especially through this last year when I needed advice the most. You were always ready to take some time away from your own projects to spend some time with me, and contributed largely to the smooth running of this PhD. You will remain for me an example of pedagogy and vulgarization, which is a side of the research world that is not enough cultivated. I wish you two good luck for the years to come and I will leave this PhD with a new mind.

I also wish to thank all the people who took part in one way or another in this work. First comes all of you who participated actively during the different phases of this work. Thank you Catherine for your precious knowledge on everything remotely related to tsunamis and for all the time you spent looking for answers and advising and reviewing me during the writing of my articles.

Thank you Thierry for taking over when neither Jean-Luc or Eric were available, and your precious advice on paleo-climatology. Thank you Pierre for initiating me to radionuclide dating and helping me all along the interpretation of the results, and for your unfailing support when I needed it. Thank you Sabine for accepting to help me with radionuclide dating despite a very late call out and your tight schedule. Thank you J.P. for the interest you took in my work, along with Reide, and offering to help with dating issues. Thank you Atun and Daniela for the work you did in Sydney on core dating. And finally thank you Laurine and Johanna who helped me in the analyses of geophysical data and cores during their summer internships.

Then the SEDIMENTO team from the EPOC Lab and especially the members of the core analysis platform. Thank you Pascal, Olivier, Isabelle, Marie-Claire and Bernard for your precious help. I wouldn't have gone very far without you to guide me through the different protocols of the core analysis instruments. Thank you also Thierry M., Emmanuelle, Hervé, Thibault, Seb and Vincent. I should also thank the DPL team from the LIENSs Lab, especially Xavier, Makhail, Guy and Cecilia.

A great thank you also goes to all the member of the SAMOA-SPT campaign, from the cruise captain Jean-François Barazer to the crew of the *R/V Alii*, along with the scientific divers Stéphane Bujan and John Butscher, and Bruce Jaffe for his helped regarding the coordination of the field survey.

Before I even started this PhD, I have also met so many people who inspired me by their passion and pushed me to accomplish my dream. For this, I wish to thank first my high school teacher Mrs. Stervinou, who was the first teacher to push me towards geology studies. Then my prep school teachers, in particular Mr. Pruchon, Mrs. Guilloux and Mrs. Le Merdy, and all of my geology teachers from ENSG, Jean-Marc Montel, Mary Ford, Yves Géraud,... Finally I want to thank from the bottom of my heart Marina, Sidonie and Jean-Loup for everything you've done for me since I know you.

Then, of course, come all the friends. First all my friends from prep school, especially the BioSup 3: Thomas, François, Gabin, Polo, Jéjé, Romain, Benjamin, P.A., Baptiste, Juliette, Maïlys, Aurélie, Léna, Majorie and Margaux; but also the B1 and B2: Samo, Clément and Clément, Bitou, Briac, Robin, Juliette, Anna, Anouk and Marjorie. These two years with you were the hardest of my life but I think it's safe to say that we will remain friends for life. After that I want to thank all my friends from ENSG. The list would be too long so I will only mention my two roommates, Arthur and Mathieu who had to deal with me for two years, but you will all recognize yourselves. Finally all those embarked on the same boat: Antoine L., Eleanor, Léa, Paul, Kelly, Calypso, Simon,

Antoine C., Stan and Natacha for the long nights in Bordeaux; Treden and Jojo l'asticot, Marc, Baptiste and Clémence for the great spirit of the Bureau 102; Vincent, Mélanie, Victoria, Monia, Garance, Clément, Mannaig, Kevin, J.R., Raphaël, Laura, Mery, Camille and Yannick for the good times in La Rochelle. Keep up the good work guys!

Finally I will never thank enough all my family. Thank you Mom and Dad for always supporting me and advising me through all those years, no matter where I was or what I was doing. I owe you so much and I wouldn't be standing here if it wasn't for you. You have always inspired me so much. Thank you also to my little sister Fanny, we had our fights when we were young but we finally managed to get along! Good luck for the years to come and I'm sure you'll do great in your new vocation. I can't leave without thanking a thousand times Mamie Marie-Claire and Papy François for always supporting me and pushing me to go on, even when you didn't understand a thing I was doing. To Mamie Nicole and Papy Alain who went away too soon. Thank you for all the great times I spent with you, I know you would have been so proud of me.

My last words go to my new wife-to-be, Pauline. Thank you for standing by my side through these three long years. Thank you for all the motivation you gave me when I needed it, for cheering me up when I had my doubts, for sharing my enthusiasm. Simply: thank you! The end of this journey is also the beginning of a new one together. To us! "You're my best friend"

Table of contents

Acknowledgments.....	3
Table of contents.....	10
List of figures.....	14
List of tables.....	22
Chapter 1: Introduction	24
1.1 Context of the study.....	24
1.2 Objectives	27
Chapter 2: Geological evidence of tsunami backwash deposits in shallow marine environments: a review	30
2.1 Tsunami generation and propagation	31
2.1.1 Earthquake-induced tsunamis	31
2.1.2 Slide-induced tsunamis	32
2.1.3 Impact-induced tsunamis	32
2.1.4 Wave propagation.....	33
2.2 Coastal impacts of tsunamis.....	33
2.2.1 Onshore impacts of tsunamis.....	34
2.2.2 Nearshore impacts of tsunamis.....	37
2.2.3 Tsunami versus storms and cyclones	56
Chapter 3: The SAMOA-SPT campaign.....	60
3.1 Seafloor bathymetry and reflectivity	60
3.2 Seismic	60
3.3 Sediment cores	61
Chapter 4: The sediment-fill of Pago Pago Bay (Tutuila Island, American Samoa): new insights on the sediment record of past tsunamis	70

4.1	Abstract	71
4.2	Summary.....	72
4.3	Introduction.....	76
4.4	Study area and setting.....	78
4.5	Material and methods.....	80
4.5.1	Dataset	80
4.5.2	Analytical methods	82
4.6	Bay infilling	83
4.6.1	Sea-floor geomorphology	83
4.6.2	Subsurface seismic analysis	84
4.6.3	Core description	88
4.7	Discussion.....	95
4.7.1	Sequence stratigraphic interpretation of the Pago Pago bay-fill.....	95
4.7.2	The 2009 South Pacific Tsunami.....	97
4.7.3	Origin of coral debris.....	99
4.8	Conclusion	101
4.9	Acknowledgements.....	102
Chapter 5: Backwash sediment record of the 2009 South Pacific Tsunami and 1960 Great Chilean Earthquake Tsunami.....		104
5.1	Abstract	105
5.2	Summary.....	106
5.3	Introduction.....	109
5.4	Study area and setting.....	111
5.5	Material and methods.....	112
5.6	Results.....	114
5.6.1	Geophysical analysis.....	114
5.6.2	Grain size analysis	116

5.6.3	Geochemical analysis	116
5.6.4	Thin section analysis	119
5.6.5	²¹⁰ Pb and ¹³⁷ Cs Dating.....	121
5.7	Implications	122
5.8	Conclusion	125
5.9	Acknowledgments	126
Chapter 6: Offshore evidence for historic tsunamis on the north shore of Tutuila (American Samoa).....		128
6.1	Abstract	129
6.2	Summary.....	130
6.3	Introduction.....	133
6.4	Study area and setting.....	135
6.5	Material and methods.....	137
6.5.1	Dataset	137
6.5.2	Methods	138
6.6	Results.....	140
6.6.1	Sea-floor bathymetry.....	140
6.6.2	Cores.....	140
6.7	Discussion.....	147
6.7.1	Origin of anomalous layers	147
6.7.2	Dating of the backwash deposits	148
6.7.3	Potential events for EL4.....	151
6.8	Conclusion	153
6.9	Acknowledgment.....	154
Chapter 7: General discussion		156
7.1	Tsunami backwash deposits around Tutuila.....	156
7.1.1	Correlation of historic tsunami backwash deposits around Tutuila.....	156

7.1.2	Insights on paleotsunami archive in Pago Pago Bay.....	159
7.2	Progress in the field of tsunami backwash.....	161
7.2.1	New identification proxy for backwash deposits.....	161
7.2.2	Highly sheltered bays: ideal preservation potential for backwash deposits ...	162
7.2.3	Tsunami backwash deposits versus storm deposits	163
Chapter 8: Conclusion and perspectives.....		166
8.1	Reminder of the initial objectives.....	166
8.2	Main results.....	167
8.3	Perspectives	170
References		174

List of figures

Figure 1.1: Evolution of the number of published articles including the word tsunami, with three peaks in 2005, 2010 and 2012 following the 2004 IOT, the 2009 SPT and the 2011 TOT respectively, from Chagué-Goff <i>et al.</i> (2017).	24
Figure 1.2: A. Location of American Samoa in the Pacific Ocean (modified from Google Earth); B. Location of the earthquake epicenter marked by a red star with its magnitude (modified from Google Earth); C. Map of Tutuila with bathymetric data (modified from NOAA).....	26
Figure 2.1: Impact of the 2004 IOT on the coast of Banda Aceh (west Sumatra, Indonesia); A. dislodged blocks from a cliff due to erosion by the wave; B. intense soil erosion with escarpment scars at the foot of a hill; C. escarpment scars at the foot of a slope and accumulation of coral debris forming a ridge on a beach; D. cliff erosion by the successive waves resulting in an enlarged trench; from Paris <i>et al.</i> (2009).	35
Figure 2.2: a. Onshore tsunami deposits in Lampuuk (west Sumatra, Indonesia) with decametric rip-up clasts of soil, a massive lower unit, flame structures and a laminated upper unit; b. onshore tsunami deposits in Lampuuk with basal erosion and large pebbles near the base; c. onshore tsunami deposits in a river bed in Lampuuk with basal erosion, a massive lower unit deposited during uprush and a chaotic upper unit enriched in organic matter deposited during backwash; from Paris <i>et al.</i> (2007).....	36
Figure 2.3: Location of study sites in the Japan area; see Table 2.1 for details on studies.	39
Figure 2.4: Location of all the sites listed in Table 2.1 focusing on marine tsunami backwash deposits around the world; a. Japan area (Figure 2.4); b. Bay of Benghal area (India, Thailand and Indonesia) (Figure 2.5); c. Mediterranean Sea (Italy, Sicily and Greece) (Figure 2.6); d. Gibraltar Detroit area (Portugal and Spain) (Figure 2.7); e. eastern Mediterranean Sea (Israel and Jordan (Figure 2.8)); f. south Chile (Figure 2.9).	39
Figure 2.5: Location of study sites in the northern Mediterranean Sea; see Table 2.1 for details on studies.	40
Figure 2.6: Location of study sites around the Gulf of Benghal; see Table 2.1 for details on studies.	40

Figure 2.7: Location of study sites in the Gibraltar Detroit area; see Table 2.1 for details on studies.....	41
Figure 2.8: Location of study sites in eastern Mediterranean Sea; see Table 2.1 for details on study.....	41
Figure 2.9: Location of study site in south Chile; see Table 2.1 for details on studies.	41
Figure 2.10: A. Side-scan sonar image of a submarine accumulation of boulders displaced by the 2004 IOT backwash forming a ridge parallel to the coast with wave ripples induced by the backwash current offshore Lhok Nga (Indonesia, see Table 2.1 and Figure 2.5, site INS-2), from Paris <i>et al.</i> (2010); B. side-scan sonar image illustrating variations of surface sediment lithology induced by channelization of the 2004 IOT backwash current offshore Khao Lak (Thailand, see Table 2.1 and Figure 2.5, site TH-1), from Feldens <i>et al.</i> (2012).....	43
Figure 2.11: a. Paleotsunami backwash deposits outcrop with basal erosion including megaflutes and a thin basal shear carpet on the Chilean coast (see Table 2.1 and Figure 2.9, site CH-1), from Le Roux and Vargas (2005); b. paleotsunami backwash deposits outcrop showing six stacked units (unconsolidated sand forming the hollows) emplaced by two tsunamis (T2 and T3) intercalated between massive mudstone layers (Japan, see Table 2.1 and Figure 2.4, site JP-3), from Fujiwara and Kamataki (2007); c. and d. tsunami backwash deposits composed of sand, gravel and shell and coral fragments in cores collected offshore Khao Lak (Thailand, see Table 2.1 and Figure 2.6, site TH-1), from Sakuna-Schwartz <i>et al.</i> (2015).....	45
Figure 2.12: Schematic idealized shallow marine tsunami backwash sequence, including all distinctive characteristics gathered from all studies focusing on backwash deposits, with two stacked units emplaced by two successive waves of a single tsunami; each unit is composed of a lower coarse sub-unit and an upper fine laminated sub-unit.	47
Figure 2.13: Lithological and mineralogical composition of the 2004 IOT backwash layer (Zone II in gray) observed offshore Nagapattinam (India, see Table 2.1 and Figure 2.5, site IND-1), from Veerasingam <i>et al.</i> (2014).....	49
Figure 2.14: Geochemical composition of the 2004 IOT backwash deposits observed offshore Nagapattinam (India, see Table 2.1 and Figure 2.5, site IND-1), from Veerasingam <i>et al.</i> (2014).....	51
Figure 2.15: Comparison of idealized sedimentary depositional sequences between storm deposits with HCS (left), from Walker <i>et al.</i> (1983), tsunami backwash deposits and hyperpycnal flash-flood deposits, from Mulder <i>et al.</i> (2003).....	58

Figure 3.1: Map of Tutuila with bathymetric data acquired during the SAMOA-SPT campaign (modified from Google Earth).....	62
Figure 3.2: Map of Pago Pago Bay with bathymetric data acquired during the SAMOA-SPT campaign; a. track of all seismic profiles acquired during the campaign; b. all cores collected during the campaign (core names starting with P are for manual cores, CA for short cores and K for Kullenberg cores, see Table 3.1 for details).....	64
Figure 3.3: Map of Masefau Bay with bathymetric data acquired during the SAMOA-SPT campaign; a. track of all seismic profiles acquired during the campaign; b. all cores collected during the campaign (core names starting with P are for manual cores and K for Kullenberg cores, see Table 3.1 for details).....	65
Figure 3.4: Map of Fagafue Bay with bathymetric data acquired during the SAMOA-SPT campaign; a. track of all seismic profiles acquired during the campaign; b. all cores collected during the campaign (core names starting with P are for manual core and K for Kullenberg cores, see Table 3.1 for details).....	66
Figure 3.5: Map of Moloata Bay (north-east) and Poloa Bay (south-west) with bathymetric data acquired during the SAMOA-SPT campaign; a. track of all seismic profiles acquired during the campaign; b. all Kullenberg cores collected during the campaign (see Table 3.1 for details)..	67
Figure 3.6: Map of Se'etaga Bay with bathymetric data acquired during the SAMOA-SPT campaign; a. track of all seismic profiles acquired during the campaign; b. all Kullenberg cores collected during the campaign (see Table 3.1 for details).....	68
Figure 4.1: A. Location of American Samoa in the Pacific Ocean (modified from Google Earth), B. Location of the earthquake epicenter marked by a red star with its magnitude (modified from Google Earth), C. Map of Tutuila with bathymetric data (modified from NOAA).....	76
Figure 4.2: A. Photo of the bottom of Pago Pago Bay in the inner part of the bay with a ladder, zinc house roof parts and other waste material (photo from NOAA), B. Photo of <i>Acropora</i> coral found on the fringing reef of Pago Pago bay (photo by Stéphane Bujan).....	79
Figure 4.3: Map of Pago Pago Bay with 2 m high resolution processed bathymetric data acquired during campaign (5 m isobaths), 10 coring sites (8 interface cores and 9 Kullenberg cores), 38 HR seismic profiles and inundation limit of 2009 SPT; the two morphologic domains observed on seafloor are shown limited by the 40 m isobath.....	81

Figure 4.4: W-E raw (top) and interpreted (bottom) seismic profile Pago-21 with 3 zooms showing raw vs interpreted data in key areas to understand interpretation method; cores SPT K01, K02 and K03 were added after depth-to-time conversion.....	85
Figure 4.5: N-S raw (top) and interpreted (bottom) seismic profile Pago-14.....	86
Figure 4.6: Photographs of: A. facies A; B. facies B; C. facies C; taken at different depths of core SPT-K05 with description.	89
Figure 4.7: Photographs of samples of the main fragmented coral species found in the cores from facies B and C: a. <i>Porites cylindrica</i> (SPT-K05, 203 cm); b. <i>Fungia fungites</i> (SPT-K04, 67 cm); c. <i>Mycedium elephantotus</i> (SPT-K04, 30 cm).....	90
Figure 4.8: Interpretative core cross section (scale of seafloor not respected for optimal viewing) from proximal (left) to distal (right) with facies distribution (greyish brown for facies A, beige for facies B and yellow for facies C) and interpreted unit correlation based on core-to-seismic correlation; cal. BP dates obtained from radiocarbon dating are noted and pointed by arrows; accumulation rates estimated by ^{210}Pb dating are noted by an asterisk next to corresponding cores.	91
Figure 4.9: Core depth-to-time conversion and core-to-seismic correlation quality check for SPT-K01 core using SeiSee software.	95
Figure 4.10: Multi-proxy approach of 2009 SPT deposits identification on core CA07: from left to right respectively, photograph, X-ray and grain size do not show any evidence of tsunami backwash deposits (no variations), while a peek of terrestrial input can be spotted between 7 and 9 cm on XRF data.....	98
Figure 5.1: a. Location of American Samoa and Tutuila in the southwest Pacific Ocean (modified from Google Earth); b. map of Tutuila with bathymetric data (modified from NOAA, 2018); c. and d. map of Pago Pago Bay with 1 m high resolution processed bathymetric data and seafloor reflectivity data respectively, acquired during the SAMOA-SPT campaign (5 m isobaths) and location of the ten cores.....	110
Figure 5.2: Interpreted west-east seismic profiles Pago-27 (top) and Pago-22 (bottom), simplified according to the interpretation and nomenclature given by Riou <i>et al.</i> (2018), with the location of cores CA04, CA05, CA01 and CA08 on the profiles.....	115
Figure 5.3: Multi-proxy analysis of core CA08; from left to right, respectively, photograph, grain size (mean and D90), Ti/Ca ratio, excess ^{210}Pb excess activities (raw and corrected), ^{137}Cs activities and age model. Grey shaded bars represent the 2009 South Pacific Tsunami and the 1960	

Great Chilean Earthquake Tsunami event layers. ^{137}Cs activities below the detection limit are plotted to 0 mBq/g. NWT: Nuclear Weapon Tests..... 117

Figure 5.4: Correlation of all ten cores projected along a west (left) to east (right) transect (see Figure 1), with photograph and Ti/Ca ratio for each core. Grey shaded bars represent the 2009 South Pacific Tsunami event layer (EL1) and 1960 Great Chilean Earthquake Tsunami event layer (EL2)..... 118

Figure 5.5: Multi-proxy analysis of core CA08; from left to right, photograph, grain size, magnetic susceptibility and XRF geochemical data (Ti/TC, Ca/TC, Ti/Ca, Ti/Sr, Zr/Ca, Zn/Ca, Pb/Ca). For all element ratios, high values represent an increase in the terrestrial input. Ti and Ca are normalized over the total counts (TC). Grey shaded bars represent the 2009 South Pacific Tsunami event layer (top) and the 1960 Great Chilean Earthquake Tsunami event layer (bottom). 119

Figure 5.6: Photograph and Ti/Ca profile for core CA08, with interpretative sections of interest from the core and photographs of thin sections and their position in the core. Note that photographs are shown twice, once in analyzed light (left) and once in analyzed polarized light (right). Note that photographs **a**, **c** and **e** represent the top of each interval with high Ti/Ca, while photographs **b**, **d** and **f** represent their base. F1: homogenous silt, micritic mud and aggregates, shells, organic matter (OM). F2: normally graded very fine to fine sand, micritic aggregates, clay aggregates rich in organic matter (OM), opaque minerals (Op), shells (Sh), plant debris, iddingsite (Id), clinopyroxene (Cpx) and plagioclase (Pl). F3: non-graded terrigenous clay with asymmetric flame structures (fl) and rip-up clasts at the base. F4: normally graded clayey silt, mix of terrigenous clay (F3) and micritic mud and aggregates (F1) with shells (Sh)..... 120

Figure 5.7: Interpretative tsunami backwash depositional model illustrating simplified transport and deposition mechanisms during each phase of the tsunami. The right-hand side panels represent the processes linked to a possible second wave such as during the 2009 SPT. The zoom in panel **d**. illustrates a complete event layer in the case of a single major tsunami wave, such as seen in core CA08 for the 1960 GCET. The zoom in panel **g**. illustrates a complete event layer in the case of two tsunami waves, such as seen in core CA08 for the 2009 SPT..... 125

Figure 6.1: **a.** Location of American Samoa and Tutuila in the southwest Pacific Ocean (modified from Google Earth); **b.** map of Tutuila with bathymetric data (modified from NOAA, 2018); **c.** map of Masefau Bay with 1 m-high resolution bathymetric data acquired and cores collected during the SAMOA-SPT campaign; **d.** map of Masefau Bay with 1 m-high resolution bathymetric data acquired and cores collected during the SAMOA-SPT campaign. 134

Figure 6.2: **a.** Photograph of vascular plant debris found in core K08 (14 cm, see Table 6.1 for details) and dated for radiocarbon; **b.** photograph of *Halimeda* calcified plates sampled in core K16 (82 cm, see Table 6.1 for details) and dated for radiocarbon; **c.** photograph of *Operculina Ammonoides* sampled in core K08 (69 cm, see Table 6.1 for details) and dated for radiocarbon. 139

Figure 6.3: Multi-proxy analysis of core K08; from left to right, respectively, ages obtained by radiocarbon dating, photograph of the core, grain size distribution, mean grain size, Ti/Ca ratio, K_{norm} ratio, excess ^{210}Pb activities, age model and ^{137}Cs activities; grey shaded bars represent anomalous layers EL1, EL2 and EL4; NWT: Nuclear Weapon Tests..... 142

Figure 6.4: Multi-proxy analysis of core K16; from left to right, respectively, ages obtained by radiocarbon dating, photograph of the core, grain size distribution, mean grain size, Ti/Ca ratio, excess ^{210}Pb activities, age model and ^{137}Cs activities; grey shaded bars represent anomalous layers EL1, EL2, EL3 and EL4; NWT: Nuclear Weapon Tests..... 143

Figure 6.5: Correlation of event layers deposited following the 2009 SPT, the 1960 GCET/1957 AIT and the 1868 SAT between the bays of Fagafue (K08) and Masefau (K16), based on sedimentological and geochemical characteristics and ^{210}Pb and ^{14}C dating. 150

Figure 7.1: Large-scale correlation of tsunami backwash deposits identified in the shallow marine sediment record of Tutuila (2009 SPT, 1960 GCET, 1957 AIT, 1917 TTT and 1868 SAT) between the north shore (Masefau and Fagafue bays, K08 and K16, left) and the south shore (Pago Pago Bay, CA06, K06, CA03 and K03, right); A correlation is also proposed for the deeper sediment record of Pago Pago Bay between anomalous layers detected in cores from the outer part of the bay (K06 and K03)..... 157

Figure 7.2: Proposed schematic correlation of event deposits between the inner part of Pago Pago Bay and the outer part of the bay with lateral facies variations based on seismic and lithological evidence in the inner part and geochemical evidence in the outer part of the bay..... 158

Figure 8.1: Map of the Pacific Ocean and surrounding continents with the Pacific Ring of Fire highlighted by the tectonic plate boundaries, recent earthquake epicentres and active volcanoes, from <https://www.earthobservatory.sg/resources/maps/ring-fire>; location of Figures 8.2 and 8.3 indicated on the map..... 173

Figure 8.2: **a.** Location of Atka Island (Alaska) along the Aleutian Trench (modified from Google Earth); **b.** Map of western Atka Island with location of proposed future study sites marked with a red star (modified from Google Earth). 173

Figure 8.3: a. Location of Moorea Island (French Polynesia) (modified from Google Earth);	
b. Map of Moorea Island with location of five proposed future study zones marked with a red star (modified from Google Earth).	173

List of tables

Table 2.1: List of studies focusing only on marine tsunami backwash deposits around the world with their location and proxies used for identification of deposits; studies marked with a * were conducted on immersed outcrops..... 38

Table 2.2: List of studies focusing only on marine tsunami backwash deposits around the world with their location and proxies used for identification of deposits; studies marked with a * were conducted on immersed outcrops..... 38

Table 3.1: List of all cores collected during the SAMOA-SPT campaign with details on core type, length and location and depth of sampling..... 63

Table 4.1: Characteristics of seismic units, corresponding sediment facies based on core-to-seismic correlation and estimated ages (from base to top)..... 88

Table 4.2: Facies distribution with depth of occurrence in each core from proximal (top) to distal (bottom)..... 90

Tableau 4.3: Radiocarbon dating data for each core from proximal (top) to distal (bottom); calibration was made using Calib 7.1 software (Stuiver *et al.*, 1986, <http://calib.org/>) with integrated Marine13 calibration curve; the 1 sigma interval corresponds to the 68.3 % confidence age interval (age uncertainty)..... 93

Tableau 4.4: ^{210}Pb dating data for cores CA02, CA07, CA08 and CA01 (estimated supported ^{210}Pb activity based on α counting in core CA08 is 0.84 dpm/g); each profile is plotted with a logarithmic X-axis (for cores CA07 and CA08 respectively, samples at 32 cm and 11 cm show incoherent activities and were left apart for the sedimentation rate estimation)..... 93

Table 6.1: Radiocarbon dating data for core K08 and K16; calibration was made using OxCal 4.3 software (Bronk Ramsey, 2009a; <https://c14.arch.ox.ac.uk/oxcal/OxCal.html>) with an integrated calibration curve; the 1 sigma interval corresponds to the 68.3 % confidence age interval (age uncertainty) and the 2 sigma interval to the 95% confidence age interval..... 146

Chapter 1:

Introduction

1.1 Context of the study

Since the beginning of the 21st century, two major tsunamis, the 2004 IOT (Indian Ocean Tsunami) and the 2011 TOT (Tohoku-Oki Tsunami), have had an international coverage. The enormous number of casualties and damage caused in the countries impacted by these tsunamis, mainly Indonesia, Thailand, India and Japan, raised a global awareness amongst the scientific community on the urge to increase our general knowledge on tsunamis. Indeed, if the interest on tsunami research initially started in the late 1980's around 30 years ago (Atwater, 1987), the number of studies has increased exponentially following the 2004 IOT and 2011 TOT (Chagué-Goff *et al.*, 2017) (Figure 1.1). Studies first focused on the identification and characterization of tsunami deposits (Dawson, 1994; Moore *et al.*, 2006; Bahlburg & Weiss, 2007; Dawson & Stewart, 2007; Paris *et al.*, 2007; Bourgeois *et al.*, 2009; Szczuciński *et al.*, 2012; Costa *et al.*, 2015), with the

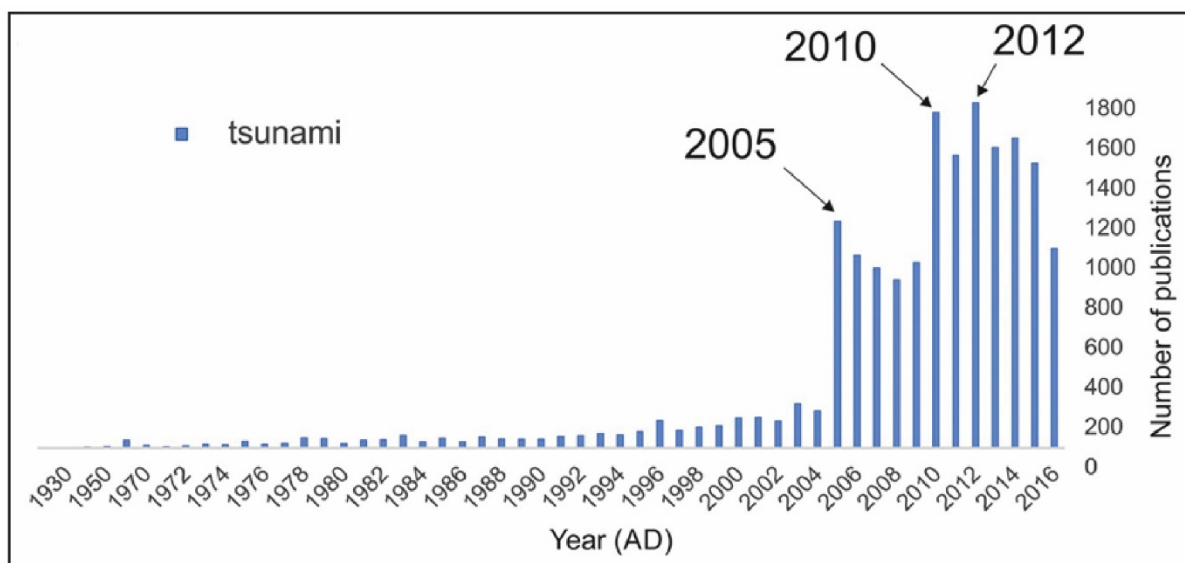


Figure 1.1: Evolution of the number of published articles including the word tsunami, with three peaks in 2005, 2010 and 2012 following the 2004 IOT, the 2009 SPT and the 2011 TOT respectively, from Chagué-Goff *et al.* (2017).

1. Introduction

development of extensive proxy toolboxes based largely on these two recent tsunamis (Chagué-Goff *et al.*, 2011, 2017). Then, the attention switched to geological evidence of older historic and paleotsunamis (e.g. Papadopoulos *et al.*, 2000; Monecke *et al.*, 2008; Goff *et al.*, 2010, 2012; Rubin *et al.*, 2017; La Selle *et al.*, 2019), in order to expand local and regional archives of past tsunamis, crucial for coastal risk assessment. A last major point which concentrated the interest lately is the distinction between tsunami and storm (or cyclones, hurricanes, typhoons) deposits (e.g. Goff *et al.*, 2004; Kortekaas and Dawson, 2007; Morton *et al.*, 2007; Phantu Wongraj and Choowong, 2012).

However, if nowadays we have a good knowledge of these three main research axes in tsunami exploration on land, it is hardly the case offshore. The number of studies focusing on offshore deposits is still distinctively lower than for onshore deposits (Le Roux & Vargas, 2005b; Abrantes *et al.*, 2008; Feldens *et al.*, 2012; Smedile *et al.*, 2012; Veerasingam *et al.*, 2014; Sakuna-Schwartz *et al.*, 2015). Yet, hydrodynamic and sedimentary processes involved in the sub-aerial domain and in the marine domain are very different. In most cases, only the uprush phase is recorded onshore, while the backwash phase is only recorded offshore (Einsele *et al.*, 1996). Thus, it is crucial to also study offshore backwash deposits emplaced during a tsunami in order to have a full understanding of the hydrodynamic and sedimentary processes at stake during a tsunami surge, from the uprush with inundation of the coastal plain to the backwash with discharge into the sea. The general characteristics of such backwash deposits have been described following the 2004 IOT and 2011 TOT (e.g. Sugawara *et al.*, 2009; Jonathan *et al.*, 2012; Tipmanee *et al.*, 2012; Toyofuku *et al.*, 2014; Veerasingam *et al.*, 2014; Sakuna-Schwartz *et al.*, 2015; Tamura *et al.*, 2015) and are starting to be well known. However, most of these studies were carried out in open and dynamic shallow marine environments. Such study sites are not favorable for long-time preservation of event deposits. Hence, only a limited number of studies focus on marine paleotsunami deposits (e.g. Fujiwara *et al.*, 2000; Goodman-Tchernov *et al.*, 2009; Le Roux and Vargas, 2005; Smedile *et al.*, 2011), and only one provide a catalog of marine backwash deposits (Sakuna-Schwartz *et al.*, 2015). In order to tackle this issue, we believe that sheltered shallow marine environments that are frequently impacted by tsunamis should be investigated since they are inferred to offer ideal preservation potential.

The island of Tutuila (American Samoa) is a volcanic island located in the south west Pacific Ocean, near the northern end of the Tonga Trench (Figures 1.2.A and 1.2.B). As a consequence of the erosion and collapse of some of its calderas, its coastline is very indented and draws highly sheltered bays (Figure 1.2.C). Owing to its very calm hydrodynamic setting, the biggest and most sheltered of these bays, Pago Pago Bay (Figure 1.2.C), is home to one of the main deep-water

1. Introduction

harbors in the southern Pacific. Thus, this highly protected shallow marine environment seems ideal for event deposits preservation. In addition, its location in the middle of the Pacific Ocean and surrounded by the Pacific Ring of Fire makes it an excellent study zone for studying tsunami backwash deposits. Local catalogs of events date back no further than the middle of the 19th century (Pararas-Carayannis & Dong, 1980; NGDC, 2018). Tutuila was severely hit by the September 29th 2009 South Pacific Tsunami (SPT) (Goff & Dominey-Howes, 2011). This tsunami was generated by a large earthquake ($M_w=8.1$) near the northern end of the Tonga Trench, only 160 km south-west of Tutuila (Beavan *et al.*, 2010; Lay *et al.*, 2010) (Figure 1.2.B). The tsunami reached the shores of Tutuila only 15 minutes after the earthquake, delivering waves reaching up to 7 m in Pago Pago Bay and 8 m near Fagafue Bay and causing 183 deaths in the Samoan Islands, 34 of which in American Samoa (Dominey-Howes & Thaman, 2009). Prior to the 2009 SPT, several other destructive tsunamis have hit Tutuila: the 1960 Great Chilean Earthquake Tsunami (GCET) (Cifuentes, 1989) with waves reaching 4 m height in Pago Pago Bay, the 1957 Aleutian Islands Tsunami (AIT) (Johnson *et al.*, 1994) with waves reaching 1.5 m height on the north shore and the 1917 Tonga Trench Tsunami (ITT) (Okal *et al.*, 2011) with waves reaching 2.5 m height in Pago Pago.

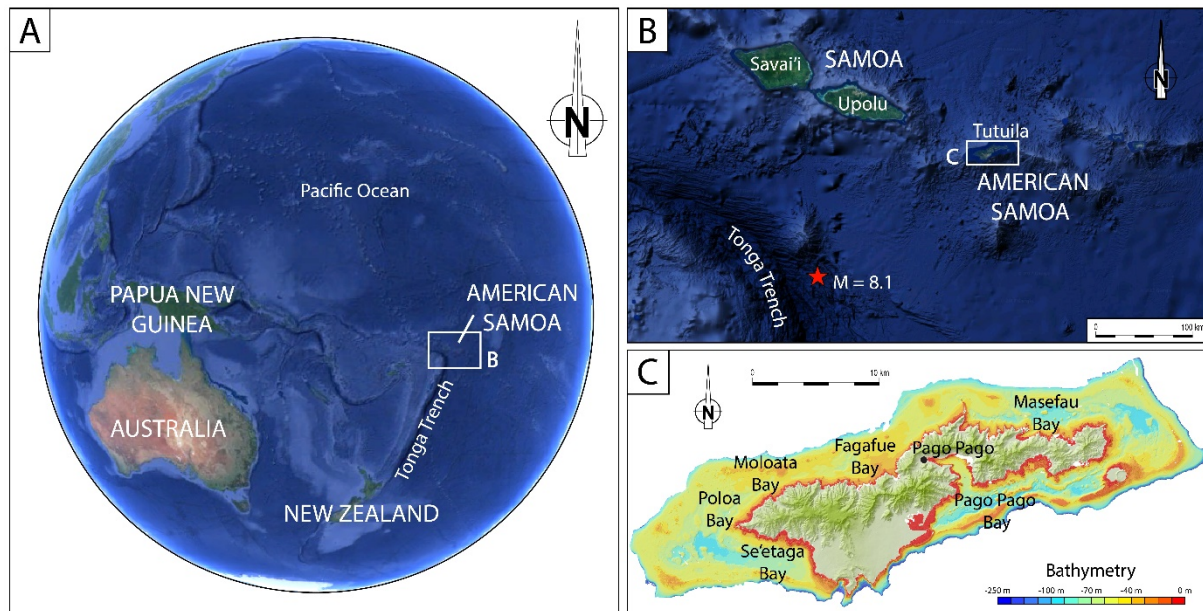


Figure 1.2: A. Location of American Samoa in the Pacific Ocean (modified from Google Earth); B. Location of the earthquake epicenter marked by a red star with its magnitude (modified from Google Earth); C. Map of Tutuila with bathymetric data (modified from NOAA).

1.2 Objectives

In order to fill those gaps in the understanding of the processes engaged in a tsunami backwash and the archiving of local tsunamis and their geological evidence, a field survey was organized in Tutuila to collect geophysical and sedimentary data (SAMOA-SPT cruise on board *R/V Alis*, 27th August to 10th September 2015), which led to this PhD thesis. So as to implement these ambitions and answer all the issues that it involved, five main objectives were formulated to guide the study:

- Investigate and describe for the first time the Pago Pago Bay sediment-fill in order to understand the sedimentary history of the bay and consider the influence of tsunamis on the sedimentation of sheltered bays;
- Identify the backwash deposits emplaced during the 2009 SPT and describe in details the sedimentological and geochemical characteristics in order to learn more about hydrodynamic and sedimentary processes at stake during the backwash phase of a tsunami in a shallow marine environment;
- Identify and date older historic tsunami and paleotsunami backwash deposits in the sediment record and assign them to major tsunamis or earthquakes reported in the area and beyond, in order to extend the local/regional archive of geological evidence of tsunami deposits and possibly identify new tsunamis not yet reported;
- Identify and describe tsunami backwash deposits in different bays around the island of Tutuila and correlate them with the backwash deposits identified in Pago Pago Bay in order to assess the influence of the orientation and morphology of the coast on backwash deposits record and preservation;
- Identify and describe cyclone deposits in the sedimentary record of the bays of Tutuila and propose new criteria for distinguishing them from tsunami backwash deposits in shallow marine environments.

For the purpose of this study and to tackle the objectives listed above, this memoir will focus in the first place on a thorough review of the characteristics of tsunami backwash deposits based on the literature. Following this exhaustive state of the art based on published literature, the sedimentary history of Pago Pago Bay will be exposed based on the data collected during the field survey. Still based on this data, we will then concentrate on the backwash deposits emplaced in

1. Introduction

Pago Pago Bay during the 2009 SPT and older tsunamis, before driving our attention to backwash deposits in the bays of the north shore of Tutuila. Finally, all the results obtained through this project will be discussed in response to one another, finishing with some perspectives and future research work proposal about tsunami backwash deposits and paleotsunami submarine archiving.

Chapter 2:

Geological evidence of tsunami backwash deposits in shallow marine environments: a review

To be submitted to: *Earth Science Review*

**BRIEUC RIOU^{1,2}, ERIC CHAUMILLON¹, JEAN-LUC SCHNEIDER² and
CATHERINE CHAGUÉ³**

¹ LIENSs, UMR 7266-CNRS, Université de La Rochelle, La Rochelle CEDEX, F-17000, France
(E-mail: briec.riou@u-bordeaux.fr)

² EPOC, UMR 5805-CNRS, Université de Bordeaux, Pessac CEDEX, F-33615, France

³ School of Biological, Earth and Environment Sciences, University of New South Wales, Sydney
2052, Australia

In preparation

2.1 Tsunami generation and propagation

Tsunamis can have various triggering events, which may be categorized in two main types: “bottom-up” and “top-down” (Dawson & Stewart, 2007). “Bottom-up” displacements describe a motion impacting the water column from bottom to top. This includes seabed-related disturbances, such as earthquakes and submarine landslides. “Top-bottom” displacements describe a motion impacting the water column from top to bottom. This includes atmospheric disturbances striking a water body, such as extra-terrestrial impacts and subaerial landslides. Eruption-related tsunamis can be classified either as “bottom-up” or “top-down” since the triggering event is not directly the eruption but can be an earthquake or a submarine landslide induced by the eruption itself (“bottom-up”), or a pyroclastic/debris flow or collapse of the caldera into the water body associated to a landslide (“top-down”). More detailed generation and propagation characteristics of each type of tsunamis have been described by (Dawson & Stewart, 2007) in their review.

2.1.1 Earthquake-induced tsunamis

Most devastating tsunamis recorded in historical times were triggered by subduction zone earthquakes along subduction trenches (Ward, 2002; Fryer *et al.*, 2004). A famous example of these tsunamis is the 2004 Indian Ocean Tsunami, generated by a magnitude $M_w=9.0$ earthquake, 160 km west of Sumatra, with waves reaching 10 to 30 m locally along the coast of Indonesia and Thailand (Wang & Liu, 2006). Another example is given by the 2011 Tohoku-Oki Tsunami, also generated by a magnitude $M_w=9.0$ earthquake, east offshore Japan, with waves reaching around 10 m and inundating more than 5 km inland in Sendai Plain (Sugawara *et al.*, 2012).

In these cases, the initial amplitude of the resulting tsunami is roughly proportional to the vertical deformation of the seafloor, and cannot significantly exceed the absolute vertical slip movement of the rupture (Ward, 2002; Okal & Synolakis, 2004). Following this rule, maximum tsunami initial wave heights in open ocean usually don’t exceed 10 m (Ward, 2002). Based on the initial wave height (itself depending on the fault rupture), the amplitude attenuation with distance and the estimated minimum wave height needed when reaching the coast, the minimum theoretical earthquake magnitude for a resulting tsunami to have recognizable coastal impacts is 8 (Dawson & Stewart, 2007).

Meanwhile, if the wave amplitude of an earthquake-induced tsunami is limited, the usually large distance covered by the fault rupture results in low frequency, long wavelength and long

period waves. This characteristic means that the waves are less attenuated with distance, and thus have a more far-reaching potential. The long period of tsunami waves also has for effect to accentuate the inundation potential of tsunami waves when reaching the coast, due to the prolonged duration of the inflow (Ward, 2001).

The first motion of the tsunami wave depends on the direction of the fault rupture. If the wave is generated by a collapse of the seabed, the leading wave motion will be a trough. If it is an uplift of the seafloor, the leading wave motion will be a crest.

2.1.2 Slide-induced tsunamis

If most known historic tsunamis were triggered by earthquakes, the largest and locally most oversized tsunamis were triggered by landslides and collapses (Ward, 2001). Famous examples of such tsunamis include the 1958 record-breaking Lituya Bay Tsunami, with a maximum run-up altitude reaching 520 m, generated by a rockslide due to a mass failure of a flank of the inlet (Miller, 1960; Pararas-Carayannis, 1999; Fritz, 2001; Mader & Gittings, 2002), and 1883 Krakatau eruption-related tsunami generated by a collapse of the caldera, provoking waves up to 40 m height (Choi *et al.*, 2003; Mader & Gittings, 2006).

For slide-induced tsunamis, the initial generated wave is proportional to the size (thickness and volume) and speed of the slide (Harbitz *et al.*, 2006): the larger the sliding mass, the higher the wave. Typically, the wave generated when the sliding mass enters the water body is roughly as tall as the mass is thick (Ward, 2001; Ward & Day, 2005). However, a wave related to a slide-induced tsunami usually attenuates rapidly and loses most of its amplitude within a few tens of kilometers. Thus, slide-induced tsunamis can be very devastating in the near-field but have very low impact on the far-field (Okal & Synolakis, 2004). That said, a few known slide-induced tsunamis have had considerable far-field impacts for various reasons. For example if the speed of the sliding mass matches the speed of the generated tsunami wave, both are in phase which amplifies the wave amplitude (Dawson & Stewart, 2007). The first motion of the slide-generated tsunamis is a seaward leading crest accompanied by a landward leading trough (Okal & Synolakis, 2004).

2.1.3 Impact-induced tsunamis

Impact-induced tsunamis have a similar generation mechanism as slide-induced tsunamis. They have probably been the largest and most devastating events the Earth has ever known.

Unfortunately, no historic evidence for such events are available given their paucity, and only simulations can allow estimation of potential effects. For example, the Eltanin asteroid (2.15 Ma), estimated with a 4 km diameter from its crater 1500 km south-west of Cape Horn, presumably delivered a 200 to 300 m wave in the Antarctica Peninsula and the southern tip of Chile (Ward & Asphaug, 2002). Another famous example is the Chicxulub meteorite, which impacted the Yucatan Peninsula in southern Mexico, generating tsunami waves estimated between 50 and 100 m on the coast of Texas nearly 1000 km from the crater (Bourgeois *et al.*, 1988). In the case of more reasonably sized bolides, measuring 1 to 500 m and reaching our planet every 1000 to 100,000 years, the waves generated would face rapid attenuation on a short distance (Ward & Asphaug, 2002, 2003). However, a 100 m bolide, expected to reach the Earth every 3000 to 10,000 years (Hills & Goda, 1999; Ward & Day, 2005) would still be capable of triggering waves up to 10 m 1000 km from its impact.

2.1.4 Wave propagation

Once generated, a tsunami propagates in open sea as a wave train, composed typically of three to six waves. It is characterized by a very long wavelength (L), ranging from around 50 to 300 km depending on the intensity of the generating mechanism. Hence, tsunami waves are considered as shallow water waves in most cases and fall under the rules of the shallow water equations (wavelength \gg ocean depth). Based on these equations, the speed of the wave train can be simplified as:

$$v = \sqrt{g \cdot D}$$

where g is the acceleration of gravity and D is the ocean depth. Thus, the speed of a tsunami wave is only dependent on the depth of the water column. This implies that the speed of a tsunami wave decreases drastically when passing from deep sea to a continental shelf or volcanic hotspot island, ranging from 600-1000 km.h⁻¹ in deep sea (for depth from 3 to 8 km) to 50 km.h⁻¹ in nearshore zones (for 20 m depth).

2.2 Coastal impacts of tsunamis

When arriving in coastal areas, tsunami waves can trigger all sorts of deposits. Traces of these deposits can be found both onshore and offshore, and can be related to both inflows (uprush)

and outflows (backwash). While onshore deposits register mostly the uprush phase, offshore deposits register mostly the backwash phase (Einsele *et al.*, 1996). Onshore transport and deposition processes have been widely studied over the past decades and are well known. Several reviews have already been published, exposing in detail the characteristics of onshore tsunami deposits and their proxies (Dawson & Stewart, 2007; Bourgeois *et al.*, 2009; Chagué-Goff *et al.*, 2011; Goff *et al.*, 2012; Shanmugam, 2012; Costa *et al.*, 2015) and will be briefly summarized in a first section. However, marine deposits represent only a small fraction of the studies focusing on tsunami deposits and no review has yet offered to gather all information on the characteristics of nearshore tsunami deposits. This crucial aspect of tsunami research will be treated in a second section.

2.2.1 Onshore impacts of tsunamis

2.2.1.1 Geomorphological signature

Onshore impacts of tsunamis can be of various nature and with different lifespan. They are prone to be induced by both the uprush and the backwash. The most evident impact, which can be observed immediately after the tsunami, is the geomorphological and landscape changes of inundated areas. These changes are operated by strong erosion during the uprush but also during the backwash, including destruction of man-made infrastructure and coastal geomorphological features such as sand dunes, coastline retreat, vegetation removal and soil-stripping during uprush and inundation (Dawson, 1994; Paris *et al.*, 2009) (Figure 2.1). Some studies have also shown that return flows have a huge erosive potential and can erode up to a couple of meters deep locally, forming return channels (Dawson, 1994; Costa *et al.*, 2015).

2.2.1.2 Sedimentary signature

Another impact, not always as evident but very important for identification of onshore tsunami deposits, is the sediment redistribution. Due to the amplitude and period of each tsunami wave and the velocity of the flow associated when inundating coastal areas, a tsunami wave is capable of eroding and displacing all sizes of sediment, from clay to boulders sometimes as heavy as a few thousand tons (Shanmugam, 2012; Costa *et al.*, 2015). The only limiting factor for sediment transport is the availability (Bourgeois *et al.*, 2009). Typically, boulder fields with exotic boulders can be found in the foreshore and backshore area and are used as a proxy to identify tsunami

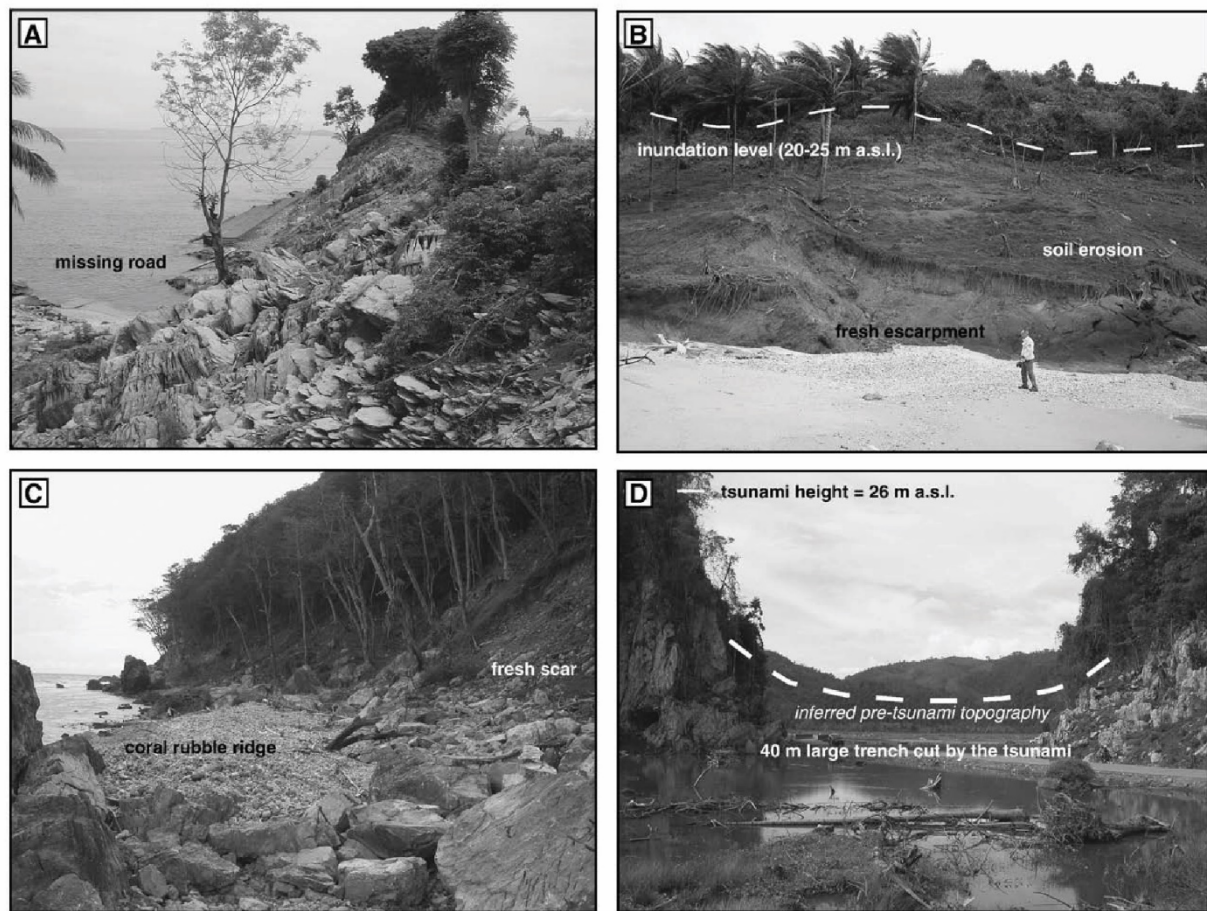


Figure 2.1: Impact of the 2004 IOT on the coast of Banda Aceh (west Sumatra, Indonesia); **A.** dislodged blocks from a cliff due to erosion by the wave; **B.** intense soil erosion with escarpment scars at the foot of a hill; **C.** escarpment scars at the foot of a slope and accumulation of coral debris forming a ridge on a beach; **D.** cliff erosion by the successive waves resulting in an enlarged trench; from Paris *et al.* (2009).

deposits. Further inland, coarse sand sheets, eroded from the beach and shallow marine environment, can be found (Bourgeois *et al.*, 2009). The depositional sequences observed for most onshore tsunami deposits show similarities, which may provide as many sedimentological proxies for recognition of tsunami deposits. Characteristics observed in every sequence include a basal erosive surface, a fining upward layer coarser than the background sediment with intraclasts and horizontal planar laminae (Goff *et al.*, 2012; Shanmugam, 2012; Costa *et al.*, 2015) (Figure 2.2). Basal soft sediment deformation and loading structures such as convolutes or flame structures are also common (Goff *et al.*, 2012; Shanmugam, 2012) (Figure 2.2.a). Intraclasts include rip-up mud or sand clasts and pebbles, and are commonly imbricated in the flow direction (Goff *et al.*, 2012; Shanmugam, 2012). Some units show broken bioclasts-rich laminae. Heavy mineral laminae (magnetite, ilmenite, sillimanite, zircon) were reported in some cases, with a high magnetic susceptibility (Chagué-Goff *et al.*, 2011; Goff *et al.*, 2012). In fewer examples, cross-stratifications

2. Geological evidence of tsunami backwash deposits in shallow marine environment: a review

have been observed (Goff *et al.*, 2012; Costa *et al.*, 2015). Moreover, these classic sequences all have fining inland trends. They represent a single high-energy event, which deposited during a unique laminar inflow regime. Vertical stacking of these sequences is commonly observed, attesting of successive waves of a tsunami and can be separated by a fine mud drape emplaced during flow deceleration and stagnation in-between waves. In fewer cases, the presence of a fining seaward uppermost unit, interpreted as backwash deposits, was noted (Paris *et al.*, 2007; Costa *et al.*, 2015). This unit can erode deep into the underlying sequences and attest of a turbulent outflow (Costa *et al.*, 2015) (Figure 2.2.c).

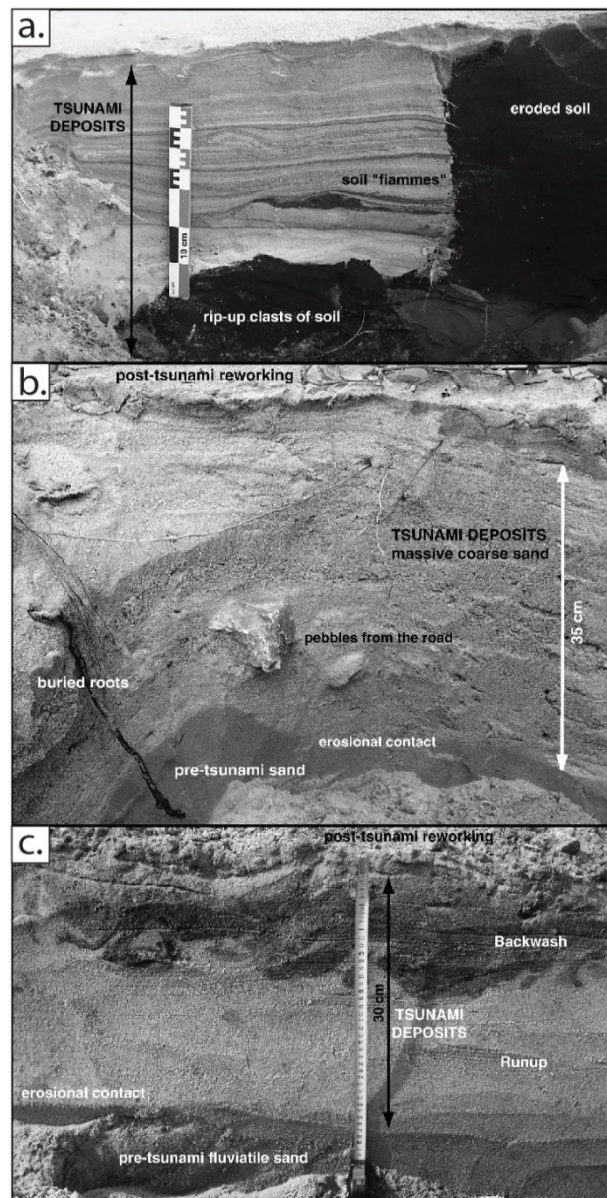


Figure 2.2: **a.** Onshore tsunami deposits in Lampuuk (west Sumatra, Indonesia) with decametric rip-up clasts of soil, a massive lower unit, flame structures and a laminated upper unit; **b.** onshore tsunami deposits in Lampuuk with basal erosion and large pebbles near the base; **c.** onshore tsunami deposits in a river bed in Lampuuk with basal erosion, a massive lower unit deposited during uprush and a chaotic upper unit enriched in organic matter deposited during backwash; from Paris *et al.* (2007).

2.2.1.3 Geochemical signature

This spatial redistribution of coastal sediment during a tsunami event is also reflected by specific geochemical signatures. For onshore deposits, we look for traces of abnormal marine submersions, such as saltwater inundation, or unusual geochemical components. Typically, onshore tsunami deposits have a higher concentration in saltwater indicative elements, such as Na, K, Mg, Cl, Sr, S, Ca, Br and I, although not all are always found together (Chagué-Goff *et al.*, 2011, 2017; Costa *et al.*, 2015). Marine provenance is also noted by an increase of carbonates and shells (CaO) and beach sand (SiO₂) in onshore tsunami layers in comparison with the under- or over-lying units (Chagué-Goff *et al.*, 2011; Goff *et al.*, 2012; Costa *et al.*, 2015). An increase in the concentration of heavy metals (Pb, Cu, Ni, Zn, Cd) and other metalloids (As, Sb, Se) was also reported in some tsunami deposits and are attributed to contamination by major industries in the region (Chagué-Goff *et al.*, 2011, 2017).

2.2.1.4 Paleontological signature

Another important criterion to identify onshore tsunami deposits is the source of the sediment. This criterion can be obtained using paleontology. Microfossils and macrofossils present in onshore deposits have been used to estimate the sediment source, particularly the habitat and depth of origin of the deposits. Commonly used fossils are foraminifera, diatoms, ostracods and mollusk shells (Goff *et al.*, 2012; Costa *et al.*, 2015). Typically, changes in the population assemblages within tsunami deposits for each group of fossil have been reported in different studies. In most cases, the abundance of fully marine species in onshore deposits attest of transport by the tsunami wave of marine sediment from depths greater than for storm waves, several meters to kilometers inland. Some specific assemblages of diatoms can even help understanding flows during successive stages of the event (see Goff *et al.*, 2012; Costa *et al.*, 2015).

2.2.2 Nearshore impacts of tsunamis

If onshore deposits are easier and more direct to study for recent tsunamis, nearshore and offshore deposits are still under-represented. Yet, they are crucial for understanding hydrodynamic and sedimentary processes during the backwash phase of a tsunami, which is recorded almost only offshore, and may offer a high potential for long-term preservation of tsunami deposits, and thus should not be overlooked. Recently, an increasing number of studies have focused on shallow

2. Geological evidence of tsunami backwash deposits in shallow marine environment: a review

marine tsunami deposits, They are listed in Table 2.1, and their locations are shown on Figures 2.3 to 2.9.

Table 2.1: List of studies focusing only on marine tsunami backwash deposits around the world with their location and proxies used for identification of deposits; studies marked with a * were conducted on immersed outcrops.

Site code	Tsunami	Location	Reference	Proxies
JP-1	Multiple, Miocene	Chita Peninsula, Japan *	Shiki and Yamazaki (1996)	Grainsize, sedimentological features, macrofossils
CH-1	Multiple, Miocene-Pliocene	Chile *	Le Roux and Vargas (2005)	Grain size, sedimentological features
SP-1	Messinian	Sorbas Basin, Spain *	Puga-Barnabéu and Aguirre (2017)	Macrofossils
MED-1	Multiple, Middle Pliocene	Salento, Italy *	Massari and D'Alessandro (2000)	Grainsize, sedimentological features, macrofossils
MED-2	Multiple, Lower Pleistocene	Rhodes Island, Greece *	Slootman et al. (2018)	Grain size, sedimentological features, macrofossils
JP-2	Multiple, Upper Pleistocene	Makinohara Upland, Japan *	Takashimizu and Masuda (2000)	Grain size, sedimentological features
JP-3	Multiple, Holocene	Boso Peninsula, Japan *	Fujiwara and Kamataki (2007)	Grain size, sedimentological features
JP-3	Multiple, Holocene	Boso Peninsula, Japan	Fujiwara et al. (2000)	Grainsize, sedimentological features, macrofossils, microfossils
MED-3	Multiple, 1700 BCE - present	Augusta Bay, Italy	Smedile et al. (2011)	Grain size, magnetic susceptibility, density, microfossils
MED-3			Smedile et al. (2012)	Microfossils, grainsize
IS-1	1630-1550 BCE Santorini eruption	Caesarea, Israel	Goodman-Tchernov et al. (2009)	Grain size, sedimentological features, macrofossils
IS-1			Tyulencva et al. (2018)	Grain size, mineralogy, major elements, FTIR, μ -XRF, XRD
IS-2	800 BCE Red Sea Tsunami	Aqaba-Eilat Gulf, Israel	Goodman-Tchernov et al. (2016)	Grain size, microfossils
IS-1	Multiple, AD 115 and AD 800	Caesarea, Israel	Goodman-Tchernov and Austin (2015)	Subsurface analysis, macrofossils
PT-1	1755 Lisbon Tsunami	Lisbon, Portugal	Abrantes et al. (2008)	Grain size, magnetic susceptibility, major elements
PT-2		Faro, Portugal	Quintela et al. (2016)	Grain size, microfossils
INS-1	1883 Krakatau eruption	Teluk Banten, Indonesia	Van den Bergh et al. (2003)	Grain size, magnetic susceptibility, density, major elements
PT-2	1969 Lisbon Tsunami	Faro, Portugal	Quintela et al. (2016)	Grain size, microfossils
JP-4	2003 Tokachi-Oki Tsunami	Eastern Hokkaido, Japan	Noda et al. (2007)	Grain size, sedimentological features, microfossils
TH-1	2004 Indian Ocean Tsunami	Pakarang Cape, Thailand	Feldens et al. (2009)	Bathymetry, reflectivity, subsurface analysis
TH-1			Sugawara et al. (2009)	Microfossils
TH-1			Pongpiachan and Schwarzer (2013)	PAHs, SVOCs
TH-1			Pongpiachan et al. (2013.a)	μ -XRF
TH-1			Pongpiachan et al. (2013.b)	FTIR
TH-1			Pongpiachan et al. (2013.c)	PAHs
TH-1			Pongpiachan (2014)	PAHs
TH-2		Krabi, Thailand	Sugawara et al. (2009)	Microfossils
INS-2		Lhok Nga, Indonesia	Paris et al. (2010)	Bathymetry, reflectivity, boulder displacement analysis
IND-1		Nagapattinam, India	Srinivasulu et al. (2010)	Grain size, carbonates, OC, major elements
IND-2			Veerasingam et al. (2014)	Grain size, magnetic susceptibility, mineralogy, major elements
IND-2		Chennai, India	Jonathan et al. (2012)	Grain size, carbonates, OC, microfossils
TH-1		Khao Lak, Thailand	Feldens et al. (2012)	Bathymetry, reflectivity, grain size, macrofossils
TH-1			Sakuma et al. (2012)	Grain size, sedimentological features, major elements, radioisotopes, density
TH-1			Sakuma-Schwartz et al. (2015)	Grain size, sedimentological features, major elements, radioisotopes, density
TH-1			Tipmanee et al. (2012)	PAHs
TH-1			Milker et al. (2013)	Grain size, sedimentological features, microfossils
JP-5	2011 Tohoku-Oki Tsunami	Shimokita, Japan	Toyofuku et al. (2014)	Grain size, microfossils
JP-6		Sendai Bay, Japan	Tamura et al. (2015)	Grain size, sedimentological features, radioisotopes
JP-6			Yoshikawa et al. (2015)	Bathymetry, subsurface analysis, grain size, sedimentological features, radioisotopes
JP-7		Tohoku, Japan	Nomaki et al. (2016)	Grain size, TOC, TN, C/N, radioisotopes

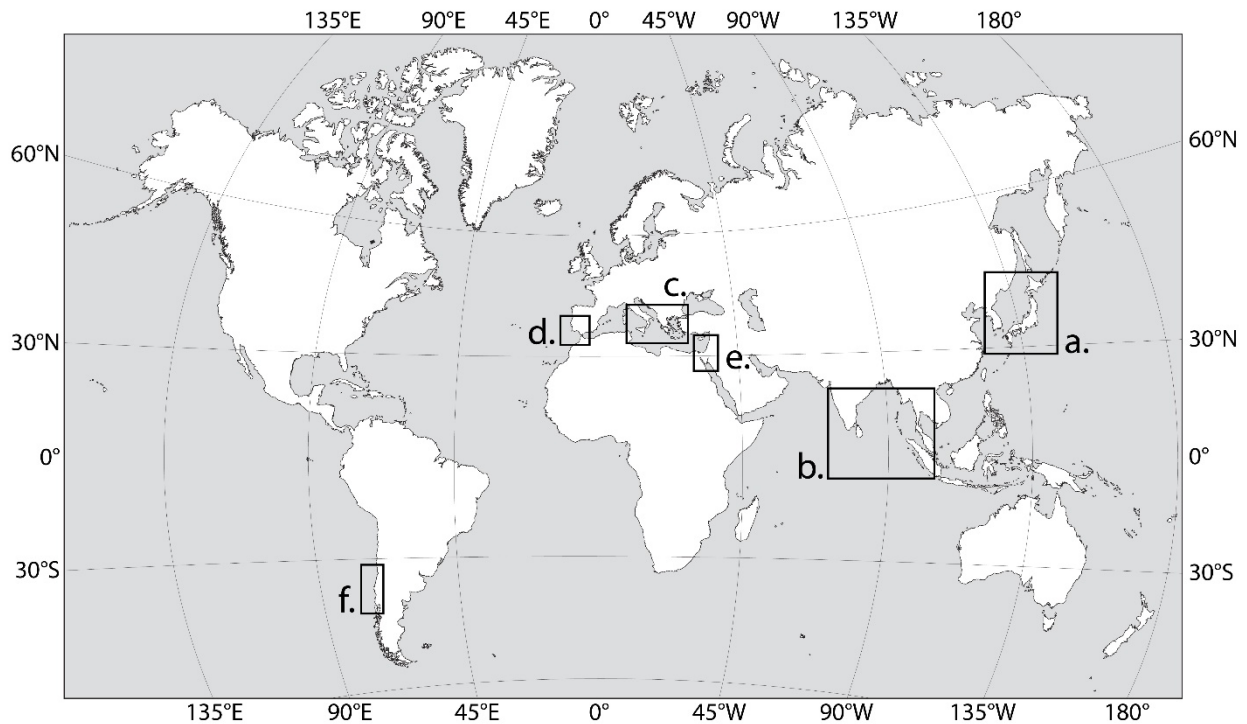


Figure 2.4: Location of all the sites listed in Table 2.1 focusing on marine tsunami backwash deposits around the world; **a.** Japan area (Figure 2.4); **b.** Bay of Bengal area (India, Thailand and Indonesia) (Figure 2.5); **c.** Mediterranean Sea (Italy, Sicily and Greece) (Figure 2.6); **d.** Gibraltar Detroit area (Portugal and Spain) (Figure 2.7); **e.** eastern Mediterranean Sea (Israel and Jordan (Figure 2.8)); **f.** south Chile (Figure 2.9).

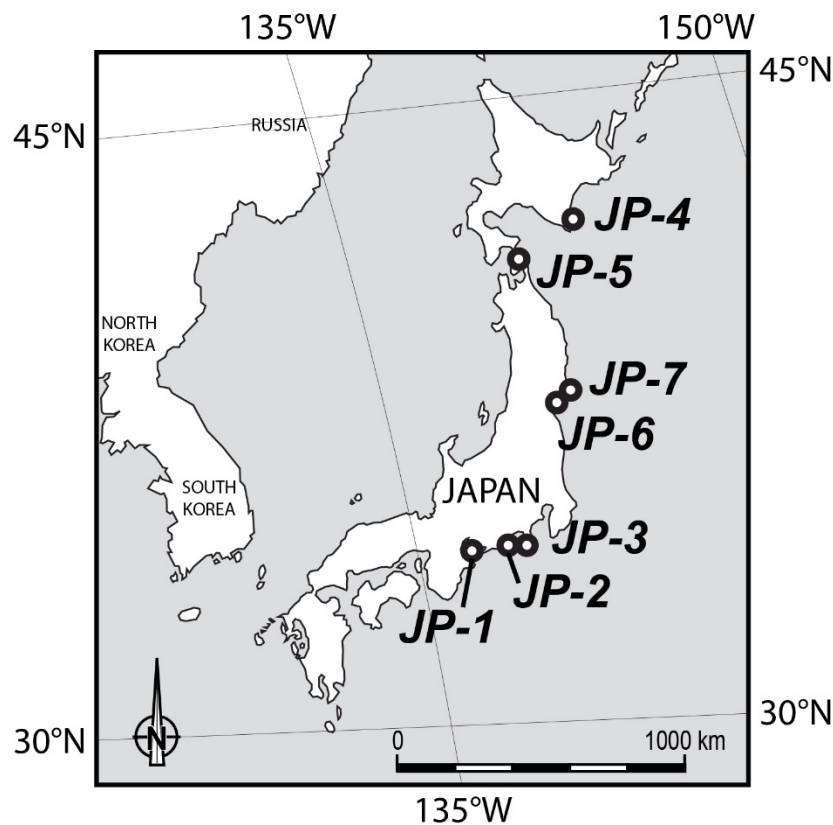


Figure 2.3: Location of study sites in the Japan area; see Table 2.1 for details on studies.

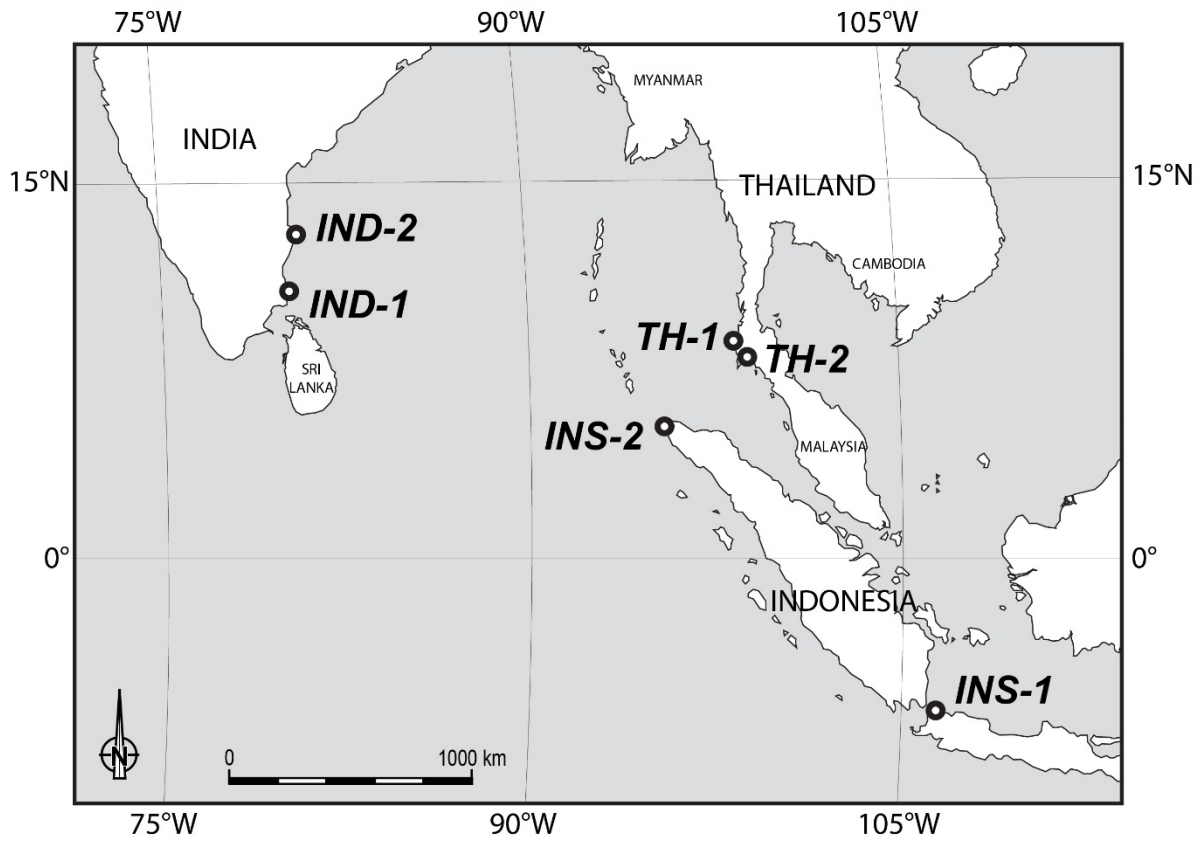


Figure 2.6: Location of study sites around the Gulf of Bengal; see Table 2.1 for details on studies.

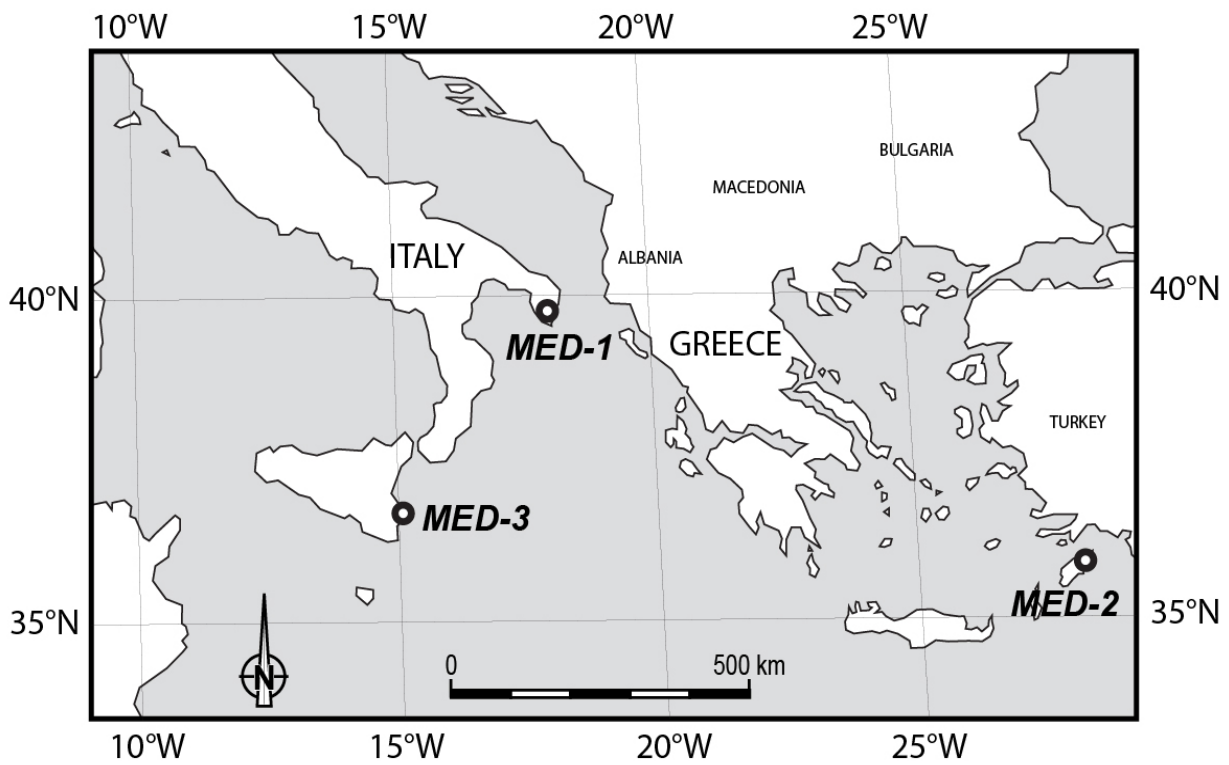


Figure 2.5: Location of study sites in the northern Mediterranean Sea; see Table 2.1 for details on studies.

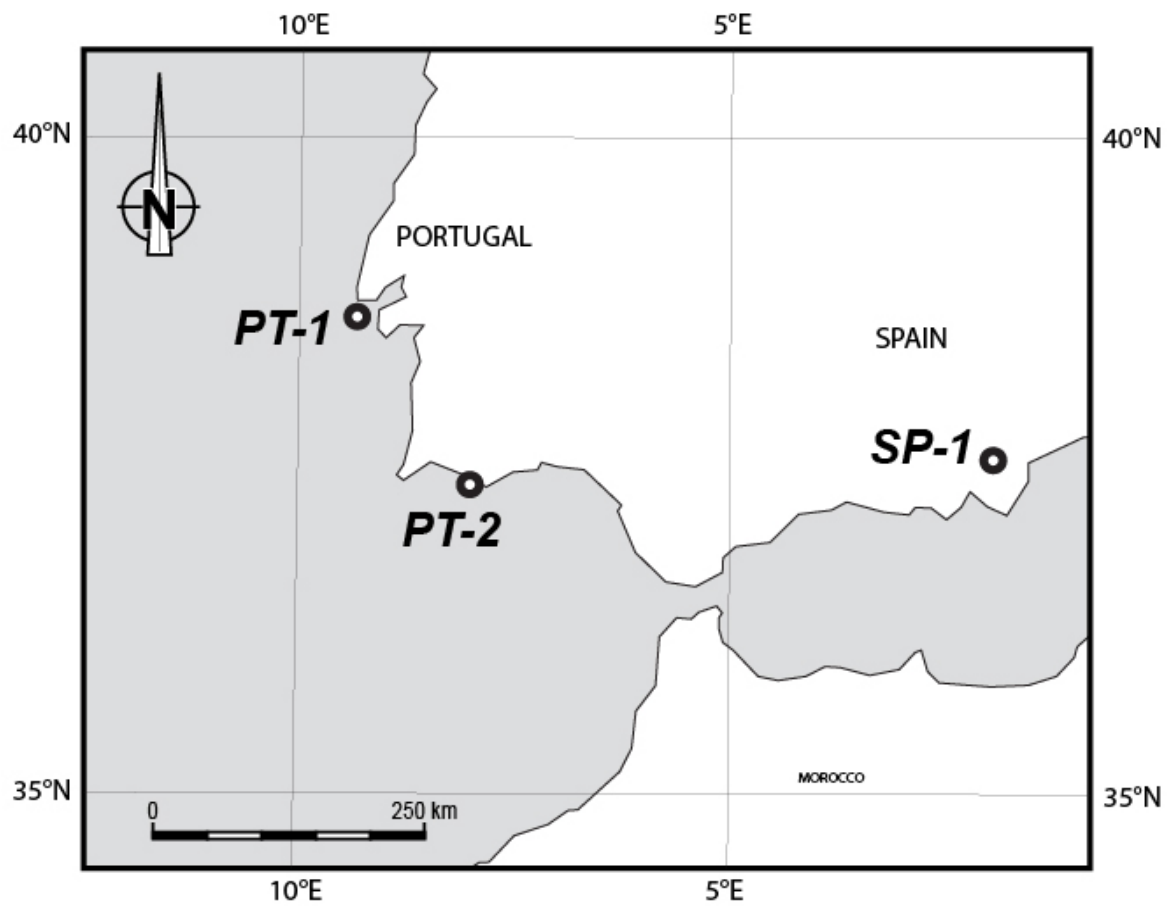


Figure 2.9: Location of study sites in the Gibraltar Strait area; see Table 2.1 for details on studies.

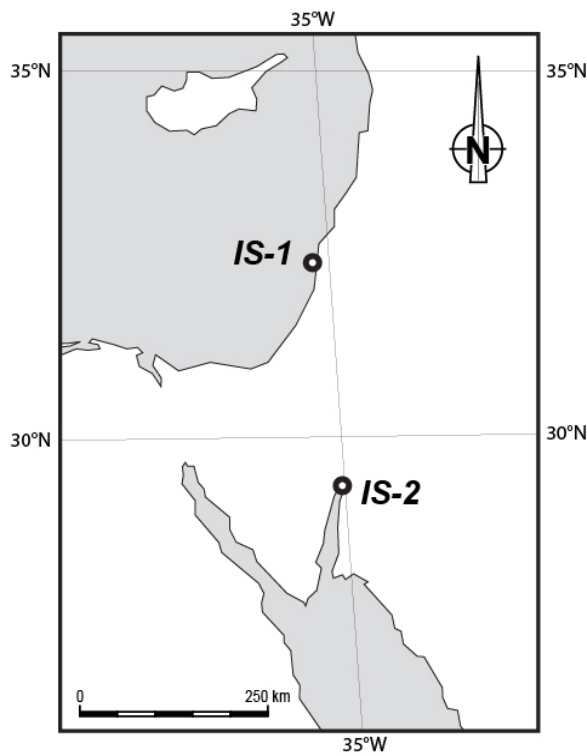


Figure 2.8: Location of study sites in eastern Mediterranean Sea; see Table 2.1 for details on study.

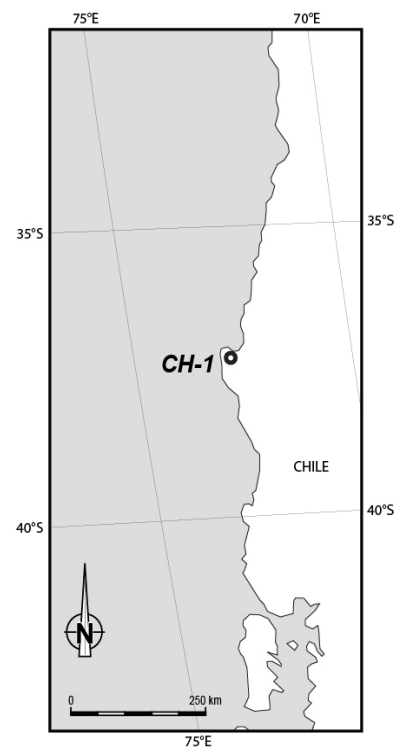


Figure 2.8: Location of study site in south Chile; see Table 2.1 for details on studies.

2.2.2.1 Geomorphological signature

Marine sediment redistribution and other nearshore geomorphological features induced by a tsunami can be assessed shortly after the event based on reflectivity and bathymetric and seismic profiles. Bathymetric and seismic surveys conducted by Yoshikawa *et al.* (2015) offshore Sendai Plain shortly before and after the 2011 TōT revealed the relation between erosion and deposition in nearshore environments and the influence of topography. Erosion is dominant in the foreshore domain where the slope is steep, while deposition starts as soon as the slope decreases. Yoshikawa *et al.* (2015) also noted that one or two erosion surfaces can be seen on high-resolution seismic profiles at the base of the backwash deposits. Following the 2004 IOT, Feldens *et al.* (2009) and Di Geronimo *et al.* (2009) observed wide channels just off Pakarang Cape (Thailand) (Figure 2.10.b). These 0.5 to 2 m deep and 50 to 200 m wide asymmetrical channels have a direction parallel to that of the backwash flow observed during the 2004 IOT event and show good correlation with onshore rivers and incisions made by the successive in- and outflows. Feldens *et al.* (2012) observed later a system of smaller channels incised in an ancient reef platform connecting the onshore incisions and rivers and the nearshore wide channels. Goodman-Tchernov & Austin (2015) also noted such channelization of outflows in the marine domain following multiple Holocene paleotsunamis impacting the ancient harbor of Caesarea (Israel). Le Roux & Vargas (2005b) describe channelized backwash flows induced by submarine topography in multiple Pliocene to Pleistocene paleotsunamis in Chile.

Following the 2004 IOT, several studies focused on the spatial distribution of different fractions of tsunami backwash deposits based on the reflectivity of the seafloor (Feldens *et al.*, 2009, 2012; Paris *et al.*, 2010). Feldens *et al.* (2009, 2012) observed elongated fine sediment patches, with a direction yet again parallel to that of the marine outflows. These fine sediment patches result of high-density turbulent hyperpycnal flows. Paris *et al.* (2010) reported the presence of lobe-like sorted coarse sediment accumulations, including many boulders, offshore Banda Aceh (Thailand) (Figure 2.10.a). These coarse sediment plumes show seaward coarsening, with the largest boulders (several meters wide) at the front and edges of the lobes. Sand ripples are found at the forefront of the lobes. These accumulations result from high-density debris flows and are driven by gravity and slope angle, with deposition where the slope decreases.

These studies attest that, if the channelization of tsunami backwash flows is commonly admitted onshore (Dawson, 1994; Dawson & Stewart, 2007; Costa *et al.*, 2015), submarine backwash flows and deposits are also channelized and influenced by local topography of the

2. Geological evidence of tsunami backwash deposits in shallow marine environment: a review

seafloor. This channelization results in an uneven deposition of potential tsunami backwash deposits in patches dispersed across the nearshore continental shelf.

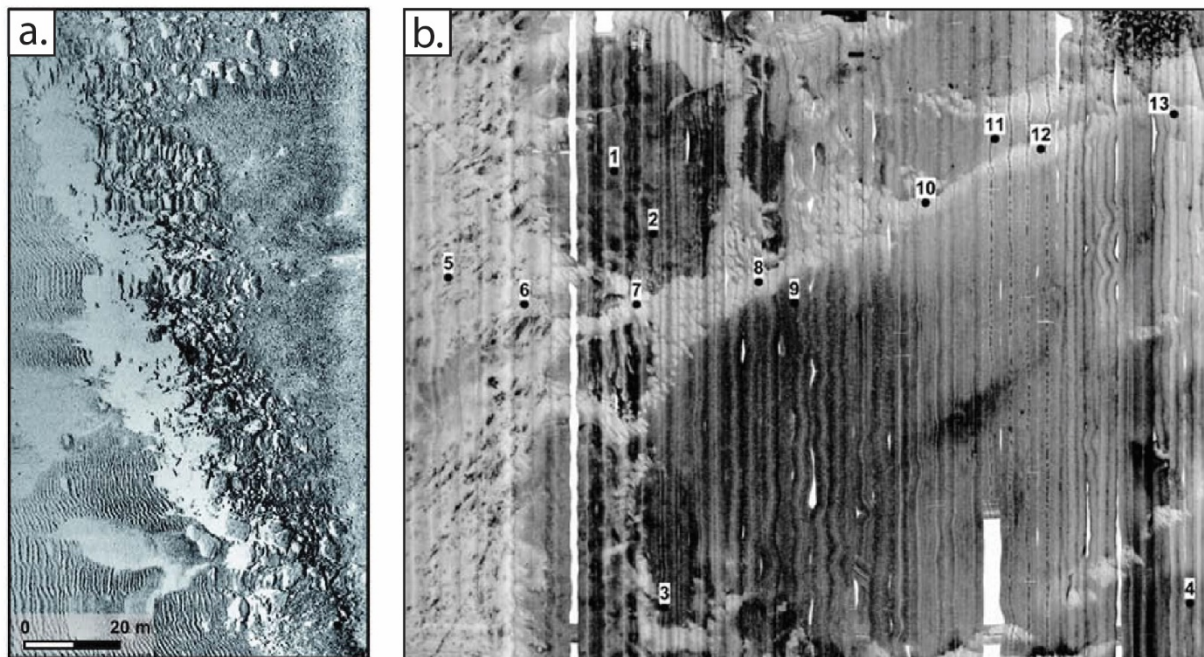


Figure 2.10: **A.** Side-scan sonar image of a submarine accumulation of boulders displaced by the 2004 IOT backwash forming a ridge parallel to the coast with wave ripples induced by the backwash current offshore Lhok Nga (Indonesia, see Table 2.1 and Figure 2.5, site INS-2), from Paris *et al.* (2010); **B.** side-scan sonar image illustrating variations of surface sediment lithology induced by channelization of the 2004 IOT backwash current offshore Khao Lak (Thailand, see Table 2.1 and Figure 2.5, site TH-1), from Feldens *et al.* (2012).

2.2.2.2 Sedimentary signature

2.2.2.2.1 Grain size and sedimentary features

Grain size analysis and sedimentological description of anomalous layers are the most commonly used proxies to study marine tsunami deposits. These observations are applied on outcrops for ancient paleotsunamis and cores for recent paleotsunamis and historic tsunamis. For reported all ancient paleotsunami outcrops, a general mean grain size increase, in comparison to the surrounding sedimentation, was noted (Shiki & Yamazaki, 1996; Fujiwara *et al.*, 2000; Massari & D'alessandro, 2000; Takashimizu & Masuda, 2000; Le Roux & Vargas, 2005b; Fujiwara & Kamataki, 2007; Slootman *et al.*, 2018). In terms of grain size trends and sedimentary features, most of these studies report similar observations. Each marine tsunami deposit sequence is described either as an altogether fining upward sequence (Fujiwara *et al.*, 2000; Massari & D'alessandro, 2000; Takashimizu & Masuda, 2000; Le Roux & Vargas, 2005b; Fujiwara & Kamataki, 2007; Slootman *et*

al., 2018) or stacking of a coarse basal sub-layer and a finer upper sub-layer (Shiki & Yamazaki, 1996). Locally, a thin (< 10 cm) basal inverse graded fine layer, acting as a shear carpet, can be found at the base of the sequence (Le Roux & Vargas, 2005b; Fujiwara & Kamataki, 2007) (Figure 2.11.a). Stacking of two or more overall fining upward sequences is commonly observed for a single event (Shiki & Yamazaki, 1996; Massari & D'alessandro, 2000; Fujiwara & Kamataki, 2007) and is interpreted as a succession of waves or successive uprush and backwash phases (Figure 2.11.b). Each event, represented by one or several superimposed sequences, has a thickness ranging from 1 to 15 m. Each sequence is characterized by a basal erosive surface (Shiki & Yamazaki, 1996; Fujiwara *et al.*, 2000; Massari & D'alessandro, 2000; Takashimizu & Masuda, 2000; Le Roux & Vargas, 2005b; Fujiwara & Kamataki, 2007; Slootman *et al.*, 2018) with scour and fill structures, such as flute casts (Figure 2.11.a). Intense pressure increases due to the earthquake shock and tsunami wave passing are reflected in some cases by injection structures such as dykes reaching up to several meters long or convolute beds (Shiki & Yamazaki, 1996; Takashimizu & Masuda, 2000; Le Roux & Vargas, 2005b). In most cases, a poorly sorted, massive and structureless clast-supported conglomerate layer is typically found at the base of the sequence (Shiki & Yamazaki, 1996; Le Roux & Vargas, 2005b; Fujiwara & Kamataki, 2007; Slootman *et al.*, 2018). It is composed of mixed angular blocks and gravel, rounded beach pebbles, rip-up clasts, various shell fragments and wood debris. In some cases, the clasts appear to be imbricated (Shiki & Yamazaki, 1996; Fujiwara & Kamataki, 2007). In rare cases, the basal conglomeratic layer shows backset bedded laminations, explained by Slootman *et al.* (2018) by the presence of a hydraulic jump in the nearshore slope, accommodated during the early phase of the tsunami backwash. In other cases, the basal layer simply consists of structureless sandy sediment mixed with rip-up clasts, poorly sorted shell fragments and wood debris (Fujiwara *et al.*, 2000; Massari & D'alessandro, 2000; Takashimizu & Masuda, 2000). The coarse basal layer gradually evolves to finer sandy to silty sediment, with occasional remains of shell and wood debris. This upper part of the tsunami deposit is marked by the presence of planar parallel and cross laminations, including hummocky cross stratification (HCS). Commonly, planar laminations are found just over the conglomeratic layer while cross laminations are found in the upper part of the sequence (Shiki & Yamazaki, 1996; Massari & D'alessandro, 2000; Slootman *et al.*, 2018), but planar laminations can be absent (Takashimizu & Masuda, 2000; Le Roux & Vargas, 2005b) or alternating without distinction with cross laminations (Fujiwara *et al.*, 2000; Fujiwara & Kamataki, 2007). Fujiwara & Kamataki (2007) reported the presence of mud drapes separating the stacked sequences. Takashimizu & Masuda (2000) reported the presence of an upper thin silt layer with wave ripples, attesting of the return to normal nearshore sedimentation. One last characteristic noted in a few studies is the absence of

2. Geological evidence of tsunami backwash deposits in shallow marine environment: a review

bioturbation as compared to the under- and overlying highly bioturbated sediment (Takashimizu & Masuda, 2000; Slootman *et al.*, 2018).

As for recent paleotsunamis and historic tsunamis, most of the previous characteristics can also be found in different studies. The main difference with ancient paleotsunamis is the thickness of a single event deposit and the absence of outcrop observations. Indeed, paleotsunami backwash deposits can be a few decimeters up to more than 10 m in thickness while recent tsunami backwash deposits usually don't exceed a few decimeters. The mean grain size increase as compared to the surrounding sediment was reported in all studies of recent paleotsunamis in the eastern

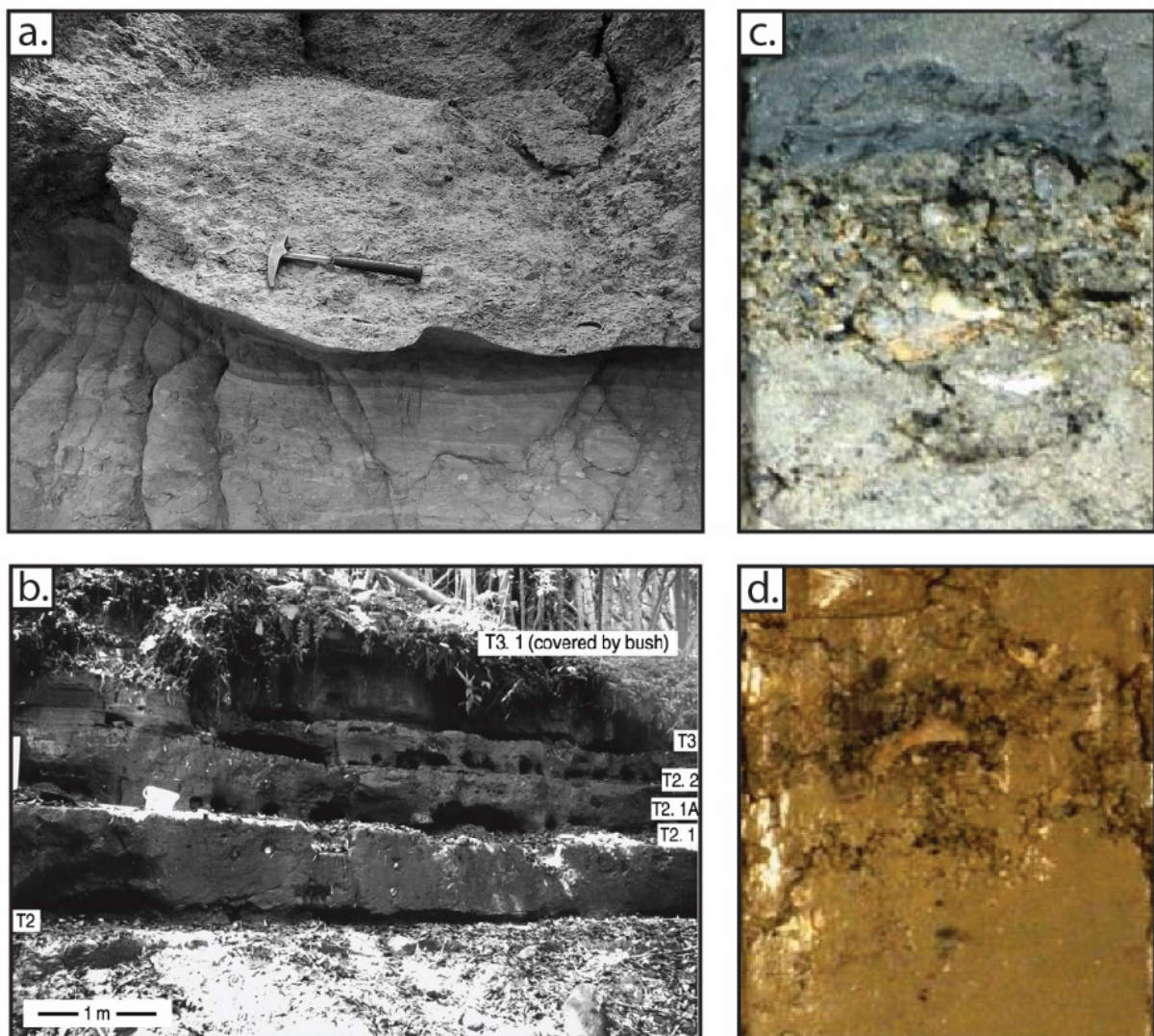


Figure 2.11: **a.** Paleotsunami backwash deposits outcrop with basal erosion including megaflutes and a thin basal shear carpet on the Chilean coast (see Table 2.1 and Figure 2.9, site CH-1), from Le Roux and Vargas (2005); **b.** paleotsunami backwash deposits outcrop showing six stacked units (unconsolidated sand forming the hollows) emplaced by two tsunamis (T2 and T3) intercalated between massive mudstone layers (Japan, see Table 2.1 and Figure 2.4, site JP-3), from Fujiwara and Kamataki (2007); **c.** and **d.** tsunami backwash deposits composed of sand, gravel and shell and coral fragments in cores collected offshore Khao Lak (Thailand, see Table 2.1 and Figure 2.6, site TH-1), from Sakuna-Schwartz *et al.* (2015).

2. Geological evidence of tsunami backwash deposits in shallow marine environment: a review

Mediterranean Sea (Goodman-Tchernov *et al.*, 2009; Smedile *et al.*, 2011, 2012; Tchernov *et al.*, 2016; Tyuleneva *et al.*, 2018), the 1755 and 1969 Lisbon tsunamis (Abrantes *et al.*, 2008; Quintela *et al.*, 2016), the 1883 Krakatau eruption tsunami (Van Den Bergh *et al.*, 2003), the 2004 Indian Ocean Tsunami (Srinivasalu *et al.*, 2010; Feldens *et al.*, 2012; Jonathan *et al.*, 2012; Sakuna *et al.*, 2012; Milker *et al.*, 2013; Veerasingam *et al.*, 2014; Sakuna-Schwartz *et al.*, 2015) (Figures 2.11.c and 2.11.d) and the 2003 Tokachi-Oki and 2011 Tohoku-Oki tsunamis in Japan (Noda *et al.*, 2007; Tamura *et al.*, 2015; Yoshikawa *et al.*, 2015). However, Noda *et al.* (2007) also reported grain size decrease for tsunami deposits at depths greater than 50 m after the 2003 Tokachi-Oki Tsunami, while Smedile *et al.* (2011, 2012) and Abrantes *et al.* (2008) reported the absence of grain size variation respectively for multiple prehistoric tsunami deposits and the 1969 Lisbon Tsunami. Fining upward sequences were reported for several studies (Van Den Bergh *et al.*, 2003; Goodman-Tchernov *et al.*, 2009; Feldens *et al.*, 2012; Sakuna *et al.*, 2012; Milker *et al.*, 2013; Sakuna-Schwartz *et al.*, 2015; Tamura *et al.*, 2015; Yoshikawa *et al.*, 2015; Quintela *et al.*, 2016), while coarse non graded sequences were reported in others (Van Den Bergh *et al.*, 2003; Abrantes *et al.*, 2008; Sakuna *et al.*, 2012; Milker *et al.*, 2013; Tyuleneva *et al.*, 2018) (Figures 2.11.c and 2.11.d). Backwash sequences were found superimposed in bunches of up to three stacked sequences in some cases for the 2004 Indian Ocean Tsunami (Feldens *et al.*, 2012; Sakuna *et al.*, 2012; Sakuna-Schwartz *et al.*, 2015) and 2011 Tohoku-Oki Tsunami (Tamura *et al.*, 2015). In a few studies, sequences showed a first thin inverse graded layer followed by a fining upward general trend (Van Den Bergh *et al.*, 2003; Yoshikawa *et al.*, 2015). As for ancient paleotsunami deposits, most studies described the basal contact of the coarse-grained sequences as an erosive surface (Van Den Bergh *et al.*, 2003; Abrantes *et al.*, 2008; Goodman-Tchernov *et al.*, 2009; Feldens *et al.*, 2012; Sakuna-Schwartz *et al.*, 2015; Tamura *et al.*, 2015; Yoshikawa *et al.*, 2015; Quintela *et al.*, 2016; Tyuleneva *et al.*, 2018) (Figures 2.11.c and 2.11.d). Grain size of coarse-grained sequences vary depending on the available sediment supply during backwash, and range from silt to gravel size. The lower and coarser part of the deposit commonly includes floating rip-up clasts and poorly sorted clast-supported gravels, rounded pebbles, shell and wood debris as well as anthropogenic material (Van Den Bergh *et al.*, 2003; Abrantes *et al.*, 2008; Goodman-Tchernov *et al.*, 2009; Feldens *et al.*, 2012; Sakuna *et al.*, 2012; Sakuna-Schwartz *et al.*, 2015; Tamura *et al.*, 2015; Tyuleneva *et al.*, 2018) (Figures 2.11.c and 2.11.d). The upper part of the deposit is composed of sand and silt and may exhibit parallel sub-horizontal or slightly inclined planar laminations, cross laminations and HCS (Noda *et al.*, 2007; Feldens *et al.*, 2012; Sakuna *et al.*, 2012; Milker *et al.*, 2013; Sakuna-Schwartz *et al.*, 2015; Tamura *et al.*, 2015; Yoshikawa *et al.*, 2015). Finally, the interruption of bioturbation within the tsunami deposits as compared to the under- and overlying deposits was noted in several cases (Tamura *et al.*, 2015; Yoshikawa *et al.*, 2015).

2. Geological evidence of tsunami backwash deposits in shallow marine environment: a review

Based on these observations of ancient paleotsunami outcrops and recent historic and paleotsunamis core deposits, an idealized marine backwash sequence including all reported characteristics can be constructed (Figure 2.12). It is composed of one or several stacked units for a total thickness ranging from a few centimeters to tens of meters. Each unit displays a fining upward general trend and is decomposed in two sub-units. The lower contact is erosional with injection (dykes) and scour (flute casts) structures and filled by a thin inverse graded shear carpet. On top of the shear carpet, the lower sub-unit (sub-unit 1) is a massive and structureless conglomerate composed of a coarse sand matrix with clast-supported rip-up clasts, angular

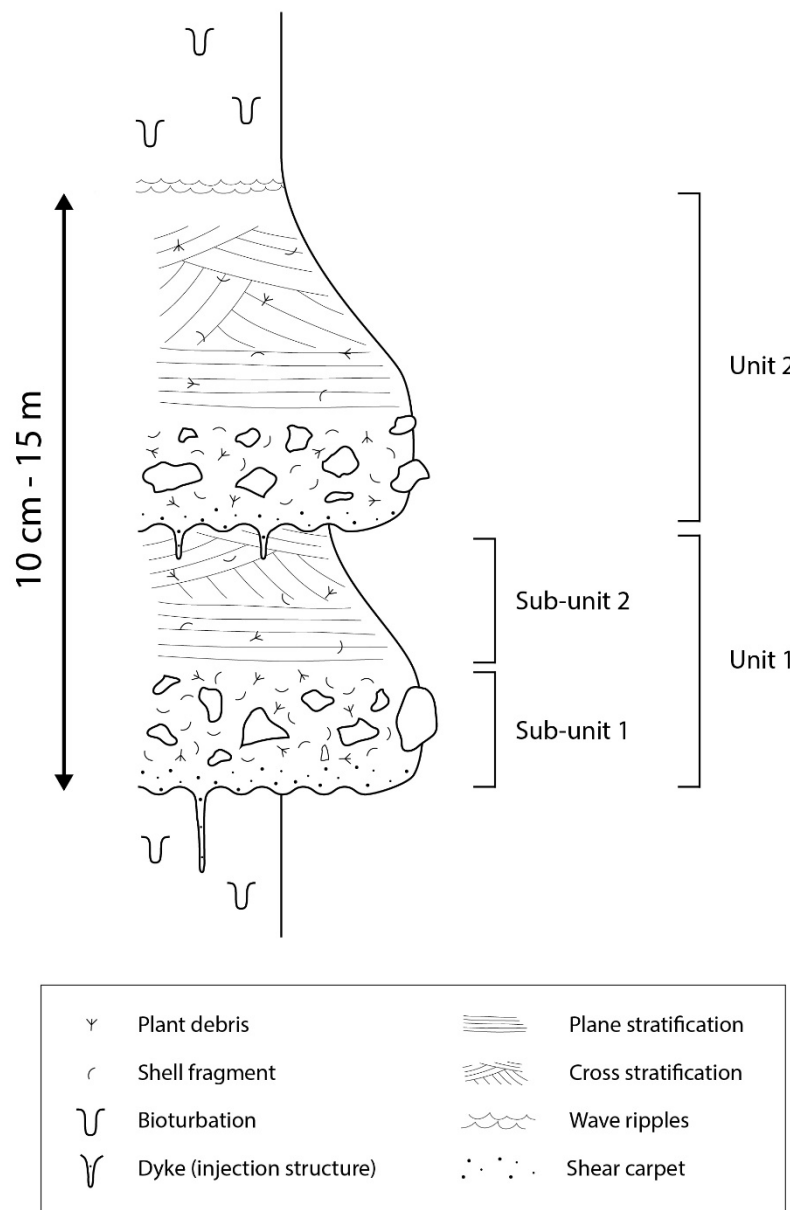


Figure 2.12: Schematic idealized shallow marine tsunami backwash sequence, including all distinctive characteristics gathered from all studies focusing on backwash deposits, with two stacked units emplaced by two successive waves of a single tsunami; each unit is composed of a lower coarse sub-unit and an upper fine laminated sub-unit.

boulders and gravels, well rounded pebbles, shell and wood debris. It may display locally backset lamination. The upper sub-unit (sub-unit 2) is a fining upward sandstone with remains of shell and wood debris. Sub-unit 2 displays parallel planar stratification in its lower part, evolving in cross stratification or HCS in the upper part and topped by a mud drape. Locally, planar and cross stratification can alternate. Finally, the sediment deposited on top of the event sequence signs a return to normal background sedimentation, with notably a recovery of fine sedimentation and bioturbation.

This sequence attests of the high pressure increase on the seafloor due to the earthquake shock and arrival of the tsunami wave, followed by erosion and shearing by a dense and highly cohesive return debris flow (Le Roux & Vargas, 2005b). The lower massive sub-unit represents the poorly sorted base of the debris flow. The upper fining upward sub-unit represents the top of the debris flow and attests of the evolution of the flow regime from a laminar regime resulting in plane-bedding to a turbulent regime with chaotic flow orientation resulting in cross-bedding (Mulder *et al.*, 2009; Slootman *et al.*, 2018). The mud drape attests of the last phase of the backwash debris flow, the settling of fine suspended sediment. If this sequence is an idealized sequences summarizing all characteristics observed and described in the literature, all backwash deposits are different from one another and most of them only a few of the presented characteristics are found depending on the context of the study zone.

2.2.2.2.2 Magnetic susceptibility

Magnetic susceptibility of analyzed sediment can translate its nature and source. In tsunami deposits, contradictory results were reported and are attributed to different geological context and sources. Hence, it is very important to have a strong understanding of the overall general context of the study area and nature and mineralogy of potential sediment sources. Van Den Bergh *et al.* (2003) reported a strong increase of the magnetic susceptibility in tsunami backwash deposits following the 1883 Krakatau eruption. Two sources were identified for this increase in magnetic material in the deposits: the presence of land-derived volcanic minerals in sandy layers, and in some layers the presence of tephra and pumices from the eruption resulting in even higher magnetic susceptibility peaks. Similarly, Abrantes *et al.* (2008) reported very strong but short magnetic susceptibility peaks at the base of the 1755 Lisbon Tsunami backwash deposits. These peaks are correlated with ARM (Anhysteretic Remanent Magnetization), which confirms a high concentration of magnetic minerals. They interpret this as an occurrence of reworked land-derived sediment input. On the opposite, Veerasingam *et al.* (2014) observed a decrease in magnetic

susceptibility in the 2004 Indian Ocean Tsunami backwash deposits offshore India, correlated with a decrease of the ARM and SIRM (Saturation Isothermal Remanent Magnetization). They attribute this decrease as resulting from a dilution of the background sediment's magnetic properties by a strong input of dia- and paramagnetic sediment. They identified the source as being the quartz-rich and carbonate shell-rich sand found on the coast and beaches of Nagapattinam.

2.2.2.2.3 Mineralogy

As for magnetic susceptibility, mineralogy of marine tsunami deposits are source-dependant and need a strong understanding of the general background of the study zone. Tyuleneva *et al.* (2018) reported layers of increased heavy mineral concentration at the base of Middle Holocene marine backwash deposits in eastern Mediterranean. Heavy minerals included mainly hornblende, zircon, limonite, rutile, magnetite but also augite, epidote, garnet, diopside, apatite and biotite, which are clearly of terrestrial origin through continental crust weathering. Increase of heavy mineral concentration has been used earlier as an indicator of high-energy events in onshore tsunami deposits (Costa *et al.*, 2015). Following the 2004 IOT, several studies analyzed the mineralogical assemblage of the resulting marine deposits. Veerasingam *et al.* (2014) noted a strong concentration increase of quartz, feldspar and carbonate in the tsunami deposits compared

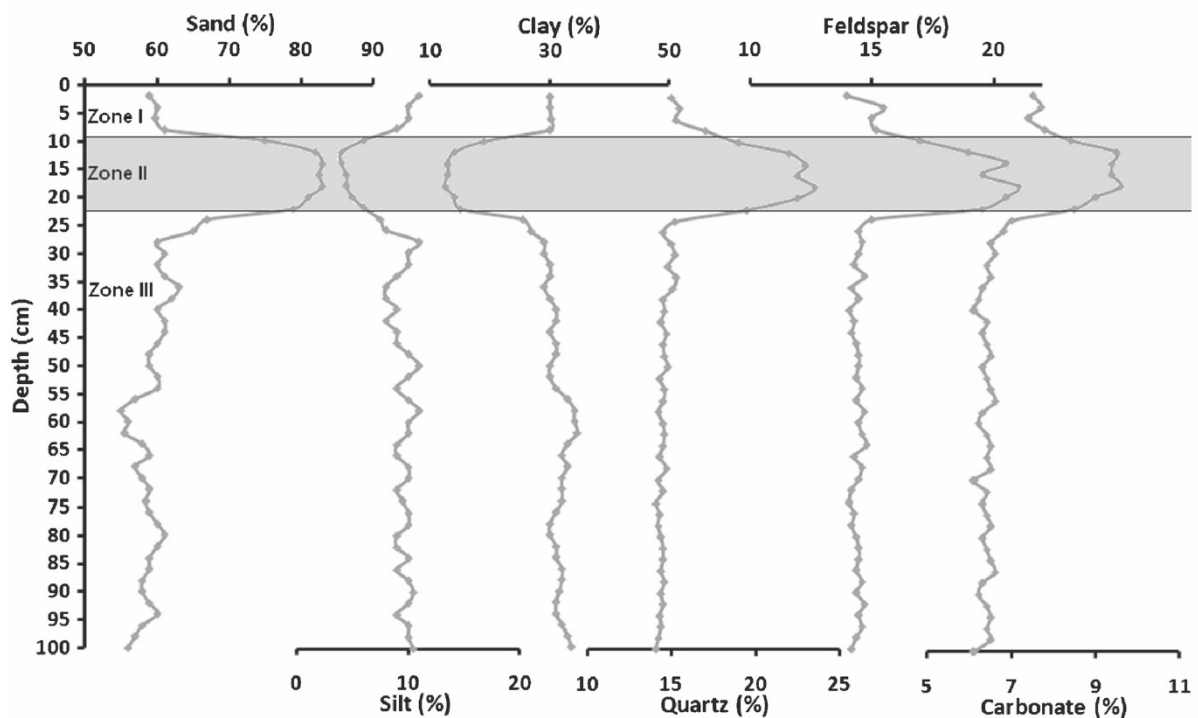


Figure 2.13: Lithological and mineralogical composition of the 2004 IOT backwash layer (Zone II in gray) observed offshore Nagapattinam (India, see Table 2.1 and Figure 2.5, site IND-1), from Veerasingam *et al.* (2014).

to the background sediment (Figure 2.13). They attributed this characteristic to the input of quartz- and shell-rich beach sand transported seaward by the outflow. Jonathan *et al.* (2012) distinguished the inflow and outflow layers and reported a variation in the concentration of carbonates in these layers. They observed a carbonate-depleted inflow layer opposed to a carbonate-enriched outflow layer. They interpret the carbonate enrichment of the backwash deposits as the result of the shell-rich beach sand input dragged by the backwash current. Srinivasalu *et al.* (2010) observed a similar trend for carbonates in undifferentiated tsunami backwash deposits. Under different circumstances, Van Den Bergh *et al.* (2003) analyzed the mineralogical assemblage of the shallow marine deposits of the 1883 Krakatau eruption-induced tsunami. The deposits included tephra, composed of microlitic and magnetite pumices in a glassy porphyritic plagioclase, augite and hypersthene matrix, land derived sand with volcanic rock fragments and fecal pellets and carbonated shell remains. Other than the tephra, the land-derived sand and shell fragments are also consistent with a land-to-sea transport and attest of abundant erosion of the coastal zone.

2.2.2.3 Geochemical signature

Geochemical signatures are being more commonly used as a proxy to help identifying and characterizing tsunami deposits, especially after recent tsunamis. Indeed, new interest in offshore tsunami deposits following the 2004 IOT and 2011 TOT introduced application of a wide range of new geochemical techniques for tsunami deposits identification. In contrast to onshore studies, for which researchers look for signs of marine incursions in otherwise non-marine sediment record, marine tsunami backwash deposits are mainly based on the identification of unusual terrestrial or anthropogenic inputs in otherwise marine-influenced sediment record (Chagué-Goff *et al.*, 2017). However, since the geochemical signatures found in tsunami deposits relate to the sediment source, it involves a very good knowledge of the general and geological context of the study site. More importantly, the methodology of analysis of geochemical signatures will be different from one site to another.

2.2.2.3.1 Major elements

XRF scanning of sediment cores reveals the geochemical composition of the sediment in terms of major elements. In the case of marine tsunami deposits, the most widely used elements in order to determine the sediment source are calcium (Ca), titanium (Ti), zirconium (Zr) and iron (Fe). In marine sediments, Ca is considered to be mainly of marine origin and due to biogenic activity (shells, foraminifera,...), while Ti, Zr and Fe are considered as indicators of terrigenous input, through land erosion (Chagué-Goff *et al.*, 2017). Tyuleneva *et al.* (2018) analyzed the geochemical composition of marine sediment cores from eastern Mediterranean, offshore Israel. They reported an increase of Ca, Ti, Zr, Fe and S (sulfur) in event layers dated from middle Holocene. They interpreted the Ca increase as the result of a shell input, sourced from the beach zone. As for the increase in Ti, Zr and Fe, more pronounced at the base of the event layers, they were interpreted as a result of the presence of a heavy mineral layer, recording a high-energy event. These criteria allowed classifying these event layers as tsunami backwash deposits. Similar increase of Ca in deposits was also noted by Abrantes *et al.* (2008) and Van Den Bergh *et al.* (2003) respectively for the 1755 Lisbon Tsunami and 1883 Krakatau Tsunami, and were also interpreted as shell input eroded and transported from nearby beaches by the backwash. Several studies also focused on the major element composition of marine tsunami deposits following the 2004 IOT. Srinivasalu *et al.* (2010) and Veerasingam *et al.* (2014) both reported a decrease of aluminum (Al) and Fe in the event layer, coupled with an increase of Ca, Ti and silica (Si) (Figure 2.14). These variations were interpreted as an evolution of the sediment source from Al- and Fe-rich alluvial

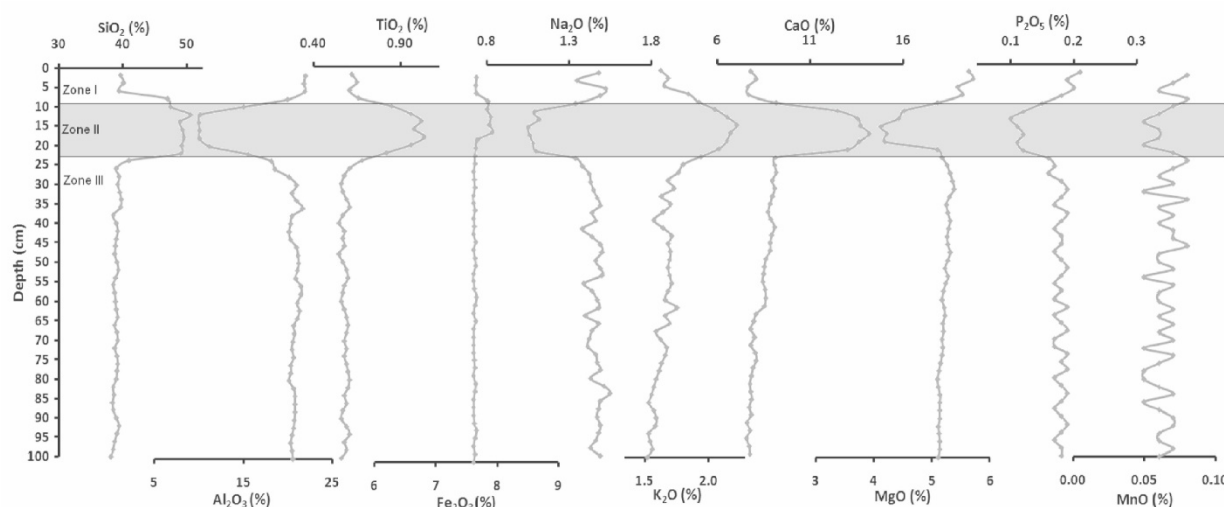


Figure 2.14: Geochemical composition of the 2004 IOT backwash deposits observed offshore Nagapattinam (India, see Table 2.1 and Figure 2.5, site IND-1), from Veerasingam *et al.* (2014).

clay to quartz- and shell-rich beach sand, dragged seaward by the backwash. Sakuna *et al.* (2012) used the Ti/Ca ratio, which was already widely spread for onshore tsunami deposits and used to represent the terrestrial to marine ratio. They reported an alternation of peaks and troughs in the tsunami event layer compared to the homogeneous background sedimentation. This was interpreted as an alternation between marine and terrestrial sources, probably influenced by successive up-rush and backwash phases. Pongpiachan *et al.* (2013a) analyzed the first-order derivative of micro XRF spectra (μ -SXRF) from marine tsunami backwash deposits and compared it to onshore tsunami deposits, typical marine sediment and coastal zone soils. They noticed that, unlike onshore tsunami deposits, which show similar signature as typical marine sediment, marine backwash deposits show similar geochemical signature as coastal zone soils, as reported in previous studies.

2.2.2.3.2 Polycyclic Aromatic Hydrocarbons

Polycyclic Aromatic Hydrocarbons (PAHs) are anthropogenic components that decompose rapidly under normal marine environment. If on land erosion is sufficient during a tsunami, PAHs may be transported seaward by backwash currents, deposited in shallow marine environment and preserved in the sediment record due to instantaneous deposition and burial (Chagué-Goff *et al.*, 2017). Thus, they can be used as a geochemical proxy for identification of anthropogenic sediment sources. Several studies focusing on PAHs were conducted in the Adaman Sea following the 2004 IOT. Tipmanee *et al.* (2012) reported the occurrence of a high concentration of PAHs in superficial nearshore sediments, believed to be the backwash deposits from the 2004 IOT. Although their observations did not give independent evidence of tsunami origin, they highlighted an increase of anthropogenic chemical components, mainly road dust and burnt oil, in marine backwash deposits. Later, using three-dimensional plots of binary PAHs ratios coupled with hierarchical cluster analysis, Pongpiachan (2014) showed that marine backwash sediments are issued from more complex terrigenous and anthropogenic sources than typical marine sediments. However, Pongpiachan & Schwarzer (2013) issued a critical review of the use of PAHs as an identification criterion for tsunami backwash deposits. They point out that, for the moment, results given by PAHs for identification of tsunami deposits weren't convincing enough, since no other evidence of tsunami origin was given in previous and undergoing studies (Tipmanee *et al.*, 2012; Pongpiachan, 2014).

2.2.2.3.3 Radioisotopes

Radioisotopes are mostly used for direct dating or indirect dating through accumulation rates estimations. ^{14}C , ^{210}Pb and ^{137}Cs are the most commonly used radioisotopes for this purpose. Consistent age-to-depth models are often a key point of tsunami studies, especially for recent historic events, and can help identifying known tsunami deposits or date ancient paleotsunami deposits. In some cases they can even be used as a proxy for the identification of tsunami sediment layers. Abrantes *et al.* (2008) reported the occurrence of three anomalously old ^{14}C ages and an almost 400-year sedimentation gap in cores taken offshore Lisbon. These anomalous ages were interpreted as older reworked sediment deposited on top of an estimated 355-year erosion and the tsunami origin was validated by sedimentological evidence and dated to the 1755 Lisbon Tsunami. Following the 2004 IOT, Sakuna *et al.* (2012) noted anomalies in the ^{210}Pb profile offshore Khao Lak (Thailand). A peak of very low ^{210}Pb activity, corresponding to the supported activity only, interrupts steady declining profile. It was interpreted as an instantaneous event layer with reworking of older sediment and related to the 2004 IOT backwash deposits. Sakuna-Schwartz *et al.* (2015) reported similar anomalously low ^{210}Pb activity values in new cores from the same site and attributed to both flash-flood and 2004 IOT backwash deposits based on additional sedimentological criteria. Following the 2011 TOT, Tamura *et al.* (2015) observed increases of ^{134}Cs and ^{137}Cs in superficial core sediment. These increases were the main proxy for identifying the tsunami backwash deposits and post-tsunami deposits from the 2011 TOT and are due to ^{134}Cs and ^{137}Cs released from the accidental destruction of the Fukushima nuclear power plant during the tsunami. Likewise, Yoshikawa *et al.* (2015) reported a strong increase of ^{137}Cs activity in the uppermost 30 cm of sediment offshore Sendai plain, which they attributed to radionuclides transported seaward by the 2011 TOT backwash current, following the Fukushima nuclear power plant accident.

2.2.2.4 Paleontological signature

2.2.2.4.1 Macrofossils

Along with reworking of terrestrial and marine sediment, the run-up and backwash of a tsunami wave is also responsible for the redistribution of local fauna and flora across the offshore to onshore transect. However, if within onshore deposits the occurrence of marine species is synonym of inundation, offshore the redistribution of marine species is harder to assess. In marine

2. Geological evidence of tsunami backwash deposits in shallow marine environment: a review

environments, a detailed survey and counting of each species is necessary to prove large scale transport of macrofauna. The environment and depth range of habitat of some species found in shallow marine deposit, along with their aspect, may therefore attest of reworking and transport by tsunami waves. Typical macrofossil proxies are shells, algae, wood, plants, but also larger animals or even anthropogenic material.

The occurrence of thick shell beds may be a first indicator of tsunami deposits, since they are mostly associated to high-energy events. In several shallow marine backwash deposits, allochthonous shells have been reported (Toyofuku *et al.*, 2014; Goodman-Tchernov & Austin, 2015; Puga-Bernabéu & Aguirre, 2017; Tyuleneva *et al.*, 2018). However, only one study managed to identify a specific source area. Shells found in the deposits are transported from all over the ramp (inner shelf), and therefore cannot be imputed to tsunami backwash deposits alone based on the origin of these shells. Only Toyofuku *et al.* (2014) suggest that allochthonous bivalves found in backwash deposits from the shelf after the 2011 TOT were dragged from the nearshore domain based on their habitat, which attests transport of the shells by backwash currents. Another argument for backwash deposits is based on the aspect and organization within the deposit of these shells and sometimes corals. They show moderate fragmentation, with a mix of broken and intact shells (Goodman-Tchernov & Austin, 2015; Tchernov *et al.*, 2016; Puga-Bernabéu & Aguirre, 2017; Tyuleneva *et al.*, 2018). Shell and coral fragments are sharp (Goodman-Tchernov & Austin, 2015; Tchernov *et al.*, 2016; Puga-Bernabéu & Aguirre, 2017) and usually very coarse and well sorted (Tchernov *et al.*, 2016; Puga-Bernabéu & Aguirre, 2017). Puga-Bernabéu & Aguirre (2017) also report that shells in the deposits are organized chaotically regarding both concavity and orientation. All these characteristics on the aspect and organization of shells attest of a rapid and turbulent very high-energy event, with low transport distances. In addition, an abundance of pottery and anthropogenic material was reported in backwash deposits from the Santorini eruption offshore Caesarea (Israel) (Goodman-Tchernov *et al.*, 2009; Goodman-Tchernov & Austin, 2015), illustrating the erosion and transport potential of strong backwash currents following tsunamis. On the same purpose, Feldens *et al.* (2009) found abundant grass and pieces of wood and terrestrial plants in backwash deposits emplaced by the 2004 IOT offshore Khao Lak (Thailand). Tyuleneva *et al.* (2018) also reported the presence of worn calcareous sandstones colonized by vermitids. These organisms usually live in brackish intertidal zones (Tyuleneva *et al.*, 2018), which explains why the sandstones are worn out, and attest of a seaward transport of shoreface material out into deeper water.

2.2.2.4.2 Microfossils

As for macrofossils, microfossils can help identifying tsunami deposits, based on their original habitat and their aspect. In the case of shallow marine backwash deposits, only foraminifera are used as proxy. A first approach consists in looking at the aspect of tests of foraminifera present in the deposits as a sign of reworking. A high increase in the proportion of heavily eroded, blackened and yellowed foraminifera tests was reported in deposits of a paleotsunami offshore Aqaba (Jordan, Red Sea; Tchernov *et al.*, 2016) and deposits from the AD 1755 and 1969 tsunamis off Portugal (Quintela *et al.*, 2016). These tests show characteristics of reworking and transport and have been previously used as proxies of onshore tsunami deposits (Pilarczyk *et al.*, 2012; Pilarczyk & Reinhardt, 2012).

A second more complex but also more precise approach for foraminifera as signature of tsunamis is the species assemblage and determination of their original habitat. Commonly, a cluster analysis (multivariate statistical analysis) is used to isolate and recognize different groups based on various criteria, such as the depth or substratum of habitat or the lifestyle of each species, in order to identify allochthonous species from autochthonous species. For these sorts of analyses, only benthic foraminifera are considered because their habitat area are more restricted than planktonic foraminifera and are less subject to being transported under normal conditions. Smedile *et al.* (2011, 2012) reported 11 layers with an enrichment in epiphytic foraminifera assemblage in a core located at 72 m depth off the coast of Italy (Augusta Bay). These epiphytic species are normally found living around or attached to a certain type of seaweed found only in a range of 30 to 40 m depth, which suggests high-energy events with backwash currents capable of dragging the test down to at least 70 m depth. After correlation with known historic events and onland dated paleotsunami deposits, along with a large scale recurrence time (~ 500 years), these layers were interpreted as tsunami backwash deposits. Similar studies were carried out following recent tsunamis, and showed similar results. High proportions of tidal marsh and inner shelf species were observed in backwash deposits dated from the AD 1755 and 1969 tsunamis on the outer shelf off the Algarve coast (Portugal; Quintela *et al.*, 2016). Sugawara *et al.* (2009) described the occurrence of tidal brackish foraminifera assemblages in backwash deposits emplaced by the 2004 IOT backwash off Thailand in water depths greater than 20 m, indicating yet again backwash transport. On the opposite, Jonathan *et al.* (2012) reported offshore species in nearshore environment as evidence of landward transport from deep zones back to coastal area by the 2004 IOT uprush. Biological surveys carried out following the 2011 TOT revealed two different trends in the assemblage of foraminifera in the backwash deposits, depending on the depth (Toyofuku *et al.*, 2014). On the shelf, a high increase

in the diversity of species and number of individuals was observed. On the opposite, at the shelf break, the tsunami wave resulted in the death of most individuals with a high decrease of diversity, followed by rapid colonization by opportunistic species.

2.2.3 Tsunami versus storms and cyclones

One of the main issues when it comes to identifying tsunami deposits is distinguishing them from storm (or typhoon, hurricane, cyclone) deposits, but also from flash-flood deposits in the marine domain. Indeed, tsunamis, storms and flash-floods are all considered to be high-energy events (Kortekaas & Dawson, 2007) and share many similar sedimentary features, such as an erosive base and a fining upward sequence with HCS near the top. This problem remains highly controversial and complicated to tackle due to the fact that few locations offer all these kinds of deposits in a close stratigraphic and areal context. Still, this matter has been widely discussed when it comes to onshore deposits but remain a source of uncertainty (Nanayama *et al.*, 2000; Goff *et al.*, 2004; Kortekaas & Dawson, 2007; Morton *et al.*, 2007; Switzer & Jones, 2008; Chagué-Goff *et al.*, 2011; Phantu Wongraj & Choowong, 2012). On land, tsunami deposits are found to have a higher areal extent (Goff *et al.*, 2004; Kortekaas & Dawson, 2007), with sediment sourced from a wider band along the coast (onshore to offshore domains for tsunamis vs. beach to nearshore domains for storms) (Switzer & Jones, 2008), in comparison with storm deposits. Also, storm deposits tend to be less erosive (Goff *et al.*, 2004; Kortekaas & Dawson, 2007), with a better grain size sorting (Nanayama *et al.*, 2000; Goff *et al.*, 2004; Switzer & Jones, 2008), where tsunami deposits often exhibit rip-up clasts at base (Kortekaas & Dawson, 2007; Phantu Wongraj & Choowong, 2012) with more complex bedding (Nanayama *et al.*, 2000; Phantu Wongraj & Choowong, 2012).

In the case of marine deposits, they are even harder to distinguish, with also flash-flood deposits adding to the possibilities as high-energy events, and have been much less discussed (Sakuna-Schwartz *et al.*, 2015). Indeed, one or more of the features exposed earlier for shallow marine tsunami deposits can also be found in storm or flash-flood deposits (Figure 2.15). One of the first arguments in separating tsunami from storm deposits is the area of deposition. Storm deposits are nearly exclusively restrained to the shoreface and upper offshore, in depths shallower than the storm wave base, whereas tsunami deposits can often be found well into the lower offshore domain (Weiss & Bahlburg, 2006; Goodman-Tchernov *et al.*, 2009; Smedile *et al.*, 2011, 2012). Then, though the sedimentary features are very similar (Figure 2.15), some slight difference can be found when compared directly with one another. Particularly, storm deposits display better grain size sorting than tsunami deposits (Goodman-Tchernov *et al.*, 2009) and are commonly less

2. Geological evidence of tsunami backwash deposits in shallow marine environment: a review

erosive at base (Massari & D'alessandro, 2000; Smedile *et al.*, 2012; Sakuna-Schwartz *et al.*, 2015). Massari & D'alessandro (2000) and Le Roux & Vargas (2005b) noted that soft-sediment deformation could be found at the base of a tsunami layer, induced by the very high pressure applied to the seafloor during the passage of the tsunami wave, which has never been observed in tempestites. Rip-up clasts and very coarse material, such as boulders, are also very frequent in tsunami deposits compared to storm deposits. Vertical stacking of several thick sub-layers with mud drapes in-between each sub-layer (Fujiwara & Kamataki, 2007) is a feature that cannot be explained in the case of sediment deposition during storms, but only during tsunamis. Indeed, it reflects a succession of high- (coarse complex bedding) and low-energy flow regime (mud drapes) that can only occur with wave trains characterized by very long wavelengths and periods, allowing a calm hydrodynamic setting in between high-energy regimes. Another argument for distinguishing storm and tsunami deposits is the area of drainage, which is reflected in the nature of the sediment found in the deposits. Puga-Bernabéu & Aguirre (2017) focused on the characteristics of the macrofauna found both in storm and tsunami layers. In the case of a tsunami, the resulting shell deposits are from all parts of the ramp while they are much more localized in the case of a storm. In addition, shells are oriented chaotically, with only few very sharp fragments in tsunami deposits while they are organized horizontally, with highly abundant smooth fragments in tempestites. Milker *et al.* (2013) also revealed the presence of foraminifera originating from the nearshore to deep offshore domain in tsunami deposits, while only shallow nearshore benthic species were found in storm-related deposits. The geochemical analysis of tsunami deposits also reveals a very important terrestrial input not found in storm deposits, relevant of the greater onshore inundation and drainage area during tsunamis than during storms. This terrestrial signature is expressed in tsunami deposits as a higher Ti/Ca ratio (Srinivasalu *et al.*, 2010; Sakuna *et al.*, 2012; Veerasingam *et al.*, 2014; Tyuleneva *et al.*, 2018) and occurrence of an important concentration of PAHs (Tipmanee *et al.*, 2012; Pongpiachan *et al.*, 2013b; Pongpiachan & Schwarzer, 2013) and anthropogenic material (Goodman-Tchernov *et al.*, 2009; Goodman-Tchernov & Austin, 2015). Finally, flash-flood deposits, which can also be induced by heavy rain during storms, exhibit a similar strong terrestrial signature (Sakuna *et al.*, 2012; Sakuna-Schwartz *et al.*, 2015). However, when compared to tsunami deposits, flash-flood deposits show better sorting with a finer grain size, are much less erosive and have little to no mud clasts (Sakuna *et al.*, 2012; Sakuna-Schwartz *et al.*, 2015).

To put it simply, there are yet no unique specific criterion to distinguish tsunami deposits from storm, hurricane, cyclone or flash-flood deposits. If most of the features presented above can be encountered in both storm and tsunami deposits, tempestites usually display a lesser range of

2. Geological evidence of tsunami backwash deposits in shallow marine environment: a review

these characteristics when compared to tsunami deposits. For historic or recent tsunami deposits, the best solution remains local historic and archeological archives of known events, which allow linking dated shallow marine deposits with specific great storms, flash-floods or tsunamis. Thus, it is very important to be well documented and study thoroughly the general context but also the study zone in which the deposits are encountered. For example, a highly sheltered bay will be less favorable to be impacted by storms compared to an open beach, and deep environments below the storm wave base are unlikely to record storm deposits. The type of sediment present in the study zone, especially onshore, is also very important when assessing the sources of the sediment deposited in event layers offshore and the extent of the impacted band, such as terrigenous or anthropogenic material in the area. Then, the distinction between tsunamis and other high-energy events is based on the combination of all these arguments rather than a single specific proxy, which

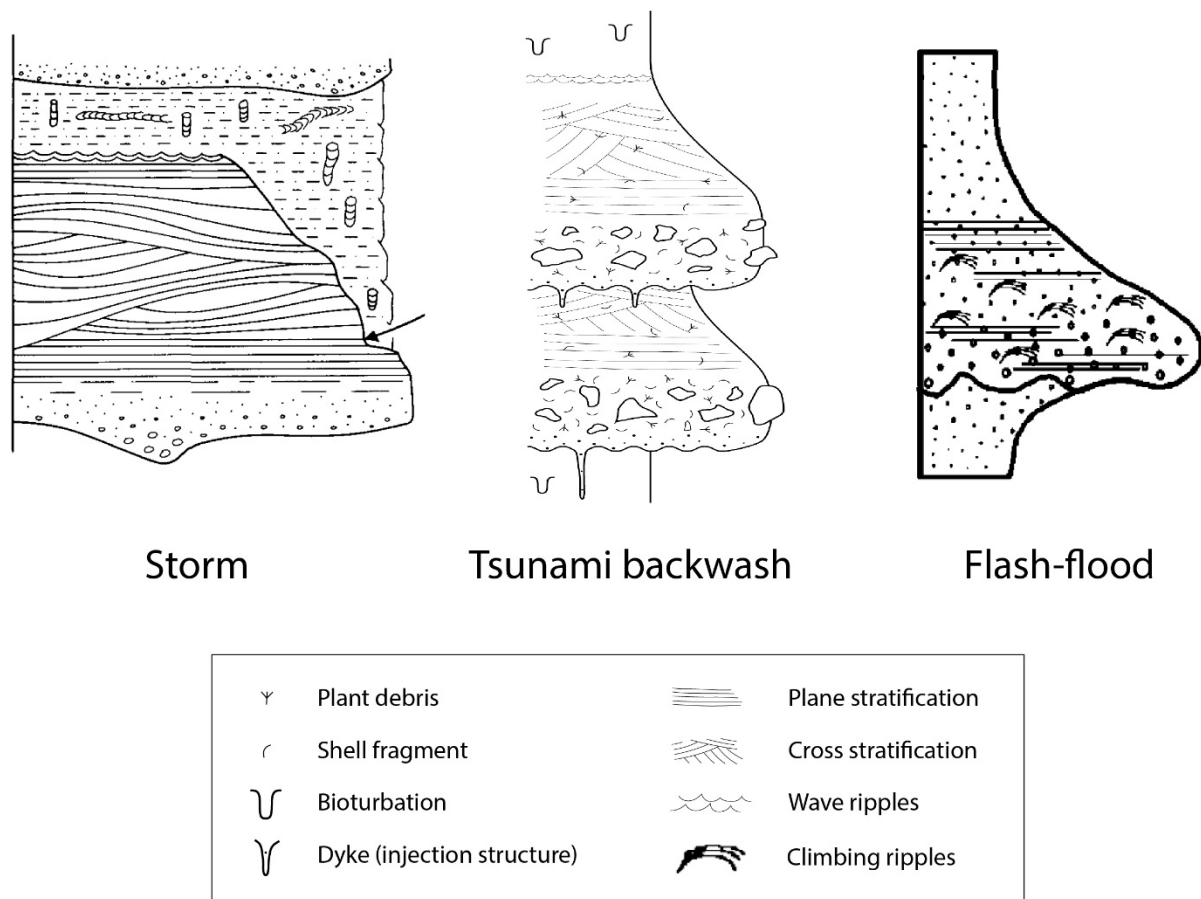


Figure 2.15: Comparison of idealized sedimentary depositional sequences between storm deposits with HCS (left), from Walker *et al.* (1983), tsunami backwash deposits and hyperpycnal flash-flood deposits, from Mulder *et al.* (2003).

often leads to tsunami studies being multi-proxy analyses.

Chapter 3:

The SAMOA-SPT campaign

The SAMOA-SPT oceanographic campaign was carried out from August 27th to September 10th 2015 on board the *R/V Alis*. Data were collected in the bays and lagoons around Tutuila Island, with emphasis on the bays of Pago Pago, Masefau, Fagafue, Maloata, Poloa and Se’etaga. Data collected comprises seafloor bathymetry and reflectivity, 2D seismic and sediment cores.

3.1 Seafloor bathymetry and reflectivity

Seafloor bathymetry and reflectivity was obtained using the EM1002 multibeam echo sounder (manufactured by Kongsberg Maritime), with a lateral resolution of 1 m. Its frequency of 95 kHz allows acquisition from 5 m to 1 000 m water depth, which is optimal for coastal zones such as Tutuila’s bays and lagoons. Prior to acquisition, daily Sippican probe shots were fired in order to calibrate the depth vs. celerity model in the water column. 120 km² of seafloor, divided into five surveys, was mapped during the campaign, in the six main bays and in the lagoons during transit between those bays (Figure 3.1). Following the campaign, each bathymetric survey was processed according to the same workflow using the CARAIBES software (CARTography Adapted to Imagery and BathymEtry of Sonars and multibeam echosounders) developed by IFREMER. It consisted of a tide correction, a wave correction when needed, a first automatic filtering and a final manual filtering to eliminate biased seeds due to celerity variations induced by salinity variations or artefacts in the water column. The bathymetry was then exported as a DEM (Digital Elevation Model) with a 1 m lateral resolution. Reflectivity surveys were processed and treated using the SonarScope software developed by IFREMER, with also correction for tide and waves.

3.2 Seismic

Seismic acquisition was recorded using an IKB-Seistec profiler (manufactured by IKB Technologies Limited), with a bandwidth of 1 to 10 kHz and a shot interval of 250 ms. The vertical

resolution was up to 25 cm with a maximum penetration of approximately 15 to 20 m depending on the nature of the subsurface sediment. 50 km of two-dimension seismic profiles were acquired in all six bays during the campaign (Figures 3.2 to 3.6), with 22 km in Pago Pago Bay alone (Figure 3.2). Raw seismic profiles were processed using DELPH Seismic software developed by iXblue. A frequency filter was applied between 900 and 10 500 Hz in order to erase all interference out of the wanted bandwidth, along with a linear AGC (Amplitude Gain Control) for a 15 ms window so as to correct amplitude loss of seismic waves. Adjacent traces were stacked three by three to clean the profiles from seismic noise.

3.3 Sediment cores

Sediment cores were collected using three different types of coring devices: a Kullenberg piston corer, a custom-made gravity box corer and a hand-held manual interface corer. The Kullenberg piston corer was used to sample long cores, up to 3 m long. It had a good sediment penetration but the superficial soft sediments (up to 1 m) was flushed or deformed during landing and penetration of the corer on the seabed. The custom-made gravity box corer was inspired from the CASQ box corer (CAlypso SQare box corer). It is 1 m long with a 10 x 10 cm square section. It has no piston and penetrates the seabed only by gravity. Given the absence of piston in the corer, its maximum penetration is reduced to 20 to 60 cm depending on the nature and compaction of the superficial sediment. However, this interface corer allows an intact sampling of the uppermost soft sediment with preservation of the stratigraphic organization. The last corer which was used during this campaign is a manual interface corer. It was used by divers to collect very short sediment cores (maximum 25 cm) in areas that could not be reached by the cruise ship (9 to 37 m depth), with intact preservation of the uppermost sediment and their layers. In total, 47 cores were retrieved throughout the six bays (Table 3.1; Figures 3.2 to 3.6), at depths ranging from 27 to 70 m, out of which 27 were in Pago Pago Bay alone (Figure 3.2). 27 cores were collected using the Kullenberg piston corer, offering a long (2 to 3 m) sediment record in every bay. In addition, 10 short interface cores (< 1 m) were recovered in the same spot as the Kullenberg cores in Pago Pago Bay, in order to pair each long sediment core with a well-preserved superficial record. Locations of the cores were chosen according to preliminary interpretation of raw seafloor bathymetry and reflectivity data and seismic profiles. 10 more short interface cores (< 50 cm) were sampled in Pago Pago, Fagafue and Masefau bays using a hand-held manual corer by scientific divers, allowing to access areas that could not be reached by the ship and offering a perfectly

3. Material - the SAMOA-SPT campaign

preserved superficial record. In total, 31.85 m of Kullenberg cores, 3.27 m of interface cores and 2.80 m of manual interfaces cores were collected in all six bays during the campaign. As a complement to these cores, sediment samples were retrieved onshore in various key locations in Pago Pago Bay. Two samples were collected in the river bed of Pago stream, two in the river bed of Lao Lao stream and two on a small beach in the extremity of Pago Pago Bay, by the Pago Airport Inn. Halimeda plates were also collected from the seafloor in living position in order to estimate the local reservoir age for radiocarbon dating of biogenic carbonated material.

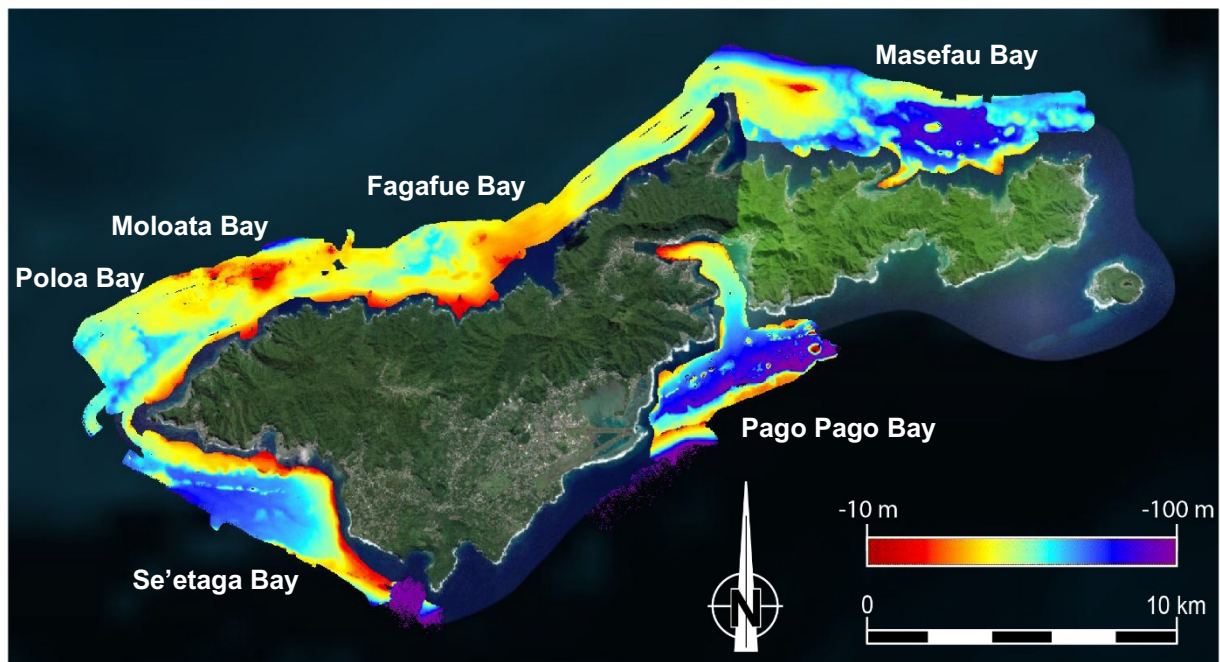


Figure 3.1: Map of Tutuila with bathymetric data acquired during the SAMOA-SPT campaign (modified from Google Earth).

3. Material - the SAMOA-SPT campaign

Table 3.1: List of all cores collected during the SAMOA-SPT campaign with details on core type, length and location and depth of sampling

Core code	Core type	Depth (m)	Location	Latitude	Longitude	Length (m)	Figure
P01	Manual core	30	Pago Pago Bay	S14°16.5042	W170°41.4938	-	Figure 3.2
P02.1	Manual core	18	Pago Pago Bay	S14°16.574	W17°40.771	16	Figure 3.2
P02.2	Manual core	18	Pago Pago Bay	S14°16.574	W17°40.771	11	Figure 3.2
P02.3	Manual core	33	Pago Pago Bay	S14°16.574	W17°40.771	6	Figure 3.2
P04.1	Manual core	23	Masefau Bay	S14°17.425	W10°45.173	14	Figure 3.3
P04.2	Manual core	23	Masefau Bay	S14°17.425	W10°45.173	12	Figure 3.3
P04.3	Manual core	20	Masefau Bay	S14°17.425	W10°45.173	7	Figure 3.3
P05.1	Manual core	37	Fagafue Bay	S14°15.290	W170°37.403	16	Figure 3.4
P05.2	Manual core	37	Fagafue Bay	S14°15.290	W170°37.403	14	Figure 3.4
P06.1	Manual core	9	Pago Pago Bay	S14°16.431	W170°41.750	37	Figure 3.2
P06.2	Manual core	9	Pago Pago Bay	S14°16.431	W170°41.750	33	Figure 3.2
P06.3	Manual core	9	Pago Pago Bay	S14°16.431	W170°41.750	-	Figure 3.2
CA01	Short core (Amaury)	39	Pago Pago Bay	S14°16.44	W170°41.23	29	Figure 3.2
CA02	Short core (Amaury)	28	Pago Pago Bay	S14°16.41	W170°41.47	28	Figure 3.2
CA03	Short core (Amaury)	45.5	Pago Pago Bay	S14°16.41	W170°40.98	49	Figure 3.2
CA04	Short core (Amaury)	29	Pago Pago Bay	S14°16.38	W170°41.40	59	Figure 3.2
CA05	Short core (Amaury)	28	Pago Pago Bay	S14°16.365	W170°41.37	48	Figure 3.2
CA06	Short core (Amaury)	46	Pago Pago Bay	S14°16.470	W170°41.064	48	Figure 3.2
CA07	Short core (Amaury)	33.5	Pago Pago Bay	S14°16.474	W170°41.391	55	Figure 3.2
CA08	Short core (Amaury)	34	Pago Pago Bay	S14°16.474	W170°41.380	57	Figure 3.2
CA09	Short core (Amaury)	27	Pago Pago Bay	S14°16.532	W170°41.455	61	Figure 3.2
CA10	Short core (Amaury)	27	Pago Pago Bay	S14°16.422	W170°41.058	64	Figure 3.2
K01	Kullenberg core	39	Pago Pago Bay	S14°16.433	W170°41.220	234	Figure 3.2
K02	Kullenberg core	28	Pago Pago Bay	S14°16.422	W170°41.443	235	Figure 3.2
K02-bis	Kullenberg core	28	Pago Pago Bay	S14°16.422	W170°41.443	176	Figure 3.2
K03	Kullenberg core	45.5	Pago Pago Bay	S14°16.413	W170°40.950	262	Figure 3.2
K04	Kullenberg core	29	Pago Pago Bay	S14°16.377	W170°41.370	251	Figure 3.2
K04-bis	Kullenberg core	29	Pago Pago Bay	S14°16.377	W170°41.370	155	Figure 3.2
K05	Kullenberg core	28	Pago Pago Bay	S14°16.378	W170°41.337	254	Figure 3.2
K05-bis	Kullenberg core	28	Pago Pago Bay	S14°16.378	W170°41.337	178	Figure 3.2
K06	Kullenberg core	46	Pago Pago Bay	S14°16.470	W170°41.064	260	Figure 3.2
K07	Kullenberg core	33.5	Pago Pago Bay	S14°16.474	W170°41.391	179	Figure 3.2
K08	Kullenberg core	50	Fagafue Bay	S14°16.973	W170°45.334	173	Figure 3.4
K09	Kullenberg core	50	Fagafue Bay	S14°16.925	W170°45.585	157	Figure 3.4
K10	Kullenberg core	65	Fagafue Bay	S14°16.703	W170°45.787	259	Figure 3.4
K11	Kullenberg core	32.5	Poloa Bay	S14°18.982	W170°50.530	152	Figure 3.5
K12	Kullenberg core	50	Poloa Bay	S14°18.792	W170°50.695	112	Figure 3.5
K13	Kullenberg core	70	Poloa Bay	S14°18.148	W170°50.811	98	Figure 3.5
K14	Kullenberg core	70	Poloa Bay	S14°18.767	W170°51.269	100	Figure 3.5
K15	Kullenberg core	44.5	Masefau Bay	S14°15.188	W170°37.364	144	Figure 3.3
K16	Kullenberg core	44.5	Masefau Bay	S14°15.164	W170°37.343	150	Figure 3.3
K17	Kullenberg core	55	Masefau Bay	S14°15.108	W170°37°166"	186	Figure 3.3
K18	Kullenberg core	31	Moloata Bay	S14°17.842	W170°49.031	55	Figure 3.5
K19	Kullenberg core	51	Moloata Bay	S14°17.624	W170°49.003	110	Figure 3.5
K20	Kullenberg core	52	Moloata Bay	S14°17.494	W170°49.017	120	Figure 3.5
K21	Kullenberg core	54.5	Pago Pago Bay	S14°16.670	W170°40.623	157	Figure 3.2
K22	Kullenberg core	56	Pago Pago Bay	S14°16.675	W170°40.38	170	Figure 3.2
K23	Kullenberg core	37	Se'etaga Bay	S14°20.203	S14°20.203	27	Figure 3.6
K24	Kullenberg core	68	Se'etaga Bay	S14°20.424	S14°20.424	73	Figure 3.6

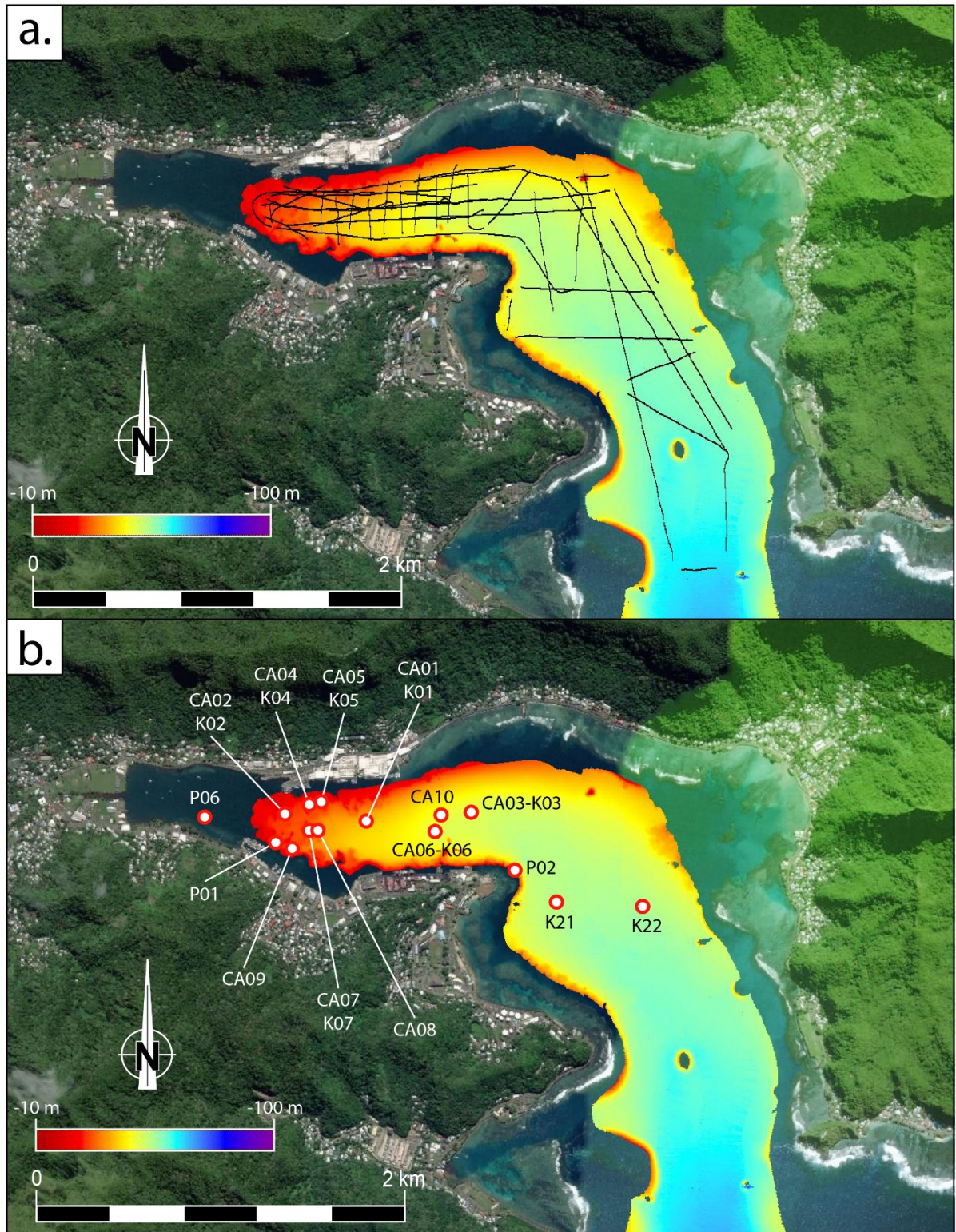


Figure 3.2: Map of Pago Pago Bay with bathymetric data acquired during the SAMOA-SPT campaign; **a.** track of all seismic profiles acquired during the campaign; **b.** all cores collected during the campaign (core names starting with P are for manual cores, CA for short cores and K for Kullenberg cores, see Table 3.1 for details).

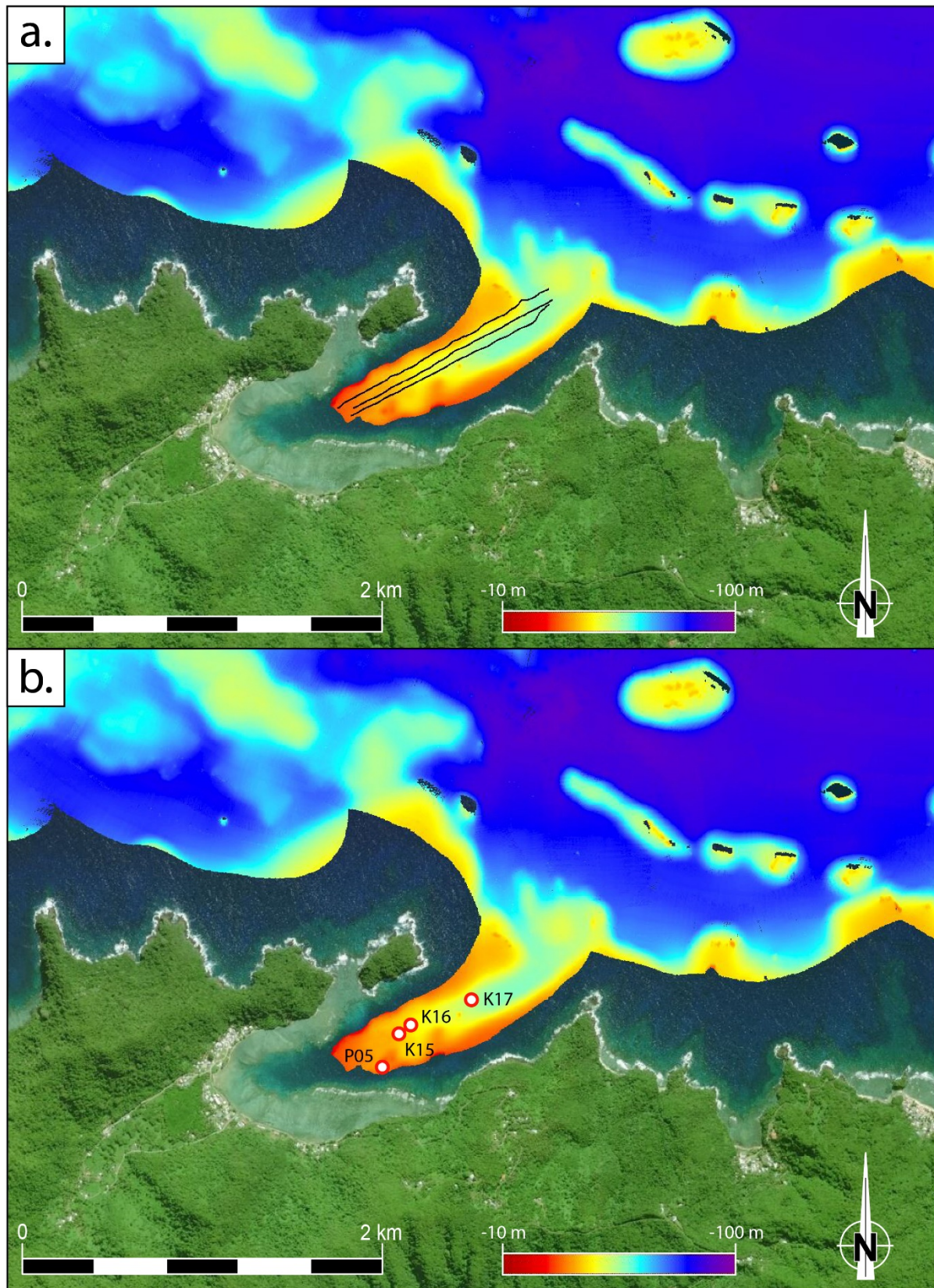


Figure 3.3: Map of Masfau Bay with bathymetric data acquired during the SAMOA-SPT campaign; **a.** track of all seismic profiles acquired during the campaign; **b.** all cores collected during the campaign (core names starting with P are for manual cores and K for Kullenberg cores, see Table 3.1 for details).

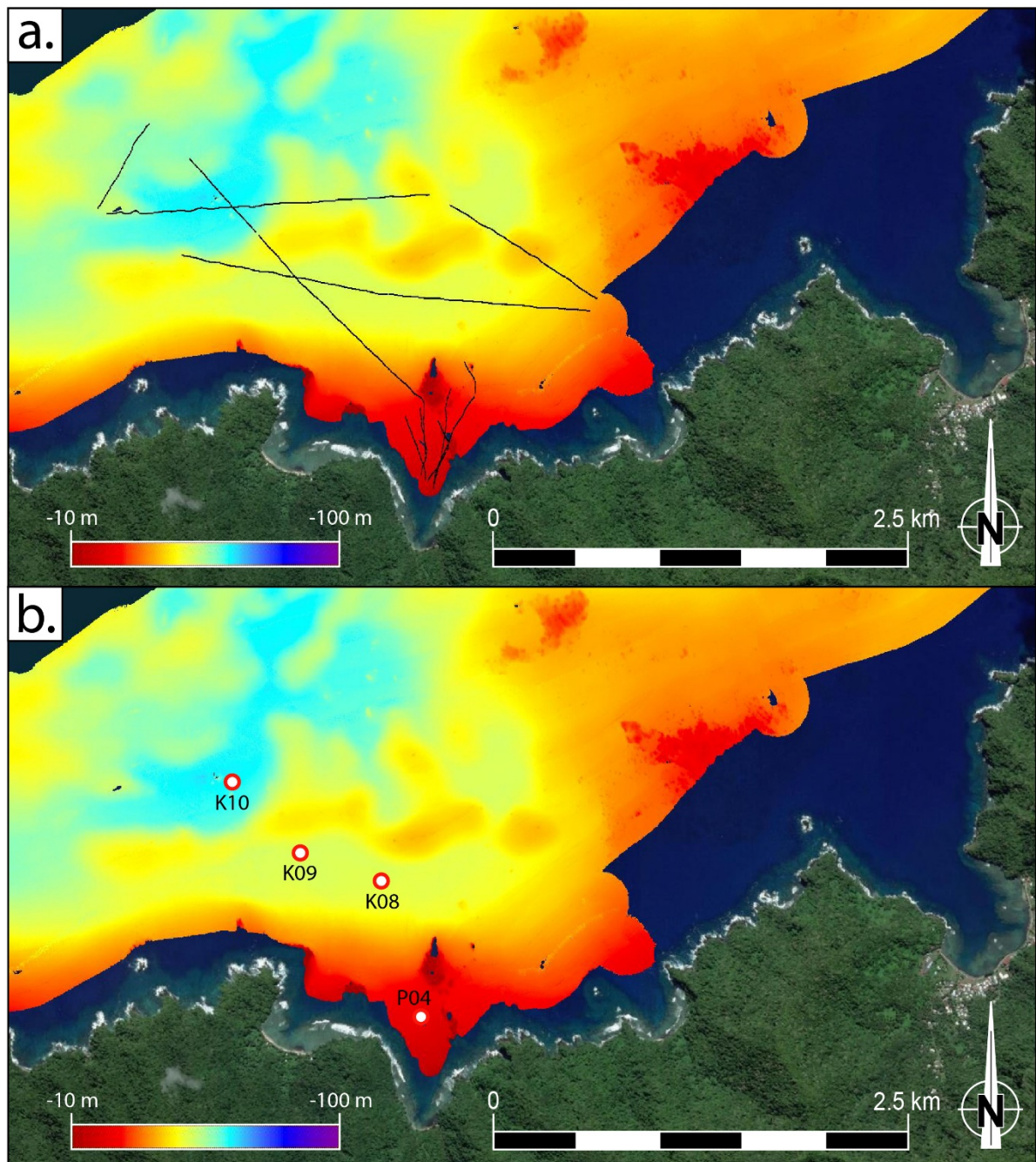


Figure 3.4: Map of Fagafue Bay with bathymetric data acquired during the SAMOA-SPT campaign; **a.** track of all seismic profiles acquired during the campaign; **b.** all cores collected during the campaign (core names starting with P are for manual core and K for Kullenberg cores, see Table 3.1 for details).

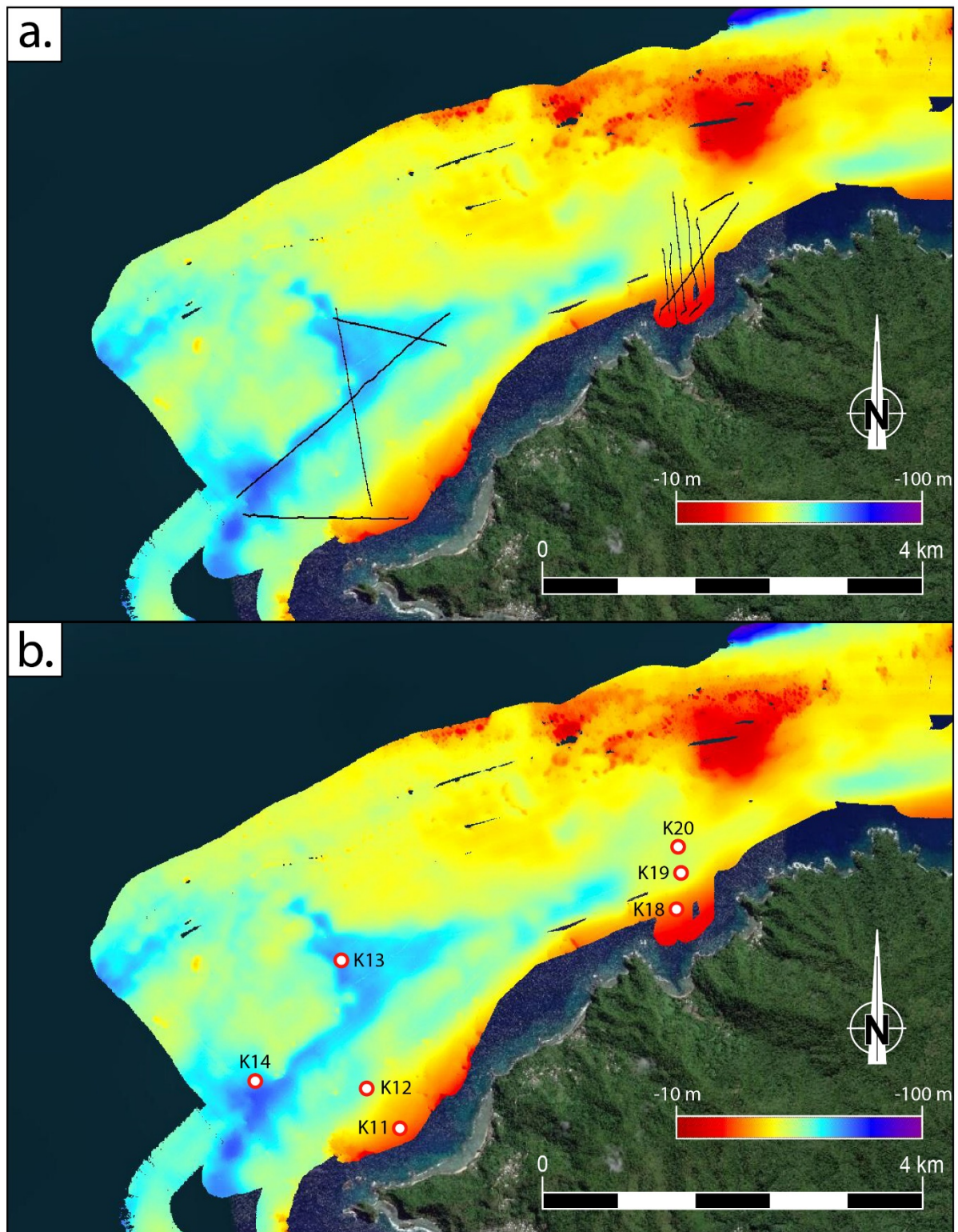


Figure 3.5: Map of Moloata Bay (north-east) and Poloa Bay (south-west) with bathymetric data acquired during the SAMOA-SPT campaign; **a.** track of all seismic profiles acquired during the campaign; **b.** all Kullenberg cores collected during the campaign (see Table 3.1 for details).

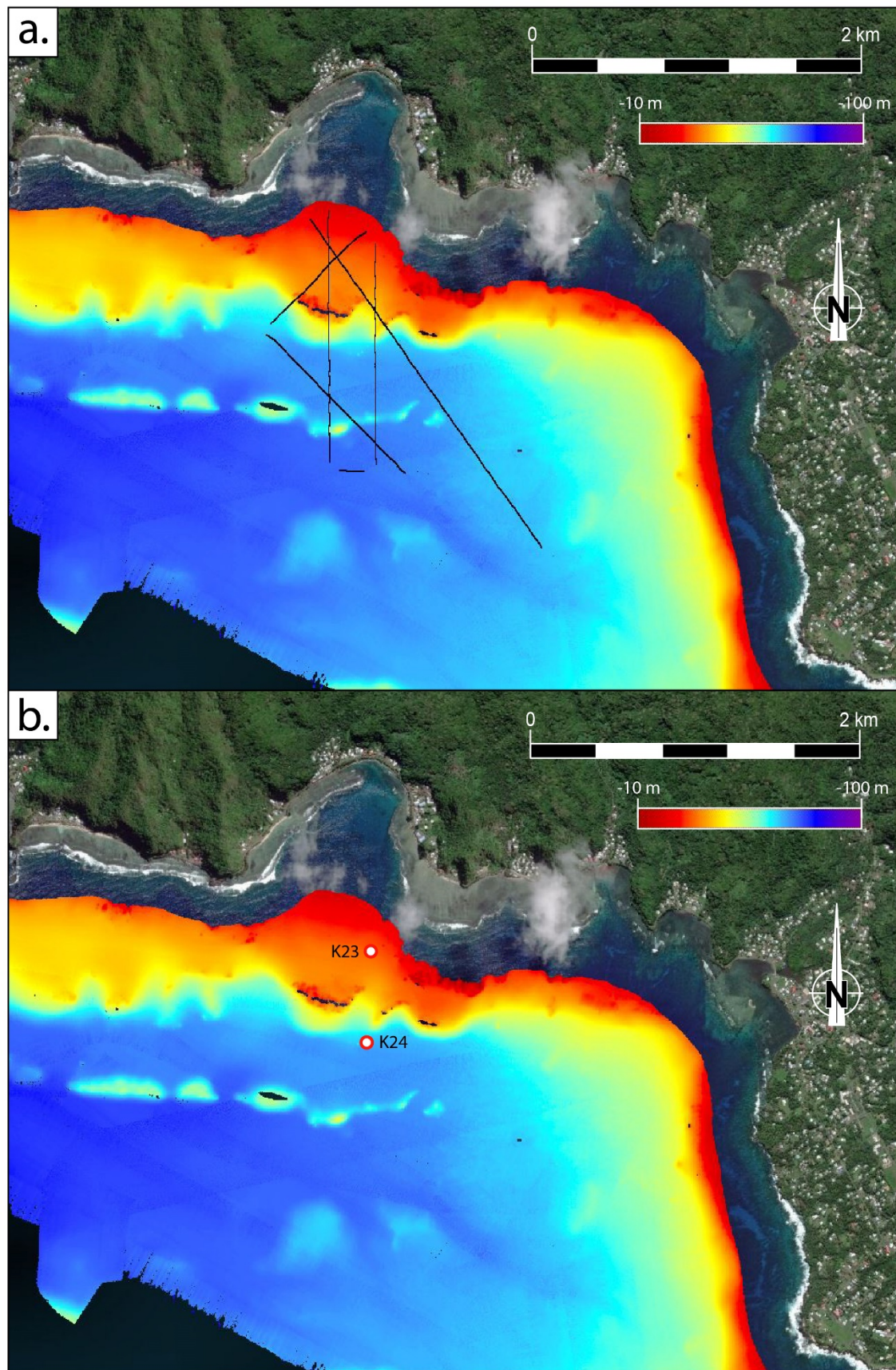


Figure 3.6: Map of Se'etaga Bay with bathymetric data acquired during the SAMOA-SPT campaign; **a.** track of all seismic profiles acquired during the campaign; **b.** all Kullenberg cores collected during the campaign (see Table 3.1 for details).

Chapter 4:

The sediment-fill of Pago Pago Bay (Tutuila Island, American Samoa): new insights on the sediment record of past tsunamis

Sedimentology (2018)

DOI: 10.1111/sed.12574

BRIEUC RIOU^{1,2}, ERIC CHAUMILLON¹, JEAN-LUC SCHNEIDER², THIERRY CORRÈGE² and CATHERINE CHAGUÉ³

¹ LIENSs, UMR 7266-CNRS, Université de La Rochelle, La Rochelle CEDEX, F-17000, France
(E-mail: brieuc.riou@u-bordeaux.fr)

² EPOC, UMR 5805-CNRS, Université de Bordeaux, Pessac CEDEX, F-33615, France

³ School of Biological, Earth and Environment Sciences, University of New South Wales, Sydney 2052, Australia

Associate Editor – Pedro Costa

Submitted: 1st June 2018

Accepted with minor revisions: 3rd October 2018

Accepted: 22nd October 2018

Published online: 5th June 2019

4.1 Abstract

Extensive bathymetric and two-dimensional seismic surveys have been carried out and cores collected in Pago Pago Bay (Tutuila, American Samoa) in order to describe and gain a better understanding of the sediment fill of the bay, which was affected by the 2009 South Pacific Tsunami. Eight sedimentary units were identified over the volcanic bedrock. The basal transgressive unit displays retrograding onlaps towards the shore, whereas the overlying seven aggradational layers alternate between four draping units and three pinching out seaward units. ‘Core to seismic’ correlation reveals that draping units are composed of homogeneous silts, while pinching out units are dominated by very coarse coral fragments showing fresh cuts, mixed with *Halimeda* plates. The basal unit is attributed to transgressive sedimentation in response to flooding of the bay after the last glacial maximum, followed by the upper aggradational units corresponding to highstand sedimentation. The changeovers in these upper units indicate an alternation between low-energy silt units and high-energy coral debris units interpreted as tsunami-induced deposits. The ^{14}C dating reveals that high-energy sedimentation units can last up to approximately 2 000 years while low-energy sedimentation units can last up to approximately 1 000 years. This alternation, deposited during the last highstand, may be explained by cycles of tectonic activity and quiescence of the Tonga Trench subduction, which is the main source of tsunamigenic earthquakes impacting the Samoan archipelago. In the uppermost silt unit, only the geochemical signature of the terrestrial input of the 2009 SPT backwash deposits was detected between 7 cm and 9 cm depth. Hence, Pago Pago Bay offers a unique sediment record of Holocene bay-fill under the impact of past tsunamis intermittently during the last 7 000 years.

Keywords: Core to seismic correlation, Holocene, sediment bay-fill, shallow marine tsunami deposits, tectonic activity cycles, tsunami.

4.2 Summary

4.2.1 Objectives

One of the main issues for sedimentologists studying tsunami deposits onshore and offshore is their preservation. Indeed, if major tsunamis around the world occur every couple of years, only very little sedimentary evidence remains in most cases after a few centuries, decades or even years in some environments. Then, it seems crucial to target study zones with a high preservation potential. Until recently, a large majority of studies on tsunami deposits have focused only on onshore deposits, which are easier to study and can be observed shortly after their deposition. However, onshore deposits are frequently reworked following sub-aerial erosion and human activities, resulting in a poor preservation potential. We assume that, if the sedimentary basin is well chosen, shallow marine deposits may offer a higher preservation potential. Shallow marine environments are a preferential area of deposition of sediment following backwash of a tsunami. Eroded material is washed back and shed to sea by strong outflow currents, dragging all sorts of material into the shoreface and upper offshore. In order for these tsunami backwash records to be preserved, they need to be kept away from reworking factors. In such setting, the dominant erosion agents are wave induced currents and other currents. Then, deep and sheltered bays with weak tidal currents, which are protected from storm waves and where the sediment is deposited below the wave base depth, seem to be ideal for tsunami backwash deposits preservation.

Pago Pago Bay (Tutuila, American Samoa), is a highly sheltered bay with a depth exceeding 30 m up to only a few hundred meters from the extremity of the bay. It's atypical morphology, long and narrow with a 90° angle, attenuates wave trains with short wavelength such as storm waves but, in contrast, amplifies wave trains with long wavelength such as tsunami waves. It was struck heavily by the 2009 SPT, with waves reaching a maximum height of 7 m. During the last 100 years, it was reportedly hit by more than 100 tsunamis, three of them reaching a maximum wave height of at least 4 m. The aim of this study is to understand the geologic and sedimentary history of Pago Pago Bay, which is here studied for the first time, in order to shed into the light the influence of tsunamis on the sedimentation within a sheltered shallow marine environment.

4.2.2 Material and methods

This study focuses on the Pago Pago Bay sediment-fill. It is supported by extensive bathymetric and two-dimensional seismic surveys, along with 16 cores collected between 27 and 55 m depth with two different corers. From each coring site was retrieved two cores: a short interface core measuring up to 20 to 60 cm and sampling the superficial soft sediment, and a longer Kullenberg core measuring 150 to 250 cm for a deeper sampling. The study is based on seafloor geomorphology and subsurface analysis of the bay-fill correlated with sedimentologic analysis of cores. Seismic profiles were first investigated for identification of sedimentary units and boundaries. Then, cores were examined and correlated with seismic interpretations in order to determine the sediment nature and characteristics of the units. Finally, sediment sampled from all cores was dated using both radiocarbon and ^{210}Pb method in order to build an age versus depth model, providing age ranges for the different sedimentary units.

4.2.3 Main results

Based on the seismic subsurface analysis, eight sedimentary units are identified and named U1 to U8 from top to bottom. Basal unit U1, which displays landward-oriented down laps on the eroded volcanic basement, is interpreted as a transgressive unit emplaced during the last sea-level rise between 12 000 and 7 000 years ago. Units U2, U4, U6 and U8 deposited on top of unit U1 display sub-horizontal and sub-parallel reflectors. They are interstratified with three units U3, U5 and U7. These units have an erosive base, pinch out seaward and display chaotic internal reflectors. Past the pinching-out of these three units, units U2, U4, U6 and U8 merge as one massive unit with no identifiable major erosional surface. Units U2 to U8 are interpreted as highstand aggradational units emplaced during the last 7 000 years.

Sedimentological analysis of cores revealed the presence of three sediment facies. The first facies (facies A) is composed of homogeneous silt and is interpreted to be a low-energy background sedimentation facies and is correlated to units U2, U4, U6 and U8. The second facies (facies B) is composed of coarse coral fragments (5 to 10 cm) with sharp edges in a silty matrix. The third facies (facies C) is composed of a mix of coarse coral fragments with sharp edges and *Halimeda* plates in a silty matrix. These two facies are interpreted to be high-energy event deposits and are correlated to unit U7 for facies B and unit U5 for facies C. Based on similar seismic characteristics, unit U3 is believed to be composed of either facies B or C.

Radiocarbon ages obtained for coral fragments sampled in units U5 and U7 revealed the age ranges for these units. For unit U7, the top is dated around 85 BP and the base around 2470 BP. For unit U5, only the top was reached in the cores and was dated at around 3380 BP, with dates of 4150 BP and 6215 BP further down the unit.

4.2.4 Main conclusions

The stratigraphic sequence of the Pago Pago bay-fill consists of a basal transgressive unit emplaced on top of the eroded volcanic basement during the last sea-level rise, dated from 12 000 to 7 000 years ago, followed by an aggradational group emplaced during the last 7 000 years. This upper aggradational group displays an alternation between low-energy phases, dated to last around 1 000 years, interrupted by three high-energy phases dated to last around 2 000 years. Based on the characteristics of the coral fragments, the depth of occurrence and the hydrodynamic setting of the bay, these high-energy intervals are most likely to have been emplaced by major tsunami backwash. The thickness of the high-energy units comes from the vertical stacking of successive tsunami deposits during approximately 2 000 years.

Two hypotheses are proposed to explain the alternation between the low-energy units and the high-energy units during the last 7 000 years. The first hypothesis suggests a cyclic disappearance of all corals in the bay available to be broken and transported by tsunami waves, probably induced by regional paleoclimate change inducing strong sea-temperature or precipitation variations. However, regional precipitation and sea-temperature variation curves do not show significant changes during the last 7 000 years that could explain the death of all corals in Pago Pago Bay, even if a local effect cannot be ruled out. The second hypothesis suggests an alternation between periods with frequent tsunami occurrence and periods with little to no major tsunamis. This alternation could be linked to tectonic cycles of the Tonga Trench, which is responsible for the two biggest tsunamis recorded during the last century in Tutuila, with phases during which the subduction is dormant and phases during which it is active. Such tectonic cycles have already been pointed out using tsunami recurrence before, but never for the Tonga Trench.

Finally, the uppermost unit U8 records the last 100 to 150 years. In this unit, no major sedimentological variations and coral debris are observed despite the occurrence of at least 3 major tsunamis, including the 2009 SPT. This is interpreted to be the result of the death and disappearance of most corals in Pago Pago Bay induced by the strong anthropization of the bay

4. The sediment-fill of Pago Pago Bay (Tutuila Island, American Samoa)

during the last century. Further work using finer analytical methods is necessary in order to identify and describe the deposits emplaced by the backwash of the 2009 SPT.

4.3 Introduction

On 29th September 2009, the Samoan Islands, including Tutuila Island (American Samoa), were struck by the 2009 South Pacific Tsunami (SPT). This tsunami was triggered by an earthquake doublet of magnitude 8.0 and 8.1, near the northern end of the Tonga Trench (about 180 km south-west of Tutuila; Figures 4.1.A and 4.1.B), where the Pacific plate is subducting under the Australian plate (Beavan *et al.*, 2010; Lay *et al.*, 2010; Goff & Dominey-Howes, 2011; Okal *et al.*, 2011). The tsunami reached the Samoan Islands 15 to 20 min after the earthquake, causing 183 deaths in Samoa (34 of them in American Samoa) and much infrastructure damage (Dominey-Howes & Thaman, 2009; NGDC, 2018). Between three and five waves were recorded on the Pago Pago Bay tide gauge (NOAA Service National Weather), with a maximum wave height of 8 m on the northern coast of Tutuila Island (Poloa Bay and Fagasa Bay) and a maximum run-up height of 20 m in Poloa Bay (Dominey-Howes & Thaman, 2009; Jaffe *et al.*, 2010; Fritz *et al.*, 2011).

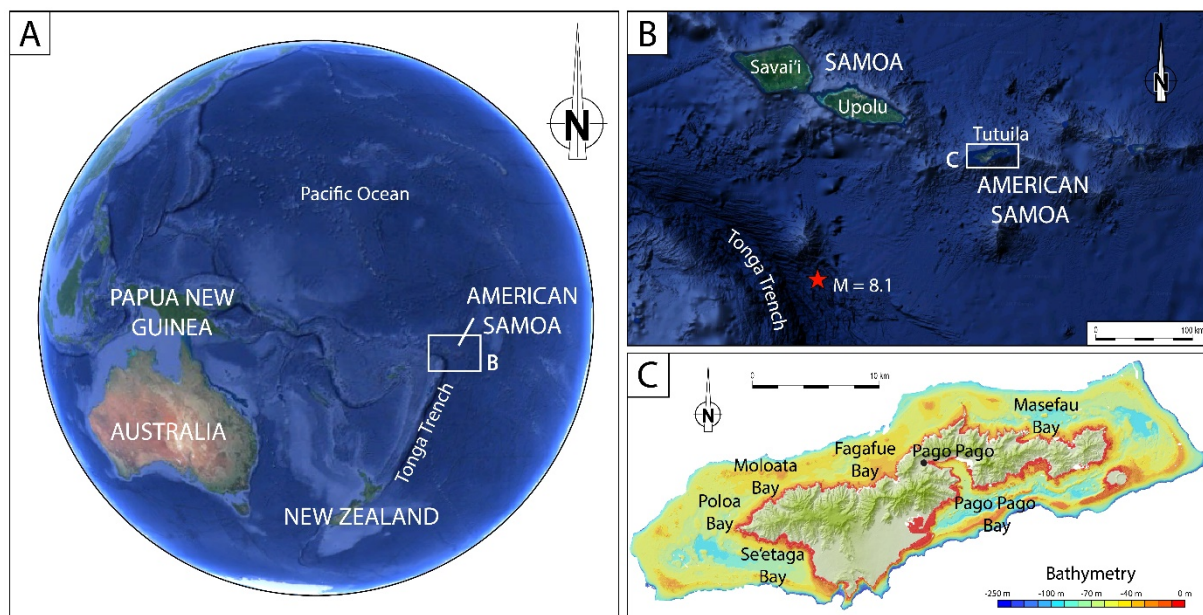


Figure 4.1: A. Location of American Samoa in the Pacific Ocean (modified from Google Earth), B. Location of the earthquake epicenter marked by a red star with its magnitude (modified from Google Earth), C. Map of Tutuila with bathymetric data (modified from NOAA).

Studying tsunami deposits, like those left behind by the 2009 SPT, is crucial to understanding the impact of such devastating events, including coastal erosion, sediment movement and water flows (Jaffe & Gelfenbaum, 2002; Jaffe & Gelfenbaum, 2007). Knowledge gained from the study of recent deposits can also be used to identify older events in the geological record, thereby helping to reconstruct the paleotsunami record over long periods of time (Pinagina

& Bourgeois, 2001; Monecke *et al.*, 2008; Ishimura & Miyauchi, 2015; Rubin *et al.*, 2017). Such information could help understand the morphological evolution of studied areas and future risk assessment (Atwater, 1987; Jaffe & Gelfenbaum, 2002; Nanayama *et al.*, 2003; Williams *et al.*, 2011). While several studies focused on inland tsunami deposits on Tutuila Island (Dominey-Howes & Thaman, 2009; Jaffe *et al.*, 2010; Apotsos *et al.*, 2011; Fritz *et al.*, 2011), none investigated shallow marine backwash deposits. In fact, few studies have been carried out on such shallow marine tsunami backwash deposits, with only a handful showing interest in recent earthquake-generated tsunamis (Abrantes *et al.*, 2008; Donato *et al.*, 2009; Sugawara *et al.*, 2009; Smedile *et al.*, 2011, 2012; Sakuna *et al.*, 2012). If well-preserved, such deposits can provide additional information. Indeed, the shallow marine environment near the shore is not subject to subaerial erosion and might preserve both uprush and backwash tsunami deposits (Dawson & Stewart, 2007; Nanayama, 2008). For this purpose, deep and sheltered bays with very low hydrodynamic settings could represent ideal study zones (Weiss & Bahlburg, 2006), because they have the potential to preserve both recent tsunami deposits and paleotsunami archives. Through the last decade, shallow marine tsunami and paleotsunami backwash deposits have been studied in such sheltered bays, but are still under-represented in the literature (Van Den Bergh *et al.*, 2003; Fujiwara & Kamataki, 2007; Sugawara *et al.*, 2009; Smedile *et al.*, 2011, 2012).

American Samoa is an ideal location for tsunami studies. Although the written historical record is not long, the tide gauge in Pago Pago Bay, Tutuila (Figure 4.1), has recorded numerous tsunami events since the beginning of the 20th Century, with an average frequency of five years (Pararas-Carayannis & Dong, 1980; Williams *et al.*, 2011). Among these, three destructive tsunamis have been recorded; the 2009 SPT, the 1960 Great Chilean Earthquake Tsunami and the 1917 event in similar conditions to the 2009 SPT (Pararas-Carayannis & Dong, 1980; Okal *et al.*, 2011). The recurrence of these events in Tutuila makes Pago Pago Bay a critical study area in reconstructing an archive of paleotsunamis that impacted the island in the past. Moreover, Pago Pago Bay is a very deep and sheltered bay, with a high preservation potential of sediment record. So far, no study has focused on the geological history of Pago Pago Bay and there is no information in the literature about the sediment architecture of the bay.

The aim of this study is to show for the first time the internal architecture and sediment-fill of Pago Pago Bay. This work is based mainly on seismic and core data, combined with radiocarbon dating to understand the geological history of Pago Pago Bay. The global objective of this work is to set the geological context in order to evaluate the potential for sediment preservation

and tsunami sediment record. This preliminary work is a prerequisite for further detailed investigations of the 2009 tsunami and of the paleotsunami record in this part of the Pacific Ocean.

4.4 Study area and setting

The Samoan archipelago is a 500 km long volcanic trail, associated with a hotspot, in the south-west Pacific Ocean (Figure 4.1.A). It is composed of three main islands. The two westernmost islands, Savai'i and Upolu, are part of Samoa, while Tutuila is part of American Samoa (Figures 4.1.A and 4.1.B). The oldest island, Savai'i, is at the western end of the trail and is 5 Ma (Koppers *et al.*, 2008). This age is consistent with a Pacific plate motion of 7.1 cm.yr^{-1} towards the west in the last million years. The islands are younger and smaller eastward, and underwater volcanic seamounts are found near the present location of the hotspot. Tutuila island's shield-building volcanism started at 1.5 Ma, with Pago being the most active volcano of the five (McDougall, 1985, 2010), which formed most of the central and eastern part of the island. Savai'i, Upolu and Tutuila also show a post-erosional recent volcanic shield that is $<0.4 \text{ Ma}$. This recent volcanism is related to a fracture of the Pacific plate, which is due to the bending induced by the nearby subduction of the Pacific plate under the Australian plate near the Tonga Trench (Koppers *et al.*, 2008).

Several consequences of the volcanic origin of Tutuila can be observed. First, the coastline is deeply indented by many bays all around the island, with Pago Pago Bay being the widest and deepest (Figure 4.1.C). These bays usually end in an amphitheater head due to the erosion of calderas following post-volcanic subsidence (McDougall, 1985), and thus are delimited by steep slopes. Second is the presence of dense tropical vegetation combined with steep slopes. Thus, the 60 000 inhabitants live concentrated along the shorelines, enhancing risk in case of tsunamis (Gelfenbaum *et al.*, 2011).

Pago Pago Bay is a long and narrow bay cutting through the southern coastline of Tutuila, with a catchment area of ca 10 km^2 (Figure 4.1.C). Given its origin, the morphology of the bay is very peculiar. It is composed of two segments separated by a right-angled corner. The outer segment is perpendicular to the coastline and is 3 km long, while the head of the bay, which extends westward after the corner, is 2 km long. This inner part of the bay is completely sheltered and is home to Pago Pago Harbor. This morphology, coupled with the presence of a wide fringing reef at the mouth of the bay, makes the harbor an area completely protected from all ocean waves,

4. The sediment-fill of Pago Pago Bay (Tutuila Island, American Samoa)

except for tsunami waves. This criterion is a very important one since it could lead to an ideal preservation of sediment records and particularly tsunami deposits. The depth of the bay ranges from around 60 m at the mouth to around 10 m at the head, with a gentle 1% slope. Most of the bay stands below wind wave base.

The bottom of the bay is mostly composed of silty to clayey material. Many waste products can be found on the bottom, such as car parts or steel/zinc house parts, attesting to recent damage around the harbor (Figure 4.2.A; NOAA, 2018). At the head of Pago Pago Bay, freshwater input combined with high turbidity inhibit coral growth, while in the open segment of the bay, fringing reefs are found on both sides (Mayor, 1920; Cornish & DiDonato, 2004). These reefs are dominated by massive foliaceous coral colonies, such as *Acropora* (Figure 4.2.B), *Diploastrea*, *Merulina*, *Lobophyllia*, *Porites* and *Fungia* species (Green *et al.*, 2002). The calcifying algae *Halimeda* can also be found attached to the reef and on sandy beds.

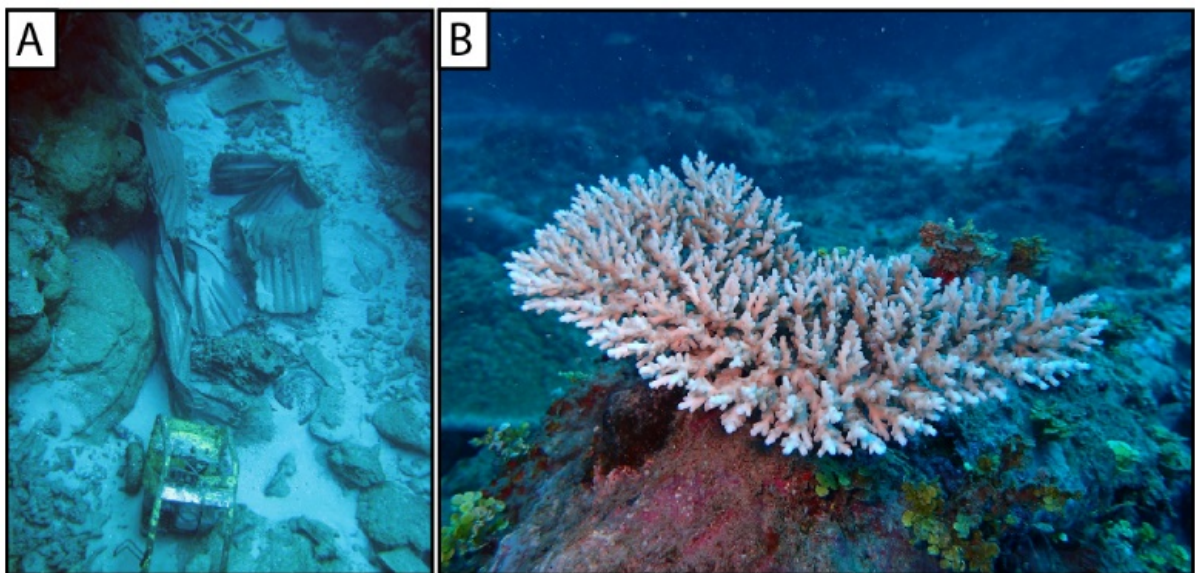


Figure 4.2: **A.** Photo of the bottom of Pago Pago Bay in the inner part of the bay with a ladder, zinc house roof parts and other waste material (photo from NOAA), **B.** Photo of *Acropora* coral found on the fringing reef of Pago Pago bay (photo by Stéphane Bujan).

Because of its location in the middle of the Pacific Ocean, the Samoan archipelago, including Tutuila, is often impacted by tsunamis originating from all around the Pacific. Unfortunately, due to a lack of written language in the Samoan culture, no data or archives are available prior to the beginning of the 19th Century. The first record of a tsunami in Tutuila dates back to 7th November, 1837 (Hitchcock, 1911; Pararas-Carayannis & Dong, 1980), but until the beginning of the 20th Century only visual observations were archived. The Pago Pago Harbor tide

gauge was set in 1948, allowing for the collection of high frequency and confident data. During the last century, more than 50 minor tsunamis have been recorded in Pago Pago Bay (Pararas-Carayannis & Dong, 1980). However, three of these stand out in terms of power and destructive potential. The earliest and most destructive tsunami prior to the 2009 SPT was the 1917 tsunami which was generated by a magnitude 8.3 earthquake in the outer border of the northern end of the Tonga Trench, about 200 km off the coast of Tutuila. The first wave was recorded at around 3 m high and demolished many houses and two churches. No human casualties were registered. The second was the 1960 Great Chilean earthquake-associated tsunami. Waves in the head of the bay reached a maximum wave height of 5 m, but caused minor damage to several houses and there were no casualties (Pararas-Carayannis & Dong, 1980). Finally, the most destructive tsunami ever recorded in Tutuila was the 2009 SPT. Studies have shown that during that event, waves were amplified in the bay due to its long and narrow morphology (Fritz *et al.*, 2011). Indeed, waves measuring around 1 m at the mouth of Pago Pago Bay reached a maximum wave height of 7 m at the head of the bay. The inundation caused considerable damage in the harbour, extending as far as 500 m inland, and reached a maximum run-up of 8 m, causing 34 casualties around the island.

4.5 Material and methods

4.5.1 Dataset

The dataset on which this work is based includes a bathymetric survey, an extensive 2D seismic survey and 16 cores (Figure 4.3). All data were collected in Pago Pago Bay during the oceanographic campaign SAMOA-SPT from 27th August to 10th September 2015 aboard the *R/V Alis*.

4.5.1.1 Bathymetry

An EM1002 multibeam sounder (Kongsberg Maritime, Kongsberg, Norway) was used for bathymetry acquisition. Its 95 kHz frequency allowed for a depth range extending from 5 to 1 000 m, which makes it a good choice for coastal studies such as in Pago Pago Bay. Daily Sippican probe shots were made prior to the acquisition in order to calibrate the depth versus velocity model in the water column. The raw data was then processed using the CARAİBES (CARTography Adapted to Imagery and BathymEtry of Sonars and multibeam echosounders) software developed by

4. The sediment-fill of Pago Pago Bay (Tutuila Island, American Samoa)

IFREMER. The first processing consisted of tide correction, before bias due to celerity variations in the water column, induced by salinity variations, was eliminated. The bathymetry was then exported as a digital elevation model (DEM) with a 2 m resolution elementary grid for Pago Pago Bay (Figure 4.3).

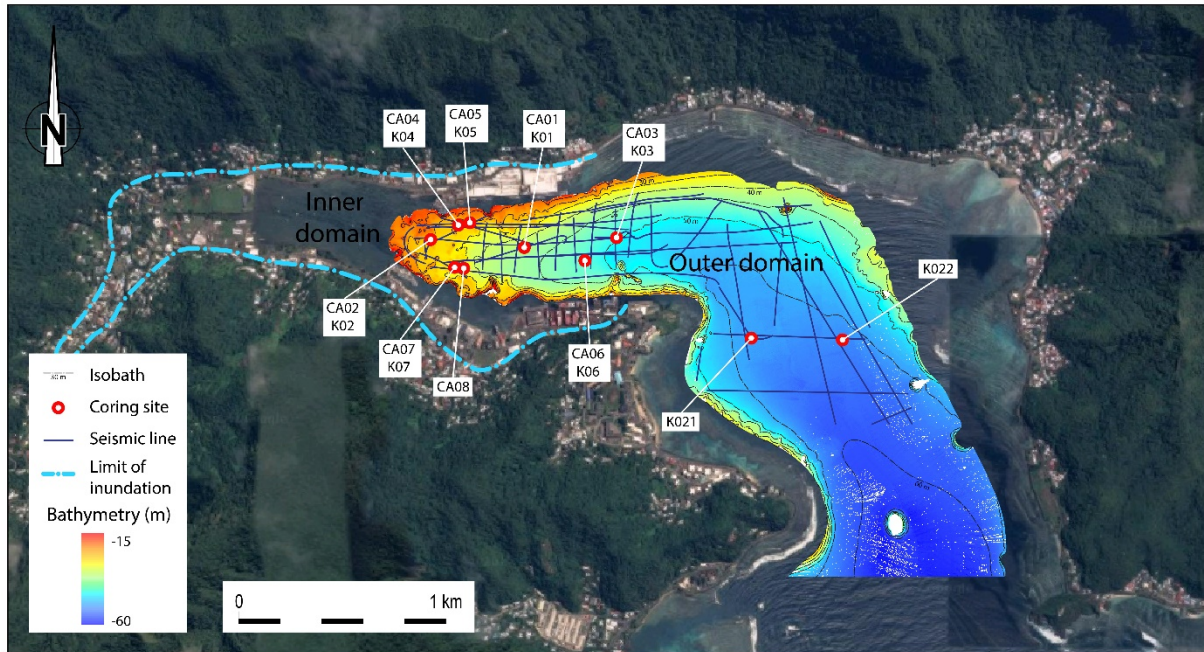


Figure 4.3: Map of Pago Pago Bay with 2 m high resolution processed bathymetric data acquired during campaign (5 m isobaths), 10 coring sites (8 interface cores and 9 Kullenberg cores), 38 HR seismic profiles and inundation limit of 2009 SPT; the two morphologic domains observed on seafloor are shown limited by the 40 m isobath.

4.5.1.2 Seismic

A Seistec-IKB boomer (IKB Technologies Limited, Dartmouth, NS, Canada) was used for the seismic acquisition (Mosher & Simpkin, 1999) (Figure 4.3). Its bandwidth ranged from 1 to 10 kHz, which gave a very high resolution (around 25 cm of vertical resolution), allowing accurate correlations with core results (Billeaud *et al.*, 2005; Chaumillon *et al.*, 2008; Allard *et al.*, 2010), with a penetration of about 20 to 100 m depending on the nature of the sediment (Simpkin & Davis, 1993). The raw profiles were processed using DELPH seismic acquisition software (iXBlue). A frequency filter was applied between 900 Hz and 10 500 Hz, combined with a linear AGC (Amplitude Gain Control) for a 15 ms window and stacking of three adjacent traces.

4.5.1.3 Cores

Two types of coring systems were used during the campaign. Among the 16 cores, nine were collected with a Kullenberg coring device, while seven were collected with an interface coring device (Figure 4.3). The Kullenberg coring system uses a piston to dig into the sediment, and therefore can penetrate deeper (Kullenberg, 1947). During this campaign, the Kullenberg piston core lengths varied between 150 and 250 cm. However, this system often leads to superficial soft sediment being flushed away when the device falls on the sea bottom. Therefore, interface cores were collected using a custom-made gravity box corer without piston (1 m long, 10 x 10 cm square section), similar in smaller dimensions to the CASQ corer (CALypso SQUARE box corer). This coring device allows sampling of the superficial soft sediment without disturbance. However, the maximum penetration with this device is only between 30 and 60 cm.

4.5.2 Analytical methods

4.5.2.1 ^{14}C dating

A total of 19 samples were collected for ^{14}C dating throughout five cores. Dating was undertaken at the Laboratoire de Mesure du Carbone 14 (LMC 14) in Paris (France) using the Artemis Accelerator Mass Spectrometry facility (AMS) (Beta Analytics, 2012; Miami, FL, USA). Samples were mostly coral fragments, although a few samples of *Halimeda* plates or gastropods were also used. The raw dates gathered were given in age BP (Before Present). Meanwhile, as measures were made on marine species, these BP ages were calibrated to take into account the reservoir age, which reflects the mixing of surface waters in equilibrium with the atmospheric ^{14}C content and older deep ocean waters upwelling in some parts of the world (Stuiver *et al.*, 1986). For this work, the CALIB 7.1 software (Stuiver *et al.*, 1986; <http://calib.org/>) was used, with the integrated Marine13 calibration curve (Reimer *et al.*, 2013) with a global correction of 400 years (more or less) depending on the age. A local component ΔR reflecting the local variations of ocean water mixing is added to his correction, with two different ΔR used depending on the age of the samples. For samples younger than 2500 BP, a ΔR of 20 ± 20 years (Petchey *et al.*, 2008) was used based on the CALIB software Marine Reservoir Correction Database (Stuiver *et al.*, 1986; <http://calib.org/marine/>). For older samples a ΔR of -101 ± 72 years was used (Clark *et al.*, 2016). The calibrated ages obtained are expressed in cal yr BP. For all ^{14}C ages given in this study, the error is given as the 68.3% confidence interval (1 sigma).

4.5.2.2 ^{210}Pb dating

The ^{210}Pb activities (half-life of 22.3 years) were used to indirectly date the silty material, following a procedure similar to that of (Nitttrouer *et al.*, 1979). Samples were spiked with a known activity of ^{209}Po , and were digested in concentrated HNO_3 and 6 N HCl acid: ^{210}Po , the granddaughter of ^{210}Pb , and ^{209}Po was then plated onto silver planchets and α -counted. Since secular equilibrium was not reached, the ^{226}Ra -supported activity was determined from samples collected in one of the cores using c-counting. The mean calculated ^{226}Ra -supported activity of 0.84 dpm.g^{-1} was then subtracted from the total activity for each measured core, leaving only the excess activity. An average accumulation rate was then calculated for each core based on the excess activity profile, so that the age of analyzed intervals could be estimated from the depth.

4.6 Bay infilling

4.6.1 Sea-floor geomorphology

Sea-floor bathymetry can provide key information that is useful in the analysis of subsurface data. When looking at the bathymetric survey of Pago Pago Bay obtained during the campaign, two main geomorphological domains stand out. The extension of these domains can be related to depth, with the limit separating the two domains corresponding to a 5 m high ‘step’ with a relatively steep slope, around 10 to 15°, located at the 40 m isobath (Figure 4.3).

The first domain, called the outer domain, extends in the outer part of the bay, in areas deeper than 40 m. Thus, it covers most of Pago Pago Bay, from the mouth of the bay up to about 1 km from its landward end. This domain is characterized by a very flat sea floor with an absence of any geomorphological features. The slope is very steady, around 0.5°. The second domain, called the inner domain, extends into the inner part of the bay and is confined in depths shallower than 40 m. Thus, it has a limited extent, and is mostly present in the last kilometer before the landward end of the bay. Unlike the outer domain, geomorphological features including mounds and troughs cover this domain. These mounds are a few meters high (<5 m), by a few tens of meters wide (<50 m) and are round-shaped. This specific geomorphology leads to the occurrence of relatively well-connected mini-basins in the troughs in between the mounds.

4.6.2 Subsurface seismic analysis

4.6.2.1 Characteristics of bounding surfaces

On the seismic profiles, eight main reflectors can be identified (Figures 4.4 and 4.5). They correspond to a variation of acoustic impedance, indicative of a contrast in either lithology or grain size, but are not all associated with an unconformity. These main reflectors, or bounding surfaces, are characterized by high to moderate amplitude reflectors, with globally good continuity but locally low continuity. They separate highly contrasted seismic units, alternating high and low reflectivity, and are distinguished based on seismic and geometric characteristics. These reflectors are described below from bottom to top.

A major regional erosional unconformity EU0 is found throughout the bay. It corresponds to a very strong amplitude, low frequency and good continuity reflector displaying a highly irregular morphology. This reflector separates two main seismic units: an underlying sub-transparent acoustic basement, imputed to the eroded volcanic basement SU0, and an overlying unit showing alternations of poorly and well reflective sub-units interpreted as the sedimentary bay-fill.

A major bounding surface S1 can be traced over a few kilometers at the scale of the bay and is identified as a downlap surface. It corresponds to a medium to strong amplitude, low frequency, partially continuous and sub-horizontal reflector. Six upper bounding surfaces are not associated with unconformities identifiable from reflector geometry (i.e. toplap, downlap, onlap and erosional truncation); they show limited lateral extension (<2 km). From base to top: (i) S2 corresponds to a high amplitude, medium frequency and sub-horizontal reflector, highly continuous in the outer domain of the bay but discontinuous in the inner domain; (ii) S3 corresponds to a high amplitude, medium frequency, discontinuous reflector; (iii) S4 corresponds to a high amplitude, medium frequency and sub-horizontal reflector, continuous in the outer domain but discontinuous in the inner domain; (iv) S5 corresponds to a high amplitude, medium frequency and sub-horizontal reflector, continuous in the outer domain but discontinuous in the inner domain; (v) S6 corresponds to a medium amplitude, medium frequency, discontinuous and subhorizontal reflector; and (vi) S7 corresponds to a medium amplitude, medium frequency, discontinuous and sub-horizontal reflector. Three of these bounding surfaces (S3 in the inner and outer domain, S5 in the inner domain and S7 in the inner domain) are characterized by a morphology displaying ridges and troughs.

4. The sediment-fill of Pago Pago Bay (Tutuila Island, American Samoa)

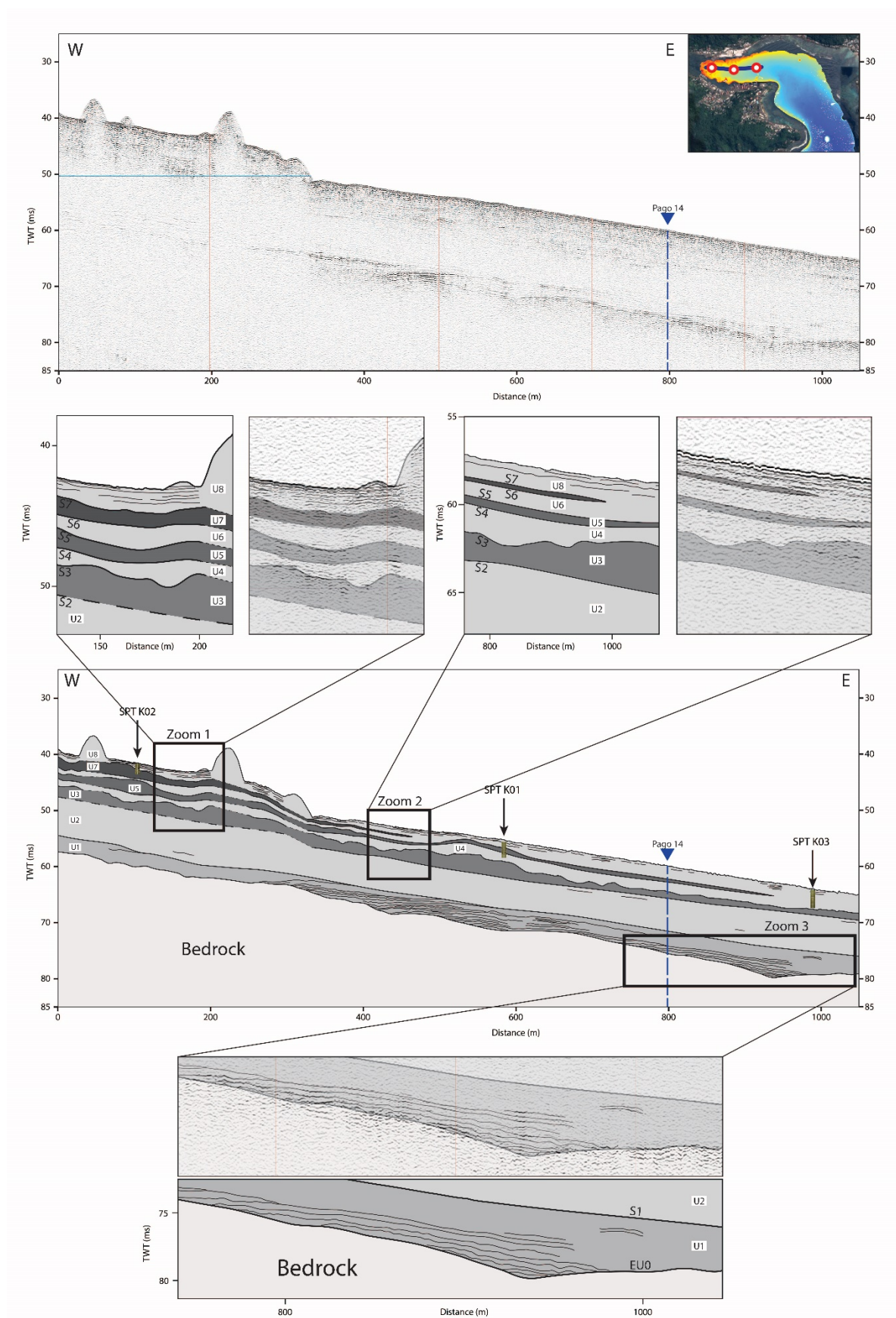


Figure 4.4: W-E raw (top) and interpreted (bottom) seismic profile Pago-21 with 3 zooms showing raw vs interpreted data in key areas to understand interpretation method; cores SPT K01, K02 and K03 were added after depth-to-time conversion.

4. The sediment-fill of Pago Pago Bay (Tutuila Island, American Samoa)

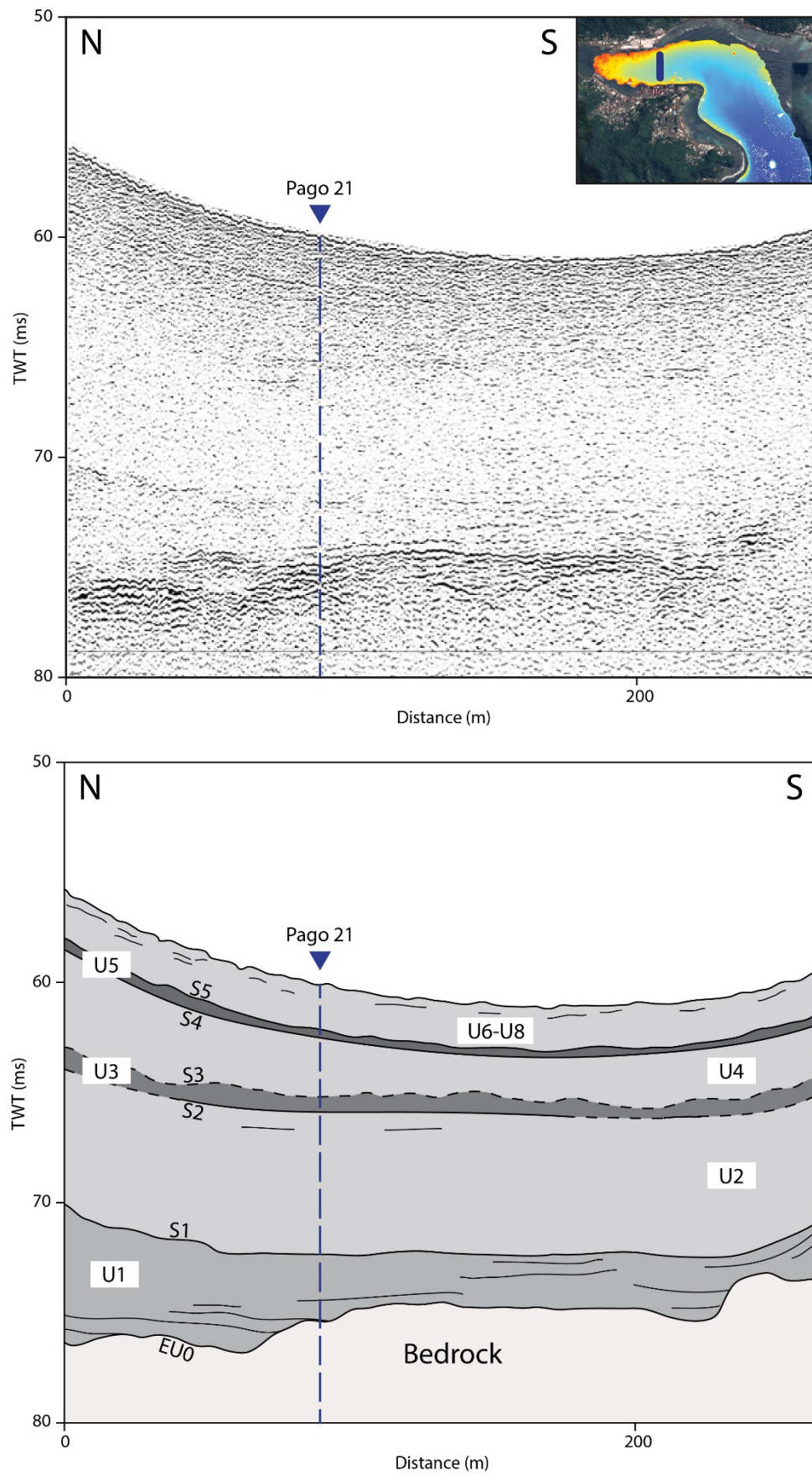


Figure 4.5: N-S raw (top) and interpreted (bottom) seismic profile Pago-14.

4.6.2.2 Characteristics of seismic units

From these eight bounding surfaces, eight seismic units are defined above the acoustic basement (SU0). These units are named U1 to U8 from base to top (Figures 4.4 and 4.5) and summarized in Table 4.1. Altogether, they represent a total estimated thickness of approximately 12 m of sediment.

The basal unit U1 is a gently seaward dipping sheet drape with constant thickness. This highly reflective unit displays high amplitude, low frequency, sub-horizontal and sub-parallel continuous reflectors. The landward termination of these reflectors is onlapping over the bedrock. Locally, internal unconformities are observed with some reflectors downlapping seaward on underlying reflectors. Unit U2 is a gently seaward dipping sheet drape with constant thickness. This poorly reflective unit displays a few medium-to-low amplitude, medium-to-low frequency, discontinuous, sub-horizontal and sub-parallel reflectors. Units U3, U5 and U7 are seaward pinching out wedges. The lower bounding surfaces of these units are sub-horizontal (S2, S4 and S6) while their upper bounding surfaces have a ridge and trough morphology (S3, S5 and S7). Internally, they display high-to-medium amplitude, medium frequency, chaotic and discontinuous reflectors. Within unit U7, several additional high amplitude, irregular and continuous reflectors are observed. The acoustic facies of units U3, U5 and U7 display variations from the inner to the outer domain of the bay, with a stronger reflectivity in the inner domain and a noisy and medium reflectivity in the outer domain. Units U4 and U6 are gently seaward dipping sheet drape units with relatively even thickness throughout the bay. These units are sub-transparent. The uppermost unit, U8, is a gently seaward dipping sheet drape unit with even thickness throughout the bay. This highly reflective unit displays high amplitude, medium frequency, sub-horizontal and sub-parallel continuous minor reflectors, notably near the top. This increase of the amplitude of the reflectors towards the top is probably due to the attenuation of the signal as it passed the first meter or so. In the troughs, between the mounds in the inner domain of the bay, some of these minor reflectors show onlapping terminations on the underlying unit. Seaward, past the pinch outs described for units U3, U5 and U7, units U2, U4, U6 and U8 merge as a unique sub-transparent, low reflectivity seismic unit without distinguishable reflectors.

4. The sediment-fill of Pago Pago Bay (Tutuila Island, American Samoa)

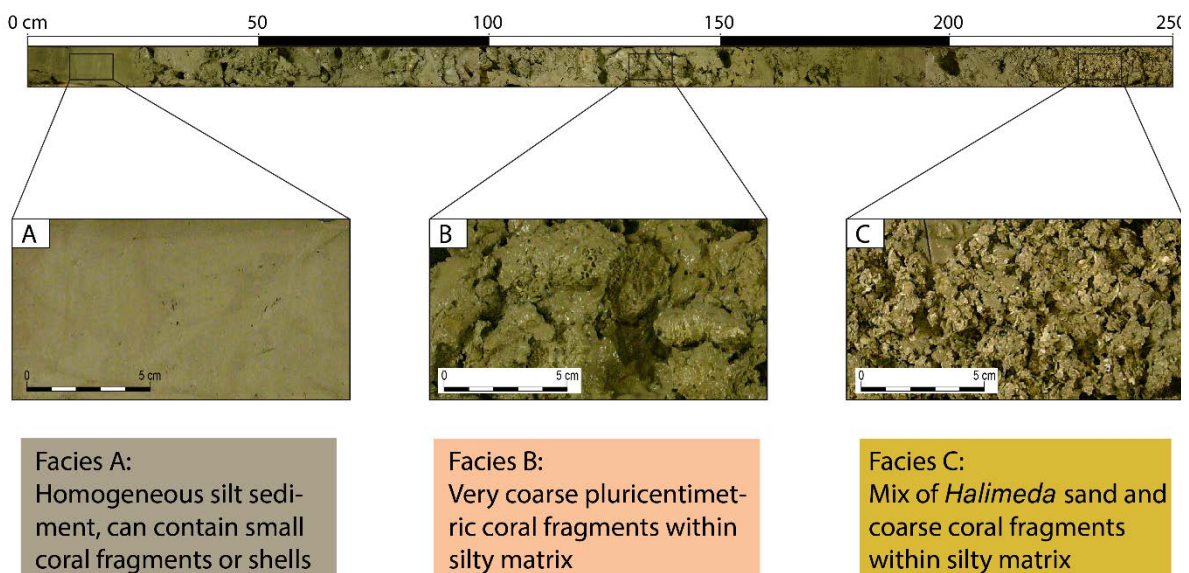
Seismic unit	Outer shape	Seismic facies characteristics	Internal architecture	Corresponding sediment facies	Estimated ages
U1	Sheet drape, constant thickness	High reflectivity, high amplitude, low frequency	Continuous sub-horizontal sub-parallel reflectors, landward onlaps on bedrock, locally seaward downlaps on underlying reflectors	Unknown	12,000 cal. BP to 7,000 cal. BP
U2	Sheet drape, constant thickness	Low reflectivity, medium to low amplitude, medium to low frequency	Discontinuous sub-horizontal sub-parallel reflectors	Most probably facies A	?
U3	Seaward pinching out wedges, ridge and trough upper limit	High reflectivity in inner domain, medium and noisy in outer domain, high to medium amplitude, medium frequency	Discontinuous chaotic reflectors	Most probably facies B or C	?
U4	Sheet drape, constant thickness	Sub-transparent	Sub-transparent	Facies A	?
U5	Seaward pinching out wedges, ridge and trough upper limit	High reflectivity in inner domain, medium and noisy in outer domain, high to medium amplitude, medium frequency	Discontinuous chaotic reflectors	Facies C	3,300 cal. BP to 6,600 cal. BP ?
U6	Sheet drape, constant thickness	Sub-transparent	Sub-transparent	Facies A	3,300 cal. BP to 2,300 cal. BP
U7	Seaward pinching out wedges, ridge and trough upper limit	High reflectivity in inner domain, medium and noisy in outer domain, high to medium amplitude, medium frequency	Discontinuous chaotic reflectors with a few high amplitude, irregular and chaotic reflectors	Facies B	2,300 cal. BP to 85 cal. BP
U8	Sheet drape, constant thickness	High reflectivity, high amplitude, medium frequency	Continuous sub-horizontal sub-parallel reflectors near top, onlaps on underlying reflectors in the troughs	Facies A	85 cal. BP

4. The sediment-fill of Pago Pago Bay (Tutuila Island, American Samoa)

4.6.3 Core description

4.6.3.1 Facies description and distribution

Based on macroscopic observations, grain size and shell content, three main sediment facies labelled A, B and C (Figure 4.6) were identified and indexed in Table 4.2. Facies A is composed of very homogeneous brown silt. No apparent layering can be recognized, but elongated darker patches are seen in some cores. Some rare small coral fragments or rhodophyte concretions along with small intact shells, mainly gastropods, are found scattered in the cores. Facies B is a non-consolidated bioclastic clast-supported breccia composed mainly of coarse coral fragments. These coral fragments are all roughly the same size, measuring from 5 to 10 cm, with very fresh cuts. The corals are mainly *Porites cylindrica*, *Fungia fungites*, *Mycedium elephantotus* and *Pocillopora damicornis* (Figure 4.7). Some *Halimeda* plates and broken gastropods can also be found mixed with the coral fragments, but in smaller amounts. The matrix is composed of brown silt, similar to that of facies A. Facies C is a bioclastic sand mainly composed of *Halimeda* plates, mixed with an important fraction of coarse coral debris, similar to those found in facies B, and measuring about 5 cm. A few broken gastropods also occur in this assemblage. This facies is fining-upward. The matrix around the *Halimeda* plates and coral fragments is composed of brown silt, similar to that of facies A.



4. The sediment-fill of Pago Pago Bay (Tutuila Island, American Samoa)

Table 4.2: Facies distribution with depth of occurrence in each core from proximal (top) to distal (bottom).

Core	Facies A	Facies B	Facies C
CA04	0 - 58 cm	-	-
K04	130 - 167 cm	0 - 130 cm	167 - 251 cm
CA05	0 - 48 cm	-	-
K05	0 - 25 cm	25 - 179 cm	203 - 253 cm
	179 - 203 cm		
CA02	0 - 28 cm	-	-
K02	0 - 90 cm	123 - 176 cm	90 - 123 cm
CA07	0 - 54 cm	-	-
K07	0 - 12 cm	12 - 178 cm	-
CA01	0 - 29 cm	-	-
K01	0 - 90 cm	-	90 - 175 cm
	175 - 234 cm		
CA03	0 - 49 cm	-	-
K03	0 - 262 cm	-	-
K06	0 - 260 cm	-	-
K21	0 - 157 cm	-	-
K22	0 - 170 cm	-	-

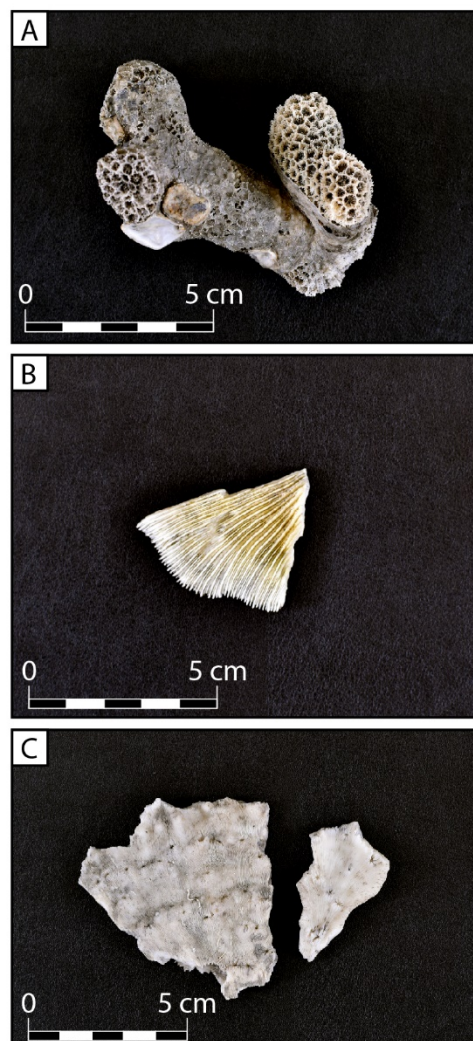


Figure 4.7: Photographs of samples of the main fragmented coral species found in the cores from facies B and C: **a.** *Porites cylindrica* (SPT-K05, 203 cm); **b.** *Fungia fungites* (SPT-K04, 67 cm); **c.** *Mycedium elephantotus* (SPT-K04, 30 cm).

4. The sediment-fill of Pago Pago Bay (Tutuila Island, American Samoa)

Different successions in the vertical distribution of these three facies are observed along a transect from the inner to the outer domain of the bay (Figure 4.8). These successions are described in the following from bottom to top. In the inner part of the bay, the sampled sedimentary succession consists of an interval of facies C at the base, followed by a thin interval of facies A, an interval of facies B and a final upper interval of facies A (Figure 4.8). The basal interval, which corresponds to the bioclastic sand of facies C, is found in the deepest cores near the edges of the bay (Figure 4.8; K04 and K05). The base of this interval was not reached, thus its approximate thickness, while being at least 80 cm, cannot be established from the core description. A thin layer of facies A, approximately 20 to 40 cm thick, is found on top of facies C. A second interval of debris, corresponding to facies B, is found on top of this interval of facies A, and is approximately 1.5 m thick. Finally, the uppermost unit corresponds to the homogeneous silty facies A, and is between a few tens of centimeters to just over 1 m thick. Unfortunately, due to a loss of the uppermost sediment record in the Kullenberg cores, the short core and long core sediment samples do not overlap. Thus it is very hard to accurately estimate the total thickness of this upper silt unit

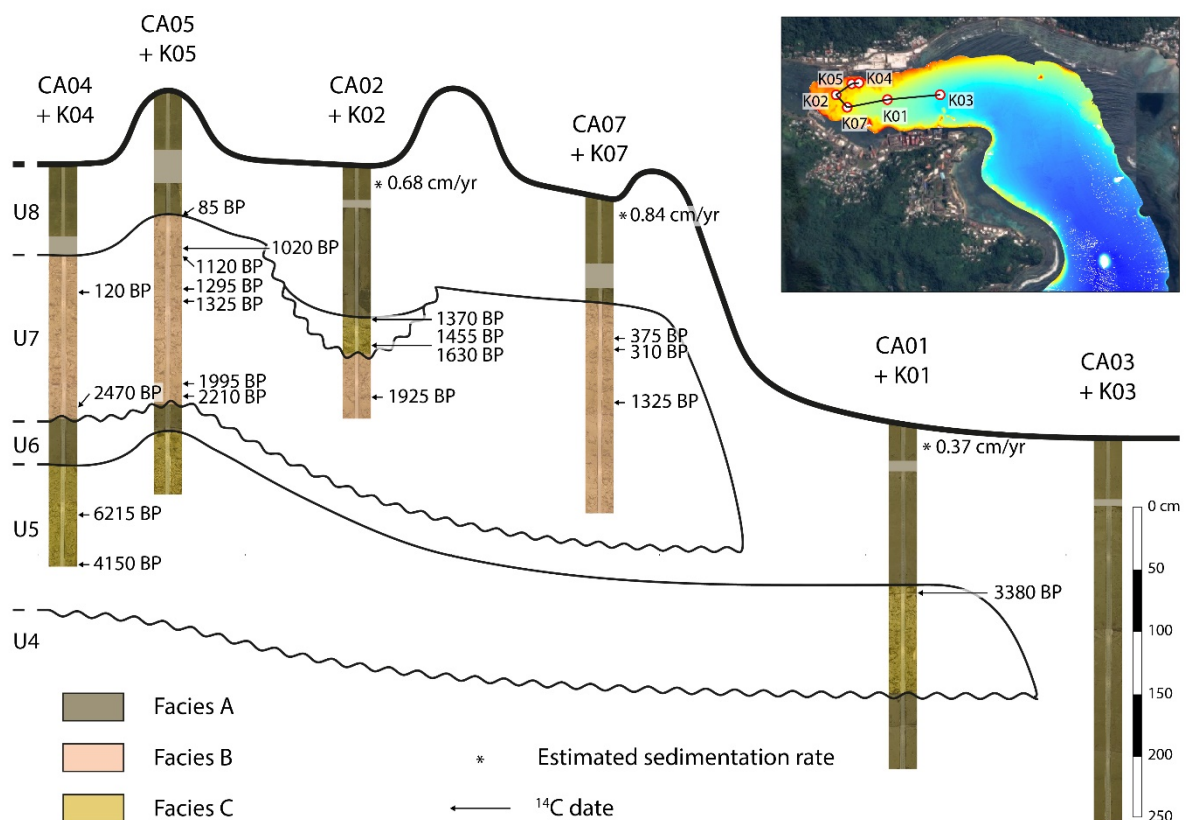


Figure 4.8: Interpretative core cross section (scale of seafloor not respected for optimal viewing) from proximal (left) to distal (right) with facies distribution (greyish brown for facies A, beige for facies B and yellow for facies C) and interpreted unit correlation based on core-to-seismic correlation; cal. BP dates obtained from radiocarbon dating are noted and pointed by arrows; accumulation rates estimated by ^{210}Pb dating are noted by an asterisk next to corresponding cores.

in the inner part of the bay. The exception to this sequence is the presence of a thin layer (approximately 30 cm thick) composed of bioclastic sand in core K02, corresponding to facies C just above the coral debris interval composed of facies B. In the shallowest part of the outer domain, the K01 core revealed three sedimentary units. A basal interval of facies A is found, followed by an interval of facies C and a final upper interval of facies A (Figure 4.8). The base of the lower silty facies A interval was not reached, thus its accurate thickness of at least 60 cm remains unknown. The bioclastic sand corresponding to facies C found on top of the facies A interval is about 90 cm thick. The thickness of the uppermost interval corresponding to the homogeneous silty facies A cannot be accurately estimated because of uppermost sediment loss during Kullenberg coring. However, its thickness is at least 1.2 m, which is thicker than the upper facies A interval in the cores from the inner domain (Figure 4.8; K04, K05, K02 and K07). It is important to emphasize that the facies B interval was found in the inner domain, but is not observed in K01 core nor more distal cores, where only facies A is found on top of facies C. Seaward, in the deeper part of the outer domain (Figure 4.3; K03, K21 and K22 cores), only facies A was retrieved in the cores (Table 4.2; Figure 4.8).

4.6.3.2 Chronology

The chronology was established using AMS ^{14}C dating of coral fragments and *Halimeda* plates sampled in most proximal cores except for K03 (Table 4.3; Figure 4.8) and ^{210}Pb activity on silty sediment from three short cores (CA02, CA07 and CA01; Figure 4.8). Samples were collected only in facies B and C for ^{14}C dating and only in facies A for ^{210}Pb dating. Results are listed from base to top (Table 4.3; Figure 4.8). Ages obtained close to the upper boundary of the lower facies C interval are: 6215 cal yr BP (K04; 40 cm from interval top); 4150 cal yr BP (K04; 80 cm from interval top) and 3380 cal yr BP (K01; 7 cm from interval top). The age inversion in core K04 is probably related to reworking of material and incorporation of old debris. The age of the basal lower facies C remains unknown, but it was deposited prior to 3380 cal yr BP. Ages obtained close to the lower boundary of the upper facies B interval are: 2470 cal yr BP (K04; 10 cm from interval base) and 2210 cal yr BP (K05; 7 cm from interval base). Ages obtained close to the upper boundary of the upper facies B interval are: 120 cal yr BP (K04; 30 cm from interval top); 85 cal yr BP (K05; at interval top); 375 cal yr BP (K07; 29 cm from interval top); 310 cal yr BP (K07; 38 cm from interval top) and 1925 cal yr BP (K02; 36 cm from interval top). Only one age inversion, close to the age uncertainty (± 30 years), is observed in core K07 (Table 4.3). Within core K02, facies B is overlain by bioclastic sand corresponding to facies C. Ages for the lower and upper boundaries of

4. The sediment-fill of Pago Pago Bay (Tutuila Island, American Samoa)

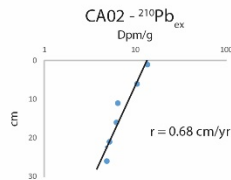
this lens are: 1630 cal yr BP (7 cm from lens base) and 1370 cal yr BP (2 cm from lens top), respectively. Accumulation rates obtained for the uppermost silt unit are (Table 4.4): 0.68 cm.yr⁻¹ (CA02); 0.84 cm.yr⁻¹ (CA07); 0.65 cm.yr⁻¹ (CA08) and 0.37 cm.yr⁻¹ (CA01).

Tableau 4.3: Radiocarbon dating data for each core from proximal (top) to distal (bottom); calibration was made using Calib 7.1 software (Stuiver *et al.*, 1986, <http://calib.org/>) with integrated Marine13 calibration curve; the 1 sigma interval corresponds to the 68.3 % confidence age interval (age uncertainty).

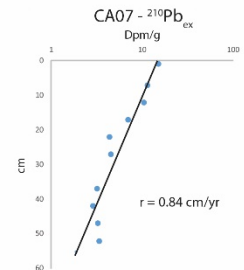
Core	Sample	Depth (cm)	Material	Conventional age (years BP)	Calibrated age (years cal. BP)	1 sigma interval (years BP)
K04	SPT1	30	Coral fragment	520 ± 31	120	55 - 149
K04	SPT2	120	Coral fragment	2635 ± 32	2470	2338 - 2571
K04	SPT3	210	Coral fragment	5700 ± 33	6215	6126 - 6299
K04	SPT4	250	Gastropod	4000 ± 30	4150	4038 - 4278
K05	SPT5	25	Coral fragment	495 ± 30	85	40 - 125
K05	SPT6	53	Coral fragment	1495 ± 30	1020	962 - 1062
K05	SPT7	59	Coral fragment	1580 ± 30	1120	1068 - 1168
K05	SPT8	82	<i>Halimeda</i> plates	1765 ± 30	1295	1261 - 1328
K05	SPT9	95	Coral fragment	1805 ± 30	1325	1287 - 1359
K05	SPT10	162	Coral fragment	2390 ± 30	1995	1937 - 2049
K05	SPT11	172	Coral fragment	2550 ± 30	2210	2151 - 2268
K02	SPT12	82	<i>Halimeda</i> plates	1850 ± 30	1370	1313 - 1406
K02	SPT13	116	Coral fragment	2080 ± 30	1630	1579 - 1685
K02	SPT14	116	<i>Halimeda</i> plates	1930 ± 30	1455	1408 - 1508
K02	SPT15	159	Coral fragment	2330 ± 30	1925	1874 - 1971
K07	SPT16	41	Coral fragment	755 ± 30	375	325 - 422
K07	SPT17	49	Coral fragment	680 ± 30	310	263 - 337
K07	SPT18	92	Coral fragment	1220 ± 30	740	691 - 775
K01	SPT19	96	Coral fragment	3395 ± 30	3380	3290 - 3472

Tableau 4.4: ²¹⁰Pb dating data for cores CA02, CA07, CA08 and CA01 (estimated supported ²¹⁰Pb activity based on α counting in core CA08 is 0.84 dpm/g); each profile is plotted with a logarithmic X-axis (for cores CA07 and CA08 respectively, samples at 32 cm and 11 cm show incoherent activities and were left apart for the sedimentation rate estimation).

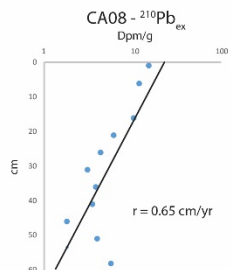
CA02	Tot ²¹⁰ Pb activity (dpm/g)	Ex ²¹⁰ Pb activity (dpm/g)	Error
Depth (cm)			
1	14.32	13.48	0.34
8	11.33	10.49	0.28
11	7.21	6.37	0.20
16	7.07	6.23	0.19
21	6.06	5.22	0.17
26	5.65	4.81	0.18



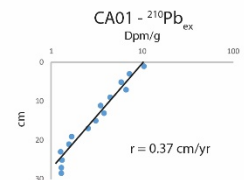
CA07	Tot ²¹⁰ Pb activity (dpm/g)	Ex ²¹⁰ Pb activity (dpm/g)	Error
Depth (cm)			
1	16.01	15.17	0.42
7	12.22	11.38	0.31
12	11.18	10.34	0.30
17	7.82	6.98	0.22
22	5.21	4.37	0.15
27	5.33	4.49	0.15
37	4.04	3.20	0.12
42	3.73	2.89	0.09
47	4.10	3.26	0.14
52	4.22	3.38	0.12
32	7.82	6.98	0.21



CA08	Tot ²¹⁰ Pb activity (dpm/g)	Ex ²¹⁰ Pb activity (dpm/g)	Error
Depth (cm)			
1	15.91	15.12	0.91
6	12.41	11.76	0.71
16	10.99	10.14	0.61
21	6.73	6.12	0.37
26	5.10	4.32	0.26
31	3.62	3.06	0.18
36	4.94	3.84	0.23
41	4.14	3.48	0.21
46	2.73	1.80	0.11
51	4.56	3.96	0.24
58	6.45	5.64	0.34
11	5.79	4.92	0.30



CA01	Tot ²¹⁰ Pb activity (dpm/g)	Ex ²¹⁰ Pb activity (dpm/g)	Error
Depth (cm)			
1	11.30	10.46	0.31
3	8.07	7.23	0.23
5	6.71	5.87	0.21
7	7.48	6.64	0.22
9	5.27	4.43	0.18
11	4.51	3.47	0.14
13	4.61	3.77	0.14
15	3.92	3.08	0.13
17	3.38	2.54	0.10
19	2.50	1.66	0.08
21	2.40	1.56	0.07
23	2.10	1.26	0.07
25	2.16	1.32	0.07
27	2.13	1.29	0.08
29	2.13	1.29	0.07



4.6.3.3 Core-to-seismic correlation

All cores were correlated to seismic profiles after depth to time conversion (Figure 4.9), using velocities of: (i) 1 600 m.s⁻¹ for silt material; and (ii) 1 800 m.s⁻¹ for coarse material, according to the relationships between P-wave velocities and sediment grain size (Hamilton, 1972). Due to the high resolution of the seismic survey, the uppermost seismic units can be correlated with the three different sedimentary facies A, B and C. Draping units U8, U6 and U4 are correlated with facies A (homogeneous silt deposits) (Figures 4.4 and 4.8; K04, K05, K02, K07, K01 and K03). Chaotic seismic unit U7 is correlated with facies B (coral debris unit) (Figures 4.4 and 4.8; K04, K05, K02 and K07). Seismic unit U5 is correlated with facies C (bioclastic sand unit) (Figures 4.4 and 4.8; K04, K05 and K01). By analogy of seismic architecture and seismic facies, seismic unit U3 is interpreted as composed of coarse debris deposits corresponding to either facies B or C (coarse coral fragments and/or bioclastic *Halimeda* sand), whereas seismic unit U2 is interpreted as composed of facies A (homogeneous silt deposit) (Figure 4.4).

The correlation between seismic profiles and sedimentary facies, together with the chronology, allow three debris units to be distinguished. From base to top, they are:

- At the base, seismic unit U3, which was not retrieved in the cores, but given its similarities with seismic units U5 and U7, is interpreted as being composed of *Halimeda* sand and/or coarse coral fragments.
- Seismic unit U5, which extends from the inner to the outer domain of the bay, is composed of a mix of *Halimeda* sand and coarse coral fragments (Figures 4.4, 4.5 and 4.8; facies C, lower debris unit) and yields ages from 3380 cal yr BP to 6215 cal yr BP (Figure 4.8).
- Seismic unit U7, which is confined to the inner part of the bay, is composed of coarse coral fragments (Figures 4.4, 4.5 and 4.8; facies B, upper debris unit) and yields ages from 85 cal yr BP to 2470 cal yr BP (Figure 4.8). Given the important age variations at the top of facies B, from 85 cal yr BP (K05) to 1370 cal yr BP (K02), it is postulated that erosion of the debris unit occurred in the area of K02. The presence of *Halimeda* sand lying on the debris unit in K02 reveals a high-energy depositional event that may have followed the erosion surface.

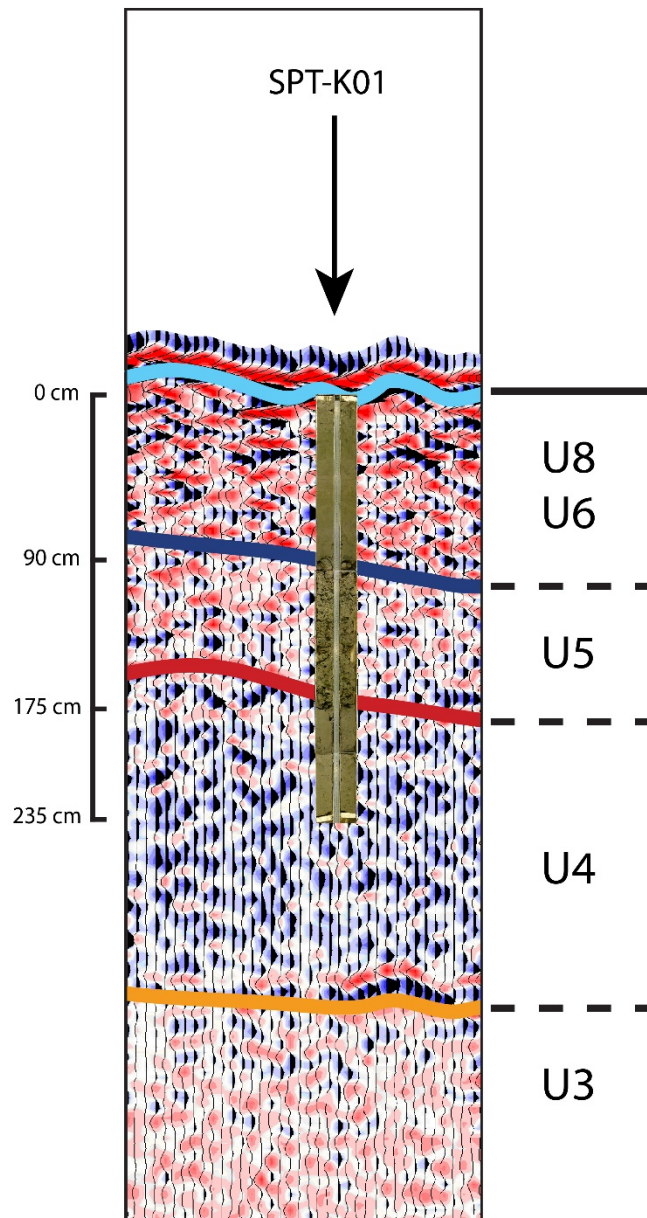


Figure 4.9: Core depth-to-time conversion and core-to-seismic correlation quality check for SPT-K01 core using SeiSee software.

4.7 Discussion

4.7.1 Sequence stratigraphic interpretation of the Pago Pago bay-fill

The sedimentary fill of Pago Pago Bay consists of eight units, overlying a regional erosional surface (EU0) associated with a strong amplitude reflector at the top of an acoustic basement. Given the origin and history of Tutuila Island as a hotspot volcanic island (McDougall, 1985;

Koppers *et al.*, 2008), and since Pago Pago Bay is described as an inundated volcanic caldera (McDougall, 1985), this basement is interpreted as volcanic bedrock. The erosional surface EU0 is interpreted as a sequence boundary formed during successive Quaternary sea level lowstands (Waelbroeck *et al.*, 2002). The lowest unit identified on top of the volcanic bedrock, unit U1, is characterized by reflectors onlapping onto surface EU0 towards the shore. This specific architecture attests to sediment deposition evolving towards the shore and is typical of transgressive sedimentation (Galloway, 1989; Christie-Blick, 1991). Many coastal lagoons, estuaries and semi-enclosed environments around the world display similar transgressive units at the base of their sedimentfill (Zaitlin *et al.*, 1994; Chaumillon *et al.*, 2010). Therefore, U1 is interpreted as a transgressive unit deposited during a period of sea-level rise. The bounding surface S1 at the top of U1 is a downlap surface (Mitchum, 1977) showing a transition from a retrogradational to a progradational pattern. The upper units (U2 to U8) display sub-parallel and sub-horizontal reflectors, with downlapping surfaces (bounding surfaces S3, S5 and S7) typical of an aggradational/progradational architecture. This architecture is consistent with deposition during a period of sea-level highstand (Catuneanu *et al.*, 2009). Results of age dating, as well as the absence of any major erosional surface between the volcanic basement and the sea bed, suggest that the whole sedimentary infilling was emplaced during the last eustatic cycle. Following this interpretation, the onlapping unit U2 would correspond to the transgressive systems tract (TST) while the upper prograding/aggrading units (U2 to U8) would correspond to the highstand systems tract (HST). In this context, S1 would correspond to the maximum flooding surface of the bay.

Since local subsidence during the Holocene is negligible (Koppers *et al.*, 2008; McDougall, 2010), the main parameter governing the accommodation space for sedimentation is sea-level variation. Therefore, considering local paleo-eustatism may help in understanding the sediment-fill of the bay. Paleo-sea-level curve reconstruction in the south-west Pacific Ocean (Woodroffe & Horton, 2005) indicates a mean sea level (m.s.l.) at -125 m (from present day m.s.l.) during the last glacial maximum, at around 20 000 cal yr BP. At around 12 000 cal yr BP, the sea level rose to -65 m (from present day m.s.l.) which is the approximate depth beneath m.s.l. of the volcanic basement in the outer domain of the bay (Figures 4.4 and 4.5). Finally, the present day m.s.l. was reached around 7 000 cal yr BP. Given the internal architecture of the Pago Pago bay-fill, which displays two main phases (retrogradation and aggradation/progradation) that were probably emplaced during one sea-level cycle (absence of a strong erosional surface within the sedimentary sequence), it is postulated that the transgressive unit U1 has been emplaced between the early flooding of the bay and the eustatic maximum, between 12 000 cal yr BP and 7 000 cal yr BP. Then, units U2 to U8 would have been deposited from 7 000 cal yr BP to present day. Ages obtained in units U5 and

U3 for reworked sediment are congruent with such an interpretation since they do not exceed 6215 cal yr BP. Given the successive highstands and lowstands that occurred in the late Quaternary, the scenario here suggests that the Pago Pago Bay infill that occurs during each highstand (i.e. interglacial period) is completely eroded during the following lowstand (i.e. glacial period).

4.7.2 The 2009 South Pacific Tsunami

Radiocarbon ages obtained near the upper boundary of unit U7 (up to 85 cal yr BP) and ^{210}Pb data from unit U8 (0.65 to 0.84 cm.yr⁻¹) in the inner part of Pago Pago Bay indicate that tsunamis from 1917, 1960 and especially 2009 should be recorded in the upper silt unit U8. Based on the sedimentation rate of 0.65 to 0.84 cm.yr⁻¹ within unit U8, the 2009 South Pacific Tsunami (SPT) deposit should be found in the first 10 cm of the short cores. Unfortunately, no visual trace of these tsunamis was observed in the cores (Figure 4.10), indicating that the 2009 SPT deposit within the sampled cores is not associated with any grain-size change and marked sedimentation change. Nevertheless, X-ray fluorescence (XRF) data measured on most of the short cores show a peak of the Ti/Ca ratio at approximately 7 to 9 cm depth (Figure 4.10). While no chemical analysis of inland tsunami deposits has previously been carried out on Tutuila Island, data from Satitua (Upolu Island, Samoa) show that the 2009 SPT inland deposit is rich in calcium (Ca), reflecting the source material from the coral reef, while the underlying soil is enriched in titanium (Ti), due to the volcanic nature of the parent rock on the island (Chagué-Goff *et al.*, 2011, 2017). High counts of Ca often indicate the occurrence of biogenic markers, such as shell, shell hash and carbonate, and are therefore used as indicators of a marine source (Chagué-Goff *et al.*, 2017). Since Tutuila Island is also volcanic, a similar approach can be used to interpret the peak in Ti/Ca in the marine sediment. Therefore, the observed peak in Ti/Ca most likely represents a terrestrial sediment input that could be associated with the backwash deposits of the 2009 SPT. No other peak, potentially associated with the historical 1917 and 1960 tsunamis, was observed clearly deeper in the cores. This could be explained by a smaller wave height and impact, hence less terrestrial sediment input. Similar findings have also been reported by (Sakuna *et al.*, 2012; Sakuna-Schwartz *et al.*, 2015) who analyzed offshore sediment cores, searching for evidence of backwash following the 2004 Indian Ocean tsunami in Thailand. It is also worth noting that chemical signatures can in some instances reveal the occurrence of event deposits that were otherwise not visible to the naked eye (Chagué-Goff *et al.*, 2016). It is the case in this study where, even if a multi-proxy approach was used to identify the 2009 SPT deposits, only through this chemical signature was it detectable. It might appear intriguing that the sedimentary record of the 2009 SPT is hardly discernible whereas much

4. The sediment-fill of Pago Pago Bay (Tutuila Island, American Samoa)

land and infrastructure damage was reported onland (Fritz *et al.*, 2011). Major soil erosion was observed and anthropogenic material was washed out to the sea during backwash (Jaffe *et al.*, 2010). It is therefore likely, given the mounds and troughs seafloor morphology, that most of the material washed out to sea was deposited and captured in mini-basins close to shore, in shallow areas (<15 m), where the ship was not able to make a seismic survey and collect cores. In relatively deep areas, it is assumed that the material deposited during and after the 2009 SPT consists of mud derived from soil erosion. Feldens *et al.* (2012) also reported that offshore deposits related to the 2004 tsunami in Thailand could only be found at shallow depths (9 to 15 m).

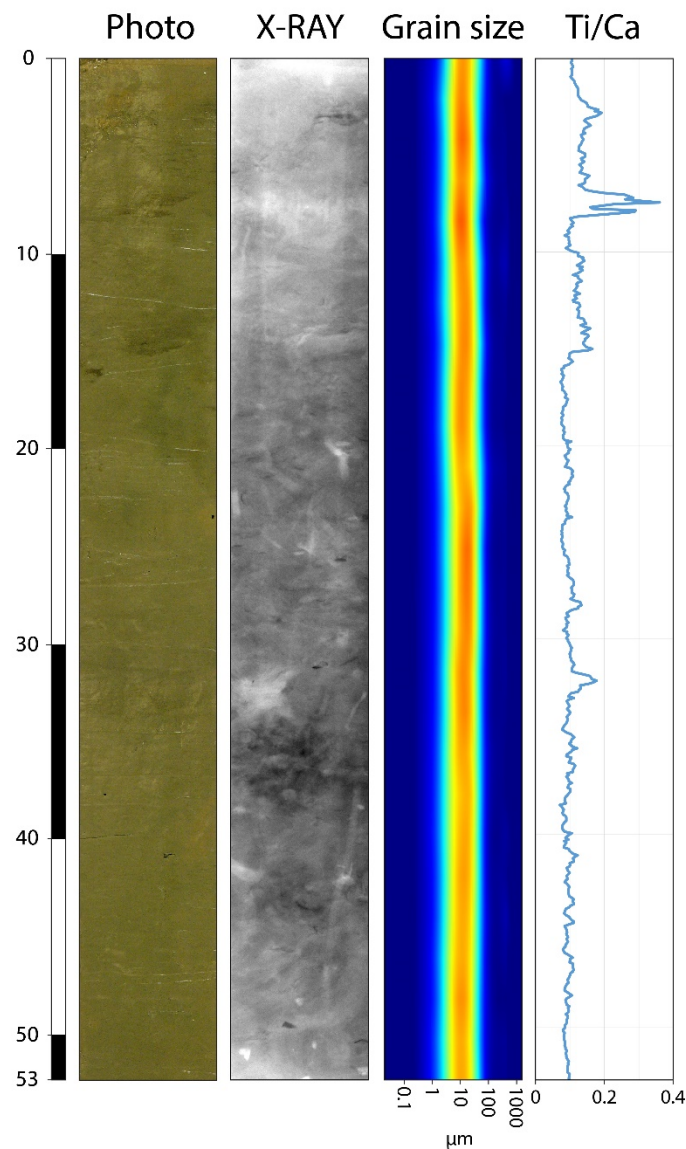


Figure 4.10: Multi-proxy approach of 2009 SPT deposits identification on core CA07: from left to right respectively, photograph, X-ray and grain size do not show any evidence of tsunami backwash deposits (no variations), while a peek of terrestrial input can be spotted between 7 and 9 cm on XRF data.

4.7.3 Origin of coral debris

The upper aggradational/progradational sequence (HST) is characterized by a changeover in the sedimentation between homogeneous low-energy silt deposits (U2, U4, U6 and U8) and very coarse coral debris and *Halimeda* deposits (U3, U5 and U7). These changeovers in the upper meters of the Pago Pago bay-fill indicate alternation of high-energy (facies B and C in U3, U5 and U7) and low-energy (facies A in U2, U4, U6 and U8) sedimentation phases. The coral fragments found in facies B (U3, U5 and U7) all show very fresh cuts (Figure 4.7) and have not been colonized by aquatic organisms after death. Besides, no intact or in living position corals are found. This suggests transportation after a high-energy event and rapid sedimentation under overlying mud. The freshness of the cuts also implies a local source, inferring that corals were most likely broken while still alive and transported over a relatively short distance. Thus, these debris indicate a very highly dynamic event, such as extreme wave events.

Two alternative processes, tropical storms and tsunamis, may have produced such highly dynamic events and must be considered. Given that the coral fragments are composed of shallow water species, both storm waves and tsunami waves are able to break and transport such fragments. Deep marine species were not identified in the debris deposits, which would have indicated reworking by long wavelength waves, such as tsunami waves, rather than storm waves. Nevertheless, the depth of marine species found in such deposits is not necessarily a criterion to differentiate storm and tsunami deposits, because onshore studies of the 2009 SPT deposits on Upolu Island (Chagué-Goff *et al.*, 2011) showed that the sediment source was from the nearshore and there was no evidence of fauna deeper than 10 m.

The only argument that may favor the tsunami origin for those coarse coral and *Halimeda* debris units is related to the morphology of the bay. Pago Pago Bay is a deep and sheltered bay whose morphology is ideal for dissipating storm waves. However, the funnel shape of the bay greatly amplified the tsunami waves from around 1 m at the entrance to 7 to 8 m in the inner bay during the 2009 SPT (Fritz *et al.*, 2011). Finally, due to the geodynamic context and the sheltered morphology of Pago Pago Bay, the most likely high-energy events responsible for the coarse coral and *Halimeda* debris units are tsunamis, which are able to break such coarse coral fragments from the mouth and sides of the bay and carry them towards the end of the bay into 60 m water depth.

The absence of coral debris in the upper sediment-fill of Pago Pago Bay, where 2009 SPT related deposits are expected to occur, seriously challenges the hypothesis of a tsunami origin for the underlying coral debris. Meanwhile, it is assumed that this absence of coral debris is a

consequence of the arrival of the settlers in Tutuila and the expansion of the harbor, which began around 150 years ago. The age of the transition between the coral debris of unit U7 and the homogeneous silts of unit U8 (Figure 4.8), at the end of the 19th Century, coincides approximately with the intense anthropization of Pago Pago Harbor. A resurvey by (Cornish & DiDonato, 2004) of a reef flat earlier described by (Mayor, 1920) allowed a comparative study between 1920 and 2004 and showed that this anthropization resulted in the decline of the coral colonies of Pago Pago Bay. Following this hypothesis, the decline of the reef colonies in the bay induced a lack of available coral to be broken and carried away during the most recent tsunamis, including that in 2009, but also during the 1917 and 1960 tsunamis, as observed in the cores. Beyond the decline of corals, anthropization has resulted in a progressive siltation of Pago Pago Bay, as shown by the thick U8 silt unit (facies A). A similar siltation of coastal environments, in response to deforestation and anthropization has been observed worldwide (Poirier *et al.*, 2011). Silty sequences are also observed in deeper U6 and U4 units, with a thousand-year period for U6. Given their age, prior to 2470 cal yr BP (Fig. 8), these deposits cannot be correlated with anthropization. Thus, two alternative hypotheses can be proposed to explain the presence of such fine deposits (facies A) interstratified between coarse coral fragments (facies B and C): either no tsunami occurred during these silty periods, or no local coral source was available for tsunami waves to mobilize.

The first hypothesis, where no tsunamis occurred during a period of a millennium or so, emphasizes an alternation between time spans with a high tsunami recurrence and some with no tsunami. However, most tsunamis, and especially those impacting the Samoan archipelago, are triggered by underwater earthquakes (Pararas-Carayannis & Dong, 1980). The two greatest historical tsunamis to hit Pago Pago Bay (Dominey-Howes & Thaman, 2009; Beavan *et al.*, 2010; Lay *et al.*, 2010; Goff & Dominey-Howes, 2011; Okal *et al.*, 2011) were triggered by earthquakes on the Tonga Trench. This alternation between periods of intense tsunami recurrence and periods without tsunamis could be related to alternation between active tectonic phases of the Tonga Trench subduction, during constraint discharge, and dormant phases, during constraint accumulation. Such long-term tectonic phases at plate boundaries have been pointed out elsewhere (Imamura, 1937; Marco *et al.*, 1996; Kelsey *et al.*, 2005; Dolan *et al.*, 2007) but never for the Tonga Trench.

The second hypothesis, where no local coral source is available for tsunami waves to mobilize, implies a variation of the availability of the local coral source over the late Holocene or a change in coral population (with the development of less fragile species such as massive *Poritidae* or *Favidae*). Such variations on the development of reef colonies could be related to paleo-climatic

or paleo-environmental changes. However, neither a sea-level variation (Lambeck *et al.*, 2014) nor drastic sea-surface temperature variations (Rosenthal *et al.*, 2013) capable of killing coral colonies were recorded during the late Holocene in the south-west Pacific Ocean. However, corals are also highly sensitive to salinity and turbidity variation (Veron & Stafford-Smith, 2000). Thus, the absence of corals could be interpreted as periods of high precipitation resulting in high erosion rates on the island and sediment supply to the coast, and lower salinity. Further paleo-climatic studies would be needed to warrant this hypothesis.

Another major question related to these findings is how many tsunami events may have produced such thick coarse coral and *Halimeda* debris units (facies B and C correlated to seismic units U5 and U7)? Unfortunately, no major discontinuity or erosion surface is visible in the cores within facies B and C, and no specific event stands out in the dating results. Thus it is impossible to say how many tsunamis occurred during these time intervals. Either way, it would have been hardly possible given the probability of erosion between different waves for the same event, but also of eroding a preceding tsunami during each event.

4.8 Conclusion

The goal of this study was to gain a better understanding of the architecture and history of the sedimentary infilling in Pago Pago Bay, in order to set the context for future more detailed studies on the impacts of the 2009 South Pacific Tsunami (SPT) and older tsunami events. Using bathymetry, the atypical geomorphology of the sea floor was first documented. Two domains bounded by the 40 m isobath were identified. The inner part of the bay, shallower than 40 m depth, is characterized by a succession of mounds and troughs. On the other hand, the outer part of the bay, deeper than 40 m, is characterized by a smooth and gentle slope with no specific geomorphological features.

Based on seismic profiles and sediment cores, eight sedimentary units were then identified overlying an eroded volcanic bedrock. These units are interpreted as corresponding to the sedimentary infilling of Pago Pago Bay during the sea-level rise that followed the last glacial maximum and reached the bay 12 000 years ago. The base of the sediment-fill is a transgressive unit, overlain by aggradational highstand tract units deposited during the last 7 000 years of high sea level. These units attest to a changeover in the nature of the sedimentation between homogeneous silt units and coarse coral and *Halimeda* debris units pinching out seaward. The size and shape of these coral fragments, combined with the highly sheltering morphology of Pago Pago

Bay, reveal the tsunami induced nature of these deposits. The reason for the alternation between homogeneous silt units and tsunami-induced coral debris units is not yet known. Two hypotheses are proposed. The first is a variation of the tectonic activity of the Tonga Trench subduction during the Holocene, resulting in phases of active tectonic activity followed by phases of tectonic quiescence connected to variations of the tsunami recurrence. As such, tectonic cycles have never been described in the south-west Pacific during the Holocene, only a new paleo-seismological study could validate or disprove this hypothesis. The second one is a variation of the paleo-climatic conditions, especially precipitation, controlling the abundance of local reef colonies, and thus the availability of the coral source. A local paleo-climatic study, using for example the geochemistry of *Halimeda* plates, could help to strengthen this hypothesis.

Evidence of backwash deposits caused by the 2009 SPT was found as a result of X-ray fluorescence (XRF) data. No other classical determination methods used nowadays to detect tsunami deposits have proved effective. A second study will focus on these discrete 2009 SPT backwash deposits using mainly geochemical analyses. Finally, the sedimentary record of Pago Pago Bay now constitutes a reference section for studies conducted in other bays around Tutuila Island and the Samoan archipelago.

4.9 Acknowledgements

We would like to thank first the CNRS-INSU “Risques et catastrophes telluriques” program and the Conseil Regional de la Région Poitou Charentes who made all of this possible by funding the whole project. A special thanks is addressed to the Commission Nationale de la Flotte Côtière, to the captain Jean-François Barazer and crew of the *R/V Alis*, to the divers Stéphane Bujan and John Butscher, along with Bruce Jaffe for his help coordinating the field survey. Appreciation also goes to John-Patrick Walsh and Reide Corbett for ^{210}Pb dating, and Pierre Sabatier for helping in its interpretation. Additional appreciation to the members of the EPOC lab core analysis platform Isabelle Billy, Pascal Lebleu, Marie-Claire Perello and Olivier Ther as well as GIS expert Vincent Hanquiez and interns Johanna Juppín and Laurine Monier. Finally, we would like to acknowledge the two anonymous reviewers along with Associate editor Pedro Costa for their thoughtful and constructive comments.

Chapter 5:

Backwash sediment record of the 2009 South Pacific Tsunami and 1960 Great Chilean Earthquake Tsunami

Scientific Reports

BRIEUC RIOU^{1,2}, ERIC CHAUMILLON¹, CATHERINE CHAGUE³, PIERRE SABATIER⁴, JEAN-LUC SCHNEIDER², JOHN-PATRICK WALSH⁵, ATUN ZAWADZKI⁶ and DANIELA FIERRO⁶

¹ LIENSs UMR 7266-CNRS, Université de La Rochelle, F-17000 La Rochelle CEDEX, France

² EPOC UMR 5805-CNRS, Université de Bordeaux, F-33615 Pessac CEDEX, France

³ School of Biological, Earth and Environmental Sciences, UNSW, Sydney 2052, NSW, Australia

⁴ Université Grenoble Alpes, Université Savoie Mont Blanc, CNRS UMR 5204, EDYTEM, F-73000 Chambéry CEDEX, France

⁵ University of Rhode Island, Narragansett, RI 02882, USA

⁶ Australian Nuclear Science and Technology Organisation, Lucas Heights 2234, NSW, Australia

Submitted: 21st May 2019

5.1 Abstract

Following recent tsunamis, most studies have focused on the onshore deposits, while the offshore backwash deposits, crucial for a better understanding of the hydrodynamic processes during such events and offering an opportunity for sedimentary archives of past tsunamis, have mostly been omitted. Here, we present a unique sedimentary record of the backwash from two historical tsunamis sampled in a sheltered bay in American Samoa, namely the 2009 South Pacific Tsunami and the 1960 Great Chilean Earthquake Tsunami. Although not always concomitant with a marked grain size change, backwash deposits are identified by terrestrial geochemical and mineralogical signatures, associated with micro-deformations. These micro-deformations are described for the first time in historic shallow marine backwash deposits and lead us to propose an improved depositional mechanism for tsunami backflow based on hyperpycnal currents. Moreover, this study brings a new criterion to the proxy toolkit for identifying tsunami backwash deposits. Sheltered shallow marine environments located in areas repeatedly impacted by tsunamis have a higher potential for the reconstruction of paleotsunami catalogs and should be preferentially investigated for coastal risk assessment.

5.2 Summary

5.2.1 Objectives

The first article focusing on the Pago Pago Bay sediment-fill has shown that the sedimentation in the bay has been largely influenced by tsunamis, with coarse coral deposits preserved over the last 7 000 years. Then, Pago Pago Bay appears to be an excellent candidate for studying modern-day tsunamis in order to gain new identification criteria for tsunami backwash deposits and reconstruct paleotsunami catalogs. However, despite the seemingly ideal preservation potential of such a deep and sheltered bay, backwash deposits from the 2009 SPT, which is the most recent tsunami known to have struck American Samoa, with waves reaching 7 m in Pago Pago Bay, were not observed in cores collected from Pago Pago Bay. Instead, an apparently homogeneous and uninterrupted silt layer was found from the seabed down to approximately 1 m below the surface, corresponding to the last 150 years or so. The absence of apparent backwash deposits was interpreted as a result of the death of most coral colonies in the bay following recent anthropization and industrialization of Pago Pago Harbor beginning at the end of the 19th century.

In the past, if most studies focusing on tsunami backwash deposits were based mainly on basic sedimentological evidences, such as visual interpretation of cores or grain size variations, a few studies have also used finer methods such as geochemical and micropaleontological methods. We assume that a multi-proxy analysis including sedimentological, mineralogical and geochemical methods may be able to reveal tsunami backwash deposits in homogenous mud where no visual sedimentological changes can be observed. Then, the goal of this study was to identify and describe tsunami backwash deposits associated with the 2009 SPT.

5.2.2 Material and methods

This work focuses on the uppermost 50 cm of the silty sediment draping unit of Pago Pago Bay. It is based on extensive 1 m-resolution bathymetric, seafloor reflectivity and 2D high-resolution seismic surveys, along with ten short sediment cores. Coring sites were selected according to onboard real-time analysis and interpretation of geophysical data. The short cores were collected between 27 and 47 m depth using a custom-made gravity box corer and measure between 20 and 60 cm. All cores were first analyzed visually, then for geochemical variations using an XRF core-scanner and for grain size using a laser particle size analyzer and a statistical analysis

software. Thin sections were extracted and prepared from all cores in 10 cm segments for mineralogical variations and compared to sediment samples collected in a nearby stream and on the beach. Finally, sediment was sampled from one core to establish an age-to-depth model using the ^{210}Pb , ^{226}Ra and ^{137}Cs activities for identification of event deposits.

5.2.3 Main results

The multi-proxy analysis reveal the occurrence of two anomalous layers (EL1 and EL2) that stand out from the background fine carbonate-dominated sedimentation. If the grain size analysis shows very little variation, geochemical and thin section analyses display pronounced variations. Geochemically, the two anomalous layers are marked by a high increase in the Ti/Ca ratio, indicating a probable increase of terrestrial input. The deeper layer (EL2) exhibits one major peak, while the shallowest layer (EL1) is divided in two peaks – a first major peak overlain by a second minor peak. These geochemical variations are correlated with mineralogical and microstructural variations. Indeed, the anomalous layers are composed of different facies from the background sediment (F1). The first facies (F3) is found at the base of both anomalous layers. It is composed of a homogeneous carbonate-depleted clay, with small volcanic mineral fragments and displays a sharp basal contact with asymmetric flame structures and rip-up clasts without mixing. The second facies (F2) is found only on top of the uppermost anomalous layer (EL1). It is characterized by a normally graded terrigenous sand composed of a mix of micritic and organic-rich clay aggregates with plant and shell debris and rounded volcanic minerals.

5.2.4 Main conclusions

The mineralogical and geochemical analysis indicate seaward transport of terrestrial material (facies F2 and F3) interstratified with marine sediments (facies F1). Indeed, the high Ti/Ca ratio, along with other terrestrial geochemical proxies, is typically used in tsunami backwash studies to identify the terrestrial source of event deposits. In addition, facies F2 and F3 are composed of abundant terrestrial material, such as organic-rich clay aggregates, vascular plant debris and volcanic minerals, in comparison with the background facies F1 composed exclusively of micritic aggregates and shell fragments of marine origin. This attests of short-lived important increase of the terrestrial input, with sediment eroded and dragged from the surrounding offshore areas. The sharp basal contact with asymmetric flame structures and absence of mixing with the rip-up clasts suggest shearing of superficial underlying sediment under a dense and cohesive gravity flow, similar to

some processes observed during turbidity currents. Then, these observations suggest a strong seaward mudflow initiated following the inundation and reworking of the coastal plain, which can be attributed to only two types of events: flash-floods or tsunami backwash currents.

Based on the age model built from the ^{210}Pb activities, the two anomalous layers are dated to 2009 ± 1 AD for EL1 and to 1960 ± 7 AD for EL2. Then, these two event layers correspond to the two strongest tsunamis known to have struck Tutuila since the middle of the 20th century, the 2009 SPT for EL1 and the 1960 GCET for EL2. The two strongest cyclones to have struck Tutuila in the same time laps were Ofa and Val, respectively in 1990 and 1991. Then, a flash-flood origin, which would have been induced by heavy rains during a major cyclone, of these two event layers was discarded. However, one of these two cyclones may have been recorded in the cores by a very short Ti/Ca peak, correlated with small dispersed terrigenous clasts without basal deformation, and dated between 1982 AD and 1992 AD.

Finally, an improved and confirmed tsunami backwash model is proposed based on these observations. Indeed, micro-deformations indicating shearing at the base of backwash deposits such as the asymmetric flame structures pointed out in this study have occasionally been described in inferred paleotsunami backwash deposits, but never before in recent historic tsunami backwash deposits. Then we propose an improved transport and deposition model for tsunami backwash deposits as a dense and cohesive hyperpycnal flow inducing shearing and buckling of the underlying sediment.

5.3 Introduction

Over the last two decades, interest in tsunami-related research has increased significantly, with peaks in the number of published articles following the 2004 Indian Ocean Tsunami (IOT), the 2009 South Pacific Tsunami (SPT) and the 2011 Tohoku-Oki Tsunami (TOT) (Chagué-Goff *et al.*, 2017). However, most studies have focused on onshore deposits, with only a few tackling the issue of backwash depositional processes (Takashimizu & Masuda, 2000; Le Roux & Vargas, 2005b; Noda *et al.*, 2007; Abrantes *et al.*, 2008; Donato *et al.*, 2009; Goodman-Tchernov *et al.*, 2009; Sugawara *et al.*, 2009; Srinivasalu *et al.*, 2010; Feldens *et al.*, 2012; Jonathan *et al.*, 2012; Sakuna *et al.*, 2012; Tipmanee *et al.*, 2012; Veerasingam *et al.*, 2014; Smedile *et al.*, 2019). Unlike onshore deposits, offshore deposits are not subject to subaerial erosion and less to anthropic reworking, but can be altered by waves, currents, mixing and bioturbation. Most of the studies of historic tsunami backwash were carried out in open beach environments following the 2004 IOT and 2011 TOT. However, such environments have a poor preservation potential due to their exposure to waves. In contrast, sheltered bays may provide a higher preservation potential due to less reworking by waves. Thus, the choice of the study zone is key when looking for marine backwash deposits. We suggest that in shallow marine sheltered environments characterized by a low hydrodynamic setting, a complete and uninterrupted record is more likely to be preserved.

Most studies of backwash deposits are based on grain size, geochemical data and microfossils (Chagué-Goff *et al.*, 2017). Shallow marine tsunami deposits are usually characterized by an increase of the mean grain size within usually fine marine mud, due to the inclusion of coarse terrestrial sediment originating from the onshore-inundated or beach areas (Noda *et al.*, 2007; Srinivasalu *et al.*, 2010; Jonathan *et al.*, 2012; Sakuna *et al.*, 2012; Sakuna-Schwartz *et al.*, 2015), often accompanied by a higher Ti/Ca ratio reflecting the terrestrial input (Sakuna *et al.*, 2012; Sakuna-Schwartz *et al.*, 2015; Smedile *et al.*, 2019). Deep offshore foraminifera species, dragged from the oceanic floor to the shallow coastal zones by the tsunami wave, can also often be found in shallow marine backwash deposits (Sugawara *et al.*, 2009; Smedile *et al.*, 2011; Jonathan *et al.*, 2012; Milker *et al.*, 2013).

5. Backwash sediment record of the 2009 SPT and 1960 GCET

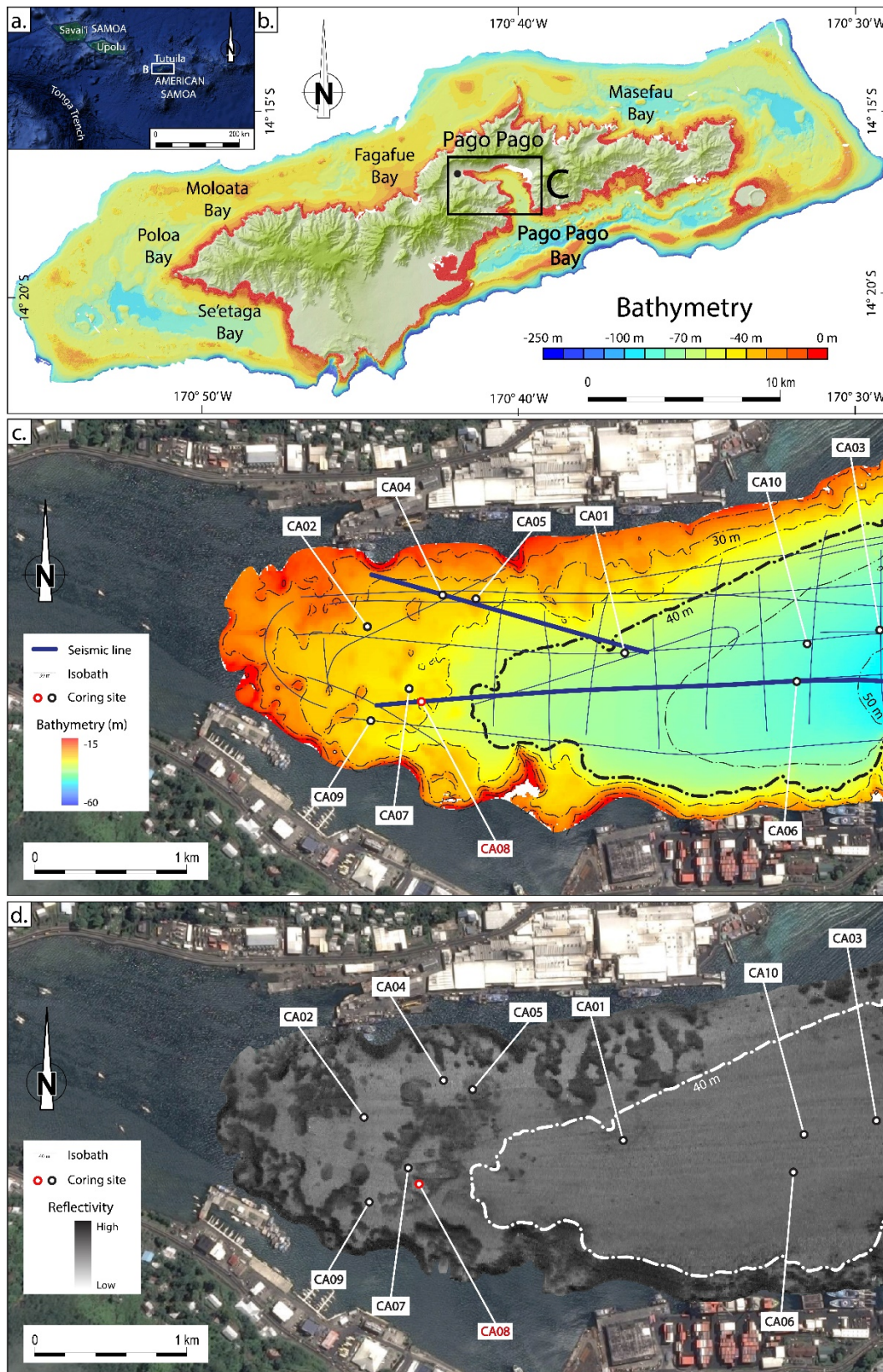


Figure 5.1: a. Location of American Samoa and Tutuila in the southwest Pacific Ocean (modified from Google Earth); b. map of Tutuila with bathymetric data (modified from NOAA, 2018); c. and d. map of Pago Pago Bay with 1 m high resolution processed bathymetric data and seafloor reflectivity data respectively, acquired during the SAMOA-SPT campaign (5 m isobaths) and location of the ten cores.

Tutuila Island (American Samoa) is a volcanic island located in the southwest Pacific less than 200 km from the northern end of the Tonga Trench (Figures 5.1.a and 5.1.b). Previous work suggests that Pago Pago Bay has been subject to at least two 1 000-year phases of frequent tsunami occurrence during the late Holocene (Riou *et al.*, 2018). More recently, the island has been hit by several destructive tsunamis generated all around the Pacific Ocean, including the 2009 SPT and the 1960 Great Chilean Earthquake Tsunami (GCET) (National Geophysical Data Center, 2018; Pararas-Carayannis & Dong, 1980). Tutuila has a very indented coastline, with deep and narrow bays (Figure 5.1.b). Owing to its very calm hydrodynamic conditions and the destructive impact of the 2009 SPT, the deepest and most sheltered bay, Pago Pago Bay (Figure 5.1), was chosen for this study because it is most likely to provide an ideal setting for the preservation of recent shallow marine tsunami deposits.

5.4 Study area and setting

Tutuila Island is part of the Samoan archipelago, a 500 km long volcanic hotspot trail (Figures 5.1.a and 5.1.b). Savai'i, which is the oldest island in the west of the volcanic trail, is approximately 5 Ma old (Koppers *et al.*, 2008), while Tutuila's shield-building volcanism started 1.5 Ma ago. The island is composed of five volcanoes, with the Pago volcano being the most active (McDougall, 2010). The dominant volcanic rocks are mainly alkaline olivine basalts that make up the calderas, overlain by basanitoids, basanites and olivine nephelinites emplaced after the erosion and collapse of the calderas. All these rocks are characterized by a high titanium content (Hawkins & Natland, 1975).

The main bay of the island, Pago Pago Bay (Figures 5.1.c and 5.1.d), was formed by the inundation of the Pago caldera due to post-volcanic subsidence and erosion (McDougall, 1985). It is a long (5 km), deep (10 to 60 m) and narrow (< 1 km) bay ending in an amphitheater head characterized by steep slopes and a reduced coastal plain. The inner part of the bay is completely sheltered from ocean and storm waves, even during the most powerful cyclones that have been reported, and is home to Pago Pago Harbor. The only waves able to reach the inner part of the bay and impact seafloor sedimentation are tsunami waves, as reported during recent events.

Over the last century, more than 100 minor tsunamis have reportedly hit Pago Pago Bay (National Geophysical Data Center, 2018; Pararas-Carayannis & Dong, 1980). However, three tsunamis stand out. The first one is the 1917 tsunami generated by an earthquake in the northern end of the Tonga Trench. The first observed wave reached 3 m in the head of the bay, causing

infrastructure damage, including houses and a church, but no casualties (Pararas-Carayannis & Dong, 1980). The 1960 GCET was recorded with a first wave reaching up to 3.5 m, causing only little damage and no casualties (Pararas-Carayannis & Dong, 1980). The latest was the 2009 SPT generated in the same area as the 1917 tsunami (National Geophysical Data Center, 2018; Beavan *et al.*, 2010; Okal *et al.*, 2011), with a first wave reaching up to 7 m (Fritz *et al.*, 2011). It was the most destructive historical tsunami recorded in Pago Pago Bay; it caused considerable damage in the bay up to 500 m inland and 34 deaths around the island (Dominey-Howes & Thaman, 2009; Goff & Dominey-Howes, 2011).

During the same period, cyclones have reached American Samoa nearly every year, with two severe cyclones standing out: Cyclone Ofa in 1990 and Cyclone Val in 1991. The former passed 160 km west of Tutuila and caused heavy rain and flooding with wind gusts up to 170 km/h (Prasad, 1990). The latter, said to be the strongest and most destructive cyclone since 1889, passed right over Tutuila with winds reaching 185 km/h, causing heavy rain and flooding (Pandaram & Prasad, 1992). Such cyclones may cause flash-floods due to heavy rain, resulting in substantial run-off in the bay. However, no large waves were recorded in Pago Pago Bay during these cyclones.

5.5 Material and methods

All data presented in this study were obtained during the oceanic campaign SAMOA-SPT from August 27th to September 10th 2015 aboard R/V *Alis* (Riou *et al.*, 2018). An extensive 2D high-resolution seismic survey was carried out, along with 1 m-resolution bathymetric and seafloor reflectivity surveys. A Seistec-IKB boomer was used for the seismic acquisition, with a vertical resolution of approximately 25 cm allowed by its 1 to 10 kHz bandwidth. All raw profiles were processed using iXBlue DELPH seismic acquisition software. A frequency filter was applied between 900 Hz and 10 500 Hz, coupled with a linear AGC (Amplitude Gain Control) and stacking of three adjacent traces. A Kongsberg EM-1002 multibeam sounder was used for the bathymetric and reflectivity acquisition with a 95 kHz frequency. Raw bathymetric data were processed and corrected for tide and salinity-induced celerity bias using IFREMER CARAIBES software, while the seafloor reflectivity was processed and corrected using IFREMER SonarScope software.

Ten short cores were sampled in Pago Pago Bay (Figure 5.1) using a custom-made gravity box-coring device adapted from the CASQ (CAllypso SQuare) box corer. This coring device, with a maximum penetration of 30-60 cm, allows a slower and gentler penetration of the sediment surface, permitting an intact sampling of the superficial sediment record with preservation of

sediment structures and laminae. Cores were sampled in water depth ranging from 27 to 47 m and their locations were chosen based on the raw seismic, bathymetric and reflectivity surveys. Cores were retrieved in topographic lows of the inner domain (Figures 5.1 and 5.2), and in the outer domain, where the 2009 SPT backwash deposits were believed most likely to be found.

Cores were split, photographed and logged in detail, noting all physical sedimentary structures and the vertical facies succession. Grain size analysis of samples collected from all cores in 5 mm intervals was conducted using a Malvern Mastersizer S laser particle size analyzer. Statistical analysis of the grain size data was conducted using the Gradistat 8.0 software (Kenneth Pye Associates Ltd.). All cores were analysed for XRF using an Avaatech core scanner with a 1 mm measuring step. Two complementary runs were carried out for each core in order to count the full element spectrum: a first run at 10 kV and 1 500 μ A, and a second run at 30 kV and 2 000 μ A. XRF data was analyzed as element ratios and as separate elements normalized by the total counts. Thin sections were prepared for all short cores in 10 cm intervals. Smear samples were collected in two key areas of the watershed: two samples were collected onshore from Laolao and Pago streams (Figure 5.1.c), representing the terrestrial input into Pago Pago Bay, and two samples were collected on a beach (Figure 5.1.c), representing the bay sediments.

The chronology was established for core CA08 using 1-cm thick samples taken every 5 cm down to 57 cm depth (Figure 5.1.c). ^{210}Pb , ^{226}Ra and ^{137}Cs activities were measured by gamma spectrometry at the Australian Nuclear Science and Technology Organisation (ANSTO, Lucas Heights, Australia). Approximately 3 g of samples were packed in 3 mL vials and sealed for 3 weeks before counting. Gamma photon peaks of ^{210}Pb (46 keV), ^{226}Ra (352 and 609 keV) and ^{137}Cs (662 keV) were collected for more than 48 h using an Ortec well-type HPGe (High-Purity Germanium) detector. In each sample, the ^{210}Pb excess activity ($^{210}\text{Pb}_{\text{ex}}$) was calculated by subtracting the ^{226}Ra activity (the proxy for supported ^{210}Pb) from the total ^{210}Pb activity following Golberg (1963) (Goldberg, 1963). The sedimentation rate, based on depths corrected for compaction, was estimated using the CFCS (Constant Flux Constant Sedimentation) model (Krishnaswamy *et al.*, 1971).

5.6 Results

5.6.1 Geophysical analysis

The geomorphological characteristics observed from the bathymetry of the Pago Pago Bay seafloor has already been studied and discussed by Riou *et al.* (2018). Based on the bathymetry and the reflectivity surveys, two geomorphologic domains were identified (Figures 5.1.c and 5.1.d). The outer domain is characterized by a smooth topography and a steady and gentle 0.5° slope, and extends seaward from a slope break (10 to 15° slope) between the 35 and 40 m isobaths. It displays a homogenous medium reflectivity. The inner domain, which extends between the slope break and the coastline, is characterized by an alternation of mounds and troughs. The mounds have a roughly round shape and are a few meters high (<5 m) by a few tens of meters wide (<50 m), delimitating more or less connected troughs. The troughs display low reflectivity while the mounds display very high reflectivity. Ten shallow sediment cores were collected both in the troughs and on the mounds. Sediments are very homogenous and are dominated by medium to coarse silt (77.5 to 88.5 % mud, 11.5 to 22.5 % sand). Consequently, the variations in seafloor reflectivity are most likely to be due to slope changes on the flanks of the mounds.

Nine sediment sub-units (U0 to U8) have been identified on seismic profiles Pago-27 and Pago-22 by Riou *et al.* (2018). For the purpose of this study, they have been grouped in four sets of units (Figure 5.2): (1) the volcanic basement (U0), (2) the transgressive unit (U1), (3) the aggrading units (U2 to U7) and the upper draping unit (U8). The basement is characterized by a transparent seismic facies and limited at the top by a major erosional surface (EU0). The transgressive unit is characterized by retrograding landward-oriented onlaps, while the aggrading units consist of an alternation of muddy and coarse coral debris units pinching-out seaward (Riou *et al.*, 2018). The upper draping unit composed of mud is characterized by sub-horizontal and sub-parallel continuous reflectors.

5. Backwash sediment record of the 2009 SPT and 1960 GCET

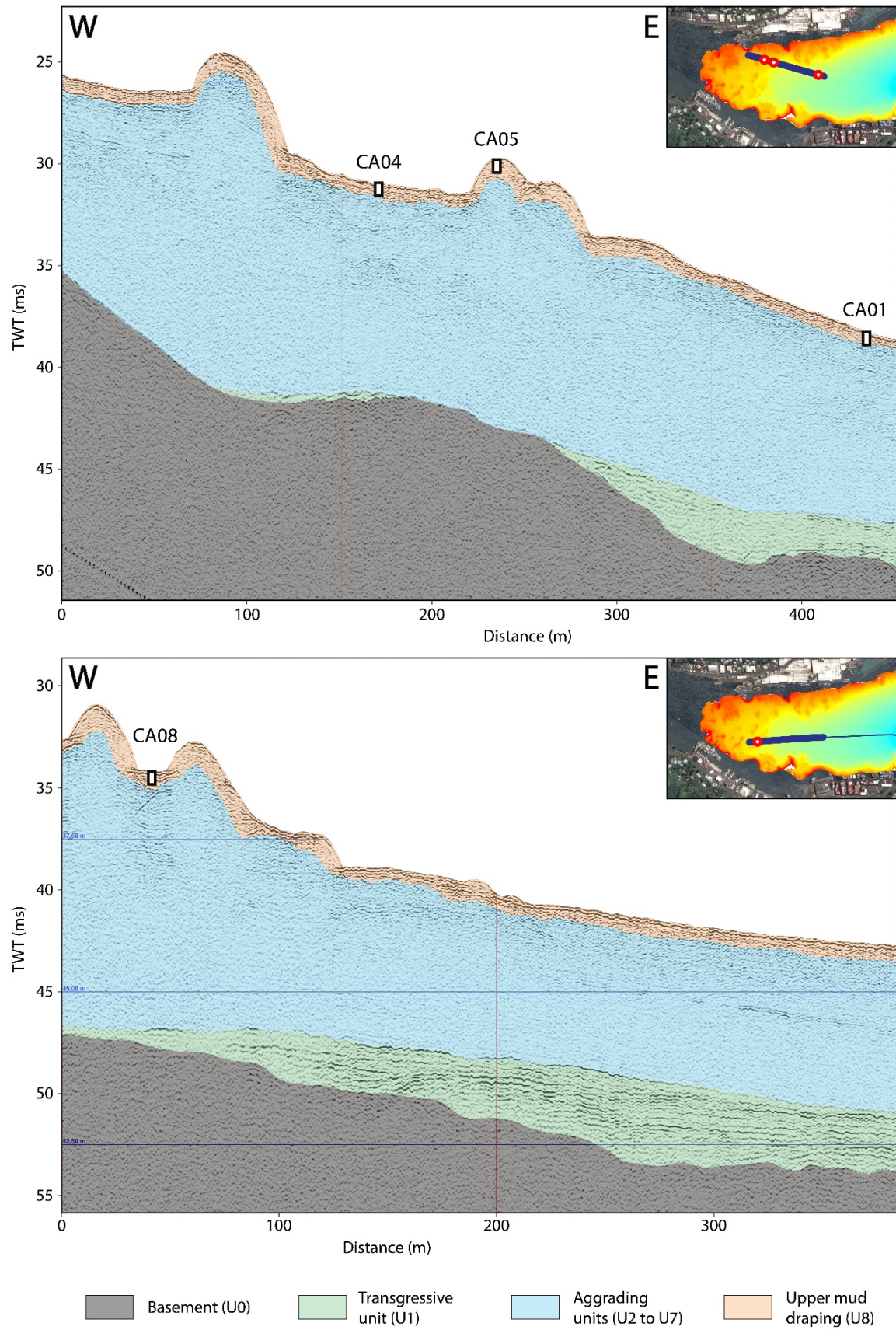


Figure 5.2: Interpreted west-east seismic profiles Pago-27 (top) and Pago-22 (bottom), simplified according to the interpretation and nomenclature given by Riou *et al.* (2018), with the location of cores CA04, CA05, CA01 and CA08 on the profiles.

5.6.2 Grain size analysis

Cores described in this study were sampled in the upper draping unit (U8) in both the inner and outer domains (Figures 5.1.c and 5.1.d). Visually, the sediment sequences are mainly homogenous except for a few discontinuous layers of slightly darker sediment. These are mostly found in the first ten centimeters, although some occur deeper in some cores. No major erosional surfaces are observed in the cores. Results of laser particle size analysis do not show major grain size variations along the cores, which are composed of seemingly homogenous silt. Only a discrete increase of the coarser fraction (D90) is observed at 5 cm depth in core CA08 (Figure 5.3).

5.6.3 Geochemical analysis

XRF analyses reveal pronounced geochemical variations in a number of cores, as shown by the Ti/Ca ratio (Figure 5.4). In core CA08, four main Ti/Ca peaks are observed (Figure 5.3): a first small peak at 4-6 cm depth, a second well-marked peak at 8-10 cm depth, a third small peak at 24-26 cm depth and a fourth very high peak at 40-42 cm depth. These Ti/Ca peaks occur in the discontinuous dark sediment layers seen in the core section. Similar peaks are observed in the first 10 cm of all proximal cores (0-5 cm, CA02; 3-7 cm, CA09; 2-8 cm, CA07; 4-10 cm, CA08; 3-10 cm, CA04; 2-6 cm CA05, Figure 5.4). In addition, a second deeper peak is found in cores CA04 and CA09, at 48-50 cm and 47-49 cm depth, respectively (Figure 5.4). In all cores, normalized Ti and Ca profiles are negatively correlated. Each Ti/Ca peak is due to an increase of Ti and a decrease of Ca, as shown for core CA08 (Figure 5.5). Similar trends are observed for the Ti/Sr, Zr/Ca, and Zn/Ca ratios. For the Pb/Ca ratio, the same four peaks are found, but several additional smaller and thinner peaks are also observed. Magnetic susceptibility obtained for core CA08 displays three peaks at 6 cm, 8 to 10 cm and 41 cm depth, correlated with the Ti/Ca peaks (Figure 5.5).

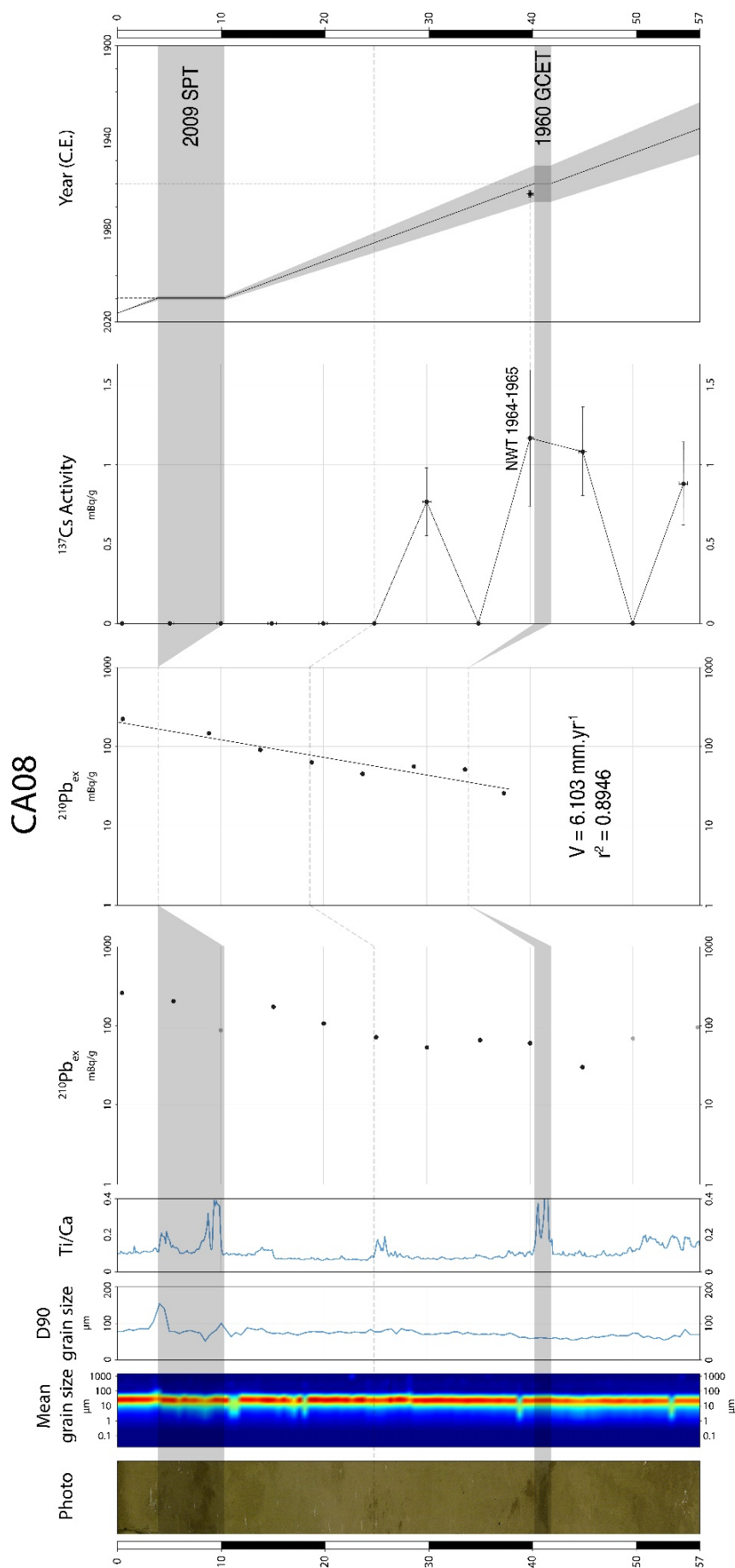


Figure 5.3: Multi-proxy analysis of core CA08; from left to right, respectively, photograph, grain size (mean and D90), Ti/Ca ratio, excess ^{210}Pb excess activities (raw and corrected), ^{137}Cs activities and age model. Grey shaded bars represent the 2009 South Pacific Tsunami and the 1960 Great Chilean Earthquake Tsunami event layers. ^{137}Cs activities below the detection limit are plotted to 0 mBq/g. NWT: Nuclear Weapon Tests.

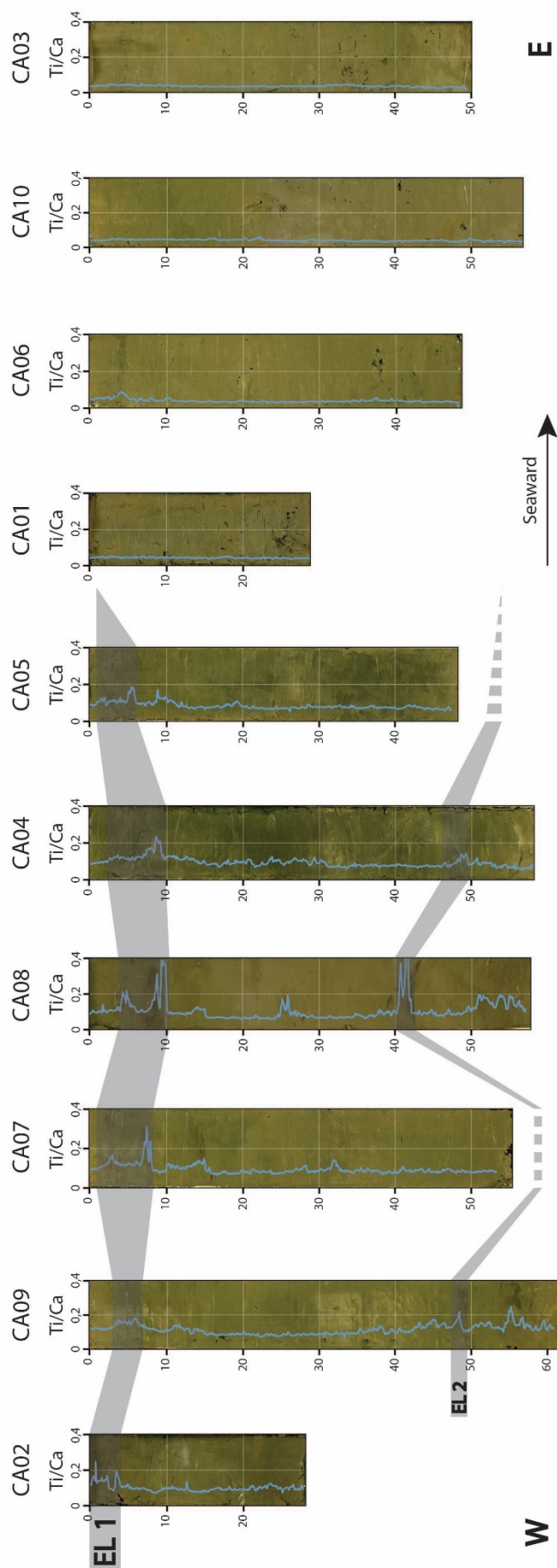


Figure 5.4: Correlation of all ten cores projected along a west (left) to east (right) transect (see Figure 1), with photograph and Ti/Ca ratio for each core. Grey shaded bars represent the 2009 South Pacific Tsunami event layer (EL1) and 1960 Great Chilean Earthquake Tsunami event layer (EL2).

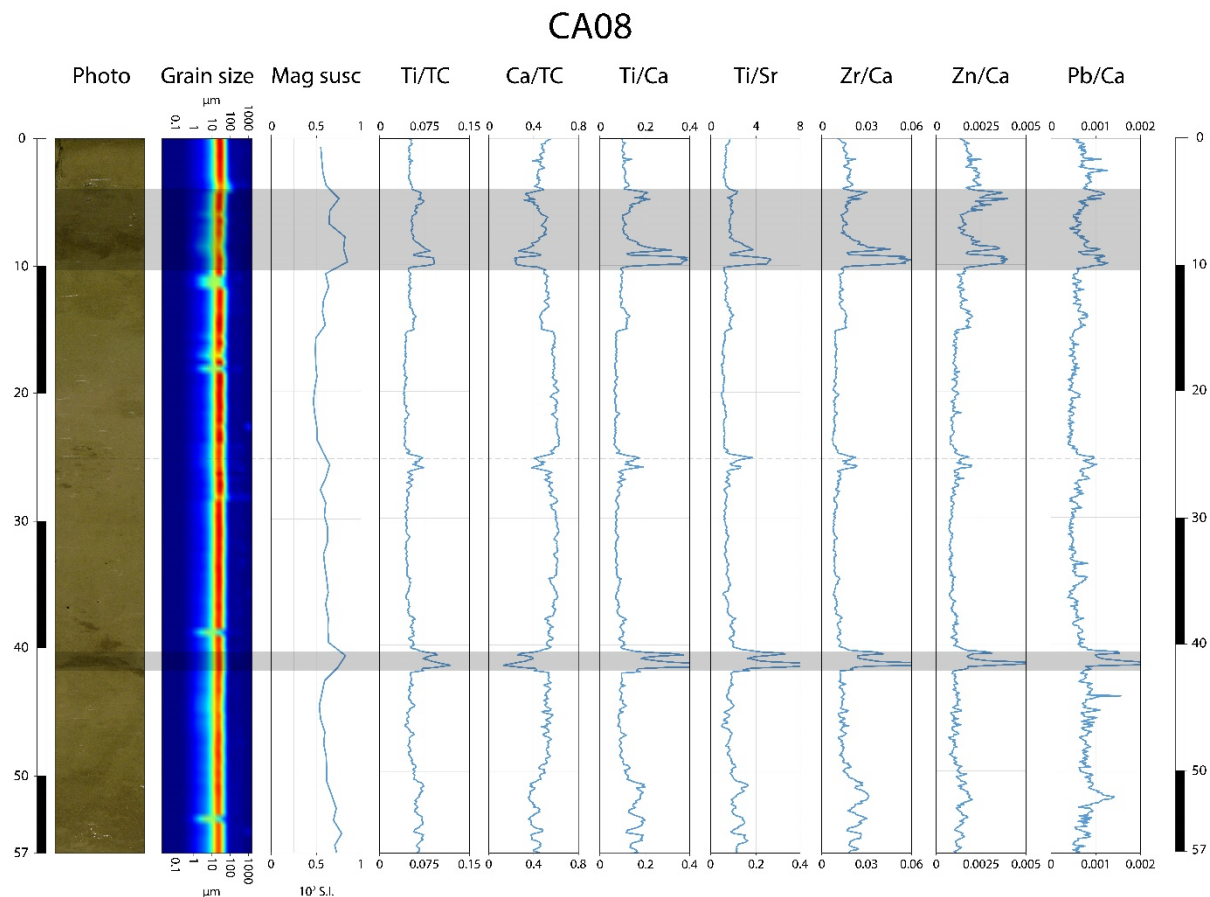


Figure 5.5: Multi-proxy analysis of core CA08; from left to right, photograph, grain size, magnetic susceptibility and XRF geochemical data (Ti/TC, Ca/TC, Ti/Ca, Ti/Sr, Zr/Ca, Zn/Ca, Pb/Ca). For all element ratios, high values represent an increase in the terrestrial input. Ti and Ca are normalized over the total counts (TC). Grey shaded bars represent the 2009 South Pacific Tsunami event layer (top) and the 1960 Great Chilean Earthquake Tsunami event layer (bottom).

5.6.4 Thin section analysis

Based on the grain size and mineralogy observations of thin sections from core CA08, five sediment facies (labelled F1, F2, F3, F4 and F5; Figure 5.6) were identified. Facies F1 corresponds to homogenous silt and exhibits a low and constant Ti/Ca ratio throughout most of the core. It is characterized, in order of abundance, by micritic mud and aggregates, bioclastic shells (bivalves, gastropods, spicules), clay aggregates with a high organic matter content, and plant debris (Figure 5.6.b).

Facies F2 is a normally graded detritic fine to very fine sand that corresponds to a short maximum in Ti/Ca at 4–6 cm depth in core CA08. It is characterized, in order of abundance, by micritic aggregates, rounded clay aggregates with high terrestrial organic content including vascular plant debris (leaves, stems, roots), bioclastic shells (bivalves, gastropods, spicules), along with

5. Backwash sediment record of the 2009 SPT and 1960 GCET

rounded 200-500 μm iddingsite (altered olivine crystals), clinopyroxene (augite) and plagioclase (labradorite) minerals. In addition, opaque minerals, possibly magnetite, are found at the base of the layer. This facies shows a sharp basal contact and a graded upper contact (Figures 5.6.a and 5.6.b).

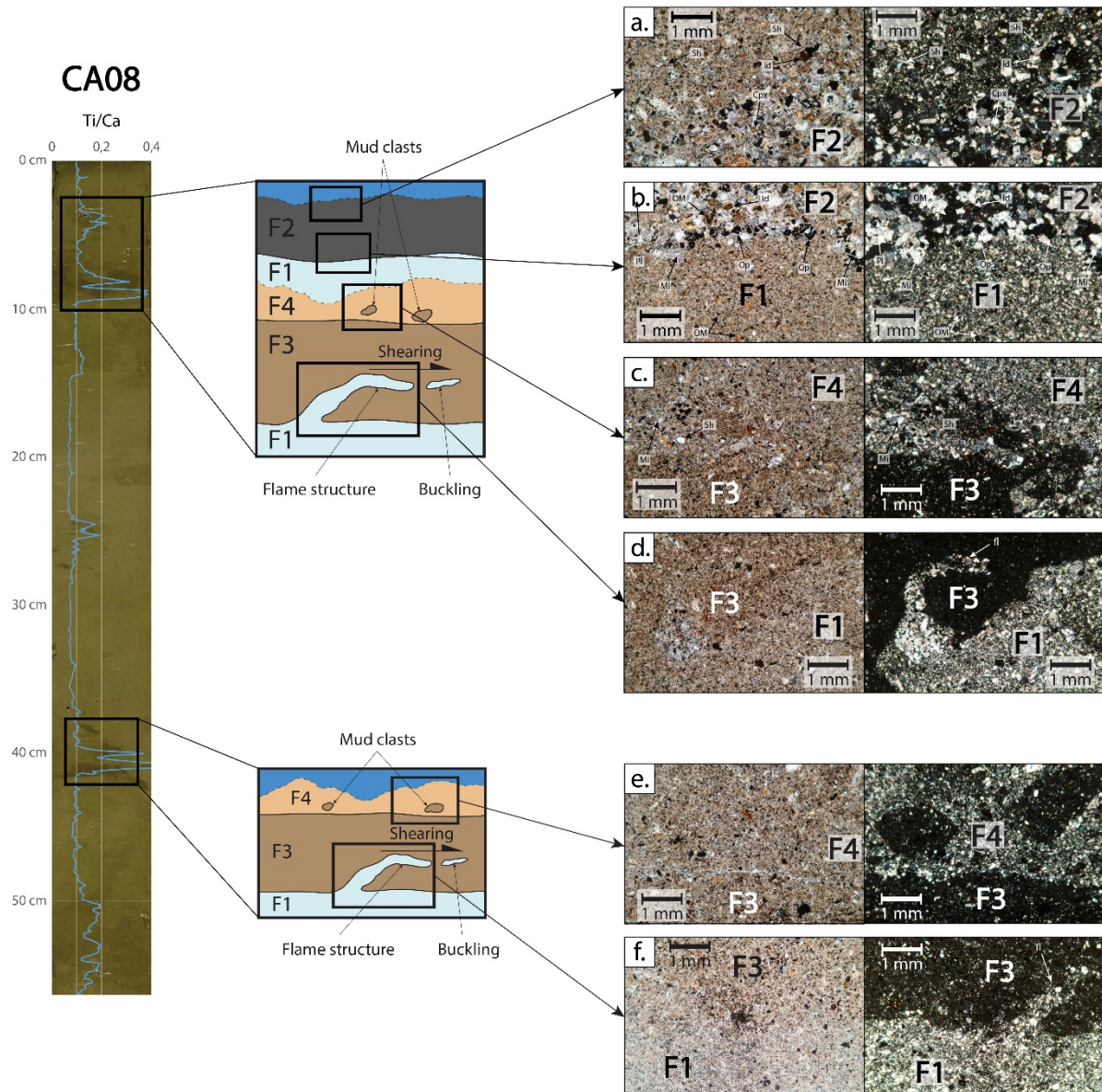


Figure 5.6: Photograph and Ti/Ca profile for core CA08, with interpretative sections of interest from the core and photographs of thin sections and their position in the core. Note that photographs are shown twice, once in analyzed light (left) and once in analyzed polarized light (right). Note that photographs **a**, **c** and **e** represent the top of each interval with high Ti/Ca, while photographs **b**, **d** and **f** represent their base. F1: homogenous silt, micritic mud and aggregates, shells, organic matter (OM). F2: normally graded very fine to fine sand, micritic aggregates, clay aggregates rich in organic matter (OM), opaque minerals (Op), shells (Sh), plant debris, iddingsite (Id), clinopyroxene (Cpx) and plagioclase (Pl). F3: non-graded terrigenous clay with asymmetric flame structures (fl) and rip-up clasts at the base. F4: normally graded clayey silt, mix of terrigenous clay (F3) and micritic mud and aggregates (F1) with shells (Sh).

Facies F3 is a detritic clay exhibiting high Ti/Ca, found at 8-10 cm and 40-42 cm depth. It is characterized by unidentified homogenous clay and the absence of carbonated material (Figures 6.c to 6.f). It includes various small volcanic mineral fragments ($<100\text{ }\mu\text{m}$) such as iddingsite, clinopyroxene and plagioclase. It stands out from the background by its darkness in analyzed polarized light. It displays sediment deformation, with a sharp basal contact. Micro-deformations are asymmetric flame structures (Figures 5.6.d and 5.6.f), evolving occasionally into rip-up clasts composed of F1 material. Even though cores are not oriented, asymmetric flame structures are all oriented in the same direction. These rip-up clasts are found mostly at the base of the layer and display no mixing with the surrounding F3 sediment.

Facies F4 is a transitional normally graded clayey silt facies exhibiting decreasing upward Ti/Ca, found at 8 cm and 40 cm depth. It consists of a clayey to silty matrix composed of a mix of F1 and F3, with F3 mud clasts at the base ($< 2\text{ mm}$, Figures 5.6.c and 5.6.e).

Facies F5 (24-26 cm, CA08) is similar to F3 in terms of mineralogy and grain size, but does not feature any micro-deformations. It is only found as small dispersed clasts ($< 5\text{ mm}$).

Smear samples from Laolao and Pago streams onshore are composed, in order of abundance, by plant debris and iddingsite, augite and labradorite minerals. Smear samples from the beach are characterized mainly, in order of abundance, by sub-rounded micritic aggregates, bioclastic shells and plant debris.

5.6.5 ^{210}Pb and ^{137}Cs Dating

The $^{210}\text{Pb}_{\text{ex}}$ activity downcore profile shows a regular decrease punctuated by a distinct drop at 10 cm depth (Figure 5.3). These low $^{210}\text{Pb}_{\text{ex}}$ activities correspond to facies F3 layers. Because it is considered an instantaneous deposit, facies F2, F3 and F4 are excluded for the construction of an event-free sedimentary record, following Arnaud *et al.* (2002). $^{210}\text{Pb}_{\text{ex}}$ activities plotted on a logarithmic scale reveal a linear trend, inferring a mean sedimentation rate of $6.1 \pm 0.2\text{ mm.yr}^{-1}$. Ages were calculated using the CFCS model (Constant Flux Constant Sedimentation) (Krishnaswamy *et al.*, 1971) applied to the original sediment sequence to provide a continuous age-depth relationship (Figure 5.3), and this age-to-depth model was then corroborated with the ^{137}Cs activities (Figure 5.3). While most samples measured were below or close to the detection limit, the ^{137}Cs maximum activity occurs at 40 cm depth. It is commonly accepted that this peak corresponds to 1964-1965 in the southern Hemisphere, following the Test Ban Treaty in 1962 (Pfitzner *et al.*,

2004; Magand & Arnaud, 2007). The good agreement between the ages derived from the $^{210}\text{Pb}_{\text{ex}}$ -CFCs model and the ^{137}Cs peak provides a well-constrained continuous age-to-depth relationship.

5.7 Implications

At first sight, the homogenous visual aspect of all cores, except for the slight change of color, and the lack of major visible grain size variations suggest that the superficial sediment fill of Pago Pago Bay could be interpreted as homogenous silty sediment settling in a calm hydrodynamic environment. However, XRF data and microscopic observations of thin sections reveal the presence of irregular and discontinuous thin layers. These layers have a different geochemical signature, mineralogical assemblage, but also grain size not always detected by the laser particle size analyzer. The only discernable change was an increase of the coarser fraction at 5 cm depth in core CA08. The higher Ti/Ca ratio most likely reflects an increase in the terrestrial inputs, as also observed elsewhere (Sakuna *et al.*, 2012; Sakuna-Schwartz *et al.*, 2015; Smedile *et al.*, 2019). Indeed, titanium originates mostly from land and is a component of several volcanic rocks forming Tutuila, such as basanitoids (Hawkins & Natland, 1975). On the other hand, the main source of calcium is most likely to be from marine carbonates (Chagué-Goff *et al.*, 2011, 2017). This trend is supported by several other element ratios, such as Ti/Sr, Zr/Ca, Zn/Ca, Pb/Ca and Mn/Ca (Figure 5.5). As for calcium, strontium is mainly found in marine carbonates, while zirconium, like titanium, is naturally present in the volcanic rocks of Tutuila. Zinc and lead are most probably sourced from industrial activities in Pago Pago and its harbor, such as the tuna cannery. The terrestrial origin of the high Ti/Ca intervals is confirmed by the mineralogical composition of the layer at 4-6 cm depth in core CA08. Pago Pago Bay has no major fluvial tributary, meaning that the background sedimentation is mostly marine-influenced and dominated by carbonated micritic sediment and shells, as described for F1, and reported by Morrison *et al.* (2010). F2 is also dominated by carbonated micritic sediment and shells but, unlike F1, shows a significant proportion of volcanic minerals (15-20 %). These minerals match those observed in the smear samples from Laolao and Pago streams and correspond to those described for the Pago volcanic rocks by Macdonald (1968). This confirms that F2 records an increase of terrestrial input, with sediment sourced from the erosion of the onshore volcanic shield. Moreover, this layer is coarser than the background sedimentation. This attests of a high-energy event, which is coherent with stronger erosion of the volcanic soil onshore.

Layers at 8-10 cm and 40-42 cm depth in core CA08 are composed of F3 and show no change in grain size. There, only the higher than normal Ti/Ca ratio suggests a higher terrestrial input. However, these layers display a very sharp basal contact with the underlying deformed sediments. The layer boundaries show asymmetric flame structures with rip-up clasts (F1, buckling) at the base of the layer (Allen, 1984; Collinson, 1994). These observed structures indicate syn-depositional reworking with shearing of superficial soft and cohesive sediment beneath a dense and cohesive gravity flow (Baas *et al.*, 2011; Butler *et al.*, 2016), as can attest the lack of mixing between the soft superficial sediment (F1) and the upper layer (F3). Similar deformation structures can be found at the base of hyperpycnal flows such as turbidites, when the underlying superficial sediment is very fine and cohesive (Clark & Stanbrook, 2001; Butler *et al.*, 2016). The higher terrestrial signature of these layers suggests a strong backflow coming from the inundated area into the bay. Given the context of Pago Pago Bay, two types of events could generate backflows with such impact on the seafloor: flash-floods due to heavy rain during a severe cyclone, or a strong tsunami backwash.

The age model derived from short-lived radionuclides allowed to link the two event layers to two specific events. The two shallowest Ti/Ca peaks in core CA08 (4-6 cm and 8-10 cm, Figure 5.3), correlated with the shallowest peaks in all proximal cores (0-5 cm, CA02; 3-7 cm, CA09; 2-8 cm, CA07; 4-10 cm, CA08; 3-10 cm, CA04; 2-6 cm CA05; Figure 5.4), are dated to 2009 ± 1 AD (event layer 1, Figures 5.3 and 5.4). The deepest Ti/Ca peak in core CA08 (40-42 cm, Figure 5.3), correlated with Ti/Ca increases at 48-50 cm depth in core CA04 and 47-49 cm depth in core CA09, (Figure 5.4) are dated to 1960 ± 7 AD (event layer 2, Figure 5.2). Based on the age estimation of the two event layers, they are unlikely to have been caused by the flash-floods associated with the two major cyclones recorded in this period, Ofa (1990 AD) and Val (1991 AD). However, these two cyclones may be recorded by the small Ti/Ca peak at 24-26 cm in core CA08, dated between 1982 and 1992 (Figure 5.3). Small dispersed clasts with similar mineralogical composition to facies F3 but showing no deformation structures are also observed at this depth (F5). The age estimations of event layers 1 and 2 based on ^{210}Pb and ^{137}Cs chronology match the date of two major historic tsunamis, with event layer 1 most likely to correspond to the 2009 SPT and event layer 2 to the 1960 GCET.

Flame structures such as those observed at the base of both event layers have occasionally been reported at the base of onshore tsunami uprush deposits, between successive waves (Matsumoto *et al.*, 2008). In the context of submarine tsunami backwash, they have only been observed once by Le Roux & Vargas (2005b) at greater scales and were attributed to large-scale

mass failures induced by possible paleotsunamis. However, these observations are based on ancient deposits and are only interpreted as caused by tsunami backwash with no unconditional evidence. Here, flame structures are observed for the first time in sediments emplaced by recent and well-documented historic tsunamis, and are proven to be of tsunami origin. Two reasons can be pointed out to explain why such micro-deformations have not been reported in earlier work. The first reason may be related to the specific morphology of the bay. Indeed, Pago Pago Bay is a deep and sheltered bay that may favor hyperpycnal flow during tsunami backwash leading to flame structures. The second reason could be that no one has yet analyzed thin sections in tsunami backwash deposits and thus have not been able to observe such features, despite their possible presence. Nevertheless, as this study proves, such sheltered environments provide an ideal preservation potential for event deposits and must not be neglected when searching for tsunami evidence.

A possible hypothesis for the shallow peak observed in core CA08 (4-6 cm) can be the occurrence of two successive waves during the 2009 SPT. The first and second waves were 7 and 3 m high, respectively, compared to the single 3.5 m-high wave recorded for the 1960 GCET (Pararas-Carayannis & Dong, 1980). We hypothesize that the first wave eroded all the available superficial clay and the second wave eroded deeper into the coarser sediment. The F1-type sediment in-between facies F2 and F3 may be explained by older sediments reworked by the first wave and settled in-between the two waves.

Based on these observations, we propose the following sediment transport and deposition model for tsunami backwash based on hyperpycnal backflow (Figure 5.7). During the uprush phase of the tsunami, the tsunami wave erodes and reworks the superficial onshore coastal sediment (Figure 5.7.a). During the backwash, a thin layer of water with highly concentrated reworked sediment is channelized and transported seaward and behaves as a hyperpycnal current after entering the sea (Figure 5.7.c). This results in the formation of a dense and cohesive inertia-driven mudflow similar to that described by Mulder *et al.* (2009) following the rupture of the Malpasset Dam. During this process, part of the superficial soft muddy sediment (F1) is incorporated due to shearing as rip-up clasts in the mudflow (F3), without mixing, in a buckling phenomenon. Finally, when the mudflow loses its inertia, it is deposited as a homogenous non- or poorly-graded layer (F3), topped by a thin transition layer (F4) due to the settling of suspended sediment (mixed F1 and F3) with a few mud clasts (F3) at the base (Figure 5.7.d).

5. Backwash sediment record of the 2009 SPT and 1960 GCET

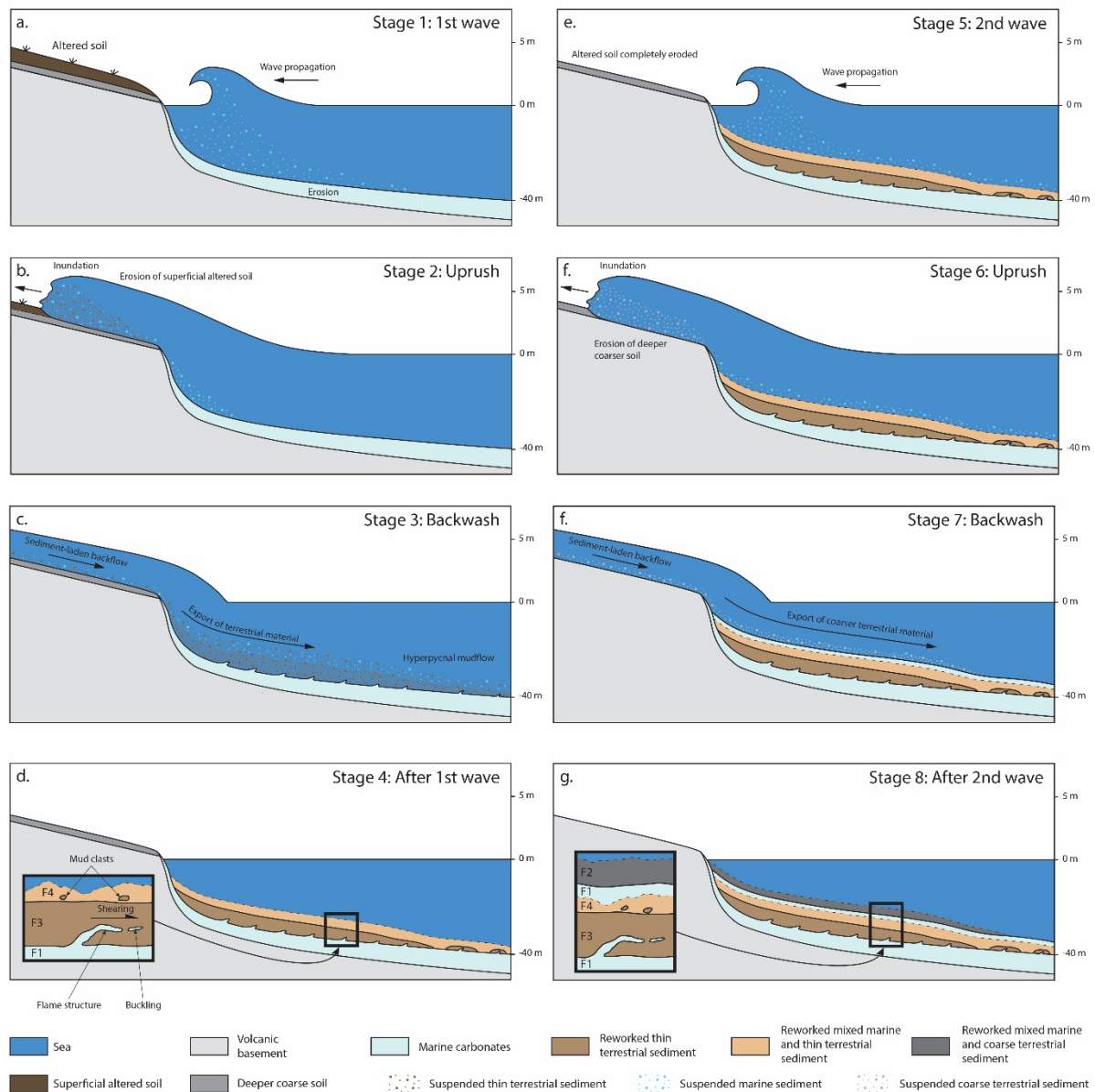


Figure 5.7: Interpretative tsunami backwash depositional model illustrating simplified transport and deposition mechanisms during each phase of the tsunami. The right-hand side panels represent the processes linked to a possible second wave such as during the 2009 SPT. The zoom in panel d. illustrates a complete event layer in the case of a single major tsunami wave, such as seen in core CA08 for the 1960 GCET. The zoom in panel g. illustrates a complete event layer in the case of two tsunami waves, such as seen in core CA08 for the 2009 SPT.

5.8 Conclusion

In this study, we present a unique 80-year sediment record in sheltered Pago Pago Bay. Despite the absence of clear visual evidence in the cores, geochemical and thin section analyses combined with geochronological dating allowed the identification of backwash deposits of two major historic tsunamis, the 2009 South Pacific Tsunami and the 1960 Great Chilean Earthquake

Tsunami. The geochemical analysis showed an increase of the Ti/Ca ratio in these layers, in line with the land-to-sea sediment transport observed around volcanic islands. Thin section analysis revealed the morphology of these deposits as a non- or poorly-graded layer exhibiting a sharp basal contact suggesting erosion. Micro-deformations revealed shearing and buckling structures attesting of a gravity-driven and inertia-driven density current. These observations lead us to propose an improvement of the existing sediment transport and deposition model for tsunami backwash, as a dense and cohesive hyperpycnal flow inducing shearing and buckling of the underlying superficial soft sediment. These observations represent a step further towards a better understanding of tsunami backwash flows. In addition, we provide a new proxy for the identification of tsunami backwash deposits in sheltered environments, which may also be used as a new criterion to differentiate tsunami and storm deposits. At a wider scale, this study has proven that sheltered bays offer an ideal preservation of event deposits and that it is urgent to consider such bays around the world for the reconstruction of paleotsunami catalogs and coastal risk assessment. Further work should concentrate on areas frequently impacted by tsunamis, such as the Pacific Islands, south-east Asia, Chile or even Alaska where deep and narrow sheltered calderas, bays or fjords could offer ideal sites for the preservation of tsunami deposits.

5.9 Acknowledgments

We acknowledge the funding from the CNRS-INSU “Risques et catastrophes telluriques” program and the Conseil Regional de la Région Poitou Charentes. We also thank the Commission Nationale de la Flotte Côtière, the captain Jean-François Barazer and crew of the *R/V Alis*, the divers Stéphane Bujan and John Butscher, along with Bruce Jaffe for helping in the coordination of the field survey. Appreciations go to the members of the EPOC core analysis platform Isabelle Billy, Pascal Lebleu, Marie-Claire Perello and Olivier Ther as well as GIS expert Vincent Hanquiez and interns Johanna Juppín and Laurine Monier.

Chapter 6:

Offshore evidence for historic tsunamis on the north shore of Tutuila (American Samoa)

To be submitted to: *Marine Geology*

BRIEUC RIOU^{1,2}, ERIC CHAUMILLON¹, JEAN-LUC SCHNEIDER², CATHERINE CHAGUÉ³, SABINE SCHMIDT² and THIERRY CORRÈGE²

¹ LIENSs, UMR 7266-CNRS, Université de La Rochelle, La Rochelle CEDEX, F-17000, France

² EPOC, UMR-5805-CNRS, Université de Bordeaux, Pessac CEDEX, F-33615, France

³ School of Biological, Earth and Environment Sciences, University of New South Wales, Sydney 2052, Australia

In preparation

6.1 Abstract

Following the 2004 Indian Ocean Tsunami and the 2011 Tohoku-Oki Tsunami, there has been a growing interest in the search for geological evidence of past tsunamis. This increasing interest led to a good understanding of hydrodynamic and sedimentary processes at stake on land during the uprush phase of a tsunami. However, studies of marine tsunami deposits emplaced during the backwash phase of a tsunami are still highly underrepresented. The number of studies focusing on marine backwash deposits is not yet sufficient to have a clear understanding of the backwash phase of a tsunami, hence the need for additional geological evidence of recent tsunamis. Here, we present a sedimentary record from two bays on the north shore of Tutuila Island (American Samoa), Masefau and Fagafue bays. The backwash deposits of four historic tsunamis were identified in two sediment cores, including deposits of the 2009 South Pacific Tsunami and likely the 1868 South American Tsunami. Together with previously published work on the south coast of Tutuila (Pago Pago Bay), this study provides the first investigation of tsunami backwash deposits all around a Pacific island, in the middle of the Pacific Ring of Fire, with identification and correlation of at least one historic event, namely the 2009 South Pacific Tsunami. In addition, this work presents the first geological evidence in American Samoa of what is interpreted as likely the 1868 South American Tsunami. With four major tsunami backwash deposits identified in a 150-year sediment record, this study shows the good preservation potential of sheltered bays for event deposits, and looks up to encouraging the scientific community to search for tsunami backwash deposits in such environments.

Keywords: tsunami, paleotsunami, backwash, flash-floods, core correlation.

6.2 Summary

6.2.1 Objectives

The second article focusing on the superficial sediment record of Pago Pago Bay has shown that at least two major tsunamis have left geological evidence of their impact in the shallow sediment record of Tutuila. These two tsunamis, the 2009 SPT and the 1960 GCET, are the strongest tsunamis reported to have impacted the island of Tutuila during the last 70 years. If no inundations or damage were reported outside of Pago Pago Bay for the 1960 GCET, the 2009 SPT is known to have impacted the entire island. It caused significant inundations all around the island, with run-up altitudes reaching just under 20 m in the northern bays of Tutuila. Then, we can assume that the 2009 SPT has likely left geological evidence of its impact offshore not only in Pago Pago Bay but also in bays all around the island.

For this purpose, the aim of this study is to search for possible backwash deposits emplaced following the 2009 SPT in the sediment record of two bays on the north shore of Tutuila, namely Fagafue Bay and Masefau Bay. In addition, the deeper sediment record will also be investigated for potential older events, such as the 1960 GCET or 1917 TIT. Indeed, Tutuila, which is located in the middle of the Pacific Ring of Fire, is frequently impacted by major tsunamis generated all around the Pacific and inundating shores all around the island.

6.2.2 Material and methods

This work focuses on the upper sedimentary record of two bays, Masefau and Fagafue, on the north shore of Tutuila. It is based on extensive 1 m-resolution bathymetric surveys along with two 150 cm-long cores, one collected in each bay. Coring sites were selected according to on-board real-time analysis in order to choose sheltered locations. The cores were sampled using a Kullenberg corer. Both cores were analyzed for visual sedimentological features, then for grain size variations using a laser particle size analyzer. Cores were then examined for geochemical variations using an XRF core-scanner. Finally, sediment was sampled for elaboration of an age-to-depth model using ^{14}C as well as ^{210}Pb , ^{226}Ra , ^{137}Cs and ^{232}Th activities.

6.2.3 Main results

Multi-proxy analysis of cores in Fagafue Bay and Masefau Bay revealed the presence of 4 anomalous sediment layers. In Fagafue Bay, three anomalous layers were identified (EL1, EL2 and EL4). Layers EL1 and EL4 are characterized by a poorer sorting than the background and a coarser base with sharp contact. In addition, they both show significant increases in the Ti/Ca ratio and K_{norm} (normalized potassium rate). The third layer, EL2, is characterized by a slightly poorer sorting and Ti/Ca and K_{norm} increases. In Masefau Bay, all four anomalous layers were identified (EL1 to EL4). EL4 is characterized by a bimodal grain size trend, with one mode similar to that of the background sediment and a second coarser mode, and a strong Ti/Ca increase. EL1 and EL3 are also characterized by a bimodal grain size trend and mean grain size coarsening, but show little-to-no Ti/Ca increases. Finally, EL2 is characterized by a slight mean grain size coarsening and a very little Ti/Ca increase. In addition, in both bays, sediment sampled in the anomalous layers show a $^{210}\text{Pb}_{\text{xs}}$ activity drop compared to sediment found right above.

6.2.4 Main conclusions

The grain size coarsening, poor sorting and bimodal trend of these four anomalous layers along with the shift in the $^{210}\text{Pb}_{\text{xs}}$ activity indicate that these anomalous layers are composed of older reworked sediment and were deposited during a high-energy event. Three types of events are capable of inducing such high-energy deposits in shallow marine environments: storms, flash-floods generated during cyclones and tsunamis. These event layers are correlated with more or less perceptible increases in Ti/Ca and K_{norm} . Since titanium and potassium are some of the main elements found on volcanic islands such as Tutuila, these increases attest of a highly probable terrestrial origin of the deposits forming event layers EL1 to EL4. Thus, they are very unlikely to be storm deposits, which mainly gather sediment from the beach and nearshore to upper offshore domains that could not explain these increases in terrestrial input. Then, flash-flood deposits are known to be better sorted, finer and less erosive compared to tsunami backwash deposits. Thus, event layers EL1 to EL4 were most likely emplaced by tsunami backwash.

Elaboration of the radionuclide-derived age model allowed dating of these events and correlation between Fagafue Bay and Masefau Bay. Event layer EL1 is dated to 2009 ± 0.5 AD in both cores and thus most likely corresponds to backwash deposits emplaced following the 2009 SPT. EL2 is dated to 1957 ± 1.3 AD in Fagafue Bay and 1960 ± 2.3 AD in Masefau Bay. At this period, two tsunamis have impacted Tutuila. The first one, the 1960 GCET, which was the

6. Offshore evidence for historic tsunamis on the north shore of Tutuila (American Samoa)

strongest of the two, induced backwash deposits in Pago Pago Bay, on the other side of the island, but no inundation was reported on the north shore. The second one, the 1957 AIT (Aleutian Island Tsunami), was estimated with less force but reportedly caused 1.5 m inundation on the north shore. Thus, both of these tsunamis could be responsible for deposition of EL2. EL3 was only encountered in Masefau Bay and is dated to 1920 ± 5.1 AD. It most likely corresponds to the 1917 TTT. Finally, EL4 is dated to 1870 ± 8.2 AD in Fagafue and 1878 ± 8.1 AD in Masefau. Unfortunately, no tsunami was reported in Tutuila at this period. However, the 1868 SAT (South American Tsunami) is known to have impacted a great number of islands in the south Pacific, including Upolu (Samoa). Thus the first and most probable hypothesis is that EL4 was deposited following the 1868 SAT. The second hypothesis is that it was induced by an older tsunami. Indeed, this age is near the limit of what can be dated using the ^{210}Pb method. Then, several candidates can be proposed, including tsunamis generated by great South American earthquakes or along the Aleutian Trench. Such South American earthquakes have occurred in 1746 AD, 1687 AD and 1586 AD. Great Aleutian earthquakes have been less reported, but one specific major event is inferred to have occurred around 1290-1390 AD.

Finally, this study, together with previous work in Pago Pago Bay, represents the first investigation of marine tsunami backwash deposits all around an island, and more interestingly in the middle of the Pacific Ring of Fire. Backwash deposits from three historic tsunamis were identified, including the 2009 SPT, the 1917 TTT and the 1960 GCET or 1957 AIT. An additional backwash layer was identified and does not correspond to any events reported on Tutuila. It was most likely emplaced by the 1868 SAT, which is known to have impacted nearby islands. This would be the first marine backwash evidence of this tsunami, even if an older origin cannot be ruled out.

6.3 Introduction

Over the last two decades, following the 2004 Indian Ocean Tsunami (IOT) and the 2011 Tohoku-Oki Tsunami (TOT), research dealing with tsunamis has increased considerably (e.g. Chagué-Goff *et al.*, 2017). This interest is motivated by the need to increase our knowledge about these events, both for social risk assessment and for sedimentary and geomorphologic impact and evolution of coastal zones. However, with most studies focusing on onshore deposits, we still lack examples of geological evidence of tsunami deposits offshore. In order to gain a better understanding of the impacts of tsunamis in coastal regions, the tsunami database needs to be expanded beyond the uprush phase only and focus more on the backwash phase. For this purpose, shallow marine environments are more prone to receive and record backwash deposits (Einsele *et al.*, 1996). In this context, geological evidence of historic tsunamis should first be investigated in shallow marine environments, helped by existing tsunami or earthquake reports, catalogs and databases around the world, both onshore and offshore (Pararas-Carayannis & Dong, 1980; Lange & Healy, 1986; Papadopoulos *et al.*, 2000; Cisternas *et al.*, 2005; Peters *et al.*, 2007; Goff & Chagué-Goff, 2014; National Geophysical Data Center, 2019). Studies of recent and known historic tsunami deposits have led to the development and recognition of specific identification proxies onshore (Dawson & Stewart, 2007; Morton *et al.*, 2007; Chagué-Goff *et al.*, 2011, 2017; Goff *et al.*, 2012; Shanmugam, 2012; Costa *et al.*, 2015). Yet, in shallow marine environments, there are still few proxies that are unanimous. This is the result of a relative paucity of identified historic tsunami backwash deposits, hence the need for extending the tsunami backwash deposits database.

A limiting factor to the identification of paleotsunami deposits is their preservation. Indeed, tsunami deposits are usually emplaced in a narrow coastal band, from a few kilometers onshore (coastal plains and lagoons) to a few kilometers offshore (nearshore domain with shallow water depths) (Costa *et al.*, 2015). However, the shoreface and to a lesser extent the upper offshore are highly dynamic and are often subject to intense erosion due to waves, currents or sometimes to anthropization, thus leading to a low preservation potential (Weiss & Bahlburg, 2006; Costa *et al.*, 2015). Thus, it is crucial to find study zones with a higher preservation potential where event deposits may be ideally preserved. Such conditions are more likely to be found in sheltered shallow marine environments. However, compared to onshore deposits, there have been fewer studies focusing on tsunami backwash deposits (Van Den Bergh *et al.*, 2003; Le Roux & Vargas, 2005b; Abrantes *et al.*, 2008; Sugawara *et al.*, 2009; Srinivasalu *et al.*, 2010; Smedile *et al.*, 2012; Veerasingam *et al.*, 2014; Sakuna-Schwartz *et al.*, 2015; Tchernov *et al.*, 2016), especially in low hydrodynamic

6. Offshore evidence for historic tsunamis on the north shore of Tutuila (American Samoa)

settings offering a high preservation potential (e.g. Takashimizu and Masuda, 2000; Fujiwara and Kamataki, 2007; Riou *et al.*, 2018; Submitted).

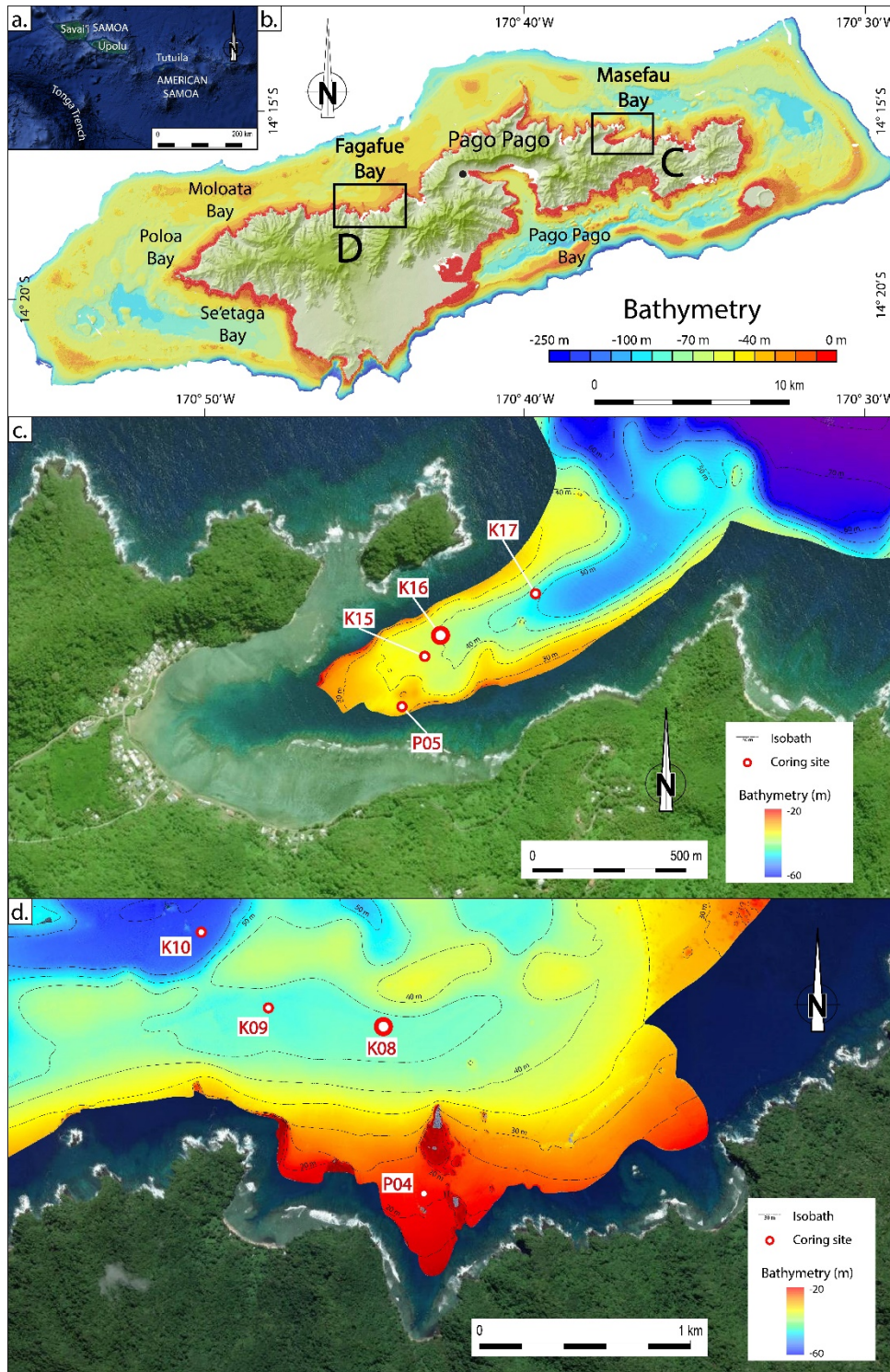


Figure 6.1: a. Location of American Samoa and Tutuila in the southwest Pacific Ocean (modified from Google Earth); b. map of Tutuila with bathymetric data (modified from NOAA, 2018); c. map of Masefau Bay with 1 m-high resolution bathymetric data acquired and cores collected during the SAMOA-SPT campaign; d. map of Masefau Bay with 1 m-high resolution bathymetric data acquired and cores collected during the SAMOA-SPT campaign.

Tutuila (American Samoa) is a volcanic island located in the south-west Pacific (Figure 6.1.a). Its highly indented coastline offers numerous sheltered bays (Figure 6.1.b) ideal for the preservation of tsunami backwash deposits (Riou *et al.*, 2018; submitted). The island is recurrently struck by tsunamis originating from all parts of the Pacific Ocean (Pararas-Carayannis & Dong, 1980; National Geophysical Data Center, 2019), the latest and most destructive known one being the 2009 South Pacific Tsunami (SPT) (Dominey-Howes and Thaman, 2009; Jaffe *et al.*, 2010; Fritz *et al.*, 2011; Richmond *et al.*, 2011; National Geophysical Data Center, 2019). Previous studies in Pago Pago Bay (Figure 6.1.b), a sheltered bay on the south coast of Tutuila have shown that the two major recent tsunamis, the 2009 SPT and the 1960 Great Chilean Earthquake Tsunami (GCET), have left discrete backwash deposits in the shallow marine sediment record (Riou *et al.*, submitted). Here we present a multiproxy analysis of two cores in two bays on the north coast of Tutuila (Figures 6.1.c and 6.1.d) presenting sedimentary evidence of past historic tsunamis, including the 2009 SPT. Together with backwash deposits of the 2009 SPT identified in Pago Pago Bay (south coast Tutuila) (Riou *et al.*, submitted), it is the first time offshore backwash deposits of one specific event are identified and correlated all around an island.

6.4 Study area and setting

The Samoan archipelago is located in the south-west Pacific Ocean, at the northern end of the Tonga Trench (Figure 6.1.a). It is a 1 200 km-long volcanic hotspot trail (Hawkins & Natland, 1975), with the oldest island in the west, Savai'i, formed 5 Ma ago (Koppers *et al.*, 2008). The hotspot trail extends east in a series of volcanic islands evolving into underwater seamounts near the present-day hotspot location. Tutuila is the third largest island of the archipelago and the largest of American Samoa. It was formed about 1.5 Ma ago by five shield-building volcanoes dominated by alkalic olivine basalts (Hawkins & Natland, 1975), characterized by high TiO_2 and MgO but low CaO (Natland, 1980). The calderas formed by these volcanoes were then eroded and collapsed, resulting in the current morphology of the island, with deep, narrow and sheltered bays ending in amphitheater heads with steep slopes, such as Masefau Bay (Figure 6.1.b). The shield volcanoes are overlain by Pleistocene post-erosional volcanic formations, dominated by olivine nephelinites and basanites (Hawkins & Natland, 1975; Natland, 1980). They are also characterized by high TiO_2 and MgO , and low CaO content (Natland, 1980). Masefau Bay is a sheltered bay located on the north shore of Tutuila (Figure 6.1.c). It is approximately 1.5 km long by 700 m wide and oriented diagonal to the coastline. It owes its morphology only to the erosion of volcanic structures and has no major

6. Offshore evidence for historic tsunamis on the north shore of Tutuila (American Samoa)

fluvial tributary. Unlike Pago Pago Bay, which is the biggest bay and home to the main harbor of the island, the head of Masefau Bay hosts only a few houses. Likewise, Fagafue Bay is located on the north shore of Tutuila (Figure 6.1.d). However, it is a widely open bay. It has no major fluvial tributary and no anthropic activity.

Due to its location in the middle of the Pacific and near the northern end of the Tonga Trench, Tutuila is an ideal study zone to investigate tsunami deposits. In the last 100 years or so, at least four major tsunamis have reportedly hit Tutuila, in 1917, 1957, 1960 and 2009 (Pararas-Carayannis & Dong, 1980; NGDC, 2018). Backwash deposits of the two most recent ones, the 2009 SPT and the 1960 GCET, were identified in Pago Pago Bay (Riou *et al.*, submitted). The 2009 SPT was generated by an 8.1 earthquake at the northern extremity of the Tonga Trench, less than 200 km off the coast of Tutuila (Okal *et al.*, 2011). The first wave in Tutuila reached a maximum height of 10 m on the northern coast, in Poloa and Fagasa bays, and reached a height of 5 m in Fagafue Bay and 4 m in Masefau Bay (Fig. 1.b) (Fritz *et al.*, 2011). The runup reached a maximum of 18 m in Poloa Bay, with 12 m near Fagafue and 6 m in Masefau (Fritz *et al.*, 2011). The 1960 GCET was generated by the most powerful historic earthquake ever instrumentally-recorded, the 1960 Valdivia earthquake, with a magnitude of 9.5. The tsunami hit Tutuila with waves reaching a maximum height around 4 m in Pago Pago Bay where a 2.4 m run-up maximum height was reported (NGDC, 2018). No data on wave height or run-up altitude was found for the north coast of Tutuila. The 1957 AIT (Aleutian Islands Tsunami) was generated by a magnitude 8.6 earthquake in the western Aleutian Islands (Johnson *et al.*, 1994). Maximum run-up heights reaching 1.5 m were reported in Fagasa, on the north shore of Tutuila (NGDC, 2018). The earliest of these four reported major tsunamis is the 1917 Tonga Trench Tsunami (TIT). It was triggered by a magnitude 8.7 earthquake near the northern end of the Tonga Trench, just over 200 km off Tutuila (Okal *et al.*, 2011). The epicenters of the 1917 and 2009 earthquakes are distant by approximately 150 km. Very little to no reports of tsunamis were found or preserved prior to early 1900's and sedimentological records of tsunamis prior to the 1960 GCET are still rare in the Samoan Islands (Williams *et al.*, 2011a; 2011b).

6.5 Material and methods

6.5.1 Dataset

This work was completed following the acquisition of a large and exhaustive dataset from the SAMOA-SPT oceanic campaign around the island of Tutuila. This campaign, carried out between August 27th and September 10th 2015 aboard the R/V *Alis*, included bathymetric and seafloor reflectivity surveys and sediment core sampling.

6.5.1.1 Bathymetry

Seafloor bathymetry was acquired using an EM1002 multibeam echo-sounder (Kongsberg Maritime), with a frequency of 95 kHz. The depth range covered by this device is from 5 to 1 000 m, which makes it a good choice for coastal zones. A raw bathymetric survey of approximately 75 km² was obtained on the north coast of Tutuila, covering most bays including Fagafue and Masefau (Figures 6.1.c and 6.1.d). Raw data was processed using the CARAĪBES (CARtography Adapted to Imagery and BathymEtry of Sonars and multibeam echo-sounders) software developed by IFREMER. This processing consisted of tide and wave corrections, followed by elimination of bias due to irrelevant celerity variations in the water column. The processed data was then exported as a 1 m-resolution DEM (Digital Elevation Model).

6.5.1.2 Cores

A total of eight cores were collected in the bays of Fagafue and Masefau. Two different devices were used for this purpose. For each bay, three Kullenberg cores and one short interface core taken using a hand-held manual corer were retrieved (Figures 6.1.c and 6.1.d). The Kullenberg coring system uses a piston allowing greater penetration in soft sediment, while the hand-held manual corer is driven by divers and has a maximum penetration of a few tens of centimeters. In this study, two 150 cm-long Kullenberg cores (one in each bay) with the best potential, based on the coring site location and morphologic characteristics, grain size and observable sedimentological patterns, were analyzed.

6.5.2 Methods

6.5.2.1 Sedimentological and geochemical analysis

All cores were split in one working half and one archive half, photographed and logged. Grain size analysis was conducted on the two selected cores. Sediment samples were collected every centimeter and analyzed using a Malvern Mastersizer S laser particle size analyzer (Malvern Panalytical Ltd.). Statistical analysis was performed using the Gradistat 8.0 (Kenneth Pye Associates Ltd.) software and grain size distribution was calculated using a MATLAB routine developed at the University of Bordeaux. Geochemical analysis was carried out with XRF (X-Ray Fluorescence) using an Avaatech XRF core scanner (Avaatech XRF Technologies). Two runs per core were made with a 1 mm measuring step in order to obtain the full element spectrum. The first run was set at 10 kV and 1 500 μ A (light elements) and the second run at 30 kV and 2 000 μ A (heavy elements).

6.5.2.2 ^{14}C dating

A total of seven samples were collected from both cores and dated at the Accelerator Mass Spectrometry (AMS) facility of the Poznan Radiocarbon Laboratory (Poznan, Poland). Dated samples were of three types (Figure 6.2): *Halimeda* (algae) calcified plates, benthic foraminifers and wood fragments. When possible, samples were collected above and below anomalous layers. When it was not possible, samples were collected where calcified material was found. Results received were given either in raw dates BP (Before Present) for samples older than 1950 or in pMC (present Modern Carbon) for sample younger than 1950. For samples older than 1950, age calibration was achieved using the OxCal 4.3 software (Bronk Ramsey, 2009a; <https://c14.arch.ox.ac.uk/oxcal/OxCal.html>) coupled with the Marine13 calibration curve (Reimer *et al.*, 2013). This curve applies a global age correction of about 400 years to take into account the reservoir effect of marine samples. This reservoir effect is due to the equilibrium between atmospheric and ocean water ^{14}C , and gives apparent ages which are roughly 400 years older for marine samples (Stuiver *et al.*, 1986). To this global reservoir age correction, a local component ΔR is added to reflect the local variations such as deep ocean upwelling or other local effects. Here, a ΔR of 28 ± 26 years was used (Petchey *et al.*, 2008; Clark *et al.*, 2016). All ^{14}C ages in this study are calibrated and expressed as calendar years (AD), and are given as an interval corresponding to the 68.3 % confidence interval (1 sigma).

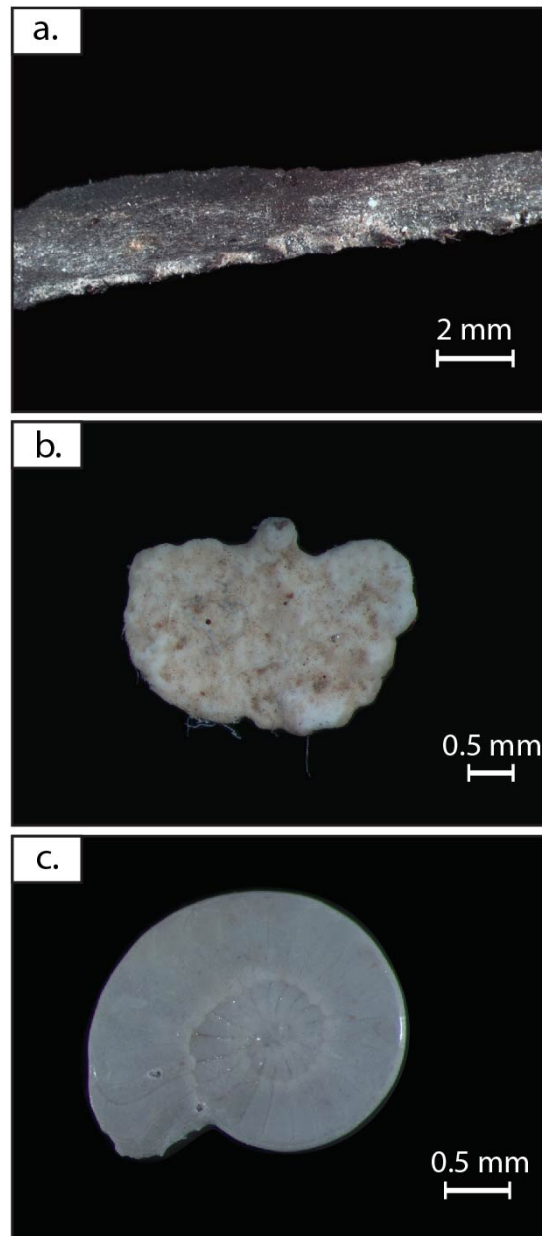


Figure 6.2: a. Photograph of vascular plant debris found in core K08 (14 cm, see Table 6.1 for details) and dated for radiocarbon; b. photograph of *Halimeda* calcified plates sampled in core K16 (82 cm, see Table 6.1 for details) and dated for radiocarbon; c. photograph of *Operculina Ammonoides* sampled in core K08 (69 cm, see Table 6.1 for details) and dated for radiocarbon.

6.5.2.3 ^{210}Pb and ^{137}Cs dating

The age models of the two Kullenberg cores over the last century were based on excess ^{210}Pb ($^{10}\text{Pb}_{\text{xs}}$; $T_{1/2} = 22.3$ years) and ^{137}Cs ($T_{1/2} = 30$ years) depth profiles. We determined activities of ^{210}Pb , ^{226}Ra , ^{232}Th and ^{137}Cs on sediment samples by gamma spectrometry using a Broad Energy germanium detector (Mirion; Schmidt and De Deckker, 2015). The coarse carbonate fraction was removed by sieving to avoid changes in activities due to dilution. The detector was calibrated using

IAEA reference material. Activities are expressed in mBq.g^{-1} and errors are based on one standard deviation counting statistics. Excess ^{210}Pb was calculated by subtracting the activity supported by its parent isotope, ^{226}Ra , from the total ^{210}Pb activity in the sediment. Sediment layers were measured downcore until reaching rather negligible excesses.

6.6 Results

6.6.1 Sea-floor bathymetry

Fagafue Bay is an open bay (Figure 6.1.c), protected from ocean waves and currents only by the outer reef barrier. In the shallow nearshore part of the bay, down to the 35 m isobath, a few mounds, likely reef mounds, are present. Less than 1 km off the coast, a roughly 1.5 km long, 500 m wide and 5 to 10 m deep (relative to the surrounding seafloor) trough is west-east oriented. This mini-basin reaches a maximum water depth of 49 m and is limited to the south by the Fagafue Bay sediment-fill and to the north by a west-east oriented ridge, culminating at 37 m water depth. Core K08 was sampled in this mini-basin at 47 m depth, inferred to offer a sheltered hydrodynamic setting near the seafloor, beyond the wave base.

Unlike Fagafue, Masefau Bay is a very narrow and more sheltered bay (Figure 6.1.d). At the mouth of the bay, a 5 to 10 m topographic high isolates the inner bay from the outer bay, delineating a small basin in the bay, ideal for seafloor sediment preservation. In the inner part of the bay, the seafloor morphology is marked by a bank suggesting a prograding sediment-fill. This bank is interrupted by occasional mounds, most likely reef mounds, down to 45 m depth. Core K16 was collected at the seaward edge of the bank, at 40 m depth.

6.6.2 Cores

Two cores, one in each bay, were selected for this study. Both core locations have been selected in the deepest parts of the bay (Figures 6.1.c and 6.1.d), where sediment preservation, below the wave base, was supposed to be maximum. In Fagafue bay, core K08 was sampled in a small trough at 47 m water depth. In Masefau bay, core K16 was sampled at 40 m water depth.

6.6.2.1 Sedimentological and grain size analysis

Visually, core K08 appears composed of relatively homogeneous fine sediment, with slightly darker intervals found occasionally (around 10-20 cm and 70-85 cm depth, Figure 6.3). No major erosional surface can be observed. However, grain size distribution obtained from laser particle size analyzer reveals major grain size variations (Figure 6.3). Throughout most of the core, grain size is very well sorted and falls in the thin sand category, with a very narrow distribution around 100 μm , interrupted by at least three intervals with different grain size signatures, named from top to bottom EL1, EL2 and EL4 (Figure 6.3):

- EL4 is observed between 66 and 88 cm. It is characterized by poorly sorted sediment, with a sharp contact and a normal graded base followed by a reverse graded top. The base and top of this layer are coarser than the background sediment while the center is finer. This grading trend is also observed in the mean grain size. Sediment from EL4 is darker than the background sediment.
- EL2 is observed between 22 and 25 cm. This layer is more poorly sorted than the background sediment, with a slight reverse grading revealed by the mean grain size. There is no change in the color of the sediment in EL2 in comparison with the background sediment.
- EL1 is observed between 5 and 18 cm. It is characterized by a sharp contact and a reverse grading with a poorly sorted, fine sand base and a well sorted coarse sand top. A thin level of reworked vascular plant debris is found near the base of this layer (13 cm, Figure 6.2.a). Visually, sediment from EL1 is darker than the background sediment at the base of the layer (10-18 cm).

Below the deepest anomalous layer (from 90 cm down to the base of the core), sediment is mostly well sorted, but the mean grain size alternates between coarse (up to 350 μm) and fine sediment.

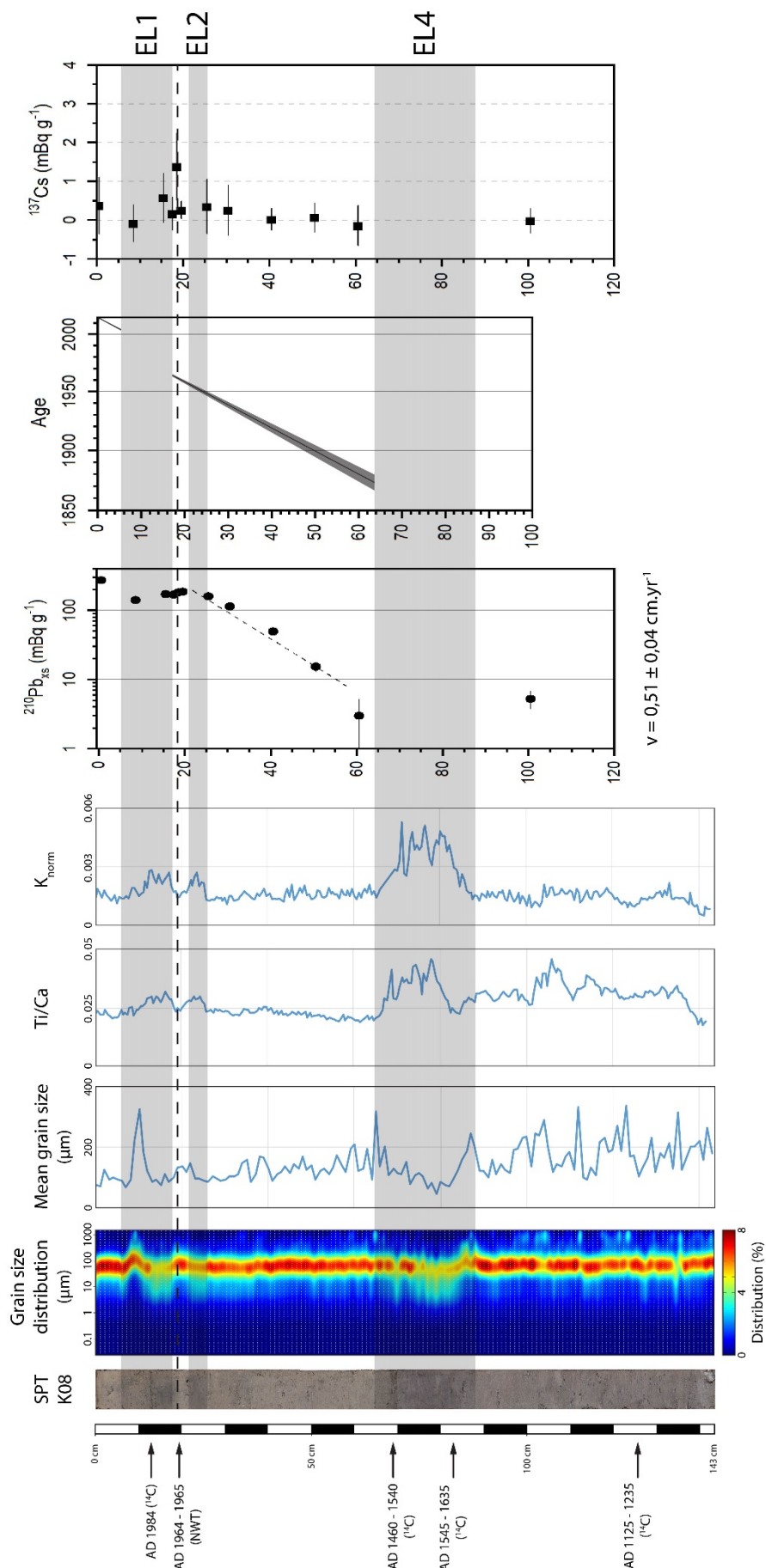


Figure 6.3: Multi-proxy analysis of core K08; from left to right, respectively, ages obtained by radiocarbon dating, photograph of the core, grain size distribution, mean grain size, Ti/Ca ratio, K_{norm} ratio, excess ^{210}Pb activities, age model and ^{137}Cs activities; grey shaded bars represent anomalous layers EL1, EL2 and EL4; NWT: Nuclear Weapon Tests.

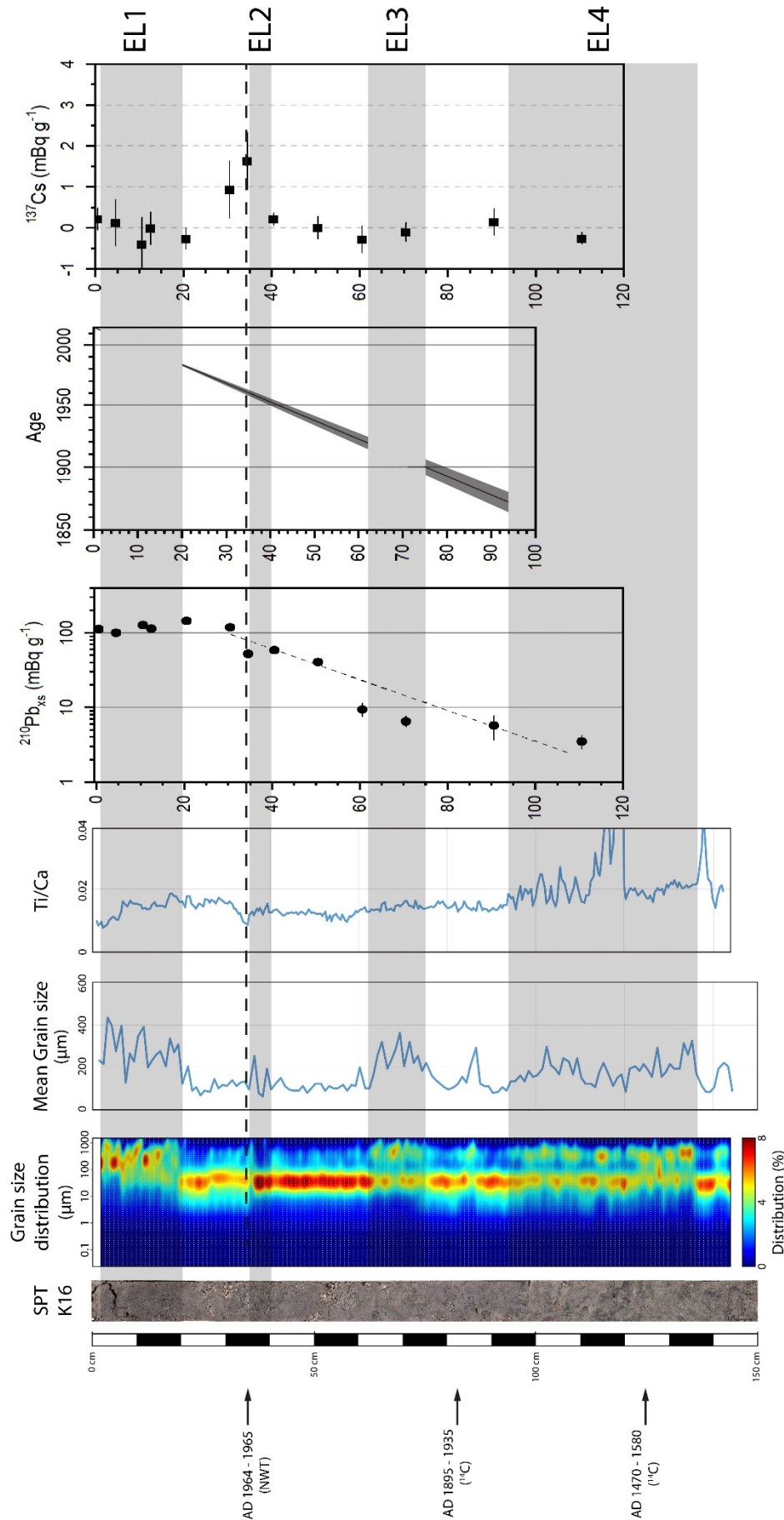


Figure 6.4: Multi-proxy analysis of core K16; from left to right, respectively, ages obtained by radiocarbon dating, photograph of the core, grain size distribution, mean grain size, Ti/Ca ratio, excess ^{210}Pb activities, age model and ^{137}Cs activities; grey shaded bars represent anomalous layers EL1, EL2, EL3 and EL4; NWT: Nuclear Weapon Tests.

Unlike core K08, core K16 seems more heterogenous and chaotic. Slightly darker and coarser sediment can be seen around the base (110-120 cm) and top (10-20 cm) of the core (Figure 6.3). This trend is confirmed by the mean grain size and grain size distribution, with a well distinguishable stratification (Figure 6.4). The background sediment is characterized by well to very well sorted grain size distribution around 60 μm . In addition, abundant *Halimeda* plates are mixed with this well sorted sediment. The background sediment is interrupted by at least four anomalous intervals based on grain size, named from top to bottom EL1, EL2, EL3 and EL4 (Figure 6.4):

- EL4 is observed between 95 and 135 cm and is correlated with discontinuous darker sediment layers. It is characterized by a very poorly sorted, coarser, bimodal sediment with a sharp basal contact. A first grain size mode, similar to that of the background sediment around 60 μm , stands out from a second coarser mode, around 300 μm . This trend is easily noted in the mean grain size as a sharp grain size coarsening. Few *Halimeda* plates are found in this layer. Visually, EL4 shows discontinuous dark sediment layers in the middle alternating with lighter sediment.
- EL3 is observed between 63 and 75 cm. It shows the same coarse and bimodal signature with sharp basal contact as the underlying anomalous layer (EL4). Few *Halimeda* plates are found in this layer.
- EL2 is observed between 36 and 40 cm. It is only characterized by a slight grain size coarsening revealed by the mean grain size. Few *Halimeda* plates are found in this layer.
- EL1 is observed from the top to 20 cm down the core and is correlated to a darker sediment interval. It is characterized by a very poorly sorted sediment layer and a very sharp grain size coarsening at base. Few *Halimeda* plates are found in this layer.

6.6.2.2 Geochemical analysis

Geochemical analyses using XRF presented in this study are focused mostly around titanium (Ti) and calcium (Ca). Indeed, the geochemical composition of the volcanic rocks constituent of Tutuila is characterized by a high titanium content and a low calcium content (Hawkins & Natland, 1975; Natland, 1980), while the marine seafloor is dominated by calcium (Morrison *et al.*, 2010). Given this duality in the geochemical composition between the onshore and marine sediment, titanium and calcium are the most eligible components in order to understand the variations of sediment source, as have shown previous studies in Pago Pago Bay (Riou *et al.*,

2018; Riou *et al.*, submitted) or Upolu (Chagué-Goff *et al.*, 2017). These elements are shown as the Ti/Ca ratio for both cores. In addition, potassium normalized to the total number of counts (K_{norm}) is used in core K08 as a tracer for onshore clay input (Morrison *et al.*, 2010).

In core K08, the Ti/Ca ratio in the upper 90 to 100 cm shows a steady background level throughout, interrupted by three major peaks very well correlated with anomalous grain size layers EL1, EL2 and EL4 (Figure 6.3). A very sharp peak occurs in EL4 between 66 and 84 cm and is very sharp. The second peak, less marked, is found in EL2 between 22 and 25 cm. The uppermost peak is found in EL1 between 5 and 18 cm. It has a well-marked base and decreases slowly to the background value. These peaks are very well correlated with very sharp peaks when looking at the K_{norm} . Below 90 cm, as for the grain size, the background level for the Ti/Ca ratio is higher and at least one short peak can be observed, where the K_{norm} stays low and constant, equal to the background level found above 90 cm.

Core K16 can be divided into two main parts when looking at the Ti/Ca ratio along the core (Figure 6.4). In the lower part of the core, corresponding to EL4, from the base to 92 cm, the Ti/Ca ratio is high and two major peaks are observed. In the upper part, from 92 cm to the top, the ratio is lower and varies in lesser proportions, but several short and more or less marked peaks and increases are observed. These variations in the lower part of the core can be correlated for some of them with anomalous grain size layers EL1, EL2 and EL3 (Figure 6.4). In the lower half of the core, the deepest of the two major peaks is found at 135 cm, at the base of EL4. It is a very narrow but strong peak. The second major peak is found between 92 and 120 cm and corresponds to the upper half of EL4. It has a very sharp increase at the base, and decreases slowly to the top. In the upper part of the core, the ratio is high from 92 to 60 cm where it decreases rapidly. A few short peaks can be noted between 65 and 75 cm, corresponding to EL3. Just above, increases slowly, with a short but marked peak between 36 and 40 cm, corresponding to EL2. A narrow drop separates this peak from another high Ti/Ca ratio interval, from 33 to 7 cm. This interval is punctuated by a few poorly marked peaks around 15 to 20 cm, at the base of EL1. Finally, the Ti/Ca value drops sharply from 7 cm to the top, which corresponds to the top of EL1. In this core, the K_{norm} does not show significative variations correlated with the Ti/Ca ratio.

6.6.2.3 Chronology

Three dating methods based on radionuclides, ^{210}Pb , ^{137}Cs and ^{14}C , were used to set the geochronological frame. First, decrease of $^{210}\text{Pb}_{\text{xs}}$ activity with depth was used to estimate mean sedimentation rate of the two investigated cores. In core K08, the $^{210}\text{Pb}_{\text{xs}}$ profile can be divided

6. Offshore evidence for historic tsunamis on the north shore of Tutuila (American Samoa)

into three domains (Figure 6.3). In the uppermost layer, the activity is, as expected, the highest (272 mBq.g^{-1}). Then, between 4 and 17 cm, the activities are much lower (around $140 - 150 \text{ mBq.g}^{-1}$), corresponding to EL1. Just below this first anomalous layer, there is a slight increase of $^{210}\text{Pb}_{\text{xs}}$ followed by an exponential decrease to reach negligible activities of 5 mBq.g^{-1} below 60 cm. To avoid the error of the determination of the thickness of the anomalous layers, we used the $^{210}\text{Pb}_{\text{xs}}$ profile section between 18 and 50 cm. The constant ^{232}Th activities (a long-lived and naturally-occurring radionuclide usually associated with the detrital fraction; around 5 mBq.g^{-1} , not shown) in this section, after event layers are subtracted, indicates the absence of changes in lithological sources or proportions, implying that the changes with depth of $^{210}\text{Pb}_{\text{xs}}$ activity are mainly related to the radioactive decay of ^{210}Pb . A mean sedimentation accumulation rate (SAR) of $0.51 \pm 0.04 \text{ cm.yr}^{-1}$ was calculated, assuming constant flux and constant sedimentation (referred to as the CF:CS model) (Figure 6.3). The deposition time of each sediment layers, in years and excluding the anomalous layers, was estimated by dividing the depth by the mean SAR, assuming the top of the core to be 2015. This age vs. depth model was then corroborated with the ^{137}Cs and ^{14}C (Figure 6.3). There is a slight increase of ^{137}Cs in subsurface, that we ascribe to the maximum atmospheric fallout (1965) in the southern Hemisphere (Quintana, 2011). In addition, four radiocarbon ages were obtained in this core (Figure 6.3, Table 6.1): in EL1, 1956-1960 AD (14 cm), in EL4, 1460-1540 AD at the top (69 cm) and 1545-1635 AD at the base (83 cm); and at the base of the core, 1125-1235 AD (125 cm).

Table 6.1: Radiocarbon dating data for core K08 and K16; calibration was made using OxCal 4.3 software (Bronk Ramsey, 2009a; <https://c14.arch.ox.ac.uk/oxcal/OxCal.html>) with an integrated calibration curve; the 1 sigma interval corresponds to the 68.3 % confidence age interval (age uncertainty) and the 2 sigma interval to the 95% confidence age interval.

Core	Sample	Depth (cm)	Material	Conventional age (years BP)	Calibrated age (1 sigma)	Calibrated age (2 sigmas)
K08	SPT20	14	Plant debris (Fig 2.a)	$120.77 \pm 0.35 \text{ pMC}$	1956-1960 AD	-
K08	SPT21	69	Foraminifera (Fig 2.b)	830 ± 30	1460-1540 BP	1445-1620 BP
K08	SP122	83	<i>Halimeda</i> plates (Fig 2.c)	740 ± 30	1545-1645 BP	1500-1670 BP
K08	SP123	125	Foraminifera (Fig 2.b)	1260 ± 30	1125-1235 BP	1070-1270 BP
K16	SPT24	82	<i>Halimeda</i> plates (Fig 2.c)	300 ± 35	1895-1935 BP	1865-1950 BP
K16	SP125	125	<i>Halimeda</i> plates (Fig 2.c)	805 ± 30	1470-1580 BP	1460-1640 BP

In core K16, the top 20 cm, corresponding to EL1, present activities around 115 mBq.g^{-1} . As observed for the core K08, this layer is depleted in $^{210}\text{Pb}_{\text{xs}}$, compared to the sediment just under EL1 (20 cm). Deeper than 20 cm, $^{210}\text{Pb}_{\text{xs}}$ presents a rather regular exponential decrease, associated with constant ^{232}Th (around 2.6 mBq.g^{-1}). It is noticeable that, between 60 and 75 cm, corresponding to EL3, the excesses are slightly lower. As for core K08, we retained the sections of the profiles below the layer EL1 to estimate a mean sedimentation rate of $0.69 \pm 0.16 \text{ cm.yr}^{-1}$ using

the CFCS model for core K16. The peak of ^{137}Cs activity at 34 cm depth validates the age depth $^{210}\text{Pb}_{\text{ex}}$ model (Figure 6.4). For core K16, two radiocarbon dates were obtained (Figure 6.4, Table 6.1): 1895-1935 AD just below EL3 (82 cm), and 1470-1580 AD in EL4 (125 cm).

6.7 Discussion

6.7.1 Origin of anomalous layers

Based on grain size and XRF analysis, between three and four anomalous layers were identified in both cores K08 and K16 from Fagafue and Masefau, respectively (Figures 6.3 and 6.4). Despite the different setting in which each core was collected, these layers share some sedimentological and geochemical similarities. All of these layers have a poorer grain size sorting compared to the background sediment, associated in most cases with a general mean grain size coarsening, and correspond to darker sediment. For core K16, the grain size is significantly coarser in these anomalous layers with a bimodal distribution. All these characteristics can be interpreted as instantaneous high-energy event deposits, mixed with the background sediment. Such high-energy deposits can be related to great storms or cyclones, which can generate strong waves or flash-floods, but also volcanic eruptions or tsunamis (Scheffers & Kelletat, 2004; Tappin, 2007; Eychenne *et al.*, 2012). The finer sediment can be interpreted as autochthonous sediment of the lower to upper shoreface, similar to that of the background sedimentation, while the coarser sediment would be allochthonous. This allochthonous sediment is most likely sourced from the coastal plain and nearshore area, which are the main sources of coarse sediment.

In addition, these sedimentological variations coincide with more or less perceptible increases of the Ti/Ca ratio and K_{norm} . As mentioned in previous studies in Pago Pago Bay, Tutuila (Riou *et al.*, submitted) and Upolu (Chagué-Goff *et al.*, 2011), titanium originates from the Ti-rich volcanic rocks composing Tutuila and more widely the samoan archipelago, while calcium is mostly found in bioconstructed marine carbonates all along the coastline. Thus, the Ti/Ca ratio reflects the terrestrial-to-marine ratio: an increase in the Ti/Ca ratio translates in an increase of terrestrial input, and inversely. As for titanium, potassium is a marker of terrestrial input. It is found mostly in terrestrial clay formed through weathering of the volcanic rocks. Both the Ti/Ca and K_{norm} increases in the anomalous layers attest of an intensification in the terrestrial input, which explains the darker color of the sediment in layers EL1 and EL4 in both cores. In comparison, the background sediment is largely marine influenced due to the absence of major fluvial tributaries in

both Fagafue and Masefau bays and dominated by carbonate-derived sediment, which results in a general low Ti/Ca and K_{norm} trend. This geochemical signature confirms that these anomalous layers EL1, EL2, EL3 and EL4 encountered in both cores K08 and K16 have a different source from the background sedimentation, with a high increase in terrestrial input. Thus, they are interpreted as event deposits and indicate a seaward transport of the sediment. This is also confirmed by the lower $^{210}\text{Pb}_{\text{xs}}$ activity found in layers EL1 to EL4, which reveals the presence of older reworked sediment, or originating from a shallower source, in the layers. Based on the terrigenous signature, the geodynamic context of Tutuila island and similar event layers encountered in a previous study in Pago Pago Bay attributed to recent tsunami backwash deposits following the 2009 SPT and the 1960 GCET (Riou *et al.*, submitted), event layers EL1 to EL4 can be either interpreted as tsunami backwash deposits or cyclone-related flash-flood deposits (Srinivasalu *et al.*, 2010; Sakuna *et al.*, 2012; Pongpiachan *et al.*, 2013a; Veerasingam *et al.*, 2014; Sakuna-Schwartz *et al.*, 2015). However, the grain size distribution of the cores display poor to very poor sorting in both cores and a bimodal trend in core K16. According to Sakuna-Schwartz *et al.* (2015), flash-flood deposits are characterized by a finer grain size when compared to tsunami backwash deposits. More specifically flash-flood deposits display a very good grain size sorting (Sakuna-Schwartz *et al.*, 2015) whereas tsunami deposits are poorly sorted and may sometimes display a bimodal grain size trend (Paris *et al.*, 2007; Tappin, 2007). Thus, event layers EL1, EL2, EL3 and EL4 were most likely emplaced following a tsunami backwash.

6.7.2 Dating of the backwash deposits

For the elaboration of the age model, event layers EL1, EL3 and EL4 were considered separately from layer EL2 (Figures 6.2 and 6.3). Event layers EL1, EL3 and EL4, which are thicker with sharp basal contact and show pronounced grain size, color, geochemical and/or $^{210}\text{Pb}_{\text{xs}}$ activity variations, are interpreted as instantaneous and erosive event deposits. Thus, they were subtracted in order to build an event-free sediment record. Layer EL2, which is thinner than EL1, EL3 and EL4, only has a very slight grain size variation, unlike for event layers EL1, EL3 and EL4. It is considered as a mixed layer with both event deposits and background sedimentation, but not as a regular event deposit. Thus, EL2 was not subtracted from the sediment record for the elaboration of the age model. The resulting $^{210}\text{Pb}_{\text{xs}}$ -derived age model, corroborated by ^{137}Cs and ^{14}C data, allowed dating of these event layers and correlation between cores K08 and K16 (Figure 6.5). For each layer, the estimated age corresponds to the date at the top of the layer. EL1, which is the shallowest event layer, is found in both cores. It is dated to 2009 ± 0.5 AD in core K08 and 2009

6. Offshore evidence for historic tsunamis on the north shore of Tutuila (American Samoa)

± 0.4 AD in core K16, and most likely corresponds to the 2009 SPT deposits. It is very thick and is characterized by a significantly coarser grain size trend in both cores. Beneath this layer, the $^{210}\text{Pb}_{\text{xs}}$ activity is lower than directly above in both cores. Since the events are considered instantaneous, this shift in the $^{210}\text{Pb}_{\text{xs}}$ activity indicates that sediment was eroded prior to the deposition of the event layer. Just below the ^{137}Cs activity peak, which is a reference point for 1964–1965 AD (Nuclear Weapons Treaty), EL2 is also found in both cores. It is dated to 1957 ± 1.3 AD in core K08 and 1960 ± 2.3 AD in core K16. Two hypotheses can be proposed as for the event responsible for this event layer: the 1960 GCET or the 1957 AIT. Following the 1960 GCET, waves and inundations were reported across most of the southern Pacific (NGDC, 2018). However, despite the east-to-west propagation direction of the waves (PacificTWC, 2016) no inundation was reported in the northern bays of Tutuila (NGDC, 2018). The 1957 AIT impacted less severely the islands in the southern Pacific (NGDC, 2018). However, probably due to the north-to-south propagation direction of the waves, a 1.5 m run-up was reported in Fagasa (NGDC, 2018), just a few kilometers east from Fagafue Bay. Therefore, EL2 may correspond either to the 1960 GCET or 1957 AIT deposits. In both cores, it is a very thin and discrete layer characterized only by a short Ti/Ca and K_{norm} peak in core K08 and by a slightly coarser mean grain size in core K16. EL3 is found only in core K16 and is dated to 1920 ± 5.1 AD. It most likely corresponds to the 1917 TTT initiated by the Tonga Trench earthquake and is only found in core K16. It is characterized by a bimodal grain size distribution, with the presence of a second coarser mode in addition to the fine background marine sediment mode, inducing a sharp mean grain size increase. As for EL1, the $^{210}\text{Pb}_{\text{xs}}$ activity beneath this event layer is significantly lower than above, which indicates substantial erosion prior to the deposition of EL3. Finally, based on the $^{210}\text{Pb}_{\text{xs}}$ -derived age model, EL4 is dated at 1870 ± 8.2 AD in core K08 and at 1878 ± 8.1 AD in core K16. However, reworked sediment from EL4, dated using radiocarbon in both cores, all give ages in a range from 1460 AD to 1635 AD.

6. Offshore evidence for historic tsunamis on the north shore of Tutuila (American Samoa)

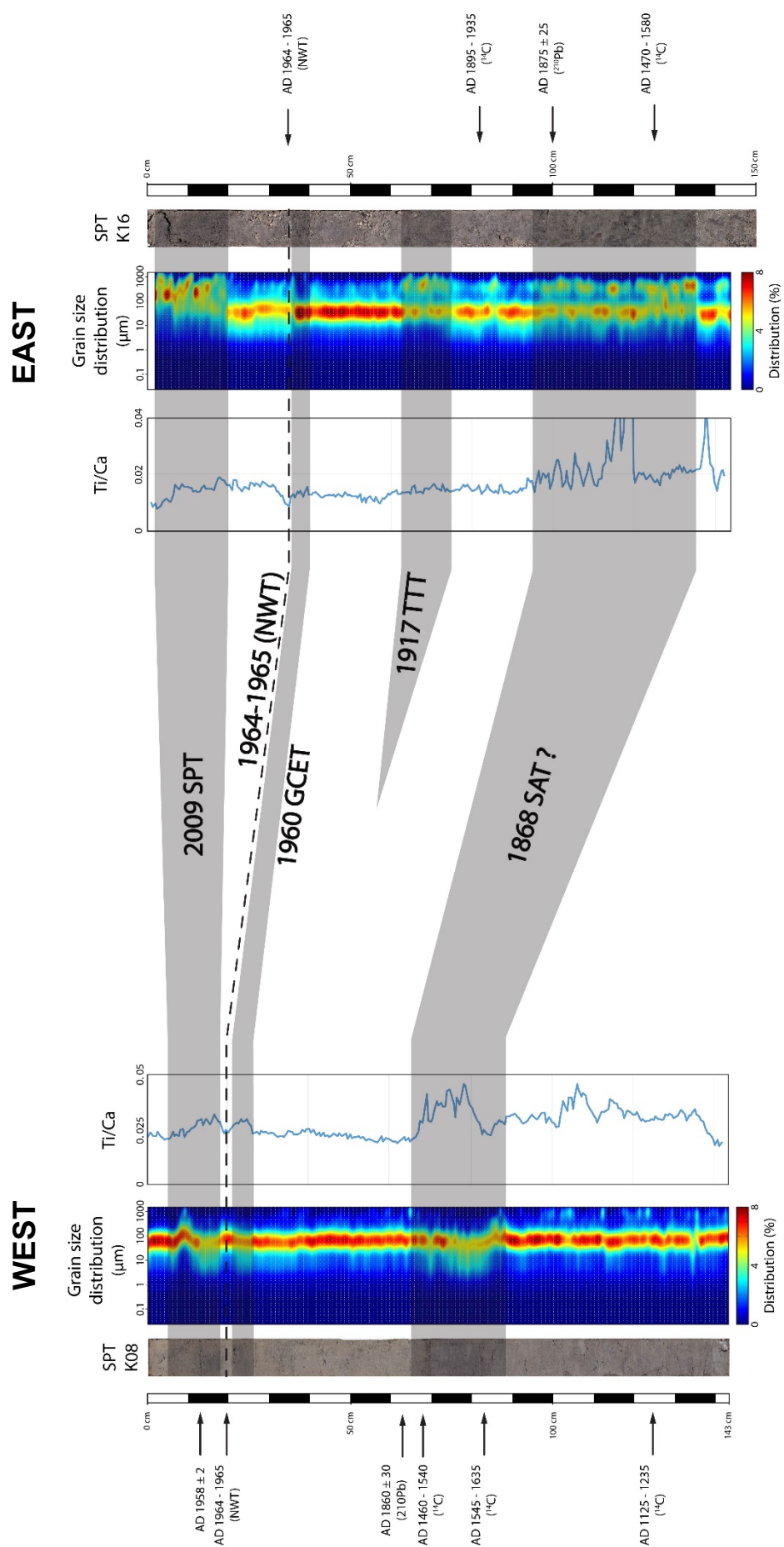


Figure 6.5: Correlation of event layers deposited following the 2009 SPT, the 1960 GCEET/1957 AIT and the 1868 SAT between the bays of Fagafue (K08) and Masafau (K16), based on sedimentological and geochemical characteristics and ^{210}Pb and ^{14}C dating.

6.7.3 Potential events for EL4

Based on the two age ranges given by the ^{210}Pb and ^{14}C dating methods for event layer EL4, two hypothetical ages can be expected for the associated tsunami: a tsunami occurring during the second half of the 19th century, or an older prehistoric tsunami. In both cases, the event responsible for EL4 deposits predates any known or reported tsunami event in Tutuila, which can be traced back no further than the end of the 19th century. The first hypothesis, relying on ^{210}Pb dating, suggests that EL4 was emplaced by a major tsunami backwash dated around the 1870's. Thus, radiocarbon ages obtained in EL4 can be justified as being either older autochthonous sediment that was reworked during the tsunami, meaning that at least 300 years of sediment record was eroded during the event, or older allochthonous sediment eroded and dragged from a different shallower or deeper source area. In this case, the most probable candidate for such an event is the 1868 South American Tsunami (SAT) (Goff *et al.*, 2010; Borrero & Goring, 2015). The 1868 SAT was generated offshore the Chile-Peru border by a magnitude 8.5 earthquake. The great amplitude of the tsunami can be explained by the shallow focal point, only 25 km deep in the oceanic crust (National Geophysical Data Center, 2019). The only sedimentological evidence of this tsunami yet found was in New Zealand, Chatham Island by Goff *et al.* (2010). It was considered the biggest known trans-South Pacific tsunami to ever hit New Zealand, with waves consistently twice as high compared to the second biggest trans-south Pacific tsunami, the 1960 GCET, and reaching 10 m maximum height (Goff *et al.*, 2010). It seems very likely that such a major distant-source tsunami also struck the samoan islands, only 3000 km north of New Zealand, and was recorded in shallow nearshore domains that are the Fagafue and Masefau bays. Modeling of the propagation and amplitude of the 1868 SAT through the south Pacific shows that it should have hit the Samoan Islands with a wave amplitude approximately 0.5 to 1 m in open sea (eCoast, 2018, <https://www.ecoast.co.nz/tsunami-of-august-1868/>; <https://www.youtube.com/watch?v=-Lv8aWhaeo8&feature=youtu.be>). In addition, the 1868 SAT was reported to have caused considerable damage on the islands of Upolu and Savaii (Samoa), with waves reaching a height at least 5 m (Pararas-Carayannis & Dong, 1980; National Geophysical Data Center, 2019). Of the three other tsunami backwash recorded in cores K08 and K16, two have a local source, the 2009 SPT and 1917 TTT, and one has a distant source, the 1960 GCET. When comparing the event layer from the two supposedly far-field tsunamis, the 1960 GCET and the 1868 SAT, the thickness of the layer and the sedimentological and geochemical signature of the terrestrial inputs in the deposits for EL4 dwarf that of the 1960 GCET (EL2). Even when compared to the 2009 SPT, which is a local-source tsunami and the largest known tsunami to have hit Tutuila, EL4 is thicker and the geochemical signature of the

6. Offshore evidence for historic tsunamis on the north shore of Tutuila (American Samoa)

deposits indicate a greater terrestrial input than for EL1. Following these characteristics it is very likely that the event responsible for EL4 is the strongest tsunami that hit Tutuila for the last 150 years at least. The force would have been greater than that of the 2009 SPT, which saw waves reaching a maximum height of 12 m surge on the north coast of Tutuila (Fritz *et al.*, 2011). Based on the intensity of the geochemical terrestrial signature in EL4, the inundation and maximum run-up also would have been more important during this event, scouring a greater amount of terrestrial sediment washed back seaward.

The second hypothesis, relying on radiocarbon dating, suggests that EL4 was emplaced by a major tsunami backwash that could be dated back to as far as the 15th century. Following this hypothesis, ²¹⁰Pb-derived dates are set aside because EL4 is at the limit of ²¹⁰Pb dating capacities. Indeed, the ²¹⁰Pb-derived age model is usually limited to the last 100 to 150 years maximum. For this hypothesis, it is harder to isolate a specific candidate. South Pacific tsunami databases only go back until the end of the 18th century. However, several potentially tsunamigenic South American earthquakes were pointed out by Goff *et al.* (2010), alongside the 1868 SAT, for tsunami risk assessment in New Zealand as possible predecessors to the 1960 GCET. These candidates include paleotsunamis in 1575 AD, 1586 AD, 1604 AD, 1687 AD and 1746 AD. Based on the characteristics of the associated earthquakes, all these paleotsunamis were assumed to be approximately as large as the 1868 SAT (Goff *et al.*, 2010). The 1575 AD tsunami was initiated by an earthquake in the same area as the 1960 GCET and with a similar magnitude (Cisternas *et al.*, 2005). Thus, the 1575 AD tsunami seems unlikely to have been able to emplace deposits as pronounced as EL4 when compared to EL2. Other candidates have a more northern origin, offshore Peru, and could be more credible candidates. They were initiated by earthquakes of magnitude estimated at 8.6 for the 1586 AD tsunami, 8.5-9.0 for the 1604 AD tsunami, 8.5 for the 1687 AD tsunami and 8.0-8.6 for the 1746 AD tsunami (National Geophysical Data Center, 2019). Propagation of South American tsunamis was modelled by Berryman (2005) depending on the location of the epicenter. This study allowed identification of main propagation pathways for the different candidates cited above. As predicted, the main trajectory for the 1575 AD tsunami, as for the 1960 GCET, sends the larger wave amplitudes north of the samoan islands towards the central Pacific. As for the four other candidates, their respective trajectories send the larger wave amplitudes towards the south Pacific Islands. Nevertheless, the 1586 AD, 1687 Ad and 1746 AD tsunamis seem to have a pathway sending the maximum amplitudes straight towards the samoan islands. They would thus be potential candidates. Other candidates include tsunamis generated along the Aleutian Trench (La Selle *et al.*, 2019; Witter *et al.*, 2019), which have a recurrence time for major tsunamis of approximately 200 years (Witter *et al.*, 2019). In particular, one major tsunami

generated along the Aleutian Trench stands out, dated around 1290 to 1390 AD, with geological evidence found in both the Aleutian Islands and Hawaiï (Witter *et al.*, 2016, 2019; La Selle *et al.*, 2019).

Finally, the list of potential candidates responsible for the occurrence of event layer EL4 is narrowed down to four known trans-south Pacific tsunamis (1586 AD, 1687 AD, 1746 AD and 1868 AD) and one prehistoric unidentified Aleutian tsunami (1290-1390 AD), even if other paleotsunamis generated anywhere around the Pacific Ring of Fire cannot be ruled out. Given that they were all induced by major earthquakes of similar magnitudes, we can expect that all these potential candidates would have been recorded in the sediment column in Tutuila. Additionally, the 1868 SAT is known to have impacted New Zealand (Goff *et al.*, 2010) and the Samoan Islands of Upolu and Savai'i (NGDC, 2018). Since EL4 is found just under the event layer corresponding to the 1917 TTT, the most likely candidate for EL4 is the 1868 SAT.

6.8 Conclusion

In this study, we present the tsunami-based history of the north coast of Tutuila Island (American Samoa) through two cores collected in the open bay of Fagafue and the sheltered bay of Masefau. Despite the different hydrodynamic settings between the two study areas, four event layers are identified based on sedimentological, grain size and geochemical criteria and interpreted as tsunami backwash deposits. ^{210}Pb and radiocarbon dating throughout the cores allow correlation of these event deposits between both cores. The first three event layers are linked to known tsunamis, the 2009 SPT, the 1960 GCET or 1957 AIT and the 1917 TTT. They are characterized by darker sediment with a mean grain size coarsening induced by a bimodal distribution. This coarser grain size mode reveals the presence of a coarser terrestrial input transported seaward by the tsunami backwash, and is supported by a Ti/Ca and K_{norm} increase. The oldest event layer was most likely emplaced following the 1868 SAT. If the tsunami wave was reported in Upolu and Savai'i (Samoa) and in several coastal regions in the south-west Pacific, the only sedimentary evidence of this tsunami prior to this study was found onshore in New Zealand. In both cores, the deposits associated with the 1868 SAT are considerably thicker and with more pronounced sedimentological and geochemical variations.

Together with backwash deposits of the 2009 SPT previously identified in Pago Pago Bay, this study provides the first correlation at the scale of an island of offshore tsunami backwash deposits from one specific event, namely the 2009 SPT. This large-scale correlation shows how the

orientation and morphology of the study site can affect the facies of the backwash deposits emplaced by a unique tsunami. This study also presents the first probable geological evidence in Tutuila of the 1868 SAT, which has already been reported in several sites in the southern Pacific Ocean. All in all, this work shows the good preservation potential for tsunami backwash deposits in sheltered shallow marine environments, and encourages to continue looking for paleotsunami backwash deposits in such study sites.

6.9 Acknowledgment

We thank the CNRS-INSU “Risques et catastrophes telluriques” program as well as the Conseil Régional de la Région Poitou Charentes for the funding of this project. We also thank the Commission Nationale de la Flotte Côtière, the captain Jean-François Barazer and the *R/V Alis* crew members, the divers Stéphane Bujan and John Butscher, along with Bruce Jaffe for his help coordinating and making possible the field survey. Finally, we acknowledge all the members of the EPOC core analysis platform Isabelle Billy, Pascal Lebleu, Marie-Claire Perello and Olivier Ther, GIS expert Vincent Hanquiez and interns Johanna Juppín and Laurine Monier.

Chapter 7:

General discussion

7.1 Tsunami backwash deposits around Tutuila

7.1.1 Correlation of historic tsunami backwash deposits around Tutuila

During this study, five potential different historic tsunamis were identified based on their backwash deposits in three different bays around Tutuila Island: Pago Pago Bay on the south coast, Fagafue Bay and Masefau Bay on the north coast (Figure 7.1). These five tsunamis are considered to be the most significant tsunamis to have impacted Tutuila during the last two centuries. The most recent tsunami, the 2009 SPT, is recorded in all three bays. However, the older tsunamis were not formally identified in all bays. The 1960 GCET was formally identified in Pago Pago, but on the north shore, a doubt remains on one event layer between the 1960 GCET and the 1957 AIT. The 1960 GCET supposedly had a greater impact on the coasts of Tutuila compared to the 1957 AIT (PacificTWC, 2016, 2017). However, inundations were reported following the 1960 GCET on the south shore of Tutuila but not on the north shore, while the 1957 AIT reportedly caused inundations on the north shore but not on the south shore. Deposits of the 1917 TTT were formally identified only in Masefau, while deposits of the 1868 SAT were found only in the northern bays of Fagafue and Masefau. Therefore, one question arises: why weren't the deposits of the 1917 TTT and 1868 SAT identified in Pago Pago Bay?

Several reasons can be pointed out for the absence of the older tsunami backwash deposits from the 1917 TTT and the 1868 SAT in Pago Pago Bay. The first one is the length of the studied cores. Indeed, the short cores used for the identification of historic tsunamis in Pago Pago Bay are only 60 cm long. Given the sedimentation rate in Pago Pago Bay (around 0.6 cm.yr^{-1}), the backwash deposits emplaced during the 1917 TTT and the 1868 SAT are expected to be found below the base of these cores (around 90 cm deep assuming a constant sedimentation rate).

7. General discussion

The second reason, unfortunately, is due to a gap between surface sediment sampled by short cores and Kullenberg cores (within unit U8). Indeed, the use of the Kullenberg coring device induced a loss of the superficial sediment when landing on the seafloor. Due to a lack of overlap between the short cores and the Kullenberg cores, the depth of the top of the Kullenberg cores cannot be measured precisely, but is estimated at approximately 0.8 to 1 m based on core-to-seismic correlations. Thus, the backwash deposits of the 1917 TTT may have been recorded in Pago Pago but were not sampled due to this hiatus in the sediment record.

The third reason is related to the nature of the sediment supply during the deposition of unit U7. Radiocarbon dating of unit U7 gives ages as young as the second half of the 19th century. Thus, backwash deposits of the 1868 SAT may be recorded near the top of U7. However, since

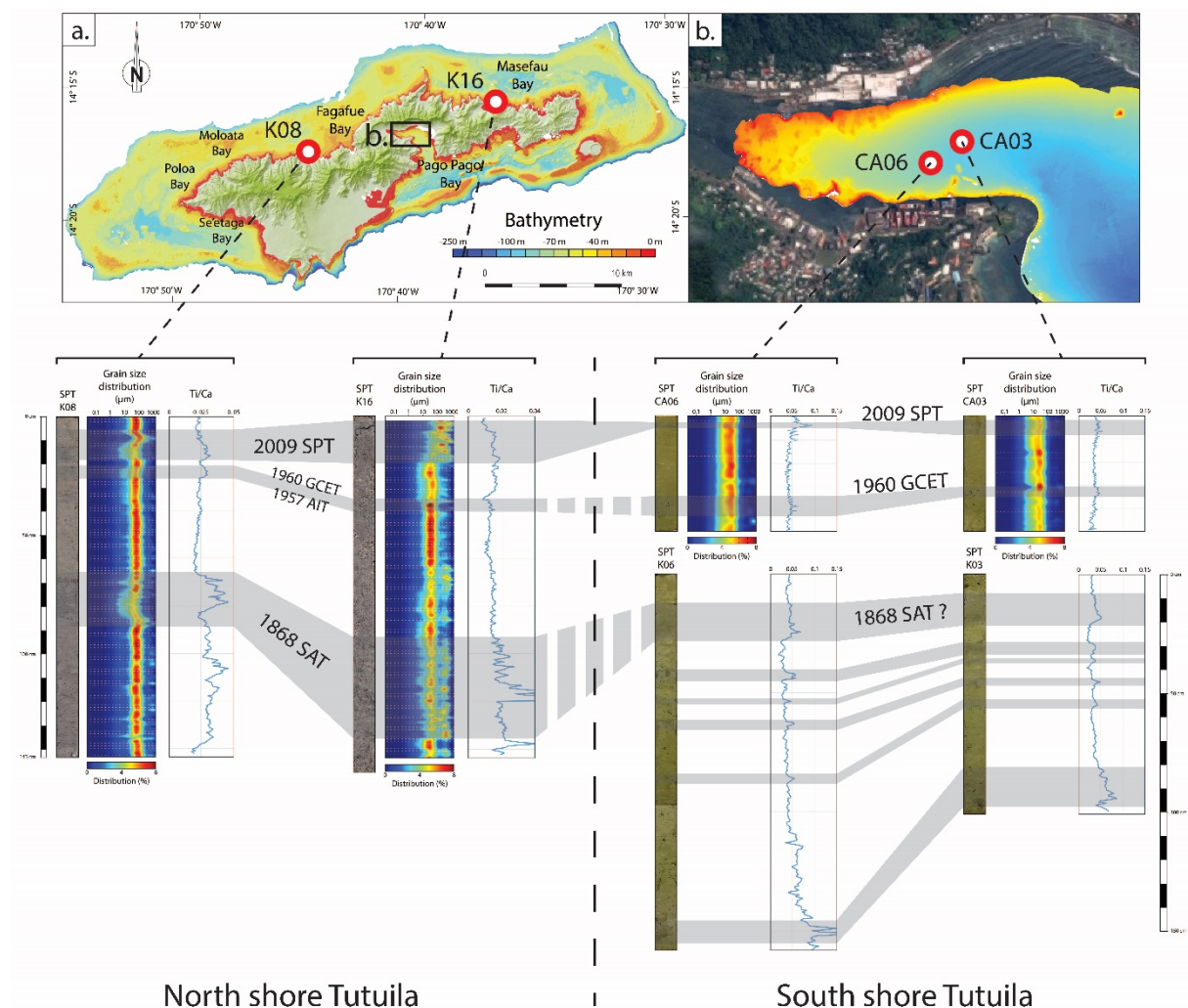


Figure 7.1: Large-scale correlation of tsunami backwash deposits identified in the shallow marine sediment record of Tutuila (2009 SPT, 1960 GCET, 1957 AIT, 1917 TTT and 1868 SAT) between the north shore (Masefau and Fagafue bays, K08 and K16, left) and the south shore (Pago Pago Bay, CA06, K06, CA03 and K03, right); A correlation is also proposed for the deeper sediment record of Pago Pago Bay between anomalous layers detected in cores from the outer part of the bay (K06 and K03).

7. General discussion

U7 is composed of coarse coral fragments without any clear stratification, identification of specific high-energy events remains impossible.

Finally, the last reason is related to the location of the cores. When first analyzing the short cores, the ones from the inner part of Pago Pago Bay (CA02, CA09, CA07, CA08, CA04 and CA05) showed pronounced geochemical and mineralogical variations, while those from the outer part of the bay (CA01, CA06, CA10 and CA03) were very homogeneous and did not show major variations. Based on these observations, Kullenberg cores from the outer part of the bay were not investigated at first.

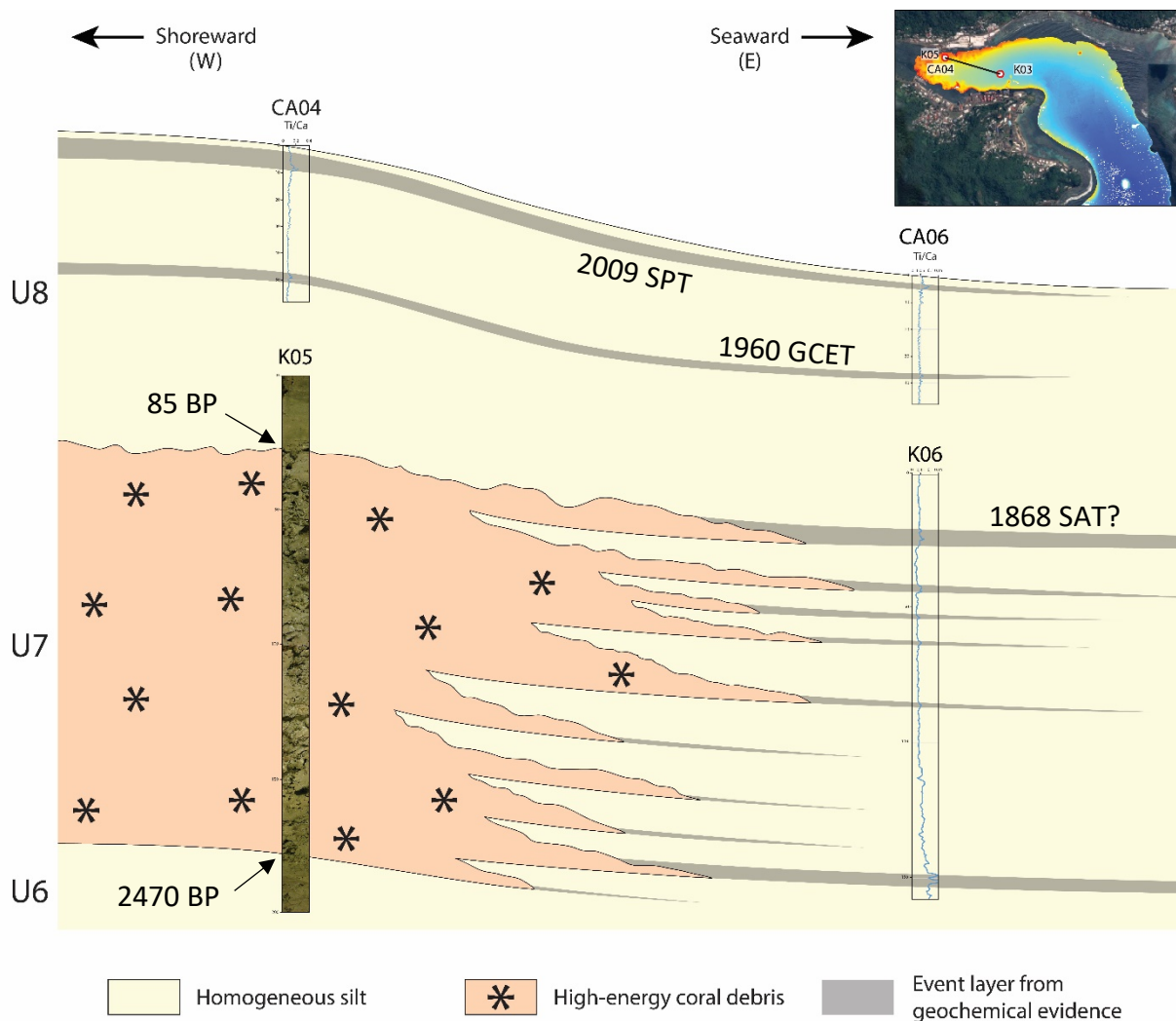


Figure 7.2: Proposed schematic correlation of event deposits between the inner part of Pago Pago Bay and the outer part of the bay with lateral facies variations based on seismic and lithological evidence in the inner part and geochemical evidence in the outer part of the bay.

Despite these limitations related both to technical issues and specificity of the study site, is a correlation still possible between the deposits interpreted as being those of the 1868 SAT on the north shore and deposits in Pago Pago Bay? Based on the modeled propagation of the 1868 SAT (eCoast,) and the strong impact it had in the north of Tutuila, as can attest the backwash deposits identified in Masefau and Fagafue bays, it is likely that the 1868 SAT could have also induced backwash deposits in Pago Pago Bay. Cores K06 and K03 collected in the outer part of Pago Pago Bay both show a very strong Ti/Ca peak near the top of the core (Figure 7.1). Given the strength of the geochemical signature and its similarities with the Ti/Ca peaks of the 1868 SAT backwash deposits in the northern bays, these peaks could potentially attest of the distal backwash deposits from the 1868 SAT (Figure 7.1). In the inner part of the bay, the uppermost coral debris in unit U7 are dated to approximately 1865 AD (K04 and K05). Thus, these coral debris may correspond to the backwash deposits emplaced during the 1868 SAT. Consequently, following these two hypotheses, the sediment signature of the 1868 SAT would be strongly variable in Pago Pago Bay (Figure 7.2). Shoreward, where the impact of the tsunami must have been greater, the backwash would have been recorded by the deposition of the uppermost coral debris in unit U7. Seaward, where the coral unit U7 pinches out and at depths where the impact of the tsunami backwash flow was less pronounced, the backwash signature would change gradually from coarse coral debris to terrestrial-dominated clay deposits (Figure 7.2).

7.1.2 Insights on paleotsunami archive in Pago Pago Bay

Historic tsunami backwash deposits found in all three bays seem to show that two main categories of tsunamis are able to reach Tutuila Island with enough strength to leave identifiable deposits in the shallow marine sediment record. The first category corresponds to local tsunamis generated near the northern extremity of the Tonga Trench, such as the 2009 SPT and the 1917 TTT. The second category corresponds to far field tsunamis like those generated on the western coast of South America, such as the 1960 GCET and the 1868 SAT, or along the Aleutian Trench. Of the four tsunamis identified on the north shore of Tutuila, the 1868 SAT left by far the thickest and most identifiable deposits.

Unfortunately, cores collected in the northern islands of Tutuila (Fagafue and Masefau) are too short and don't allow retracing paleotsunami history prior to the 1868 SAT. However, the distal cores collected in Pago Pago Bay (cores K06 and K03) provide 2.5 m of sediment record. On these two cores, at least six peaks can be observed in the Ti/Ca profile in the first 1.5 m of sediment (Figure 7.1). In core K06 a first major peak is found between 10 and 30 cm, followed by four short

peaks at 40 to 45 cm, 54 to 55 cm, 60 to 66 cm and 85 to 89 cm and one last major peak at 145 to 155 cm depth (Figure 7.1). In core K03, a first major peak is also found between 8 and 22 cm, followed by four short peaks at 27 to 34 cm, 35 to 38 cm, 44 to 47 cm and 52 to 56 cm and one last major peak at 81 to 98 cm depth (Figure 7.1). Given their similar characteristics with event deposits identified in Pago Pago, Masefau and Fagafue bays, they can be interpreted and correlated between the two cores as six successive event layers (Figure 7.1). In both cores, below the deepest of these six peaks, the Ti/Ca profile starts to increase and distinct peaks are not clearly identifiable. By analogy with the sediment record within the inner part of Pago Pago Bay and in Fagafue and Masefau bays, where the Ti/Ca peaks were interpreted as recording strong and sudden increases of terrestrial input induced by tsunami backflows, the six event layers identified in cores K06 and K03 may correspond to major tsunamis that struck Tutuila.

As it was suggested earlier, the uppermost event layer, which is the thickest of all six, could be interpreted as the backwash deposits left by the 1868 SAT (Figure 7.1). Then, each of the five lower event layers could correspond to major tsunamis prior to the 1868 SAT. As it was presented in the discussion of Chapter 5, five major earthquakes have been reported along the western coast of South America prior to the 1868 earthquake (Cisternas *et al.*, 2005; Goff *et al.*, 2010). Of these five earthquakes, four were triggered in a location close to that of the 1868 earthquake along the Peruvian and north Chilean coast, in 1746 AD, 1687 AD, 1604 AD and 1586 AD, and one close to that of the 1960 GCET in 1575 AD. For each of these earthquakes, important inundations induced by a strong tsunami were reported (Cisternas *et al.*, 2005; Goff *et al.*, 2010). Then, the main wave amplitude pathways across the Pacific Ocean for each tsunami is expected to have been similar to that of the 1868 SAT or the 1960 GCET and oriented roughly towards the Samoan archipelago (Berryman, 2005; Goff *et al.*, 2010). Therefore, the tsunamis generated by these five major earthquakes are some of the most probable candidates for the five remaining event layers identified in core K06 and K03. Other potential candidates are tsunamis originating from the Aleutian Trench. A recurrence time for major tsunamis generated in the region of approximately 150 to 250 years was estimated by Witter *et al.* (2019), with also evidence of several such paleotsunamis reaching the Hawaiian Islands (La Selle *et al.*, 2019). As for the 1868 SAT, given that the ages of high-energy coral fragments in unit U7 in the inner part of the bay (between 85 BP and 2470 BP) cover the same period as the above-mentioned tsunamis, some of the coral debris could be correlated laterally to the tsunami backwash deposits above-mentioned (Figure 7.2).

Finally, backwash deposits of five major tsunamis were identified in the bays of Tutuila, namely the 2009 SPT, the 1960 GCET, the 1957 AIT, the 1917 TTT and the 1868 SAT. Five

additional potential tsunami backwash deposits were distinguished, but their sources could not be identified. Thus, this work proves that Tutuila and sheltered shallow marine environment in general can be very favorable for the preservation of high-energy event deposits and offer promising insights on paleotsunami backwash archiving.

7.2 Progress in the field of tsunami backwash

7.2.1 New identification proxy for backwash deposits

The identification of two historic tsunamis in Pago Pago Bay offered new opportunities to analyze and describe precisely backwash deposits. Until now, most studies focusing on historic shallow marine backwash deposits were first based on obvious grain size changes in the sediment record. In Pago Pago Bay, despite the fact that the 2009 SPT is known to have severely struck the area (Goff & Dominey-Howes, 2011), no visual or grain size evidence was found at first. This early set down forced us to use finer detection methods, such as geochemistry, and explore new methods that had not yet been applied in the field of tsunami backwash identification. In order to describe tsunami backwash deposits not marked by visual or grain size evidence and only detected by geochemical variations, thin sections were examined for mineralogical and micro-structural analysis. For the two historic tsunamis formally identified based on geochemical analysis conducted on short cores sampled in Pago Pago Bay (the 2009 SPT and the 1960 GCET), similar mineralogical and micro-structural signatures were observed in the backwash deposits. As described in many previous studies, these deposits are composed of terrestrial dominated material eroded from the coastal plain and dragged seaward by the backflow. But the micro-structural analysis reveals very specific characteristics. Asymmetrical flame structures are observed at the base of both event layers. These flame structures are all oriented in the same direction. In addition, rip-up clasts are found at the base of the layers. Both the flame structures and the rip-up clasts show no mixing between the event layer sediment and the underlying layer sediment. These observations indicate shearing and buckling at the contact area between the upper dense and highly cohesive backwash layer and the underlying superficial sediment, specific to hyperpycnal currents. Such basal deformation has already been described in inferred paleotsunami backwash deposits on the Chilean coast, but at scales far greater with pluri-metric flame structures and other shear structures (Le Roux & Vargas, 2005b). Based on these observations, Le Roux & Vargas (2005b) suggested that a tsunami backwash acted as a hyperpycnal current. However, in modern deposits formally identified as

historic tsunami backwash deposits, such basal deformation has never been pointed out. Then, the micro-deformations described at the base of the 2009 SPT and 1960 GCET deposits constitute a modern analogue to ancient outcrops described by Le Roux & Vargas (2005b), and validate their theory that the backwash can be assimilated to a hyperpycnal current. The fact that shear structures are described for the first time in identified historic tsunami backwash deposits can be explained by two reasons. The first reason is that thin sections of backwash deposits are described for the first time in this study. Indeed, most previous studies on backwash deposits were based on visual or geochemical evidence and thin sections were probably not needed. The second reason is that these types of micro-deformations induced by shearing mechanisms develop preferentially within fine cohesive sediment layers. Sediment available for reworking and transport in the highly sheltered bay of Pago Pago are mostly silt and clay material, which are very favorable for developing such shear structures. Inversely, most studies of recent backwash deposits were set in open bays or beaches. In such environments, sediment available for transport are mainly sands and gravels, which are not likely to form a dense and cohesive gravity flow, necessary for the occurrence of shearing and buckling structures.

7.2.2 Highly sheltered bays: ideal preservation potential for backwash deposits

One of the main goals of this project was to investigate the preservation potential in sheltered bays. Until now, most backwash studies of historic tsunamis have been based in an open coast setting (Khao Lak, Thailand: Feldens *et al.*, 2012; Sakuna *et al.*, 2012; Nagapattinam, India: e.g. Srinivasalu *et al.*, 2010; Veerasingam *et al.*, 2014; Sendai Bay: e.g. Tamura *et al.*, 2015; Yoshikawa *et al.*, 2015). When starting this project in Tutuila and especially in Pago Pago Bay, the working hypothesis was the following: in sheltered bays, the absence of big waves and strong oceanic currents, which are largely responsible for nearshore sediment reworking, may result in a higher preservation potential of event deposits. This work in Pago Pago Bay and Masefau Bay has shown that event deposits are indeed well preserved in such sheltered bays. However, they can prove to be triggering to detect using only traditional backwash analysis methods.

Both in Pago Pago Bay and Masefau Bay, which are the two most sheltered bays of Tutuila, all backwash deposits of major recent tsunamis were found and identified in the sediment record. These deposits correspond to the four strongest tsunamis to have struck the island since the beginning of tsunami reporting in American Samoa, the 2009 SPT, the 1957 AT, the 1960 GCET

and the 1917 TTT (Pararas-Carayannis, 1999; NGDC, 2018), plus an older tsunami never reported in American Samoa, most likely the 1868 SAT. In addition, several event layers with similar geochemical characteristics to that of identified tsunami backwash deposits are observed in deeper cores from Pago Pago Bay. This suggests that older paleotsunami backwash deposits may have been preserved in the sediment record and that the tsunami catalog in Pago Pago Bay may be extended even more. Given these results, it seems fair to say that sheltered bays have a very high potential for tsunami deposits preservation, and for reconstructing local or regional event catalogs. However, a major difference between open beaches and sheltered bays is the nature and availability of nearshore sediment. Indeed, wave-dominated open coasts are characterized by a strong lateral facies variation from coarse material in the foreshore to fine material offshore (Howard & Reineck, 1981). Hence, beaches provide important amounts of coarse material, mostly sand, potentially transported offshore by the tsunami backflow. This results in marked grain size variations between the autochthonous fine-grained offshore sediment and the allochthonous coarse-grained tsunami deposits (e.g. Srinivasalu *et al.*, 2010; Jonathan *et al.*, 2012; Sakuna *et al.*, 2012; Tamura *et al.*, 2015). In the case of highly sheltered bays, with very low hydrodynamic settings, the lateral changes in sediment grain size are less marked. The shallow marine sediment is mainly fine-grained and mostly composed of silt (Morrison *et al.*, 2010). Then, if allochthonous terrestrial sediment transported offshore by the tsunami backflow is fine, such as mud originating from the wash-out of terrestrial substratum, it doesn't stand out in terms of grain size from the autochthonous background sediment. For this reason, tsunami backwash deposits in highly sheltered bays may be hard to detect using traditional sedimentological methods. However, as shown in this work, the lack of grain size variation does not mean that the backwash deposits are non-existent. They require finer methods, such as geochemical or micropaleontological analyses when possible. In this case, thin section analysis has shown its potential for detection and identification of backwash deposits relying on mineralogical, sedimentological and micro-structural characteristics.

7.2.3 Tsunami backwash deposits versus storm deposits

Another main issue for sedimentologists studying tsunami backwash deposits is distinguishing them from storm and flash-flood deposits. This distinction problem comes mainly from the fact that all these events are high-energy events that may be deposited in similar settings, and share similar characteristics. However, slight differences are commonly found between them (Figure 2.15). Mainly, tsunami deposits often include a high proportion of diverse terrestrial material, such as plant debris or anthropogenic material, which is rarely the case for storm deposits

(Goodman-Tchernov *et al.*, 2009; Sakuna-Schwartz *et al.*, 2015). Tsunami deposits are also usually poorly sorted, with material of all sizes and frequent mud clasts at base, which is not the case for flash-flood deposits (Sakuna-Schwartz *et al.*, 2015).

Yet again, this problem occurred all along this study conducted in Tutuila. Storm deposits were rapidly ruled out as a consequence of the choice of the study area. Indeed, Pago Pago Bay and Masefau Bay are two deep and sheltered bays. Then, according to their long and narrow morphology, strong storm waves cannot reach the inner and deep parts of these bays. Moreover, the cores were collected below the wave base (between 27 and 55 m depth) where reworking by wind-induced waves is very unlikely. For the open bay of Fagafue, the coring sites were also deep enough (50 m depth) and are not likely to be impacted by either storm waves or wind-induced waves. However, the major issue was to settle between flash-flood deposits, caused by heavy rains during cyclones which are very frequent in the studied area, and tsunami backwash deposits. In Pago Pago Bay, both flash-flood and backwash deposits are found in the cores (see Chapter 5). The deposits were distinguished based on both micro-structural observations and ages. Indeed, comparison between the age model and reported local events allowed precise identification of the main events that caused each deposits. In addition, tsunami backwash deposits showed frequent basal micro-deformation and mud clasts, unlike flash-flood deposits. Finally, spatial distribution analysis of flash-flood and backwash deposits allowed isolating another distinction criterion. Flash-flood deposits are found only in the most proximal cores and in the thalweg. This suggests that flash-flood deposits could likely be more channelized and limited to a shallower area than tsunami backwash deposits. Then flash-flood deposits may have a more localized spatial distribution than tsunami backwash deposits. However, this result is based on the study of a single site, and should be investigated in other sites to be confirmed or disproved.

Chapter 8:

Conclusion and perspectives

8.1 Reminder of the initial objectives

When this campaign was launched four years ago in 2015, following the 2009 SPT, five initial objectives were formulated. These goals were articulated mainly around a need from the scientific community for a better understanding of tsunami backwash processes and continuous sediment records to contribute to the paleotsunami archive. Tutuila Island, and more specifically Pago Pago Bay, was chosen for two main reasons. The first was that a strong and well-documented tsunami, the 2009 SPT, had recently severely impacted American Samoa. The second reason was related to the assumption that a highly sheltered bay located in Tutuila, with a very low hydrodynamic setting would be ideal for preservation of past high-energy events. This last point is key because until then, poor preservation of backwash tsunami deposits resulted in a relative paucity of identified paleotsunami backwash evidence. These objectives were to:

- Describe the sedimentary setting and the history of the sediment-fill in Pago Pago Bay;
- Identify and describe thoroughly the backwash deposits emplaced by the 2009 SPT in Pago Pago Bay;
- Identify older historic and paleotsunami backwash deposits for the reconstruction of a local paleotsunami catalog;
- Correlate tsunami deposits around Tutuila Island;
- Find new criteria for distinguishing tsunami from storm deposits.

In order to fulfill these objectives, a complete dataset was acquired in Pago Pago Bay and around the island of Tutuila. This dataset includes extensive geophysical data, with high-resolution bathymetric and seafloor reflectivity surveys covering 120 km² around the island and a 2D-seismic survey including more than 50 km of seismic profiles, along with 47 cores collected, representing a total length of just under 40 m of sampled sediments.

8.2 Main results

This campaign was a very ambitious project with many different objectives and an important amount of data to analyze. If the initial objectives were mostly fulfilled, some points still need to be investigated deeper.

A first global analysis of the data collected in Pago Pago Bay led to the first insights about the long-term (few millenaries) sedimentary history of the bay. The approximately 12 m thick sediment-fill is divided into eight units based on seismic and core-to-seismic analysis. The basal unit, which was deposited directly on the eroded volcanic basement, is interpreted to be a transgressive unit emplaced during the sea-level rise following the last glacial maximum, between 12 000 and 7 000 years ago. The upper seven units are interpreted to be aggradational units of the highstand systems tract emplaced during the sea-level highstand, from 7 000 years ago to present. These aggradational units show an alternation between low-energy and high-energy sedimentation. Low-energy sediment units are composed of homogeneous silt whereas high-energy sediment units are composed of coarse and sharp coral fragments, occasionally mixed with *Halimeda* plates. These high-energy units are chaotic and pinch out seaward about 1 km off the extremity of the bay. Seaward of this point, all low-energy units merge into a unique thick and continuous unit, composed entirely of silt. Given the characteristics of the coral fragments and the geodynamic setting of Tutuila and Pago Pago Bay, high-energy units are interpreted as being tsunami backwash deposits. The chronology established based on ^{210}Pb and ^{14}C dating allowed an estimation of the age of the upper tsunami deposits. The uppermost high-energy unit is dated approximately between 100 BP and 2 500 BP. It most likely corresponds to around 2 400 years' worth of stacked tsunami deposits. However, it is not possible to isolate specific events in this unit because of the absence of identifiable erosive surface. The base of the second high-energy unit was not reached by cores so only the age of the top of this unit can be dated, at approximately 3 400 BP. Based on the similar thickness as the uppermost high-energy unit, it seems reasonable to estimate that it represents roughly 2 000 to 2 500 years' worth of stacked tsunami deposits. The third high-energy unit was not reached by cores. Two hypotheses were proposed to explain the alternation between the low- and high-energy sedimentation in Pago Pago Bay. The first one assumes that tsunamis reach Pago Pago Bay with a constant frequency. This implies that only the source of deposits, which is the corals, would fluctuate over time. Local or regional paleo-climatic cyclic variations are needed to explain such fluctuations in coral colonies. The second hypothesis assumes that the frequency of tsunamis impacting Tutuila fluctuates over time, with long periods ($\sim 2\,000$ years) of high tsunami

8. Conclusion

recurrence interrupted by shorter periods ($\sim 1\,000$ years) without major tsunamis. Such change in tsunami frequency could result from alternating high and low activity phases of southern Pacific subduction zones, such as the Tonga Trench and the Peru-Chile Trench.

At first sight, the deposits from the 2009 SPT were not found in the cores sampled in Pago Pago Bay because of a lack of apparent grain size variations. However, based on the previous sediment-fill analysis, emphasis was made on the uppermost silt unit, with fine and detailed investigation of the short superficial cores. Two anomalous layers were identified in the first 50 cm of the cores based on geochemical, mineralogical and microstructural analysis. They are characterized by a high terrestrial geochemical signature, composed of terrigenous clay and sand, with plant debris, paleosol and volcanic minerals, and display shearing and buckling micro-deformations, with rip-up clasts, at base. These characteristics indicate a dense outflow with transport of sediment from land to sea by hyperpycnal currents. Two types of high-energy events can be responsible for such deposits: flash-floods and tsunamis. Based on ^{210}Pb -derived chronology and reconstitution of the historic events calendar taking into account major tsunamis and cyclones, the two event layers were dated precisely and the associated events were identified. They correspond to the two strongest tsunamis recorded in Pago Pago Bay over the last 70 years. The uppermost layer corresponds to the 2009 SPT while the deepest corresponds to the 1960 GCET. However, a third thin and discontinuous anomalous layer was found in between the deposits from the two tsunamis. It is also characterized by a strong terrigenous input, but does not display basal micro-deformation or rip-up clasts. Based on the chronology, this layer most likely corresponds to flash-flood deposits emplaced during the 1990 or 1991 cyclones, which were reported to have been the biggest cyclones recorded in over 100 years in Tutuila.

Evidence of similar anomalous deposits was found in two other bays on the north shore of Tutuila, Fagafue Bay and Masefau Bay. Based on geochemical and grain size analysis mainly, three anomalous layers were detected in Fagafue and four in Masefau. As seen in Pago Pago Bay, the geochemical signature of these layers indicates an increased terrestrial input, suggesting they were emplaced following a land-to-sea transport. The grain size signature is different between the two bays, which most likely reflects the different hydrodynamic setting for each bay and coring site. Indeed, Fagafue Bay is a very open bay and the cores were collected out of the bay, while Masefau Bay is a sheltered bay and the cores were collected inside the bay. In Fagafue, the anomalous deposits are characterized by a coarser base and poorer sorting compared to the background sediment. In Masefau, they are characterized by a poorer sorting with a bimodal grain size distribution. The first mode is roughly equivalent to the grain size of the background sediment,

with a second coarser mode. The combination of the terrestrial signature and the coarser and poorly sorted, or bimodal, grain size trends suggests a very likely tsunamigenic origin for these deposits. The chronology established based on radionuclides and radiocarbon dating was used to identify potential candidates for these event layers. In both bays, the shallowest layer corresponds to the deposits left by the 2009 SPT. The second layer, which was slightly more subtle, is dated at around 1957 AD in Fagafue and 1960 AD in Masefau. Then, two potential candidates are proposed for this layer: the 1960 GCET or the 1957 AIT. The third layer was found only in Masefau Bay and most likely corresponds to the 1917 TTT. Finally, a fourth event layer was detected deeper in the cores from both bay and dated at around 1870 AD in Fagafue and 1878 AD in Masefau. Despite a very strong geochemical and grain size signal, no record of inundation was reported in Tutuila around this period. However, one specific tsunami reached most south Pacific Islands where major inundations were reported: the 1868 SAT. Therefore, the 1868 SAT is one of the most probable candidate, even if older tsunamis generated around the Pacific may be responsible for the observed deposits.

In addition to satisfying most initial objectives, these results represent a step further in the understanding of tsunami-related processes and sediment records as well as providing useful information for coastal risk assessment in Tutuila. The sedimentary architecture and sedimentation of Pago Pago Bay revealed a strong influence by tsunamis. The recent siltation of the bay during the last 150 years, induced by the intense anthropization of the bay, resulted in an absence of visual marine sedimentary evidence left by the 2009 SPT. Indeed, no marked erosive surface or grain size change is found in the superficial sediment record. Only geochemical analysis and mineralogical and microstructural investigation through thin sections of cores allowed identifying the backwash deposits emplaced in Pago Pago Bay by the 2009 SPT, along with those emplaced by the 1960 GCET. Detailed observation of these deposits revealed basal micro-deformations (flame structures) induced by the shearing between the backwash layer and the superficial sediment. These features had yet only been described in inferred paleotsunami deposits (Le Roux & Vargas, 2005a) and are described for the first time in historic tsunami backwash deposits. These observations confirm that tsunami backflows are in fact hyperpycnal currents, as was suggested by Le Roux & Vargas (2005a). Backwash deposits from the 2009 SPT were found and correlated all around Tutuila, with deposits identified also in Masefau and Fagafue, two bays located on the north shore of the island. Investigation of offshore tsunami backwash deposits and correlation between such deposits related to the same tsunami around an island is described for the first time. For the 1960 GCET, an event layer dated around the same period was detected on the north shore, but may as well have been emplaced by the 1957 AIT. This would suggest that the orientation of the island

can have an important role depending on the amplitude of the tsunami, with some tsunamis coming from the southern Pacific recorded only on the south coast and some tsunamis coming from the northern Pacific recorded only on the north coast of Tutuila. The 1868 SAT reportedly impacted a great number of the south Pacific Islands, including Samoa, but has never been reported in Tutuila or American Samoa. Then, this work represents the first probable geological evidence of the 1868 SAT in Tutuila.

8.3 Perspectives

This work leads to a great number of questions and new insights. Some questions could be answered with just further investigation of the data collected during this campaign and additional time, some others need additional data or even whole new projects and funding in order to test new hypotheses.

In Pago Pago Bay, the lack of overlapping between the short cores and the Kullenberg cores induced a gap in the superficial sediment record. Emphasis was made only on short cores because of this limitation. However, interesting observations were made when looking at the Kullenberg cores located in the distal part of the bay. Indeed, several anomalous layers, characterized by a strong terrigenous geochemical signature, were detected. Similarities were found between the shallowest of these layers and the layer interpreted as the backwash deposits emplaced following the 1868 SAT on the north shore of Tutuila. A first hypothesis is that this anomalous layer identified in Pago Pago Bay could be the backwash deposits emplaced by the 1868 SAT, and correlated with the upper part of the high-energy coral fragments unit in the inner part of the bay. A second hypothesis can be formulated concerning the deeper anomalous layers. These layers could also correspond to the geological record of older tsunamis impacting the American Samoa. During the last 400 years prior to the 1868 SAT, at least 5 earthquakes along the Peruvian and Chilean coast reportedly generated tsunamis. Geological evidence of some of these tsunamis may have been found in Hawaii and New Zealand, suggesting that they could as well have impacted Tutuila. Similarly, geological evidence of great earthquakes generated along the Aleutian Trench have been identified in the Aleutian Islands with a recurrence of approximately 200 years. Some of them were also recorded as far as the Hawaiian Islands and thus could be potential candidates. In order to test these hypotheses, a precise and rigorous chronology must be established for these cores.

Pago Pago Bay undeniably has a high potential for the record and preservation of tsunami backwash deposits. In order to extend the paleotsunami catalog started during this work, it would be very interesting to have a longer sediment core in the bay. With a big enough boat, such as the Marion Dufresne (IFREMER), it would be possible to retrieve a core in the outer part of the bay recording the entire sediment-fill (~15 m) down to the volcanic basement. This would be a first and could represent a significant progress for paleotsunami backwash archiving in the Pacific. Since the cores in the inner part of the bay only reached the top of the second high-energy unit, it would also be interesting to collect a second long core in the inner part of Pago Pago Bay in order to date more precisely the two deeper high-energy units and investigate the lower half of the sediment-fill.

Finally, this work has proved that sheltered shallow environments can have an ideal preservation potential for past tsunamis. Then, it seems absolutely crucial to find new study areas offering sheltered environments to keep on studying the impacts of tsunamis on such environments and the characteristics of their backwash deposits, as well as providing additional paleotsunami archives. For this purpose, two approaches may be proposed based on the type of tsunamis aimed for. The first approach consists in finding a study area near a highly tsunamigenic zone that is likely to have registered all local tsunamis. The aim of this approach is to have an extensive archive of local paleotsunamis. Such study zones could be deep and highly sheltered bays located along the Pacific Ring of Fire, in areas where big earthquakes are frequent. A good example would be Beaver Bay (Atka Island, Alaska, Figures 8.1 and 8.2) in the Aleutian Islands. Indeed, the western part of the Aleutian Trench is the most active part and this specific bay is deep and highly sheltered. In addition, the archive of historic tsunamis is very rich during the last two centuries, but very little is known prior to the 19th century. Then, evidence of paleotsunamis in this area would be a very beneficial contribution, both for local risk assessment and identification of paleotsunami deposits across the Pacific Ocean. The second approach consists in finding a study area located in the middle of the Pacific Ocean and likely to have been impacted by far-field tsunamis generated all around the Pacific Ring of Fire (Figure 8.1), similar to Tutuila Island. Ideal sites would be islands with several deep and sheltered bays oriented in different directions and capable of recording tsunamis coming from all parts of the ocean. A good example of such study areas is Moorea Island (French Polynesia, Figures 8.1 and 8.3), with four deep and sheltered bays: Opunohu Bay and Cook Bay oriented north, Vai'are Bay oriented south-east and Atiha Bay oriented south-west. During the last 70 years, French Polynesia has reportedly been impacted by most major far-field tsunamis. However, the paleotsunami archives don't extend further than the middle of the 20th century. Then, investigating the shallow marine sediment record in the bays of Moorea would be a great opportunity to extend this record.

8. Conclusion

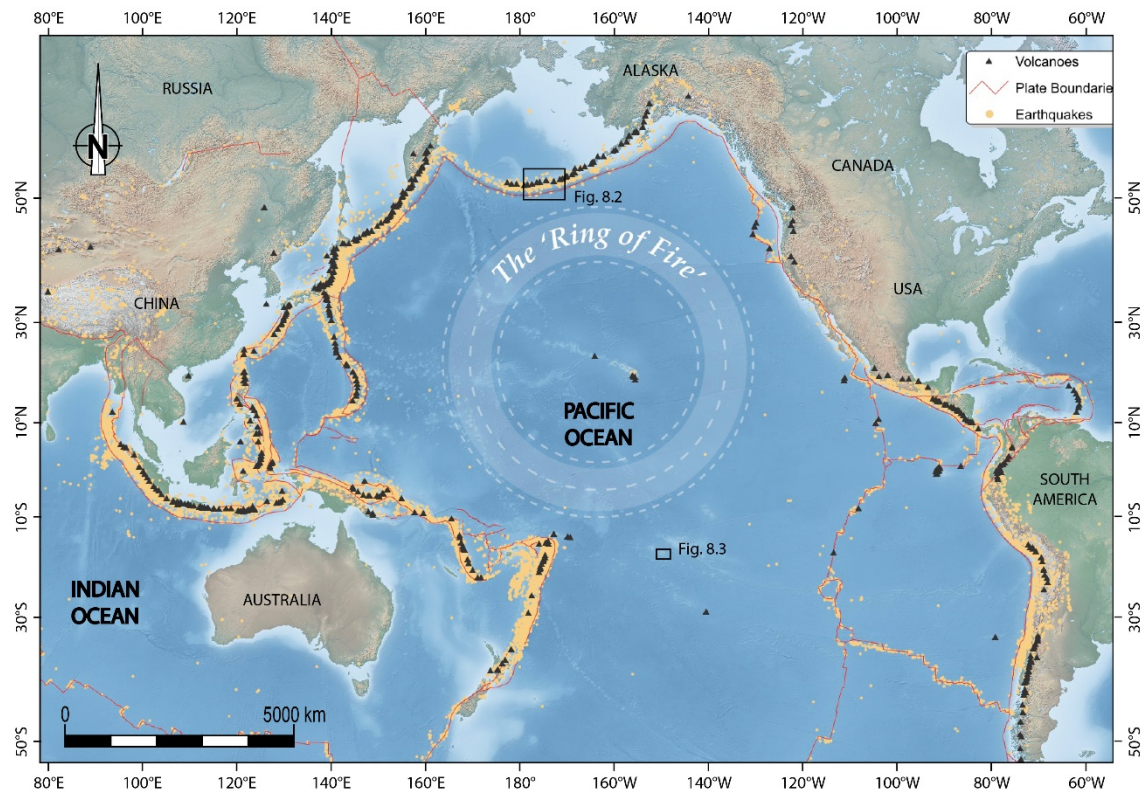


Figure 8.1: Map of the Pacific Ocean and surrounding continents with the Pacific Ring of Fire highlighted by the tectonic plate boundaries, recent earthquake epicentres and active volcanoes, from <https://www.earthobservatory.sg/resources/maps/ring-fire>; location of Figures 8.2 and 8.3 indicated on the map.

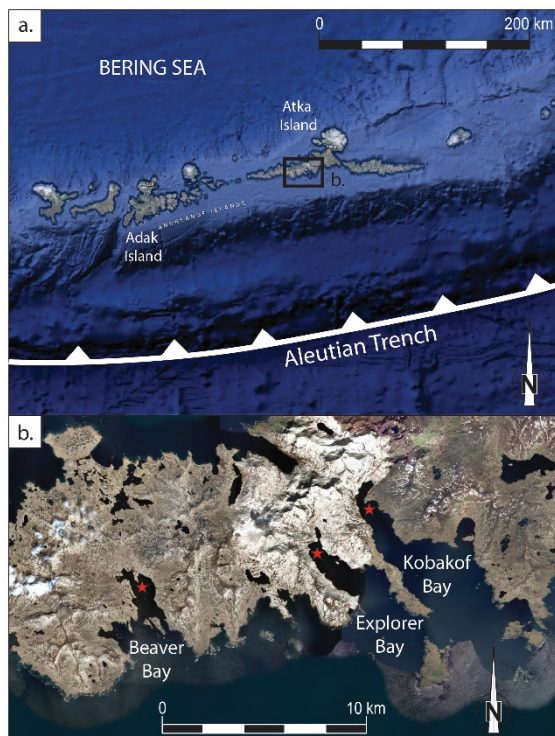


Figure 8.2: a. Location of Atka Island (Alaska) along the Aleutian Trench (modified from Google Earth); b. Map of western Atka Island with location of proposed future study sites marked with a red star (modified from Google Earth).

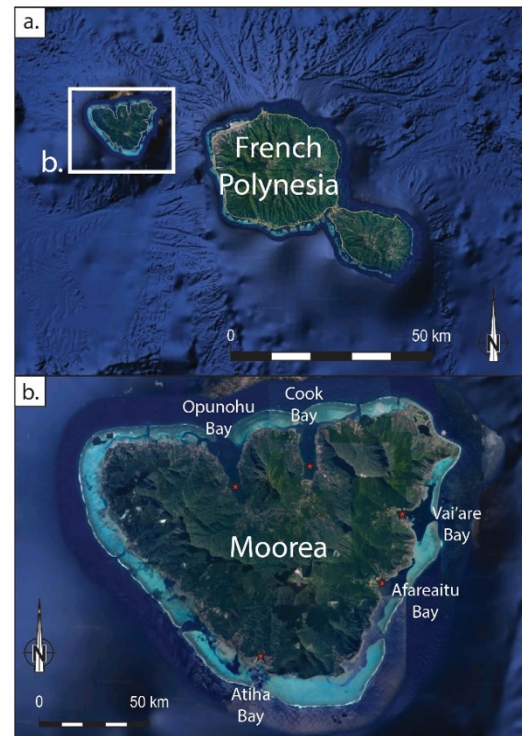


Figure 8.3: a. Location of Moorea Island (French Polynesia) (modified from Google Earth); b. Map of Moorea Island with location of five proposed future study zones marked with a red star (modified from Google Earth).

References

- Abrantes, F., Alt-Epping, U., Lebreiro, S., Voelker, A. and Schneider, R.** (2008) Sedimentological record of tsunamis on shallow-shelf areas: The case of the 1969 AD and 1755 AD tsunamis on the Portuguese Shelf off Lisbon. *Marine Geology*, **249**, 283–293.
- Allen, J.R.L.** (1984) Development in sedimentology 30: Sedimentary structures their character and physical basis. *Elsevier Science, Inc.*
- Arnaud, F., Lignier, V., Revel, M., Desmet, M., Beck, C., Pourchet, M., Charlet, F., Trentesaux, A. and Tribovillard, N.** (2002) Flood and earthquake disturbance of 210Pb geochronology (Lake Anterne, NW Alps). *Terra Nova*, **14**, 225–232.
- Atwater, B.F.** (1987) Evidence for Great Holocene Earthquakes Along the Outer Coast of Washington State. *Science*, **236**, 942–944.
- Baas, J.H., Best, J.L. and Peakall, J.** (2011) Depositional processes, bedform development and hybrid bed formation in rapidly decelerated cohesive (mud–sand) sediment flows. *Sedimentology*, **58**, 1953–1987.
- Bahlburg, H. and Weiss, R.** (2007) Sedimentology of the December 26, 2004, Sumatra tsunami deposits in eastern India (Tamil Nadu) and Kenya. *International Journal of Earth Sciences*, **96**, 1195–1209.
- Beavan, J., Wang, X., Holden, C., Wilson, K., Power, W., Prasetya, G., Bevis, M. and Kautoke, R.** (2010) Near-simultaneous great earthquakes at Tongan megathrust and outer rise in September 2009. *Nature*, **466**, 959–963.
- Berryman, K.** (2005) Review of tsunami hazard and risk in New Zealand. *Institute of Geological & Nuclear Sciences*.
- Borrero, J.C. and Goring, D.G.** (2015) South American Tsunamis in Lyttelton Harbor, New Zealand. *Pure Appl. Geophys.*, **172**, 757–772.

- Bourgeois, J., Bernard, E.N. and Robinson, A.R.** (2009) Geologic effects and records of tsunamis. *The sea*, **15**, 53–91.
- Bourgeois, J., Hansen, T.A., Wiberg, P.L. and Kauffman, E.G.** (1988) A tsunami deposit at the Cretaceous-Tertiary boundary in Texas. *Science*, **241**, 567–570.
- Butler, R.W., Eggenhuisen, J.T., Haughton, P. and McCaffrey, W.D.** (2016) Interpreting syndepositional sediment remobilization and deformation beneath submarine gravity flows; a kinematic boundary layer approach. *Journal of the Geological Society*, **173**, 46–58.
- Chagué-Goff, C., Schneider, J.-L., Goff, J.R., Dominey-Howes, D. and Strotz, L.** (2011) Expanding the proxy toolkit to help identify past events — Lessons from the 2004 Indian Ocean Tsunami and the 2009 South Pacific Tsunami. *Earth-Science Reviews*, **107**, 107–122.
- Chagué-Goff, C., Szczuciński, W. and Shinozaki, T.** (2017) Applications of geochemistry in tsunami research: A review. *Earth-Science Reviews*, **165**, 203–244.
- Choi, B.H., Pelinovsky, E., Kim, K.O. and Lee, J.S.** (2003) Simulation of the trans-oceanic tsunami propagation due to the 1883 Krakatau volcanic eruption. *Natural Hazards and Earth System Science*, **3**, 321–332.
- Cifuentes, I.L.** (1989) The 1960 Chilean earthquakes. *Journal of Geophysical Research: Solid Earth*, **94**, 665–680.
- Cisternas, M., Atwater, B.F., Torrejón, F., Sawai, Y., Machuca, G., Lagos, M., Eipert, A., Youlton, C., Salgado, I. and Kamataki, T.** (2005) Predecessors of the giant 1960 Chile earthquake. *Nature*, **437**, 404.
- Clark, J.D. and Stanbrook, D.A.** (2001) Formation of large-scale shear structures during deposition from high-density turbidity currents, Gres d’Annot Formation, south-east France. *Particulate gravity currents*, **31**, 219–232.
- Clark, J.T., Quintus, S., Weisler, M.I., Pierre, E.S., Nothdurft, L., Feng, Y. and Hua, Q.** (2016) Marine Reservoir Correction for American Samoa Using U-series and AMS Dated Corals. *Radiocarbon*, **58**, 851–868.

- Collinson, J.** (1994) Sedimentary deformational structures. In: *The geological deformation of sediments*, Springer, 95–125.
- Costa, P.J.M., Andrade, C. and Dawson, S.** (2015) Geological Recognition of Onshore Tsunami Deposits. In: *Environmental Management and Governance* (Ed. C.W. Finkl and C. Makowski), Springer International Publishing, Cham, 8, 3–32.
- Dawson, A.G.** (1994) Geomorphological effects of tsunami run-up and backwash. *Geomorphology*, **10**, 83–94.
- Dawson, A.G. and Stewart, I.** (2007) Tsunami deposits in the geological record. *Sedimentary Geology*, **200**, 166–183.
- Di Geronimo, I., Choowong, M. and Phantuwongraj, S.** (2009) Geomorphology and superficial bottom sediments of Khao Lak coastal area (SW Thailand). *Polish Journal of Environmental Studies*, **18**, 111–121.
- Dominey-Howes, D. and Thaman, R.** (2009) UNESCO-IOC International Tsunami Survey Team Samoa (ITST Samoa) Interim Report of Field Survey, 14th-21st October 2009. *Australian Tsunami Research Centre*.
- Donato, S.V., Reinhardt, E.G., Boyce, J.I., Pilarczyk, J.E. and Jupp, B.P.** (2009) Particle-size distribution of inferred tsunami deposits in Sur Lagoon, Sultanate of Oman. *Marine Geology*, **257**, 54–64.
- eCoast** (2018) Remembering the Tsunami of August 1868. In: eCoast. <https://www.ecoast.co.nz/tsunami-of-august-1868/>. Accessed 31 Jul 2019
- eCoast** 1868 Tsunami Trans-Pacific Propagation - YouTube. <https://www.youtube.com/watch?v=-Lv8aWhaeo8&feature=youtu.be>. Accessed 31 Jul 2019
- Einsele, G., Chough, S.K. and Shiki, T.** (1996) Depositional events and their records—an introduction. *Sedimentary Geology*, **104**, 1–9.
- Eychenne, J., Le Pennec, J.-L., Troncoso, L., Gouhier, M. and Nedelec, J.-M.** (2012) Causes and consequences of bimodal grain-size distribution of tephra fall deposited

- during the August 2006 Tungurahua eruption (Ecuador). *Bulletin of Volcanology*, **74**, 187–205.
- Feldens, P., Schwarzer, K., Sakuna, D., Szczuciński, W. and Sompongchaiyakul, P.** (2012) Sediment distribution on the inner continental shelf off Khao Lak (Thailand) after the 2004 Indian Ocean tsunami. *Earth Planet Sp*, **64**, 7.
- Feldens, P., Schwarzer, K., Szczucinski, W., Stattegger, K., Sakuna, D. and Sompongchaiyakul, P.** (2009) Impact of 2004 tsunami on seafloor morphology and offshore sediments, Pakarang Cape, Thailand. *Polish Journal of Environmental Studies*, **18**, 63–68.
- Fritz, H.M.** (2001) Lituya Bay case rockslide impact and wave run-up. *Science of tsunami Hazards*, **19**, 3–22.
- Fritz, H.M., Borrero, J.C., Synolakis, C.E., Okal, E.A., Weiss, R., Titov, V.V., Jaffe, B.E., Foteinis, S., Lynett, P.J., Chan, I.-C. and Liu, P.L.-F.** (2011) Insights on the 2009 South Pacific tsunami in Samoa and Tonga from field surveys and numerical simulations. *Earth-Science Reviews*, **107**, 66–75.
- Fryer, G.J., Watts, P. and Pratson, L.F.** (2004) Source of the great tsunami of 1 April 1946: a landslide in the upper Aleutian forearc. *Marine Geology*, **203**, 201–218.
- Fujiwara, O. and Kamataki, T.** (2007) Identification of tsunami deposits considering the tsunami waveform: An example of subaqueous tsunami deposits in Holocene shallow bay on southern Boso Peninsula, Central Japan. *Sedimentary Geology*, **200**, 295–313.
- Fujiwara, O., Masuda, F., Sakai, T., Irizuki, T. and Fuse, K.** (2000) Tsunami deposits in Holocene bay mud in southern Kanto region, Pacific coast of central Japan. *Sedimentary Geology*, **135**, 219–230.
- Goff, J. and Chagué-Goff, C.** (2014) The Australian tsunami database: A review. *Progress in Physical Geography*, **38**, 218–240.
- Goff, J., Chagué-Goff, C., Nichol, S., Jaffe, B. and Dominey-Howes, D.** (2012) Progress in palaeotsunami research. *Sedimentary Geology*, **243**, 70–88.

- Goff, J. and Dominey-Howes, D.** (2011) The 2009 South Pacific Tsunami. *Earth-Science Reviews*, **107**, v–vii.
- Goff, J., McFadgen, B.G. and Chagué-Goff, C.** (2004) Sedimentary differences between the 2002 Easter storm and the 15th-century Okoropunga tsunami, southeastern North Island, New Zealand. *Marine geology*, **204**, 235–250.
- Goff, J., Nichol, S., Chagué-Goff, C., Horrocks, M., McFadgen, B. and Cisternas, M.** (2010) Predecessor to New Zealand’s largest historic trans-South Pacific tsunami of 1868AD. *Marine Geology*, **275**, 155–165.
- Goldberg, E.D.** (1963) Geochronology with 210Pb. *Radioactive dating*, 121–131.
- Goodman-Tchernov, B.N. and Austin, J.A.** (2015) Deterioration of Israel’s Caesarea Maritima’s ancient harbor linked to repeated tsunami events identified in geophysical mapping of offshore stratigraphy. *Journal of Archaeological Science: Reports*, **3**, 444–454.
- Goodman-Tchernov, B.N., Dey, H.W., Reinhardt, E.G., McCoy, F. and Mart, Y.** (2009) Tsunami waves generated by the Santorini eruption reached Eastern Mediterranean shores. *Geology*, **37**, 943–946.
- Harbitz, C.B., Løvholt, F., Pedersen, G. and Masson, D.G.** (2006) Mechanisms of tsunami generation by submarine landslides: a short review.
- Hawkins, J.W. and Natland, J.H.** (1975) Nephelinites and basanites of the Samoan linear volcanic chain: Their possible tectonic significance. *Earth and Planetary Science Letters*, **24**, 427–439.
- Hills, J.G. and Goda, M.P.** (1999) Damage from comet-asteroid impacts with earth. *Physica D: Nonlinear Phenomena*, **133**, 189–198.
- Howard, J.D. and Reineck, H.-E.** (1981) Depositional Facies of High-Energy Beach-to-Offshore Sequence: Comparison with Low-Energy Sequence. *AAPG Bulletin*, **65**, 807–830.

- Jaffe, B.E., Gelfenbaum, G., Buckley, M.L., Watt, S., Apotsos, A., Stevens, A.W. and Richmond, B.M.** (2010) The limit of inundation of the September 29, 2009, tsunami on Tutuila, American Samoa. *U. S. Geological Survey*.
- Johnson, J.M., Tanioka, Y., Ruff, L.J., Satake, K., Kanamori, H. and Sykes, L.R.** (1994) The 1957 great Aleutian earthquake. In: *Shallow Subduction Zones: Seismicity, Mechanics and Seismic Potential*, Springer, 3–28.
- Jonathan, M.P., Srinivasalu, S., Thangadurai, N., Rajeshwara-Rao, N., Ram-Mohan, V. and Narmatha, T.** (2012) Offshore depositional sequence of 2004 tsunami from Chennai, SE coast of India. *Nat Hazards*, **62**, 1155–1168.
- Koppers, A.A.P., Russell, J.A., Jackson, M.G., Konter, J., Staudigel, H. and Hart, S.R.** (2008) Samoa reinstated as a primary hotspot trail. *Geology*, **36**, 435.
- Kortekaas, S. and Dawson, A.G.** (2007) Distinguishing tsunami and storm deposits: an example from Martinhal, SW Portugal. *Sedimentary Geology*, **200**, 208–221.
- Krishnaswamy, S., Lal, D., Martin, J.M. and Meybeck, M.** (1971) Geochronology of lake sediments. *Earth and Planetary Science Letters*, **11**, 407–414.
- La Selle, S., Richmond, B.M., Jaffe, B.E., Nelson, A.R., Griswold, F.R., Arcos, M.E., Chagué, C., Bishop, J.M., Bellanova, P. and Kane, H.H.** (2019) Sedimentary evidence of prehistoric distant-source tsunamis in the Hawaiian Islands.
- Lange, W.P.D. and Healy, T.R.** (1986) New Zealand tsunamis 1840–1982. *New Zealand Journal of Geology and Geophysics*, **29**, 115–134.
- Lay, T., Ammon, C.J., Kanamori, H., Rivera, L., Koper, K.D. and Hutko, A.R.** (2010) The 2009 Samoa–Tonga great earthquake triggered doublet. *Nature*, **466**, 964–968.
- Le Roux, J.P. and Vargas, G.** (2005a) Hydraulic behavior of tsunami backflows: insights from their modern and ancient deposits. *Environ Geol*, **49**, 65.
- Le Roux, J.P. and Vargas, G.** (2005b) Hydraulic behavior of tsunami backflows: insights from their modern and ancient deposits. *Environmental Geology*, **49**, 65.

- Macdonald, G.A.** (1968) A contribution to the petrology of Tutuila, American Samoa. *Geologische Rundschau*, **57**, 821–837.
- Mader, C.L. and Gittings, M.L.** (2002) Modeling the 1958 Lituya Bay mega-tsunami, II. *Science of Tsunami Hazards*, **20**, 241–250.
- Mader, C.L. and Gittings, M.L.** (2006) Numerical model for the Krakatoa hydrovolcanic explosion and tsunami. *Science of Tsunami Hazards*, **24**, 174.
- Magand, O. and Arnaud, F.** (2007) Response on the comment from Ribeiro Guevara and Arribere on the article ‘Radionuclide dating (Pb-210, Cs-137, Am-241) of recent lake sediments in a highly geodynamic setting (Lakes Puyehue and Icalma–Chilean Lake District).’ *Science of the Total Environment*, **385**, 312–314.
- Massari, F. and D’alessandro, A.** (2000) Tsunami-related scour-and-drape undulations in Middle Pliocene restricted-bay carbonate deposits (Salento, south Italy). *Sedimentary Geology*, **135**, 265–281.
- Matsumoto, D., Naruse, H., Fujino, S., Surphawajruksakul, A., Jarupongsakul, T., Sakakura, N. and Murayama, M.** (2008) Truncated flame structures within a deposit of the Indian Ocean Tsunami: evidence of syn-sedimentary deformation. *Sedimentology*, **55**, 1559–1570.
- McDougall, I.** (2010) Age of volcanism and its migration in the Samoa Islands. *Geological Magazine*, **147**, 705–717.
- McDougall, I.** (1985) Age and evolution of the volcanoes of Tutuila, American Samoa.
- Milker, Y., Wilken, M., Schumann, J., Sakuna, D., Feldens, P., Schwarzer, K. and Schmiedl, G.** (2013) Sediment transport on the inner shelf off Khao Lak (Andaman Sea, Thailand) during the 2004 Indian Ocean tsunami and former storm events: evidence from foraminiferal transfer functions. *Natural Hazards and Earth System Science*, **13**, 3113–3128.
- Miller, D.J.** (1960) The Alaska earthquake of July 10, 1958: giant wave in Lituya Bay. *Bulletin of the Seismological Society of America*, **50**, 253–266.

- Monecke, K., Finger, W., Klarer, D., Kongko, W., McAdoo, B.G., Moore, A.L. and Sudrajat, S.U.** (2008) A 1,000-year sediment record of tsunami recurrence in northern Sumatra. *Nature*, **455**, 1232–1234.
- Moore, A., Nishimura, Y., Gelfenbaum, G., Kamataki, T. and Triyono, R.** (2006) Sedimentary deposits of the 26 December 2004 tsunami on the northwest coast of Aceh, Indonesia. *Earth, Planets and Space*, **58**, 253–258.
- Morrison, R.J., Peshut, P.J. and Lasorsa, B.K.** (2010) Elemental composition and mineralogical characteristics of coastal marine sediments of Tutuila, American Samoa. *Marine Pollution Bulletin*, **60**, 925–930.
- Morton, R.A., Gelfenbaum, G. and Jaffe, B.E.** (2007) Physical criteria for distinguishing sandy tsunami and storm deposits using modern examples. *Sedimentary Geology*, **200**, 184–207.
- Mulder, T., Zaragosi, S., Jouanneau, J.-M., Bellaiche, G., Guérinaud, S. and Querneau, J.** (2009) Deposits related to the failure of the Malpasset Dam in 1959: An analogue for hyperpycnal deposits from jökulhlaups. *Marine Geology*, **260**, 81–89.
- Nanayama, F., Shigeno, K., Satake, K., Shimokawa, K., Koitabashi, S., Miyasaka, S. and Ishii, M.** (2000) Sedimentary differences between the 1993 Hokkaido-nansei-oki tsunami and the 1959 Miyakojima typhoon at Taisei, southwestern Hokkaido, northern Japan. *Sedimentary Geology*, **135**, 255–264.
- National Geophysical Data Center** Global Historical Tsunami Database.
- National Geophysical Data Center** (2019) Tsunami Data and Information | NCEI.
<https://www.ngdc.noaa.gov/hazard/tsu.shtml>. Accessed 31 Jul 2019
- Natland, J.H.** (1980) The progression of volcanism in the Samoan linear volcanic chain. *American Journal of Science*, **280**, 709–735.
- NGDC** (2018) NGDC/WDS Global Historical Tsunami Database | NCEI.
https://www.ngdc.noaa.gov/hazard/tsu_db.shtml. Accessed 15 May 2018
- Noda, A., Katayama, H., Sagayama, T., Suga, K., Uchida, Y., Satake, K., Abe, K. and Okamura, Y.** (2007) Evaluation of tsunami impacts on shallow marine sediments: An

- example from the tsunami caused by the 2003 Tokachi-oki earthquake, northern Japan. *Sedimentary Geology*, **200**, 314–327.
- Okal, E.A., Borrero, J.C. and Chagué-Goff, C.** (2011) Tsunamigenic predecessors to the 2009 Samoa earthquake. *Earth-Science Reviews*, **107**, 128–140.
- Okal, E.A. and Synolakis, C.E.** (2004) Source discriminants for near-field tsunamis. *Geophysical Journal International*, **158**, 899–912.
- PacificTWC** (2016) Tsunami Forecast Model Animation: Chile 1960.
- PacificTWC** (2017) Tsunami Forecast Model Animation: Aleutian Islands 1957.
- Pandaram, S. and Prasad, R.** (1992) Tropical Cyclone Val, 4-13 December 1991. *Fiji Meteorological Service*.
- Papadopoulos, G.A., Plessa, A. and Vassilopoulou, A.** (2000) A new tsunami catalogue of the Corinth Rift: 373 BC–AD 2000. *Historical earthquakes and tsunamis in the Corinth Rift, Central Greece, National Observatory of Athens, Institute of Geodynamics. Publ*, 122–126.
- Pararas-Carayannis, G.** (1999) Analysis of mechanism of tsunami generation in Lituya Bay. *Science of Tsunami Hazards*, **17**, 193–206.
- Pararas-Carayannis, G. and Dong, B.** (1980) Catalog of tsunamis in the Samoan Islands. *International Tsunami Information Center, Honolulu*, 74.
- Paris, R., Fournier, J., Poizot, E., Etienne, S., Morin, J., Lavigne, F. and Wassmer, P.** (2010) Boulder and fine sediment transport and deposition by the 2004 tsunami in Lhok Nga (western Banda Aceh, Sumatra, Indonesia): A coupled offshore–onshore model. *Marine Geology*, **268**, 43–54.
- Paris, R., Lavigne, F., Wassmer, P. and Sartohadi, J.** (2007) Coastal sedimentation associated with the December 26, 2004 tsunami in Lhok Nga, west Banda Aceh (Sumatra, Indonesia). *Marine Geology*, **238**, 93–106.
- Paris, R., Wassmer, P., Sartohadi, J., Lavigne, F., Barthomeuf, B., Desgages, E., Grancher, D., Baumert, P., Vautier, F. and Brunstein, D.** (2009) Tsunamis as

- geomorphic crises: lessons from the December 26, 2004 tsunami in Lhok Nga, west Banda Aceh (Sumatra, Indonesia). *Geomorphology*, **104**, 59–72.
- Petchey, F., Anderson, A., Zondervan, A., Ulm, S. and Hogg, A.** (2008) New marine ΔR values for the South Pacific subtropical gyre region. *Radiocarbon*, **50**, 373–397.
- Peters, R., Jaffe, B. and Gelfenbaum, G.** (2007) Distribution and sedimentary characteristics of tsunami deposits along the Cascadia margin of western North America. *Sedimentary Geology*, **200**, 372–386.
- Pfitzner, J., Brunskill, G. and Zagorskis, I.** (2004) ^{137}Cs and excess ^{210}Pb deposition patterns in estuarine and marine sediment in the central region of the Great Barrier Reef Lagoon, north-eastern Australia. *Journal of Environmental Radioactivity*, **76**, 81–102.
- Phantuwongraj, S. and Choowong, M.** (2012) Tsunamis versus storm deposits from Thailand. *Natural Hazards*, **63**, 31–50.
- Pilarczyk, J.E., Horton, B.P., Witter, R.C., Vane, C.H., Chagué-Goff, C. and Goff, J.** (2012) Sedimentary and foraminiferal evidence of the 2011 Tōhoku-oki tsunami on the Sendai coastal plain, Japan. *Sedimentary Geology*, **282**, 78–89.
- Pilarczyk, J.E. and Reinhardt, E.G.** (2012) Testing foraminiferal taphonomy as a tsunami indicator in a shallow arid system lagoon: Sur, Sultanate of Oman. *Marine Geology*, **295**, 128–136.
- Pongpiachan, S.** (2014) Application of binary diagnostic ratios of polycyclic aromatic hydrocarbons for identification of tsunami 2004 backwash sediments in Khao Lak, Thailand.
- Pongpiachan, S. and Schwarzer, K.** (2013) A CRITICAL REVIEW AND EVALUATION OF APPLYING SEMI-VOLATILE ORGANIC COMPOUNDS (SVOCs) AS A GEOCHEMICAL TRACER TO INDICATE TSUNAMI BACKWASH: The Bilateral, Deutsche Forschungsgemeinschaft (DFG) and National Research Council of Thailand (NRCT) Funded Project" Tsunami Deposits in Near-Shore-and Coastal Waters of Thailand (TUNWAT)".

- Pongpiachan, S., Thumanu, K., Tanthanuch, W., Tipmanee, D., Kanchai, P., Schwarzer, K. and Tancharakorn, S.** (2013a) Sedimentary features of tsunami backwash deposits as assessed by micro-beam synchrotron X-ray fluorescence (μ -SXRF) at the Siam photon laboratory. *Journal of Tsunami Society International*, **32**, 96–115.
- Pongpiachan, S., Tipmanee, D., Deelaman, W., Muprasit, J., Feldens, P. and Schwarzer, K.** (2013b) Risk assessment of the presence of polycyclic aromatic hydrocarbons (PAHs) in coastal areas of Thailand affected by the 2004 tsunami. *Marine pollution bulletin*, **76**, 370–378.
- Prasad, R.** (1990) Tropical Cyclone Ofa, 31 January to 7 February 1990. *Fiji Meteorological Service*.
- Puga-Bernabéu, Á. and Aguirre, J.** (2017) Contrasting storm-versus tsunami-related shell beds in shallow-water ramps. *Palaeogeography, Palaeoclimatology, Palaeoecology*, **471**, 1–14.
- Quintana, E.** (2011) Environmental impact of the nuclear tests in Argentina. In: *Comprehensive nuclear-test-ban treaty: Science and Technology Conference, Vienna, Austria: Commission for the Comprehensive Nuclear-Test-Ban Treaty Organization, Book of abstracts*, 45,
- Quintela, M., Costa, P.J., Fatela, F., Drago, T., Hoska, N., Andrade, C. and Freitas, M.C.** (2016) The AD 1755 tsunami deposits onshore and offshore of Algarve (south Portugal): sediment transport interpretations based on the study of Foraminifera assemblages. *Quaternary international*, **408**, 123–138.
- Reimer, P.J., Bard, E., Bayliss, A., Beck, J.W., Blackwell, P.G., Ramsey, C.B., Buck, C.E., Cheng, H., Edwards, R.L., Friedrich, M., Grootes, P.M., Guilderson, T.P., Haflidason, H., Hajdas, I., Hatté, C., Heaton, T.J., Hoffmann, D.L., Hogg, A.G., Hughen, K.A., Kaiser, K.F., Kromer, B., Manning, S.W., Niu, M., Reimer, R.W., Richards, D.A., Scott, E.M., Southon, J.R., Staff, R.A., Turney, C.S.M. and Plicht, J. van der** (2013) IntCal13 and Marine13 Radiocarbon Age Calibration Curves 0–50,000 Years cal BP. *Radiocarbon*, **55**, 1869–1887.

- Richmond, B.M., Buckley, M., Etienne, S., Chagué-Goff, C., Clark, K., Goff, J., Dominey-Howes, D. and Strotz, L.** (2011) Deposits, flow characteristics, and landscape change resulting from the September 2009 South Pacific tsunami in the Samoan islands. *Earth-Science Reviews*, **107**, 38–51.
- Riou, B., Chaumillon, E., Schneider, J.-L., Corrège, T. and Chagué, C.** (2018) The sediment-fill of Pago Pago Bay (Tutuila Island, American Samoa): New insights on the sediment record of past tsunamis. *Sedimentology*. doi: 10.1111/sed.12574
- Rubin, C.M., Horton, B.P., Sieh, K., Pilarczyk, J.E., Daly, P., Ismail, N. and Parnell, A.C.** (2017) Highly variable recurrence of tsunamis in the 7,400 years before the 2004 Indian Ocean tsunami. *Nature Communications*, **8**, 16019.
- Sakuna, D., Szczuciński, W., Feldens, P., Schwarzer, K. and Khokiattiwong, S.** (2012) Sedimentary deposits left by the 2004 Indian Ocean tsunami on the inner continental shelf offshore of Khao Lak, Andaman Sea (Thailand). *Earth, Planets and Space*, **64**, 931–943.
- Sakuna-Schwartz, D., Feldens, P., Schwarzer, K., Khokiattiwong, S. and Stattegger, K.** (2015) Internal structure of event layers preserved on the Andaman Sea continental shelf, Thailand: tsunami vs. storm and flash-flood deposits. *Natural Hazards and Earth System Science*, **15**, 1181–1199.
- Scheffers, A. and Kelletat, D.** (2004) Bimodal tsunami deposits—a neglected feature in paleo-tsunami research. *G. Schernewski und T. Dolch (Hrsg.): Geographie der Meere und Küsten, Coastline Reports 1*, 67–75.
- Shanmugam, G.** (2012) Process-sedimentological challenges in distinguishing paleo-tsunami deposits. *Natural Hazards*, **63**, 5–30.
- Shiki, T. and Yamazaki, T.** (1996) Tsunami-induced conglomerates in Miocene upper bathyal deposits, Chita Peninsula, central Japan. *Sedimentary Geology*, **104**, 175–188.
- Slootman, A., Simpson, G., Castelltort, S. and Boer, P.L. de** (2018) Geological record of marine tsunami backwash: The role of the hydraulic jump. *The Depositional Record*, **4**, 59–77.

- Smedile, A., De Martini, P.M. and Pantosti, D.** (2012) Combining inland and offshore paleotsunamis evidence: the Augusta Bay (eastern Sicily, Italy) case study. *Natural Hazards and Earth System Science*, **12**, 2557–2567.
- Smedile, A., De Martini, P.M., Pantosti, D., Bellucci, L., Del Carlo, P., Gasperini, L., Pirrotta, C., Polonia, A. and Boschi, E.** (2011) Possible tsunami signatures from an integrated study in the Augusta Bay offshore (Eastern Sicily—Italy). *Marine Geology*, **281**, 1–13.
- Smedile, A., Molisso, F., Chagué, C., Iorio, M., Martini, P.M.D., Pinzi, S., Collins, P.E.F., Sagnotti, L. and Pantosti, D.** (2019) New coring study in Augusta Bay expands understanding of offshore tsunami deposits (Eastern Sicily, Italy). *Sedimentology*. doi: 10.1111/sed.12581
- Srinivasalu, S., Jonathan, M.P., Thangadurai, N. and Ram-Mohan, V.** (2010) A study on pre- and post-tsunami shallow deposits off SE coast of India from the 2004 Indian Ocean tsunami: a geochemical approach. *Nat Hazards*, **52**, 391–401.
- Stuiver, M., Pearson, G.W. and Braziunas, T.** (1986) Radiocarbon age calibration of marine samples back to 9000 cal yr BP. *Radiocarbon*, **28**, 980–1021.
- Sugawara, D., Goto, K., Imamura, F., Matsumoto, H. and Minoura, K.** (2012) Assessing the magnitude of the 869 Jogan tsunami using sedimentary deposits: Prediction and consequence of the 2011 Tohoku-oki tsunami. *Sedimentary Geology*, **282**, 14–26.
- Sugawara, D., Minoura, K., Nemoto, N., Tsukawaki, S., Goto, K. and Imamura, F.** (2009) Foraminiferal evidence of submarine sediment transport and deposition by backwash during the 2004 Indian Ocean tsunami. *Island Arc*, **18**, 513–525.
- Switzer, A.D. and Jones, B.G.** (2008) Large-scale washover sedimentation in a freshwater lagoon from the southeast Australian coast: sea-level change, tsunami or exceptionally large storm? *The Holocene*, **18**, 787–803.
- Szczuciński, W., Kokociński, M., Rzeszewski, M., Chagué-Goff, C., Cachão, M., Goto, K. and Sugawara, D.** (2012) Sediment sources and sedimentation processes of 2011 Tohoku-oki tsunami deposits on the Sendai Plain, Japan—insights from diatoms, nannoliths and grain size distribution. *Sedimentary Geology*, **282**, 40–56.

- Takashimizu, Y. and Masuda, F.** (2000) Depositional facies and sedimentary successions of earthquake-induced tsunami deposits in Upper Pleistocene incised valley fills, central Japan. *Sedimentary Geology*, **135**, 231–239.
- Tamura, T., Sawai, Y., Ikehara, K., Nakashima, R., Hara, J. and Kanai, Y.** (2015) Shallow-marine deposits associated with the 2011 Tohoku-oki tsunami in Sendai Bay, Japan. *Journal of Quaternary Science*, **30**, 293–297.
- Tappin, D.R.** (2007) Sedimentary features of tsunami deposits—Their origin, recognition and discrimination: An introduction. *Elsevier*.
- Tchernov, B.G., Katz, T., Shaked, Y., Qupty, N., Kanari, M., Niemi, T. and Agnon, A.** (2016) Offshore Evidence for an Undocumented Tsunami Event in the ‘Low Risk’ Gulf of Aqaba-Eilat, Northern Red Sea. *PLOS ONE*, **11**, e0145802.
- Tipmanee, D., Deelaman, W., Pongpiachan, S., Schwarzer, K. and Sompongchaiyakul, P.** (2012) Using Polycyclic Aromatic Hydrocarbons (PAHs) as a chemical proxy to indicate Tsunami 2004 backwash in Khao Lak coastal area, Thailand. *Natural Hazards and Earth System Sciences*, **12**, 1441–1451.
- Toyofuku, T., Duros, P., Fontanier, C., Mamo, B., Bichon, S., Buscail, R., Chabaud, G., Deflandre, B., Goubet, S., Grémare, A., Menniti, C., Fujii, M., Kawamura, K., Koho, K.A., Noda, A., Namegaya, Y., Oguri, K., Radakovitch, O., Murayama, M., de Nooijer, L.J., Kurasawa, A., Ohkawara, N., Okutani, T., Sakaguchi, A., Jorissen, F., Reichart, G.-J. and Kitazato, H.** (2014) Unexpected biotic resilience on the Japanese seafloor caused by the 2011 Tōhoku-Oki tsunami. *Scientific Reports*, **4**, 7517.
- Tyuleneva, N., Braun, Y., Katz, T., Suchkov, I. and Goodman-Tchernov, B.** (2018) A new chalcolithic-era tsunami event identified in the offshore sedimentary record of Jisr al-Zarka (Israel). *Marine Geology*, **396**, 67–78.
- Van Den Bergh, G.D., Boer, W., De Haas, H., Van Weering, T.C. and Van Wijhe, R.** (2003) Shallow marine tsunami deposits in Teluk Banten (NW Java, Indonesia), generated by the 1883 Krakatau eruption. *Marine Geology*, **197**, 13–34.

- Veerasingam, S., Venkatachalapathy, R., Basavaiah, N., Ramkumar, T., Venkatramanan, S. and Deenadayalan, K.** (2014) Identification and characterization of tsunami deposits off southeast coast of India from the 2004 Indian Ocean tsunami: Rock magnetic and geochemical approach. *Journal of earth system science*, **123**, 905–921.
- Wang, X. and Liu, P.L.-F.** (2006) An analysis of 2004 Sumatra earthquake fault plane mechanisms and Indian Ocean tsunami. *Journal of Hydraulic Research*, **44**, 147–154.
- Ward, S.N.** (2002) Tsunamis.
- Ward, S.N.** (2001) Landslide tsunami. *Journal of Geophysical Research: Solid Earth*, **106**, 11201–11215.
- Ward, S.N. and Asphaug, E.** (2002) Impact tsunami–Eltanin. *Deep Sea Research Part II: Topical Studies in Oceanography*, **49**, 1073–1079.
- Ward, S.N. and Asphaug, E.** (2003) Asteroid impact tsunami of 2880 March 16. *Geophysical Journal International*, **153**, F6–F10.
- Ward, S.N. and Day, S.** (2005) Tsunami thoughts. *CSEG Recorder*, 38–44.
- Weiss, R. and Bahlburg, H.** (2006) A Note on the Preservation of Offshore Tsunami Deposits. *Journal of Sedimentary Research*, **76**, 1267–1273.
- Williams, S., Prasetya, G., Chagué-Goff, C., Goff, J., Cheung, K.F., Davies, T. and Wilson, T.** (2011a) Characterising diagnostic proxies for identifying palaeotsunamis in a tropical climatic regime, Samoan Islands. In: *OCEANS'11 MTS/IEEE KONA, IEEE*, 1–10.
- Williams, S.P., Goff, J.R., Sale, F., AH KAU, J., Prasetya, G., Davies, T.R., Cheung, K.F. and Wilson, T.** (2011b) Sands of Time: Evidence for palaeotsunamis and/or palaeostorms in Samoa, and what this means for tsunami risk reduction. In: *Proceedings of the Samoa National Environment Forum*, 2010, 15–25.
- Witter, R., Briggs, R., Engelhart, S.E., Gelfenbaum, G., Koehler, R.D., Nelson, A., Selle, S.L., Corbett, R. and Wallace, K.** (2019) Evidence for frequent, large tsunamis

spanning locked and creeping parts of the Aleutian megathrust. *GSA Bulletin*, **131**, 707–729.

Witter, R.C., Carver, G.A., Briggs, R.W., Gelfenbaum, G., Koehler, R.D., La Selle, S., Bender, A.M., Engelhart, S.E., Hemphill-Haley, E. and Hill, T.D. (2016) Unusually large tsunamis frequent a currently creeping part of the Aleutian megathrust. *Geophysical Research Letters*, **43**, 76–84.

Yoshikawa, S., Kanamatsu, T., Goto, K., Sakamoto, I., Yagi, M., Fujimaki, M., Imura, R., Nemoto, K. and Sakaguchi, H. (2015) Evidence for erosion and deposition by the 2011 Tohoku-oki tsunami on the nearshore shelf of Sendai Bay, Japan. *Geo-Marine Letters*, **35**, 315–328.

Abstract

Following recent destructive tsunamis, especially the 2004 Indian Ocean Tsunami and the 2011 Tohoku-Oki Tsunami, and their worldwide coverage, there has been a growing interest in tsunami research amongst the scientific community. However, most of the studies dealing with geological evidence of past tsunamis focus on onshore deposits, leaving aside marine deposits despite their potential for recording of the backwash phase. Moreover, the few studies on tsunami marine deposits were carried out in open and dynamic shallow marine environments, which are not favorable for long-time preservation. In this study, we focus on sheltered bays of Tutuila (American Samoa) frequently impacted by tsunamis, supposed to offer ideal preservation potential, to gain knowledge on tsunami backwash deposits. The sediment-fill of Pago Pago Bay was first examined. The internal architecture and sediment facies show that the bay infilling was emplaced during the last 12 000 years through the last sea-level rise and highstand. The upper bay-fill consists of alternations between low-energy and high-energy sediment units, interpreted as stacked tsunami backwash deposits, emplaced during the last millenaries. Within the uppermost meter-thick silty unit, backwash deposits emplaced following the 2009 South Pacific Tsunami and the 1960 Great Chilean Earthquake Tsunami were identified based on geochemical, mineralogical and micro-structural signatures. Basal microstructural features give evidence that those tsunami backflows behave as hyperpycnal currents. Finally, backwash deposits of four recent tsunamis were identified in bays located along the north shore of Tutuila, including the 2009 South Pacific Tsunami, the 1960 Great Chilean Earthquake Tsunami or the 1957 Aleutian Islands Tsunami, the 1917 Tonga Trench Tsunami and an older tsunami never reported in American Samoa, most likely the 1868 South American Tsunami. Backwash deposits emplaced by the 1868 South American Tsunami would represent the first marine geological evidence of this tsunami. As a whole, this study shows the great potential of sheltered shallow marine environments for tsunami backwash archiving, with at least four tsunami backwash deposits identified for the last 150 years in the bays of Tutuila. In addition, this work provides new identification criteria for tsunami backwash deposits, particularly in comparison with flash-flood deposits.

Keywords: tsunami, backwash, plaeotsunami, shallow marine, sediment-fill, hyperpycnal currents



UMR 7266-CNRS, Littoral ENvironnements et Sociétés, Université de La Rochelle
2 rue Olympe de Gouges, F-17000, La Rochelle